AGING PHENOMENA IN

FERROUS MARTENSITES

by

KEITH ALLEN TAYLOR

S.B., Massachusetts Institute of Technology
(1980)

Submitted in partial fulfillment of the requirements

for the degree of

DOCTOR OF SCIENCE

at the

MASSACHUSETTS INSTITUTE OF TECHNOLOGY

June 1985

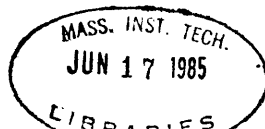© Massachusetts Institute of Technology

Signature of Author_____
Department of Materials Science and Engineering
May 3, 1985

Certified by_____
John B. Vander Sande
Thesis Supervisor

Certified by_____
Gregory B. Olson
Thesis Supervisor

Certified by_____
Morris Cohen
Thesis Supervisor

Accepted by_____
Bernhardt J. Wuensch
Chairman, Departmental Committee on Graduate Students

AGING PHENOMENA IN FERROUS MARTENSITES

by

KEITH ALLEN TAYLOR

Submitted to the Department of Materials Science and Engineering
on May 3, 1985 in partial fulfillment of the requirements
for the Degree of Doctor of Science in Metallurgy

ABSTRACT

Transmission electron microscopy (TEM) and electrical resistivity measurements have been used to follow the aging and first stage of tempering of martensitic steels. TEM was employed to study structural changes directly, while the resistivity measurements provided important kinetic data. Two Fe-Ni-C alloys (Fe-25Ni-0.4C and Fe-15Ni-1C) with subambient M_s temperatures were selected for this study in order to eliminate the complications of autotempering which are normally encountered in binary Fe-C alloys.

The martensites of both alloys display the common plate-like morphology. The substructure consists of {112} transformation twins, <111> lattice screw dislocations, as well as planar defects having a {011} habit. Carbon atoms tend to occupy only one of the three available octahedral interstitial sublattices in virgin martensite; however, the carbon atoms in {011} defects are related to those in their surroundings by a twinning operation on {011}. Moderate volume fractions of such twins are sufficient to account for anomalous axial ratios previously measured in these martensites.

Aging at room temperature results in the rapid development of a structural modulation along the four equivalent <20$\bar{3}$> directions of the tetragonal martensitic structure. The result is a fine-scale "tweed" morphology which is readily detected by TEM throughout the entire martensitic phase. The initial wavelength decreases with the alloy carbon content; it is about 2.5 and 1.5 nm for Fe-25Ni-0.4C and Fe-15Ni-1C, respectively. The activation energy (Q) is initially about 84 kJ/mole (20 kcal/mole), but increases by about 10 kJ/mole during aging. However, in the early stages of aging Q is consistently 8 - 25 kJ/mole higher in Fe-15Ni-1C as compared to Fe-25Ni-0.4C. The magnitude of Q indicates that carbon diffusion is the single rate-controlling process during aging. The increase in Q with carbon content is qualitatively consistent with predictions of a concentration dependence of the diffusivity of carbon in tetragonal martensite. The martensitic substructure does not appear to exert any substantial influence on the overall aging process.

Results from a concurrent atom-probe study at Oxford University show that the tweed structure represents a periodic modulation in carbon concentration and that the composition amplitude increases with aging time; prolonged aging of Fe-15Ni-1C at room temperature leads to alternating carbon-rich and carbon-poor bands containing about 11 and 0.2 at pct

2

carbon, respectively. The increase in composition amplitude and the aligned nature of the aging product indicate that a coherent spinodal decomposition is occurring. Given the ordered nature of virgin martensite as well as some previous evidence for secondary ordering during aging, it appears appropriate to call the reaction a conditional spinodal decomposition. A simple phenomenological thermodynamic model is presented which predicts a miscibility gap (consistent with the atom probe results) in the Fe-C system when a carbon ordering energy is included.

Spinodal decomposition is followed by transition carbide precipitation both at and above room temperature. The carbides do not display hexagonal symmetry. They may be a partially ordered version of the ϵ-carbide structure, e.g. the η-carbide structure proposed in other recent TEM studies. The carbides adopt a plate-like shape with a habit near {102} and exhibit basal plane stacking faults which are spaced at 1 - 1.5 nm intervals. The morphologic and crystallographic features of these carbides are explained in terms of an invariant-plane strain transformation. There is strong evidence that carbides nucleate heterogeneously on the carbon-rich bands which form during aging. Nucleation is aided by the favorable shape strain which relates a tetragonally-distorted high carbon band to its low-carbon surroundings. The similarity of the carbide and spinodal habits enables the carbide to align with the interface between high- and low-carbon bands and thereby take advantage of the available interfacial free energy. No nucleation was directly observed on lattice dislocations; however {112} twin boundaries can influence the precipitation behavior.

The apparent activation energy increases to 125 - 145 kJ/mole (30 - 35 kcal/mole) during tempering. The continuous increase during aging and on into tempering indicates that the kinetics of carbide precipitation become influenced by a process other than carbon diffusion. It is suggested that the propogation of the martensite/carbide interface, as well as carbon diffusion, are the processes which influence the carbide growth rate; the conservative nature of the invariant-plane strain which converts carbon-enriched martensite to the transition carbide does not require any intrinsic diffusional transport of metal atoms for sustained growth.

The two alloys of this study exhibit identical aging and tempering behavior, apart from slight differences in kinetics. The similarity of the current {203} tweed and the {102} tweed in Fe-C, Fe-Cr-C, and Fe-Mn-C alloys indicates that spinodal decomposition is an aging reaction common to a wide variety of iron-base carbon martensites. Moreover, the severe coherency strains associated with decomposition may be responsible for the inherent brittleness of nominally untempered martensites.

Thesis Supervisors: Dr. John B. Vander Sande
                     Professor of Materials Science

                     Dr. Gregory B. Olson
                     Principal Research Associate

                     Dr. Morris Cohen
                     Institute Professor, Emeritus

3

TABLE OF CONTENTS

LIST OF FIGURES

9

10

LIST OF TABLES

ACKNOWLEDGEMENTS

CHAPTER 1

INTRODUCTION

Perhaps one of the most fundamental concepts guiding metallurgists in their research is the notion that crystallography and microstructure have a profound influence on the physical properties of materials. So-called "structure-property relations" have been and are currently being sought in all areas of materials research. Steel, a very important engineering material, is certainly no exception and is undoubtedly the most extensively studied alloy class. Indeed, without steel, modern industrial society as we know it would be impossible.

Great strides have been made in our understanding of the physical metallurgy of steels over the years, thanks to the painstaking efforts of a list of investigators so long it could fill this thesis. For example, we now know that the polymorphic transformation which converts face-centered cubic (FCC) iron to body-centered cubic (BCC) can, in the presence of dissolved carbon, produce the metastable "martensite" phase, important for its high strength. We also know that if such martensite is heated to intermediate temperatures, giving rise to some carbon segregation, ductility can be substantially improved with little loss of strength. The latter treatment has been traditionally referred to as "tempering."

It did not take long for metallurgists to realize that the decomposition of ferrous martensites (tempering) consists of a complicated series of reactions whose end product is essentially a dispersion of cementite in a ferritic matrix, plus possibly other carbides when carbide-forming elements are present. The carbide which precipitates first during tempering was discovered by Jack [1]. He called it "epsilon-carbide" and its appearance has since been referred to as the "first stage of

20

tempering." Other stages of tempering have also been identified.

In addition, we now also know that structural changes occur in martensite well before epsilon-carbide can be identified. Olson and Cohen [2] have suggested that such changes be referred to as "aging" so that the designations of the traditional stages of tempering may remain intact. This thesis is intended to provide further insights into the nature of aging and the relation between aging and the precipitation of epsilon-carbide, i.e. the first stage of tempering. It is hoped that this research will eventually lead to a better understanding and control of the mechanical behavior of quenched and tempered steels.

CHAPTER 2

LITERATURE REVIEW

2.1 Martensite Formation

This review of the aging and tempering of ferrous martensites begins with the origin of martensite; the portion of the iron-carbon phase diagram of Figure 2-1 provides a useful aid for subsequent discussion. The phases of primary interest here are the high-temperature FCC γ-phase, austenite, and the low-temperature BCC α-phase, ferrite. Carbon is soluble to some extent in both phases, but the maximum solubility is much higher in austenite as compared to ferrite ($\sim$2.1 vs. 0.02 wt pct at the eutectic and eutectoid temperatures, respectively). From this diagram then, one would predict that an austenite containing more than 0.02 wt pct carbon would decompose into a two-phase low-carbon ferrite + cementite (or graphite) mixture upon cooling to room temperature; with slow cooling this is indeed the case. However, if cooling is sufficiently rapid so as to prevent carbon segregation, austenite can be converted in a diffusionless manner to a body-centered phase. The transformation product is then supersaturated with respect to carbon and is given the name "martensite" in order to distinguish this phase from ferrite formed via higher-temperature reactions where diffusion occurs.

The transformation which produces martensite from austenite is the prototype for an entire subclass of reactions known as martensitic transformations. A martensitic transformation is a first-order solid-state structural change which is (a) displacive, (b) diffusionless, and (c) dominated in kinetics and morphology by strain energy arising from shear-like displacements. These three characteristics have recently been suggested by Cohen et al. [4] as both necessary and sufficient conditions
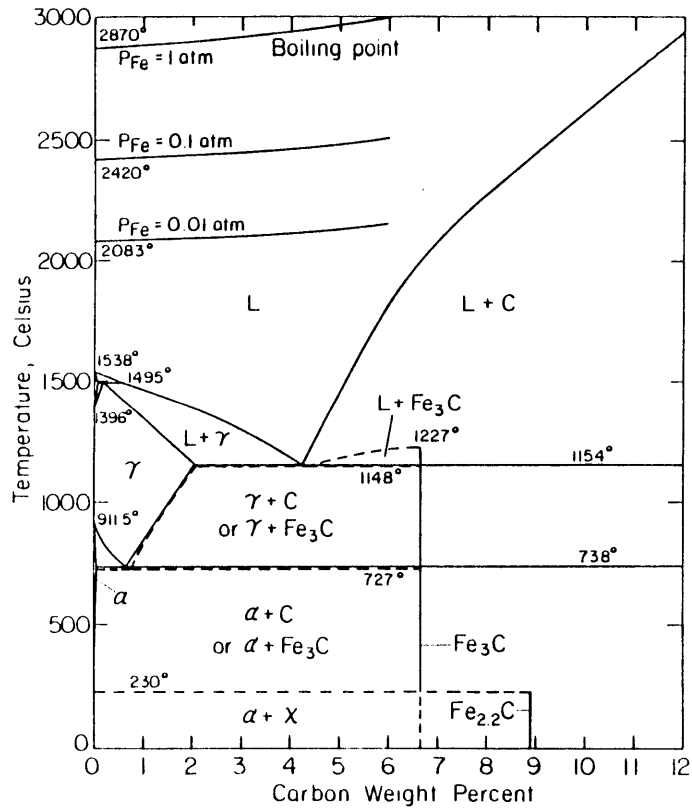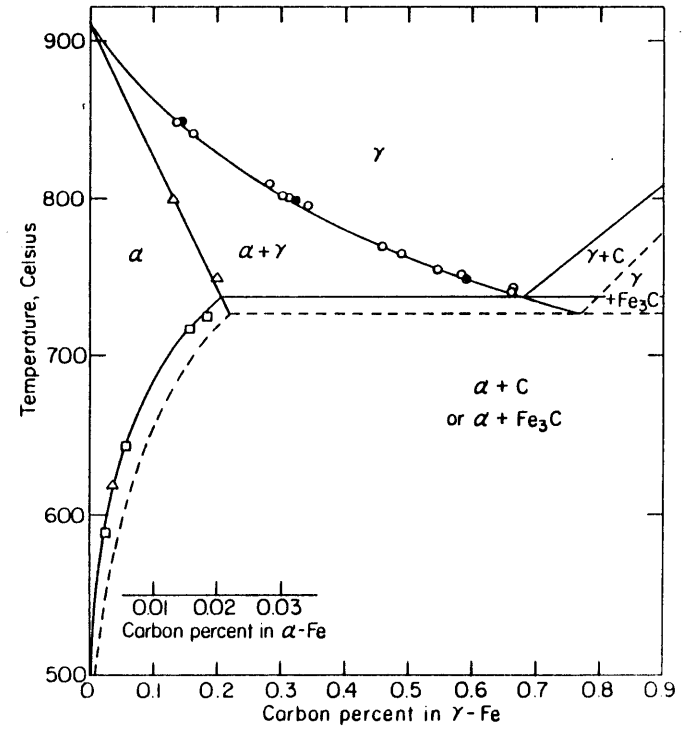
Figure 2-1. The iron-carbon phase diagram, (A). An enlargement of the region most important for steel treating is shown in (B). The metastable system iron-cementite (Fe_3C) is denoted by dashed lines (from Chipman [3]).

for defining a martensitic transformation. Because the transformation
itself is diffusionless, extremely high growth rates can be attained,
approaching the velocity of elastic waves in the alloy [5]. In alloys
where fast growth occurs, the overall transformation kinetics are limited by
nucleation. The nucleation step is then regarded as athermal in the sense
that more and more nuclei are activated during cooling due to the
increasing thermodynamic driving force.

Another interesting aspect of the iron-carbon system is the fact that
carbon tends to stabilize the austenite, i.e. lowers the temperature at
which ferrite or martensite forms. Other austenite stabilizers
particularly effective in lowering the "martensite start" (M_s) temperature
include nitrogen, manganese, and nickel. Ferrite stabilizers such as
chromium and molybdenum lower M_s to a lesser extent. Aluminum, cobalt,
titanium, and vanadium are noteworthy in that they raise M_s.

The thermodynamics and kinetics of martensitic transformations, though
an important and active area of research over the years, will not be
discussed further here. For more extensive coverage the reader is referred
to the early but excellent review by Kaufman and Cohen [6] and to the more
recent book by Nishiyama [7] and review paper by Cohen and Wayman [8].

2.2 The Structure of Austenite

Austenite is a solid solution with FCC (space group Fm3m) iron as the
solvent. Substitutional solute atoms are often present; the most common
ones for steels include manganese, silicon, nickel, and chromium. In low-
alloy steels, these elements may be assumed to occupy lattice sites at
random and therefore the austenitic solution retains its cubic symmetry.
If there is a size misfit, substitutional solutes may produce either an

overall expansion or contraction of the lattice which (at small

concentrations) varies linearly with solute content. Following

Khachaturyan [9], a tensor, u_{ij}, can be defined which describes the

macroscopic lattice strain associated with unit concentration of solute.

Some of the elements of the lattice expansion tensor are identically zero

in cases where solute atoms occupy lattice sites of high symmetry. For

FCC, all lattice sites are equivalent and possess m3m point symmetry. Thus

we need only consider one lattice expansion tensor; furthermore, since the

expansion is equal along the three crystal axes there is only one

independent, non-zero element in the tensor:

$$u_{ij}^{FCC} = \begin{bmatrix} u_{11} & 0 & 0 \\ 0 & u_{11} & 0 \\ 0 & 0 & u_{11} \end{bmatrix}. \tag{2-1}$$

The lattice constant, a, is then given by

$$a = a_o(1 + u_{11}n) \tag{2-2}$$

where n is the fraction of lattice sites occupied by solutes and a_o is the

lattice constant of the pure solvent (iron).

As an example of the above concept, consider the variation of the

austenite lattice constant with nickel content. Ruhl [10] suggests the

following relation:

$$a(Fe\text{-}Ni) = 0.3572 + 0.00003(w/oNi) \text{ nm}$$

or in terms of Equation 2-2,

$$a(Fe\text{-}Ni) = 0.3572(1 + 0.0084n_{Ni}) \text{ nm}. \tag{2-3}$$

Note that the lattice expansion produced is quite small, consistent with the fact that iron and nickel have similar atomic radii.

Interstitial solutes also exist in the austenite phase, carbon being the most important for steels. There seems to be some disagreement regarding the site occupancy of interstitials in austenite, but investigations utilizing Mössbauer effect spectroscopy (MES) [11-13] and neutron diffraction [14] leave little doubt that the vast majority of carbon atoms occupy octahedral interstitial sites (OIS). The location of several OIS are shown in the schematic drawing of the FCC structure of Figure 2-2. Each OIS is crystallographically equivalent, possessing the same symmetry as the host lattice sites. There are four OIS per unit cell, each coordinated by six iron atoms located at the vertices of a regular octahedron (hence the name "octahedral" site). Note that the FCC lattice sites and the OIS form two interpenetrating FCC lattices.

Since interstitials in OIS occupy positions of cubic symmetry, their lattice expansion tensor is also given by Equation 2-1. Ruhl [10] suggests the following relation between the austenite lattice constant and carbon content for Fe-C alloys:

$$a(\text{Fe-C}) = 0.3572 + 0.0033(\text{w/oC}) \text{ nm}$$

or $\qquad a(\text{Fe-C}) = 0.3572(1 + 0.199 n_C) \text{ nm}$ $\hfill$ (2-4)

where n_C is given by N_C/N_{Fe}, the ratio of carbon atoms to iron atoms. This ratio is identically equal to the fraction of OIS occupied by carbon since the total number of OIS is identically equal to the total number of iron atoms.

The investigators of References [11-13] were able to carry their interpretation of Mössbauer spectra a step further and drew conclusions

26

● METAL ATOMS

○ OCTAHEDRAL INTERSTICES

● METAL ATOMS

○ TETRAHEDRAL INTERSTICES
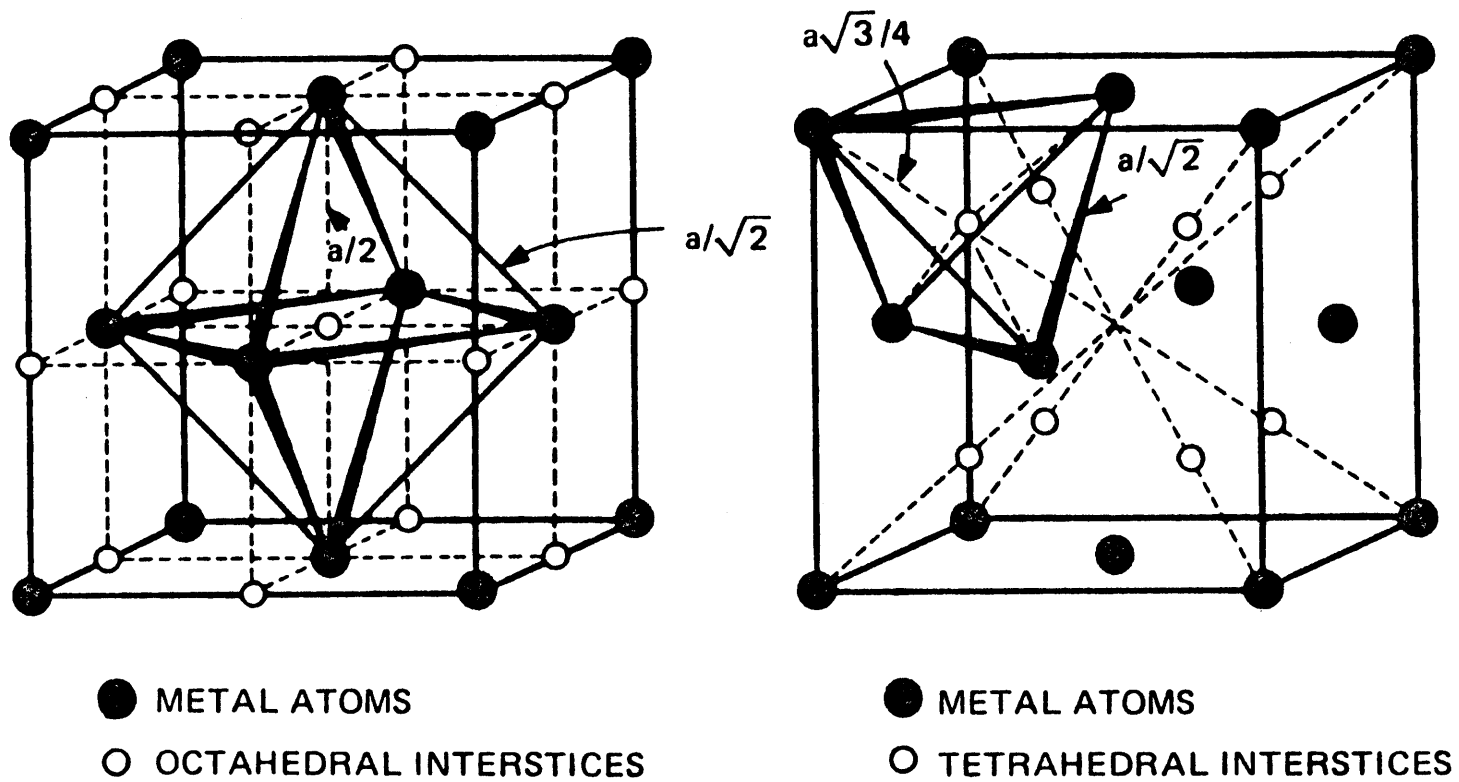
Figure 2-2. Schematic representation of the FCC structure showing octahedral and
tetrahedral interstitial sites (from Leslie [15]).

regarding the distribution of carbon atoms in the austenite. They found

only two peaks in their spectra: one due to iron atoms having no near-

neighbor carbon atoms and another split peak due to iron atoms having one

near-neighbor carbon. No peak was detected which could be associated with

iron atoms having two near-neighbor carbons, even though a random

distribution of carbon would produce such a peak since 8-10% of all iron

atoms would then have had two near-neighbor carbons (at the carbon

concentrations which were studied). Clearly, this is evidence of a non-

random solution where the relative intensities of the two kinds of

Mössbauer peaks are consistent with a repulsive carbon-carbon interaction

which tends to disperse carbon and inhibits carbon clustering. A repulsive

carbon-carbon interaction in austenite has also been suggested on

thermodynamic grounds [16].

2.3 The Structure of Virgin Martensite

As stated previously, the martensitic FCC → BCC transformation in

ferrous alloys is diffusionless and, in fact, belongs to the broader class

of diffusionless/displacive solid-state transformations. Displacive

structural changes require a coordinated shift of atoms and are sometimes

referred to descriptively as "military" transformations [8]. This implies

the existence of a <u>lattice</u> <u>correspondence</u> between the austenite and

martensite phases, such as indicated in Figure 2-3. Figure 2-3(A) shows

two unit cells of the FCC structure, where the alternative body-centered

tetragonal (BCT) unit cell is also outlined. The BCT unit cell, Figure 2-

3(B), can be transformed to a BCC cell, Figure 2-3(C), by appropriate

contraction along the z-axis and expansion along the x'- and y'-axes. Such

a <u>lattice</u> <u>deformation</u> was originally proposed by Bain [18] and is known as
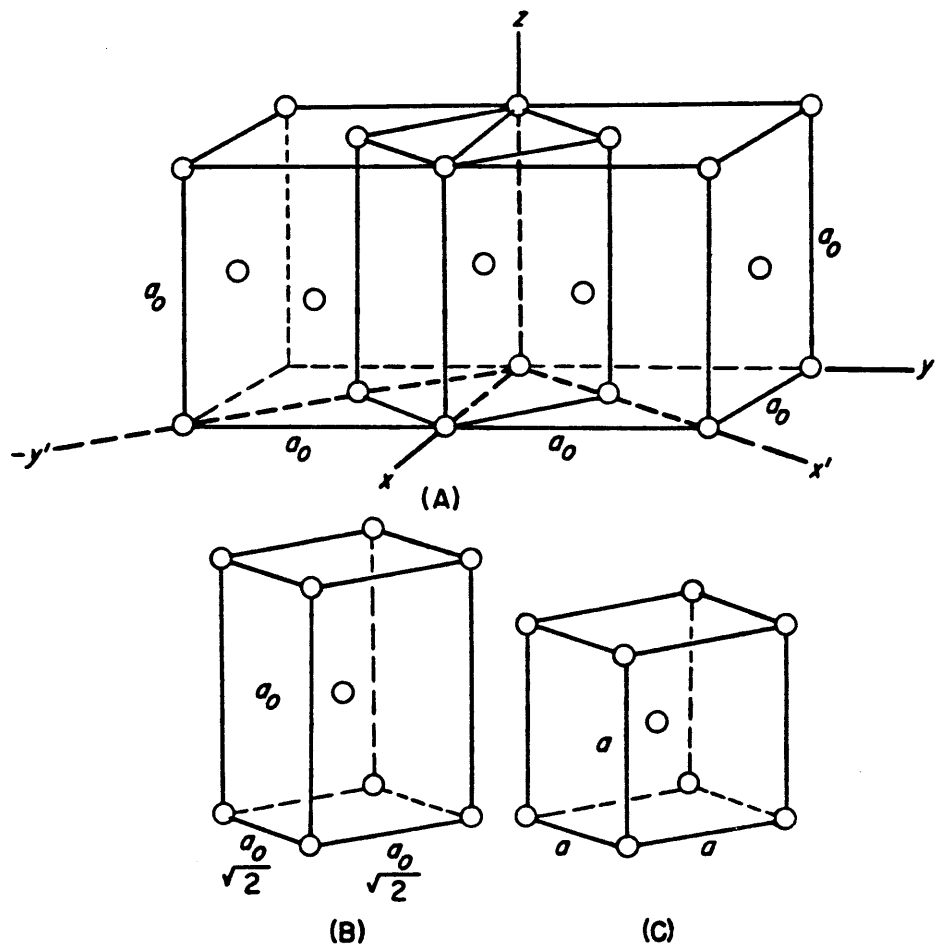
Figure 2-3. The Bain distortion for the FCC → BCC
transformation. The BCT cell is outlined in
the FCC structure in (A), and shown alone in
(B). The Bain distortion converts (B) to (C)
(from Reed-Hill [17]).

the "Bain distortion."

Each site of the FCC and BCC Bravais lattices possesses the same point symmetry, m3m. However, the Bain distortion reduces the symmetry of the OIS from cubic (point group m3m) in the case of FCC to tetragonal (point group 4/mmm) in the case of BCC. Furthermore, additional OIS arise as a result of the distortion. The OIS of the BCC lattice are indicated in Figure 2-4, where careful examination will reveal six such sites per unit cell (three per lattice site as compared with one per lattice site in the case of FCC), each characterized by shorter interatomic distance along one of the cube axes. Thus, there are three sets of OIS which together form three interpenetrating BCC sublattices. Each sublattice is designated as either O_x, O_y or O_z, depending on whether the nearest BCC lattice points lie along the [100], [010] or [001] directions, respectively.

Since the Bain distortion results in a symmetry change, the lattice expansion tensor for BCC octahedral interstitials is different in form from that for FCC. An interstitial (such as carbon) in the O_z sublattice produces a distortion which is different and more severe along [001] than along [100] and [010], requiring the lattice expansion tensor to take on the following form:

$$u_{ij}^{BCC}(z) = \begin{bmatrix} u_{11} & 0 & 0 \\ 0 & u_{11} & 0 \\ 0 & 0 & u_{33} \end{bmatrix}.$$
(2-5)

Similar tensors exist for interstitials in the O_x and O_y sublattices.

Close inspection of Figure 2-3 reveals an interesting aspect of the Bain correspondence, namely that all FCC OIS are transformed to BCC O_z sites. This correspondence produces a "virgin" martensite (unaltered in
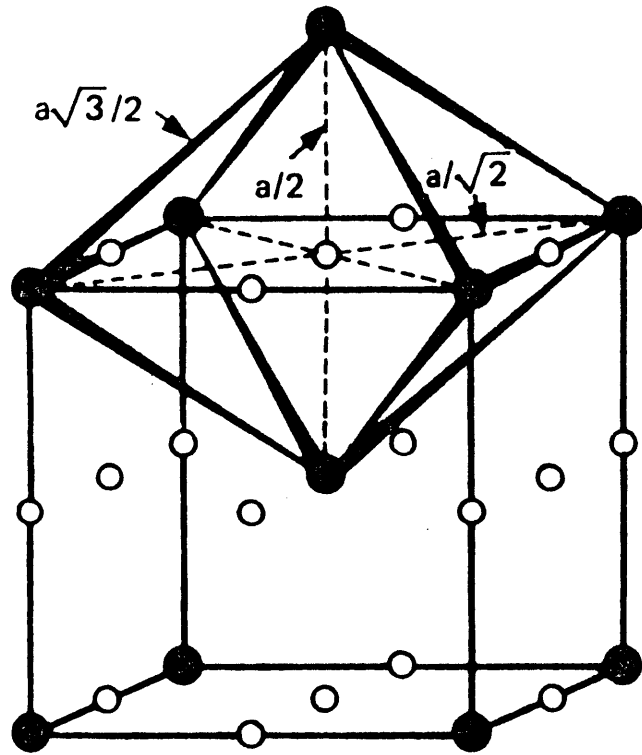
31
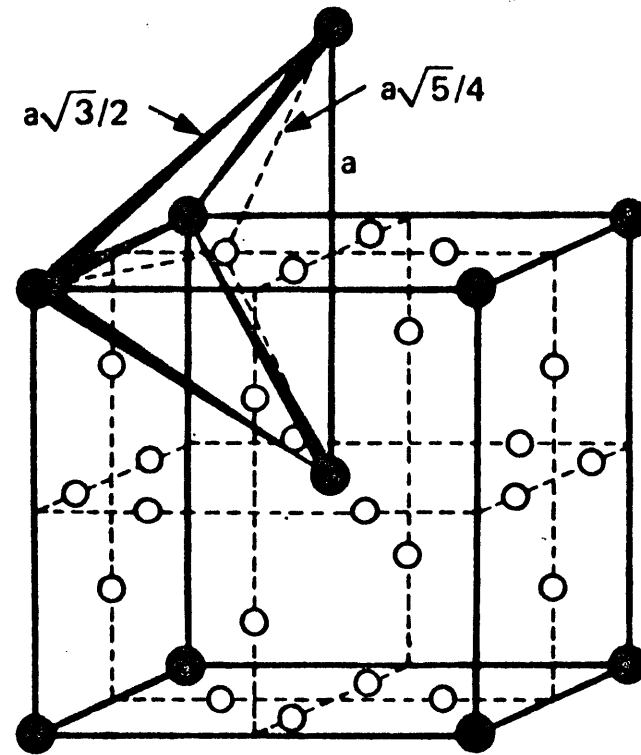
Figure 2-4. Schematic representation of the BCC structure showing octahedral and tetrahedral interstitial sites (from Leslie [15]).

structure by thermally-activated diffusive processes) whose carbon concentration-dependent lattice constants are given by

$$a = b = a_o^{BCC}(1 + u_{11}n_C) \qquad (2\text{-}6A)$$

$$c = a_o^{BCC}(1 + u_{33}n_C), \qquad (2\text{-}6B)$$

where a_o^{BCC} is the lattice constant of pure BCC iron. The macroscopic tetragonality of iron-carbon martensites is familiar to metallurgists and is convincing evidence of the preferential occupation of the O_z sublattice by carbon. Moreover, this ordered (in the sense that only one of the three OIS sublattices is populated) arrangement is somewhat stable since the macroscopic tetragonality of martensite persists for long times at ambient temperature, where the diffusivity of carbon is appreciable.

Mössbauer spectra of virgin and freshly-formed martensites have accordingly been interpreted in terms of octahedral-site occupancy by carbon [19], although conventional MES cannot distinguish between O_z and O_x or O_y occupancy. Fujita et al. [20] and Ino et al. [21] also suggest that some carbon atoms occupy tetrahedral interstitial sites (TIS) in virgin martensite (Figure 2-4). However, the corresponding contribution to their Mössbauer spectra disappeared upon aging near ambient temperatures and was taken to reflect the migration of carbon from unstable TIS to O_z sites. Several investigators have found evidence indicating that carbon atoms are not distributed randomly among the O_z sites in virgin martensite [12,13,22], but are as widely separated as possible, a configuration presumably inherited from the austenite phase via the Bain correspondence.

To summarize, structural investigations of virgin and freshly-formed martensites indicate that carbon atoms tend to occupy interstitial sites of the O_z kind. Thermodynamic treatments of the "ordered" distribution of

carbon atoms have been presented by Zener [23,24] and Khachaturyan [9] using arguments based on the elastic interaction between carbon atoms in BCC iron. Sherman [25] has reviewed various early treatments of the carbon-carbon interaction and points out that the predictions of all are qualitatively similar; namely that a critical temperature for ordering exists (above which martensite is cubic with each OIS sublattice equally and randomly populated) which is about 1000 times the weight percent carbon in the alloy (in $^{\circ}$K). These theories, however, cannot explain the experimentally measured room-temperature tetragonality of iron-carbon martensites down to 0.2 wt pct carbon, where the theories predict a critical temperature of about -70°C. Khachaturyan [9] has revised his theory of carbon ordering; he now concludes that alloys containing more than 0.03 wt pct carbon are tetragonal at room temperature.

2.4 Martensitic Morphology and Substructure

Two distinct martensitic morphologies have been observed in iron-carbon alloys. In low- and medium-carbon steels (containing less than about 0.6 wt pct carbon) with high M_s temperatures the martensitic units take on the shape of laths, grouped into sheaves or packets and often separated by low-angle boundaries [26,27]. The laths possess a substructure consisting of dislocation cells with estimated dislocation densities of $10^{10} - 10^{12}$ cm/cm^3 [28-30] and a habit plane about 5° from $\{111\}_{\gamma}$* [31].

"Plate martensite" is formed in high-carbon steels with lower M_s temperatures. Here, the martensitic units appear as individual lenticular plates and are often characterized by the presence of a "midrib" containing a high density of $\{112\}_{\alpha}$ twins about 5 - 10 nm in thickness [32]. The midrib is believed to constitute a rapid growth event, prior to the general

*The subscripts "γ" and "α" refer to austenite and martensite, respectively.

33

thickening of the plate [8]. The twins generally do not extend to the
sides of the plates, but degenerate into a complex dislocation array [26].
Patterson and Wayman [33] report a similar morphology in iron-high-nickel
alloys, where arrays of long, straight screw dislocations in regions away
from the midrib are observed. The variation of M_s and morphology with
composition in the Fe-Ni-C system is illustrated in Figure 2-5.

The morphological and substructural features of some ferrous
martensites have been successfully explained by several crystallographic
theories [35-37]. Cohen and Wayman [8] present an excellent overview of
the basic concepts which apply to these theories. The theories are based
on the existence of a lattice correspondence (such as the Bain
correspondence) between the parent austenite and product martensite phases.
This implies that a tensor relationship exists between the two crystal
lattices, from which the transformation strain tensor, ε_{ij}^T, can be derived.

Embodied in ε_{ij}^T is the lattice deformation which converts one lattice
homogeneously to another. The crystallographic theories also recognize
that lattice-invariant deformations (such as slip or twinning where no
change occurs in the structure generated by the lattice deformation) may
operate in order to reduce the distortion (strain energy) produced by the
transforming volume. Linear elasticity theory has been applied to the case
where ε_{ij}^T describes an invariant-plane strain (IPS), i.e. where the lattice
and lattice-invariant deformations leave a lattice plane macroscopically
undistorted and unrotated. The result indicates that the transformational
strain energy is minimized when the product assumes a thin plate shape [38].

Within the framework of the crystallographic theories, different
observables such as the habit plane and orientation relationship can be
predicted by assuming an IPS and specific lattice-invariant deformation(s).
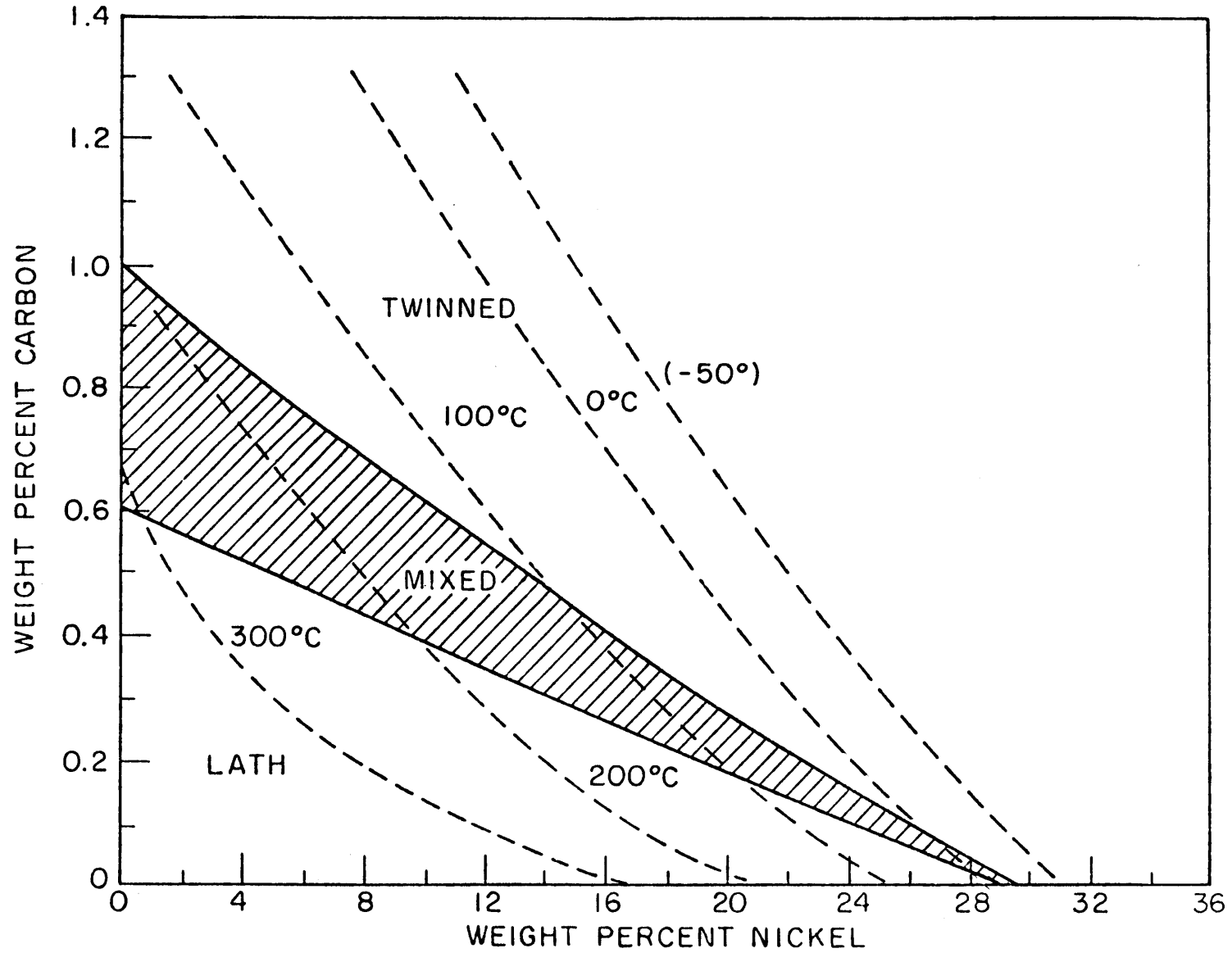
Figure 2-5. The morphology and M_s temperature of iron-nickel-carbon martensites as a function of composition (after Winchell [34]).

In plate-like Fe-high Ni-C alloys, where the lattice-invariant deformation involves twinning on $\{112\}_\alpha$ planes, the theories successfully predict the observed $\{3,10,15\}_\gamma$ habit plane. However, the theories have not been completely successful in predicting the morphology of iron-carbon martensites, where the change in habit plane from $\sim\{111\}_\gamma$ to $\{225\}_\gamma$ to $\{259\}_\gamma$ with increasing carbon content has not yet been explained [8].

In addition to lattice dislocations and $\{112\}$ twins, a third substructural feature has been postulated by Roytburd and Khachaturyan [39] in order to explain anomalous axial ratios (c/a's) in Fe-Mn-C, Fe-Ni-C and Fe-Al-C martensites. If all carbon atoms occupy O_z sites, then, making use of Equation 2-6,

$$c/a = (1 + u_{33}n_C)/(1 + u_{11}n_C)$$
$$\cong 1 + (u_{33} - u_{11})n_C. \tag{2-7}$$

Thus c/a is a linear function of carbon content, as has indeed been found in a number of Fe-X-C systems. However, the carbon concentration coefficient has been found to be different for different alloy systems. Some relevant observations reviewed recently by Kurdjumov and Khachaturyan [40] include:

(1) Fe-Mn-C alloys containing 0.6 to 1.8 wt pct carbon exhibit a smaller axial ratio than corresponding Fe-C alloys, and the axial ratio increases upon heating to room temperature (but still remains smaller than c/a for Fe-C). Furthermore, martensites with such abnormally-low axial ratios actually have different "a" and "b" parameters, i.e. the martensite lattice is macroscopically orthorhombic.

(2) Fe-Al-C and Fe-high Ni-C martensites are found to have abnormally high axial ratios and have a $\cong$ b. Here, the axial ratio tends to decrease

36

upon warming to room temperature.

Roytburd and Khachaturyan rationalized the above facts by assuming that some carbon atoms occupy O_x and O_y sites. Section 2.3 showed that the Bain correspondence leaves carbon atoms only in the O_z sublattice; the hypothesis of Roytburd and Khachaturyan is consistent with this if the lattice-invariant deformation involves the $<01\underline{1}>\{01\underline{1}\}_\alpha^*$ twinning system, Figure 2-6. Although it is not meaningful to speak of such a twinning system for BCC iron, such twinning is possible in the BCT lattice where the $\{01\underline{1}\}$ planes no longer possess mirror symmetry. Figure 2-6 illustrates that such twins can be formed when carbon atoms shuffle a distance of $a/2<01\underline{1}>$, producing slight displacements of nearby iron atoms.

----

*An underlined Miller index indicates that the martensite lattice is tetragonal; its absolute value is fixed when obtaining possible variants.

The shear strain, γ, produced by twinning on $\{01\underline{1}\}$ is very small and depends on the axial ratio of the lattice:

$$\gamma = \frac{(c/a)^2 - 1}{c/a} \tag{2-8}$$

where c/a is the axial ratio with only O_z occupancy. As an example, c/a is about 1.07 for Fe-7.0Al-1.0C [41], a value which is abnormally high (compared to 1.045 for Fe-1.0C) and may be taken to represent 100% O_z occupancy. For such an axial ratio the shear produced by twinning on $\{01\underline{1}\}$ is only about 0.14, compared to a shear of about 0.7 for conventional $<111>\{112\}$ twinning.

Roytburd and Khachaturyan state that if the $\{01\underline{1}\}$ twins are thin enough, they will coherently scatter radiation and produce a diffraction
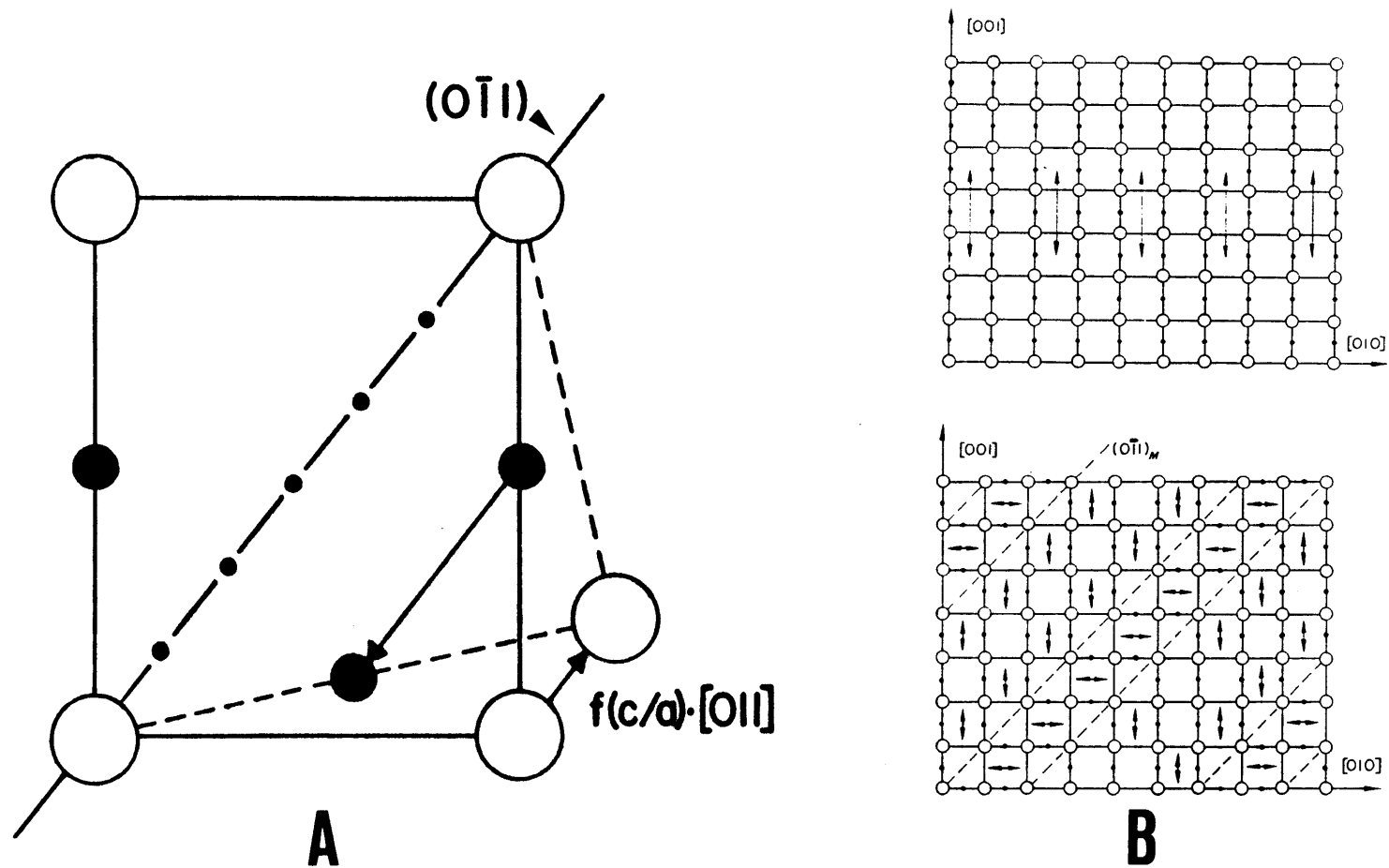
Figure 2-6. The <011>{011} twinning system in BCT lattices. Location of lattice and O_z sites in the (100) plane, (A). The directions of the tetragonal axes are indicated both before and after [011](0$\bar{1}$1) twinning. Such twinning transforms O_z to O_y sites, (B) (from Sachdev [42] and Kurdjumov and Khachaturyan [40]).

pattern corresponding to an orthorhombic lattice. The lattice constants of the martensite are then given by

$$a = a_o[1 + u_{11}(n_2 + n_3) + u_{33}n_1] \qquad (2-9A)$$

$$b = a_o[1 + u_{11}(n_3 + n_1) + u_{33}n_2] \qquad (2-9B)$$

$$c = a_o[1 + u_{11}(n_1 + n_2) + u_{33}n_3], \qquad (2-9C)$$

where n_1, n_2, and n_3 are the ratio of the number of carbon atoms in O_x, O_y, and O_z sites, respectively, to the number of host atoms. When $n_1 \neq n_2$, the lattice is macroscopically orthorhombic, as is the case for alloys with abnormally low "tetragonality." The changes in c/a upon heating to room temperature are assumed to reflect changes in n_1, n_2, and n_3. Such changes may reflect the attainment of new thermodynamic equilibrium values [40] or may be driven by internal stresses.

Experimental observations of planar features on {011} have been made by Sachdev in Fe-Mn-C alloys [42] and by Wayman et al. in Fe-C and Fe-(Mn,Cr)-C alloys [43-45].

2.5 The Aging and Tempering of Martensite

The practical benefits of aging and tempering lie in the desirable changes in mechanical properties which can be obtained by suitable thermal treatments. Generally, substantial increases in ductility can be realized with only modest decreases in hardness and strength. In fact, when suitable carbide-forming elements are present, the original as-quenched strength can be largely regained by allowing alloy carbide precipitation to occur.

As mentioned in Section 2.1, freshly-formed martensite is highly supersaturated with respect to carbon and therefore post-transformation carbide precipitation can be expected. Early work suggested that several

distinct reactions take place during the decomposition of martensite and these now comprise the various "stages of tempering" which are familiar to many metallurgists. By the 1960's, as analytical capabilities grew, it became increasingly clear that structural changes occur in martensites on a fine scale prior to the widely-recognized first stage of tempering. That such "aging" reactions went largely undetected for so long stems partially from the fact that they proceed quickly at room temperature and can only be observed when the martensite is formed at a relatively low temperature. "Virgin" martensite is obtained when the M_s is low enough that no thermally-activated redistribution of carbon atoms occurs before the first experimental measurement or observation.

The remaining sections of this chapter are devoted to a review of previous research on aging and tempering. The most pertinent results (where a variety of techniques including x-ray diffraction, electron microscopy, electrical resistivity, Mössbauer spectroscopy, atom-probe field ion microscopy, and mechanical property measurements have been employed) will be discussed, first as they relate to tempering. The more recent work on aging is presented afterward. During subsequent discussion, the reader may wish to refer to Table 2-1, where structural information regarding the various iron-carbides which have been detected in steels is given. The formation of the individual carbides is influenced by carbon content, other alloying elements, internal substructure, and temperature. Jack and Jack [46] and Imai [47] have given comprehensive reviews on the phases which form during tempering.

2.5.1 The Stages of Tempering

The first stage of tempering (T1) is associated with the precipitation

TABLE 2-1

STRUCTURAL PARAMETERS FOR VARIOUS IRON CARBIDES WHICH PRECIPITATE DURING AGING AND TEMPERING
(After Imai [47] and Sachdev [42])

IRON CARBIDE	COMPOSITION w/o C	a/o C	CURIE TEMP. ($^{\circ}$C)	BRAVAIS LATTICE	LATTICE PARAMETERS (nm)	V/N_{FE} (nm^3)	ORIENTATION RELATIONSHIP	HABIT
$Fe_{2.4}C$ (ϵ)	8.2	29.4	450-500	hexagonal	a = 0.275 c = 0.435 c/a = 1.58	0.0142	$(101)_{\epsilon} \parallel (101)_{\alpha}$ $(001)_{\epsilon} \parallel (011)_{\alpha}$	{100} <211>
Fe_2C (η)	9.7	33.3		orthorhombic	a = 0.283 b = 0.470 c = 0.432	0.0144	$(010)_{\eta} \parallel (011)_{\alpha}$ $[001]_{\eta} \parallel [100]_{\alpha}$	{100} {011}
Fe_5C_2 (χ)	7.9	28.6	247	monoclinic	a = 1.156 b = 0.457 c = 0.506 β = 97.74°	0.0133	$(100)_{\chi} \parallel (11\bar{2})_{\alpha}$ $[010]_{\chi} \parallel [1\bar{1}0]_{\alpha}$ $[001]_{\chi} \parallel [111]_{\alpha}$	{112}
Fe_3C (θ)	6.7	25.0	215	orthorhombic	a = 0.509 b = 0.674 c = 0.452	0.0129	$(100)_{\theta} \parallel (1\bar{1}0)_{\alpha}$ $[010]_{\theta} \parallel [111]_{\alpha}$ $[001]_{\theta} \parallel [11\bar{2}]_{\alpha}$	{112} {011}

of epsilon-carbide (ε-carbide). Precipitation typically takes place within the 150 to 200°C temperature range, and was first detected by Jack using x-ray diffraction [1]. He concluded that the structure of epsilon is based on an hexagonal arrangement of iron atoms with carbon atoms randomly occupying octahedral interstitial sites, where the stoichiometry lies somehwere between Fe_2C and Fe_3C. Lement later estimated the composition to be $Fe_{2.4}C$ based on dilatometric results [48].

Jack also proposed an orientation relationship between epsilon and low-carbon martensite featuring parallelism between closest-packed planes and directions. Subsequent electron microscopy by Wells [49] confirmed this, with the orientation relationship given as

$$(0001)_\varepsilon || (011)_\alpha$$
$$\text{and } (10\bar{1}1)_\varepsilon || (101)_\alpha.$$

Various morphologies have been reported for ε-carbide. Among these are a plate-like morphology with a $\{100\}_\alpha$ habit as observed in twinned martensite [49] and ferrite [50], and a rod-like morphology with maximum growth along $<211>_\alpha$ as reported by Murphy and Whiteman [51].

More recent work by Hirotsu and Nagakura [52] suggests that carbon atoms in ε-carbide may take on an ordered arrangement which results in a distortion of the structure to orthorhombic symmetry and the appearance of superlattice spots in electron diffraction patterns. This ordered version of epsilon has been designated as "eta-carbide" (η-carbide) and was observed to grow as rod-like aggregates of tiny individual carbide particles.

Early x-ray diffraction studies by Cohen and coworkers [48,53] indicated that the first stage of tempering is a discontinuous reaction.

The appearance of a distinct, new $(002)_\alpha$ peak was noted, corresponding to the formation of low-carbon martensite containing about 0.25 wt pct carbon. The original (002) peak remained, but decreased in intensity, indicating that the first stage proceeds by the formation of an aggregate of ε-carbide and low-carbon martensite at the expense of the high-carbon martensite. However, the notion that T1 involves a simple nucleation and growth process is now open to question due to the revelation of pre-T1 processes by subsequent investigations (see Section 2.5.2).

The second stage of tempering (T2) involves the transformation of retained austenite (if any is present in the steel), usually in the temperature range of 200 to 300°C. The product is a mixture of ferrite and cementite. On the other hand, this stage of tempering may be absent in high-alloy steels where the austenite is stabilized to the extent that no observable decomposition results from conventional tempering treatments.

Electron microscopy has recently shown that austenite can be retained even in high-M_s lath martensites in the form of thin interlath films [54]. During T2, interlath carbides can then precipitate from the retained austenite and may be associated with the transgranular mode of tempered-martensite embrittlement which occurs in medium-carbon steels.

Orthorhombic Fe_3C, also known as cementite or θ-carbide, is precipitated generally in the third stage of tempering (T3), in the temperature range of 200 to 300°C. There is a strong tendency for cementite to be nucleated at $\{112\}_\alpha$ twin boundaries. Not only does the elimination of twin-boundary area aid this process, but BCC iron twinned on {112} has been shown to be structurally very similar to cementite [55]. Therefore, {112} twin boundaries can in some sense be thought of as cementite "embryos". In untwinned regions, cementite appears to grow on {011}

planes. Various orientation relationships have been proposed for cementite. These tend to be closely related and have the common feature of parallelism between closest-packed planes [55,56], i.e. $\{103\}_\theta \parallel \{101\}_\alpha$.

Cementite initially develops a plate-like habit, with a $\{112\}_\alpha$ or $\{011\}_\alpha$ habit plane. Prolonged third-stage tempering leads to the coarsening and spheroidizing of the cementite. Recovery and recrystallization processes may also set in at higher temperatures, with the end result being a nearly defect- (and carbon-) free ferrite + cementite mixture. The cementite is commonly believed to nucleate separately from the prior epsilon precipitates. Arguments based on morphological and crystallographic differences between the two phases have been put forward [49]. In addition, cementite has been observed to form in systems where first-stage precipitation is absent [57,58].

There is increasing evidence for the formation of an additional carbide, Fe_5C_2, in the regime of the third stage. This phase has been designated "chi-carbide" (χ-carbide). Though its structure is monoclinic, its unit cell is simply related to that of cementite as follows: $a_\chi \cong 2b_\theta$, $b_\chi \cong c_\theta$, and $c_\chi \cong a_\theta$. The close similarity between the theta and chi structures has been born out by observations of in situ $\chi \to \theta$ transformations [59] and even microsyntactic (inter)growth of the two phases [60]. Jack and Jack [46] suggests that thin plates of chi and theta are structurally identical, where the distortions generated by a mixture of the two would be sufficient to account for anomalous Curie temperatures and electron microscopic observations.

A fourth stage of tempering can ensue at about 500 to 600°C when strong carbide-forming elements (such as chromium, molybdenum, or vanadium) are present. As mentioned earlier, alloy carbide precipitation can

significantly retard the softening which characteristically accompanies tempering or it may even cause "secondary hardening." Many structures and stoichiometries have been observed for these complex compounds. Andrews et al. [61] have published a good tabulation of such findings.

2.5.2 Studies of Aging

Earlier, mention was made of significant structural changes which occur in martensites prior to the first stage of tempering. By the 1960's the evidence for such changes included the following: (1) Oketani et al. [62] measured heat evolution from a high-carbon steel beginning at temperatures below $-100^{o}C$, and (2) Winchell and Cohen [63] observed an increase and peak in hardness and electrical resistivity during the aging of initally-virgin Fe-Ni-C martensites in the vicinity of room temperature. Since that time, transmission electron microscopy (TEM) and diffraction studies have probably been the most fruitful in characterizing the processes which occur during aging.

Izotov and Utevskiy [64] studied high-carbon martensites by electron microscopy. Diffraction patterns from samples aged at room temperature exhibited diffuse scattering along the four $<10\underline{2}>_{\alpha}$ reciprocal lattice directions, as well as diffuse, split superlattice spots. The geometry of the superlattice reflections indicated the formation of a second phase based on a BCC arrangement of iron, but with a larger (tetragonal) unit cell due to carbon ordering. Perfect ordering results in the regular occupation of one quarter of the O_z sites and the Fe_4C stoichiometry. The diffuse scattering was interpreted as a shape effect, indicating that Fe_4C is plate-like in shape, about 1 by 4 nm in size with a $\{10\underline{2}\}_{\alpha}$ habit plane.

The results summarized in a recent review paper by Nagakura and coworkers [65] provide additional insight. They applied high-resolution

electron microscopy to martensitic carburized iron films and observed

essentially the same diffraction effects as did Izotov and Utevskiy. Dark-

field imaging along $[010]_\alpha$ revealed a criss-cross or basketweave morphology

consisting of fine striations lying roughly parallel to the traces of $\{10\underline{2}\}$

planes. This morphology is similar to the tweed structures which have been

observed in elastically-anisotropic BCC alloys and modelled by arrays of

interacting particles acting as centers of tetragonal strain [66].

Accordingly, Nagakura et al. conclude that the $\{10\underline{2}\}$ tweed is produced by

$<10\underline{2}>$ modulations in the density of small ($\sim$1 nm) carbon clusters with

approximately one-half the O_z sites occupied in these high-carbon clusters.

In a more recent paper, Nakamura and Nagakura suggest that T1 carbides may

nucleate preferentially in the high-carbon clusters of the tweed [67].

Nagakura et al. attribute the split superlattice reflections to a

different phase which forms after the tweed. The structure of this phase

is based on the Fe_4C structure of Izotov and Utevskiy, but has a longer-

period carbon-atom arrangement due to faulting on (001) planes.

Though the work of Izotov and Utevskiy and of Nagakura and coworkers

provides important information on aging, their observations were not

systematic; little attention was paid to the kinetics of aging and tweed

development, and furthermore the results from other workers using different

experimental approaches were largely ignored by Nagakura and coworkers.

Two studies have, however, shown systematically the progress of aging and

tempering, particularly with respect to the aging and early carbide-

formation stages. One, done by Winchell and coworkers [68,69], employed an

elegant pseudo-single-crystal x-ray diffraction technique to follow the

changes in the shapes, positions, and integrated intensities of the $(200)_\alpha$,

$(020)_\alpha$, and $(002)_\alpha$ peaks during the aging and tempering of martensitic Fe-

18Ni-0.98C. Their results indicate that between -40 and +40°C, carbon atoms remain in 0_z sites but undergo a clustering reaction, consistent with the interpretations given above. Aging at 40°C gave rise to a new, weak and diffuse peak on the high-angle side of (002). This was attributed to the formation of carbon-depleted regions of negative tetragonality (c/a < 1) sandwiched between small carbide platelets. It was suggested that these carbides may be early forms of carbides traditionally associated with the first stage of tempering.

The other study, summarized by Sherman et al. [70], measured the electrical resistivity of Fe-Ni-C alloys containing 18 to 24 wt pct nickel and 0.003 to 0.62 wt pct carbon. The alloys were quenched in liquid nitrogen to produce virgin or nearly-virgin martensite and up-quenched to temperatures between -90 and 350°C for isothermal aging and tempering. Characteristic changes in resistivity permitted, with appropriate assumptions, the calculation of activation energies from the data. They noted an increase in activation energy from about 75 kJ/mole (18 kcal/mole) to about 100 kJ/mole (24 kcal/mole) during aging, in general agreement with estimates of carbon diffusivity in martensite [71] and consistent with TEM observations of carbon clustering.

Mössbauer spectra obtained by Kaplow et al. [12,19] from splat-quenched Fe-1.86C have provided additional clues to the structure of the high-carbon regions formed during aging. Two components with an apparent population ratio of 1:3 and a ratio of hyperfine magnetic fields of 3:2 were identified in the spectra. From the similarity of these features to those of the two iron atoms in the γ'-Fe_4N structure, an isomorphous Fe_4C structure has been proposed as a reasonable model for the "clustered state." More recent Mössbauer work on Fe-Ni-C alloys [72] has also been

47

interpreted in terms of Fe_4C precipitation during aging. This interpretation is consistent with the conclusions drawn from the TEM studies, but the breadth of the Mössbauer peaks suggests a distribution of compositions deviating from exact Fe_4C stoichiometry. Accordingly, Ino et al. [21] propose the formula "Fe_4C_x (x << 1)" for the clustered state, based on their MES study of carburized iron foils.

The only direct measurement of variations in carbon composition in aged martensites comes from the atom-probe field-ion microscopy (AP/FIM) by Miller, Smith, and coworkers [73,74]. Surprisingly, some evidence was obtained for carbon clustering in as-quenched virgin Fe-Ni-0.4C martensites, with local concentrations as high as 7.8 at pct carbon (1.6 wt pct). However, the possibility exists that this "clustering" is an artifact due to carbon migration on the specimen surfaces during field-evaporation. Aging at room temperature enhanced the observed clustering, although the carbon-rich regions remained below 10 at pct carbon in composition. Even though nothing approaching the ideal Fe_4C composition (25 at pct carbon) has been measured, the AP/FIM results may be consistent with the Mössbauer interpretations when allowance for possible non-stoichiometry is made and when uncertainties regarding the statistical analyses of the raw AP/FIM data are eventually resolved.

2.6 Substructural Effects on Aging and Tempering

Previous investigations [26,28] have indicated that the martensitic morphology can exert a substantial influence on the tempering behavior. For example, segregation of carbon to dislocations and lath boundaries has been considered to involve a large fraction of the total carbon in low-carbon steels. Calculations suggest that more than 0.1 wt pct carbon may

be accommodated by dislocations for the densities typical of lath martensites [28,58]. However, the experimental evidence for dislocation trapping has come from Fe-C alloys with high M_s temperatures where potential auto-tempering effects cannot be ignored. Sherman [25] has recently measured the effects of aging on the resistivity behavior of both lath and twinned martensites with near- or sub-ambient M_s temperatures. Here the behavior varied linearly with carbon content; an effect not consistent with the saturation of preferred carbon sites near dislocations. Nonetheless, his observations cannot be taken to rule out segregation to dislocations; it may be that either (1) clustering dominates the resistivity changes, or (2) the dislocation densities in the martensites studied varied in such a way that no significant variation occurred in the fraction of such segregated carbon atoms.

Additional direct evidence for the dislocation trapping of carbon comes from observations of the re-solution of ε-carbide as a result of strain-tempering [57,58]. However, Sherman et al. [70] point out that such observations are not inconsistent with their finding that clustering, rather than carbon migration to defects, is the dominant process during the aging of undeformed martensites. It is conceivable that dislocations newly-generated by plastic deformation are more potent carbon traps than are the dislocations arising from the martensitic transformation itself.

With regard to tempering, Sherman et al. suggest that dislocations may play an important role late in the first stage when ε-carbides are coarsening. Here, their calculated activation energies are consistent with control by dislocation pipe diffusion of iron atoms. Alloy carbides have also been observed to precipitate on dislocations during secondary hardening [26].

Finally, twin boundaries have also been found to play a role in aging and tempering. They appear to provide preferred sites for the nucleation of stage three carbides, as discussed in Section 2.5.1. In addition, some segregation of carbon to twin boundaries has been detected at room temperature by AP/FIM [74].

2.7 Summary

In summary, carbon atoms predominately occupy octahedral interstitial sites in austenite and virgin martensite. Furthermore, the Bain correspondence results in the preferential occupation of a single interstitial sublattice (0_z) in virgin martensite, a configuration which appears to be thermodynamically stable. The first step in the decomposition of virgin martensite appears to involve the diffusion-controlled clustering of carbon atoms on a fine scale. Elastic anisotropy plays an important role in clustering, leading to structural modulations along <10$\underline{2}$> directions. Concomitant or subsequent ordering of carbon atoms may also occur; the Fe_4C composition may be approached in high-carbon regions, but considerable evidence exists which suggests significant departure from stoichiometry.

Epsilon- (or eta-) carbide eventually replaces the carbon clusters during T1 tempering. These carbides probably dissolve during T3 tempering, at the expense of cementite formation. Epsilon appears to nucleate uniformly throughout the martensitic phase, whereas the nucleation of cementite and other T3 carbides can occur preferentially at {112} twin boundaries. Strain energy plays an important role in the growth of carbides during tempering; cementite assumes a planar morphology during the early stages of its growth and epsilon may adopt either a plate-, lath-, or rod-like morphology.

50

Some investigators have concluded that dislocations play an important role during aging and tempering. These defects may provide low-energy sites which trap carbon atoms. In addition, dislocations may provide short-circuit diffusive paths for iron atoms which could assist in the process of carbide coarsening.

CHAPTER 3

PURPOSE AND PLAN OF STUDY

The length of the literature review in Chapter 2 indicates that a good deal of work has already been devoted toward a better understanding of aging and tempering. Nonetheless, there has been a conspicuous absence of <u>systematic</u> studies which follow the fine-scale microstructural changes that occur during aging. Of particular interest here is the possible influence of aging reactions on subsequent carbide precipitation during the first stage of tempering. An additional issue, which remains controversial, concerns the role of substructural features such as dislocations and twin boundaries. The present investigation was undertaken with the above points in mind, considering that the recent aquisition of a JEM 200CX transmission electron microscope would make direct microstructural observations possible at greater resolution than was previously obtainable at MIT. Secondary issues, also addressed in this work, include the tetragonality of martensite and the nature of the electrical resistivity changes which are observed during low-temperature aging of virgin martensites [25,70,75].

In order to study the aging from its earliest stages, the alloys used in this study had subambient M_s temperatures so that virgin martensites could be obtained. Aging and the precipitation of transition carbides (T1) were investigated by electron microscopy. The kinetics of aging and tempering were also measured by means of electrical resistivity in order to determine the rate-controlling processes. Knowing the kinetics also facilitates the comparison of both (1) observations made on alloys of different compositions, and (2) observations made on samples which were aged/tempered at different time/temperature combinations.

52

CHAPTER 4

EXPERIMENTAL PROCEDURES

4.1 Materials Selection and Processing

The selection of materials for this investigation was influenced by
recommendations made at an informal tempering seminar held at MIT in the
spring of 1980. Those participating in the seminar recognized the need for
more work on aging and tempering and designated "standard" alloy
compositions so that future experiments could apply diverse techniques
towards clearer interpretation of structures developed under identical
conditions of composition, temperature, and time. The two compositions (in
wt pct) proposed were Fe-15Ni-1.0C and Fe-25Ni-0.4C. These particular
compositions were selected for several reasons: (1) carbon and nickel are
present in amounts such that both alloys have estimated M_s temperatures of
$-40^{\circ}C$, low enough that auto-aging effects can be essentially ignored. (2)
Precise single-crystal x-ray diffraction results already exist for aged and
tempered Fe-18Ni-1.0C [69]. (3) A large data-base also exists for
martensites with $\sim$0.4C, a carbon content near that of many commercially-
important martensitic steels. (4) The kinetics of aging at 1.0 wt pct
carbon are slow enough to allow convenient room-temperature observation.

In keeping with the recommendations made at the MIT tempering seminar,
the two Fe-Ni-C alloys designated above became the primary subjects of this
investigation. Hot-worked bars nominally one-half inch square in cross-
section were furnished by the Climax Molybdenum Company. The as-received
bars were completely austenitic with an equiaxed (recrystallized) grain
structure. Chemical analyses of both materials are given in Table 4-1.
The actual composition of the higher-carbon alloy fell somewhat short of
1.0 wt pct. Therefore, this alloy will subsequently be referred to as "Fe-

TABLE 4-1

COMPOSITION OF ALLOYS STUDIED (WEIGHT PERCENT)
(uncertainties represent one standard deviation [67% confidence])

Alloy	C	Ni	Al	N
Fe-25Ni-0.4C	0.39 ± 0.01[1]	25.0 ± 1.8[2]	0.09	0.0006
Fe-15Ni-1C	0.88 ± 0.08[3]	15.0 ± 0.2[2]	0.06	0.0010
Fe-25Ni-0.2C (Ref. [25])	0.19	25.5	–	–
Fe-1.8Mn-1.8C (Ref. [42])	1.8	–	–	–

[1]based on 3 different analyses

[2]based on 4 different analyses

[3]based on 5 different analyses

15Ni-1C", with the understanding that the actual carbon content of the alloy is 0.88 wt pct.

Sections were cut from the bars and ground to remove scale. Austenitizing was conducted at 950°C for one hour, followed by quenching in room-temperature water. For this, the sections were encapsulated in argon back-filled vycor tubes; the tubes were broken during the quenching process to obtain fast cooling rates. Chips from a cast-iron bar were also included in the capsules to minimize decarburization.

Two other alloys were also examined by TEM in order to obtain results on aging over a broader range of carbon content. One alloy, Fe-25Ni-0.2C, comes from the study by Sherman [25]; the other, Fe-1.8Mn-1.8C, comes from a study by Sachdev [42]. Sherman's alloy had previously been received in the form of hot-rolled plates and were cold-worked, annealed, and machined to rods 0.48 cm in diameter. The present author further machined a rod to 3 mm in diameter and austenitized it for one hour at 950°C. A 3 mm-diameter rod of the Fe-1.8Mn-1.8C alloy required rapid cooling from the austenitizing temperature of 1140°C in order to minimize cementite precipitation during the cooling. This was kindly performed by Dr. A. K. Sachdev by using the rapid quenching technique described in Reference [25].

4.2 Optical Metallography

Samples for optical microscopy were mounted, ground, and polished using standard procedures. Two procedures were used to tint-etch the austenitic phase of each alloy for grain size measurement. For Fe-25Ni-0.4C, a solution consisting of (by volume) 5%HF-55%H_2O-40%H_2O_2 was found to give good results. Here the samples were etched only momentarily, followed by rinsing in water and drying with ethanol and a hot-air dryer. The

austenitic Fe-15Ni-1C was immersed in a 4% nital/picral solution for about 15 seconds, rinsed, and dried as above. For martensitic samples, a nital etch usually produced good results, although sometimes better results were obtained on Fe-25Ni-0.4C with 35% sodium metabisulfite. The amount of retained austenite (after quenching in liquid nitrogen) was determined for both alloys by point counting. Enough points were counted to give ±5% accuracy of the data. X-ray diffraction was also employed to verify these results.

4.3 Electron Metallography

TEM samples were prepared from 3 mm-diameter rods which were previously machined from austenitized sections of the wrought bars. Discs about 0.2 mm (0.008 inch) in thickness were spark-cut from the rods and ground to about 0.1 mm (0.004 inch) with 600-grit emery paper. All quenching (to form martensite) and subsequent tempering were done with the samples in this "bulk" state. Final thinning was carried out electrochemically in a twin-jet apparatus with a solution of (by volume) 10% perchloric acid/90% methanol at about -55°C. A voltage of 20 V (corresponding to a total current of about 20 mA) was found to give good results, although a higher voltage was required for tempered samples. The thinned samples were carefully rinsed in ethanol or methanol and dryed between two pieces of filter paper. Electron microscopy was conducted on either a Philips EM300 (operating at 100 kV) or a JEOL JEM 200CX (operating at 200 kV). Both microscopes were equipped with single- and double-tilting holders; however, because the samples were strongly ferromagnetic, use of the JEOL double-tilting holder was precluded.

4.4 Electrical Resistivity Measurements

Samples for resistivity measurements were cut from austenitized bars on a low-speed diamond saw. The samples were typically 3 cm long and about 1.5 mm square in cross-section. Pure nickel lead wires were spot-welded to each end of the samples for the measurements. A Keithley Model 503 Milliohmmeter was used to measure resistance, with a rated accuracy of ±0.5%. The resistances were converted to resistivities by using the formula:

$$\rho = R \cdot \frac{A}{L} \qquad (4-1)$$

where ρ = resistivity

               R = measured resistance

               A = cross-sectional area of sample

and L = test length of the sample.

The accuracy of the absolute resistivity values is estimated to be about ±2.0%, due to the combined error in dimensional and resistance measurements. However, the sensitivity to _relative_ changes in resistivity was limited only by the accuracy of the milliohmmeter, ±0.5%.

A number of different resistivity samples were prepared from both alloys. After forming martensite, each sample was isothermally aged or tempered while monitoring its resistance. The data from such experiments provided information on the kinetics of aging and tempering, as discussed in Chapter 6. Martensite was formed by quenching the samples in liquid nitrogen (T = -196°C) for 15 minutes. The samples were also subsequently "preaged" for one hour in a bath of isopentane (2-methylbutane) maintained at -130°C. The reason for this is described in Chapter 6 and Appendix B. All resistance measurements on martensitic samples were made in liquid

nitrogen. Here, the temperature is low enough that the thermal contribution to the resistance is small and no aging of the sample occurs during the measurement itself.

Several different baths were used for aging and tempering, depending on the temperature: methanol between -40 and 0°C (inclusive); distilled water at 26°C; mineral oil between 40 and 125°C; silicone oil between 150 and 250°C; and a salt bath (Heatbath "Tempering A") between 300 and 400°C. Baths above room temperature were heated by conventional electric methods. An FTS Systems Multi-Cool unit (model # MC-4-130) was used to maintain baths below ambient. All baths were thermostatically-controlled, with a temperature variation of less than ±0.5°C below 150°C and less than ±2°C above 150°C.

4.5 Differential Scanning Calorimetry

The heat effects due to aging and tempering were measured on both Fe-Ni-C alloys using a Perkin-Elmer Model DSC-2 Differential Scanning Calorimeter. The instrument was calibrated with a pure indium standard and a heating rate of 5°K/min was employed for all runs. Austenitic samples, in the shape of 3 mm-diameter discs, were encapsulted in aluminum pans and immersed in liquid nitrogen to form martensite. The runs spanned the temperature range -40 to 400°C. However, in order to minimize condensation, the heating stage was kept at 0°C while the samples were introduced. The mass of each sample was measured prior to encapsulation in order to convert specific heat capacity to molar heat capacity.

CHAPTER 5

RESULTS AND DISCUSSION: MARTENSITIC MORPHOLOGY

AND SUBSTRUCTURE

5.1 Martensite Formation

One of the primary objectives of this research was to study the course of aging from its very beginning. This requires a system where the martensite forms at low temperatures where diffusivities are negligible and therefore no redistribution of carbon atoms occurs before the first experimental observation or measurement. The alloys which were selected for this study meet this criterion by virtue of their subambient M_s temperatures. In the preliminary stages of this work, however, it became clear that the M_s could be varied to some extent by varying the pre-transformation austenitizing treatment, i.e. raising the austenitizing temperature tended to raise M_s. Here, the M_s was measured resistometrically by noting the temperature at which a sharp change in resistance occurred, corresponding to the initial "burst" transformation which is common in Fe-Ni-C alloys [7]. The temperature at which the burst occurs (sometimes designated "M_b") appears to be a function of the austenitic grain size, in that austenitizing at higher temperatures results in larger grains and raises M_b. For example, when Fe-15Ni-1C was austenitized at 930°C for one hour, the grain size (mean linear intercept, counting twin boundaries as grain boundaries) was found to be about 12 μm and the burst at about -53°C. In contrast, austenitizing at 1060°C for the same time resulted in a grain size of 145 μm and an increase in the burst temperature by 33° to -20°C.

The particular austenitizing temperature employed for this work was chosen with the above transformation behavior in mind. The temperature-

and composition-dependent diffusion coefficient for carbon in martensite, D_C^α, suggested by Hillert [71] is given by

$$D_C^\alpha = (2 \times 10^{-6})\exp -\left[\frac{84.1 + 14.0 \cdot (\text{w/o C}) \text{ kJ/mole}}{RT}\right] \text{ m}^2/\text{sec}, \qquad (5-1)$$

where R is the gas constant. Hillert's expression predicts that carbon diffusion becomes extremely sluggish below about -40°C and therefore a transformation temperature near or below this temperature seemed acceptable. By trial and error, it was found that burst temperatures below -40°C could be produced by austenitizing below approximately 950°C, Table 5-1. This upper limit of 950°C was employed for all subsequent austenitizing treatments.

Optical micrographs of untransformed austenite in the two alloys are presented (after austenitizing) in Figure 5-1. Both alloys exhibit an equiaxed grain structure with a number of annealing twins. The Fe-15Ni-1C alloy sometimes exhibited a bimodal grain size distribution, with significantly larger grains toward the center of the wrought bar. Similar abnormally large grains were also noted in the "as-received" material, presumably resulting from discontinuous grain growth during hot-working.

For all subsequent study, virgin martensite was formed in both alloys by cooling to -196°C (quenching in liquid nitrogen). After such quenching, the samples also underwent a small amount of additional isothermal transformation at this temperature. This was indicated by a small decrease in resistance (at -196°C) from the initial as-quenched value. The low-temperature isothermal transformation is discussed in more detail in Chapter 6 and in Appendix B.

Both Fe-Ni-C austenites tend to form surface martensite, particularly

60

TABLE 5-1

GRAIN SIZE, BURST TEMPERATURE, AND VOLUME FRACTION OF
MARTENSITE AFTER AUSTENITIZING ONE HOUR AT 950°C

Alloy	Grain Size[1], μm (mean linear intercept)	M_b[2], °C	Volume Fraction of Martensite[3]
Fe-25Ni-0.4C	61 [42]	-48	0.85
Fe-15Ni-1C	33 [20]	-38	0.67

[1] Values in brackets were obtained by counting both twin boundaries _and_ grain boundaries.

[2] Average of three different specimens.

[3] After cooling to -196°C and warming back to room temperature.
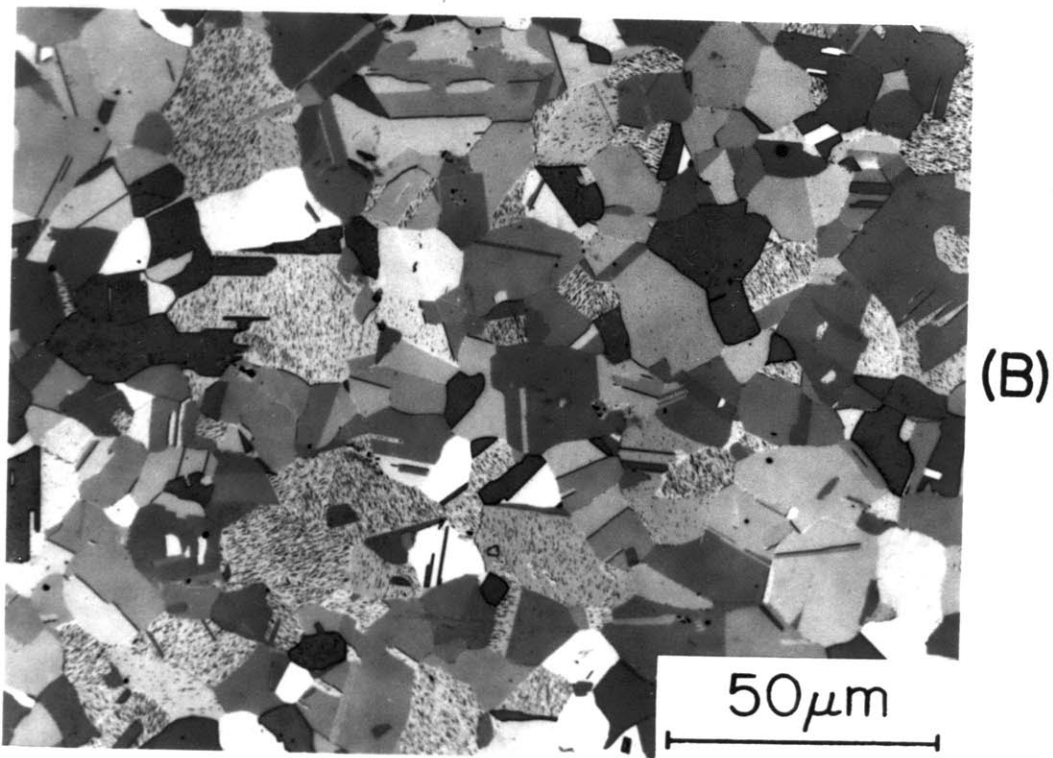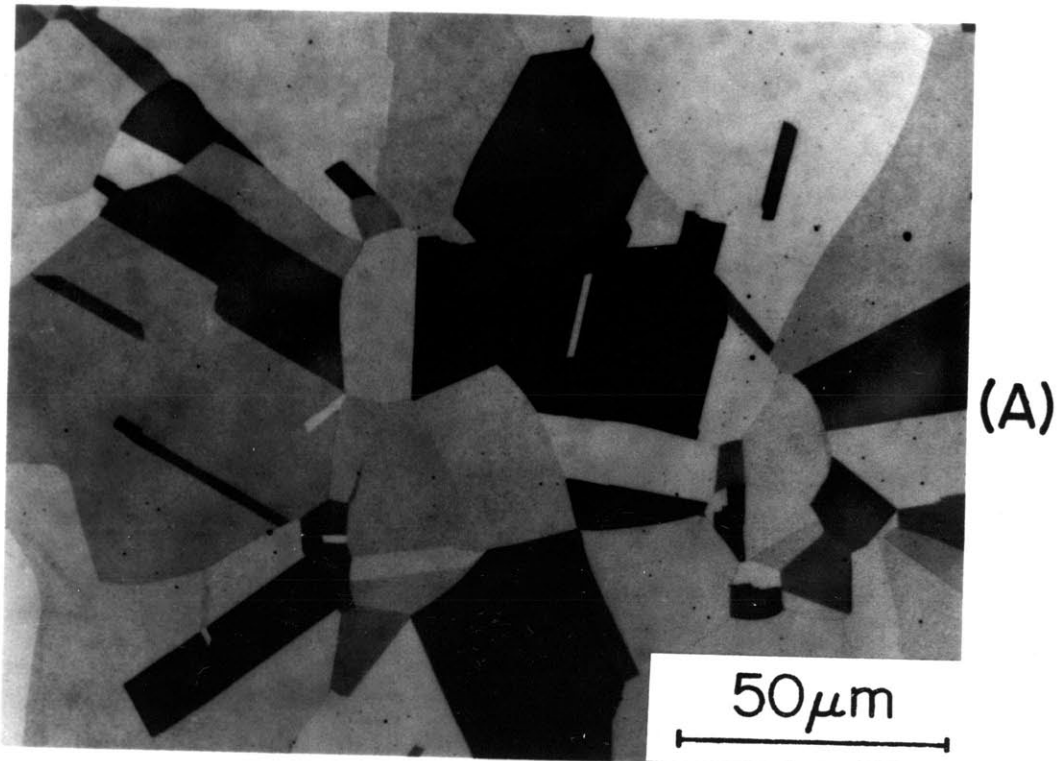
Figure 5-1.   Optical micrographs of austenitic Fe-25Ni-0.4C (A)
and   Fe-15Ni-1C (B).   Both samples were austenitized
one hour at 950°C, followed by water quenching.

when polished by mechanical methods. Such martensite displayed a characteristic "chevron" morphology as shown in Figure 5-2. This morphology, sometimes referred to as "butterfly martensite," has also been reported by Eldis [75] and Umemoto and Tamura [76] in Fe-Ni-C alloys; extensive studies of its crystallography (in Fe-Ni alloys) have been reported by Clark [77] and (in Fe-Ni-Cr-C alloys) by Umemoto et al. [78]. In the current study, there was a marked propensity for this phase to form near the perimeter of the metallographic samples, its nucleation and growth possibly being catalyzed by slight decarburization during austenitizing and/or hot-working. When samples were polished electrochemically (using a chromic-acetic acid solution), much less surface martensite formed, indicating that the unavoidable stresses produced by mechanical polishing may play a more important role in its formation. In any case, the martensite which is inadvertently formed on sample surfaces appears to involve only a tiny volume fraction of material and can safely be ignored for the purposes of this research.

Surface martensite was also apparent in all of the TEM foils prepared by jet thinning. The conditions of low temperature (-55°C) and extremely small foil thickness tended to promote the martensitic transformation during the final stages of thinning. In the vicinity of the perforation, the foils were invariably severely buckled and displayed a greater proportion of martensitic phase than the "bulk" material in the thicker regions of the foils. This effect was particularly obvious in tempered specimens, where the martensitic phase formed in the bulk contained transition carbides while the martensite newly-formed during thinning was carbide-free. Such "thin-foil martensite" displays a range of morphologies, but can often be described as "massive" in character. Care

63
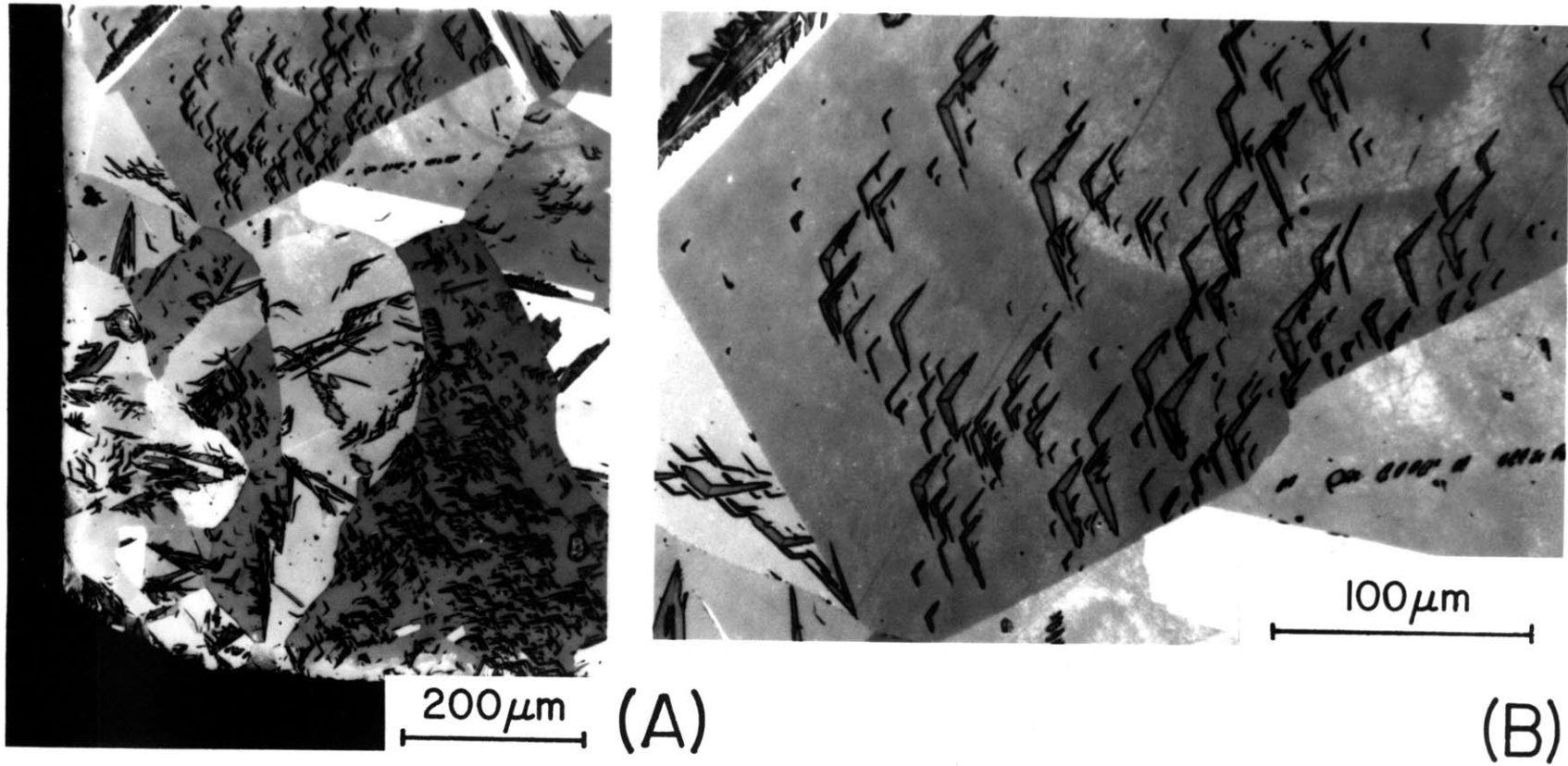
Figure 5-2. "Butterfly" martensite near the edge of a mechanically-polished sample of austenitic Fe-15Ni-1C. (B) is a higher magnification view of part of the region shown in (A). This sample was austenitized one hour at 1060°C.

was taken to avoid regions of thin-foil martensite in subsequent studies of aging. The bulk martensite could usually be easily identified by its lenticular morphology.

Figure 5-3 shows optical micrographs of both Fe-Ni-C alloys after quenching. Each exhibits the lenticular, plate-like martensitic morphology. Significant amounts of retained austenite are also present in both alloys; the volume fraction of martensitic phase was determined for each alloy by point counting and verified by x-ray diffraction. The results are included in Table 5-1.

In the following sections the most prominent substructural features of the martensitic phase are described. This includes {112} transformation twins, dislocation arrays, and twinning on {011} planes. The subject of substructure is revisited in Chapters 7 and 8, where the role which the substructure plays during aging and tempering reactions is discussed in some detail.

5.2 Twinning on {112}

Close inspection of Figure 5-3 reveals a tendency for the martensitic units of both alloys to exhibit etching contrast in the vicinity of the midrib region. This represents a volume of dense twinning on {112} planes, consistent with the predictions of the crystallographic theories. Figure 5-4(A) shows that the twin thickness can vary from about 2 - 20 nm. This high concentration of twins, forming the midrib, is the distinguishing feature of partially internally-twinned martensites such as the alloys of this study.

Figure 5-4(B) shows the midrib region of a martensitic plate in the [111] orientation with the (112) twinning plane inclined by 19° to the

(A)

50μm

(B)

50μm
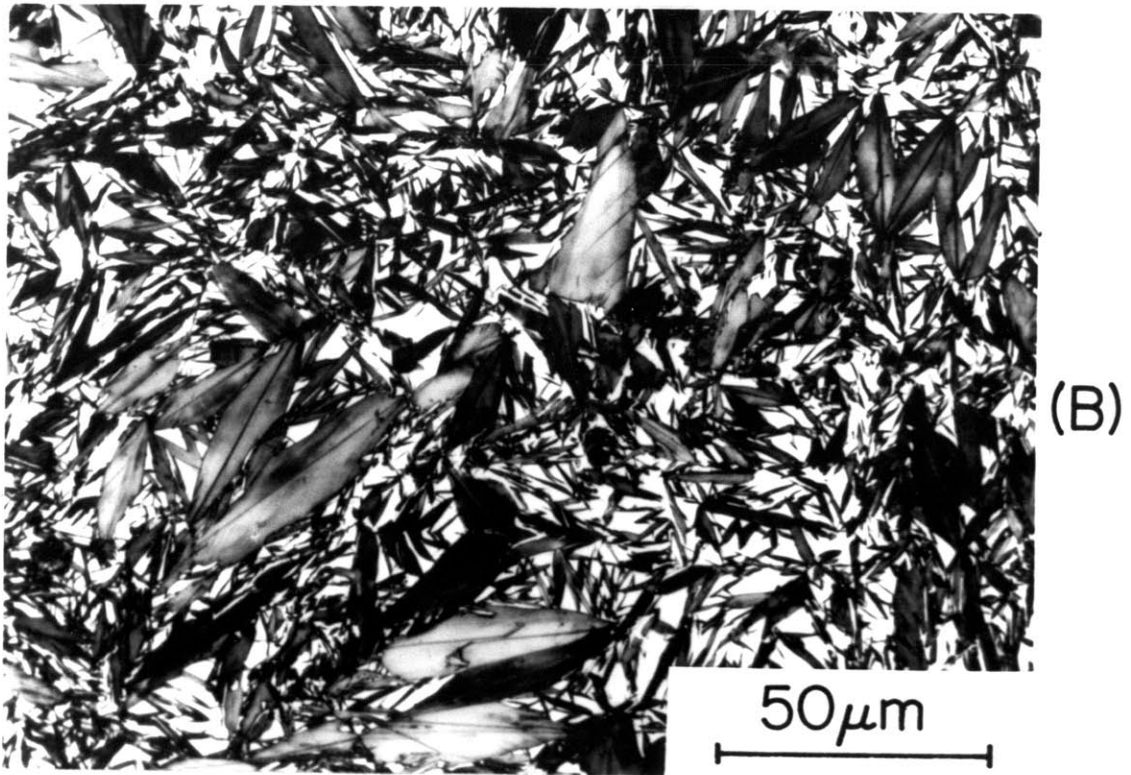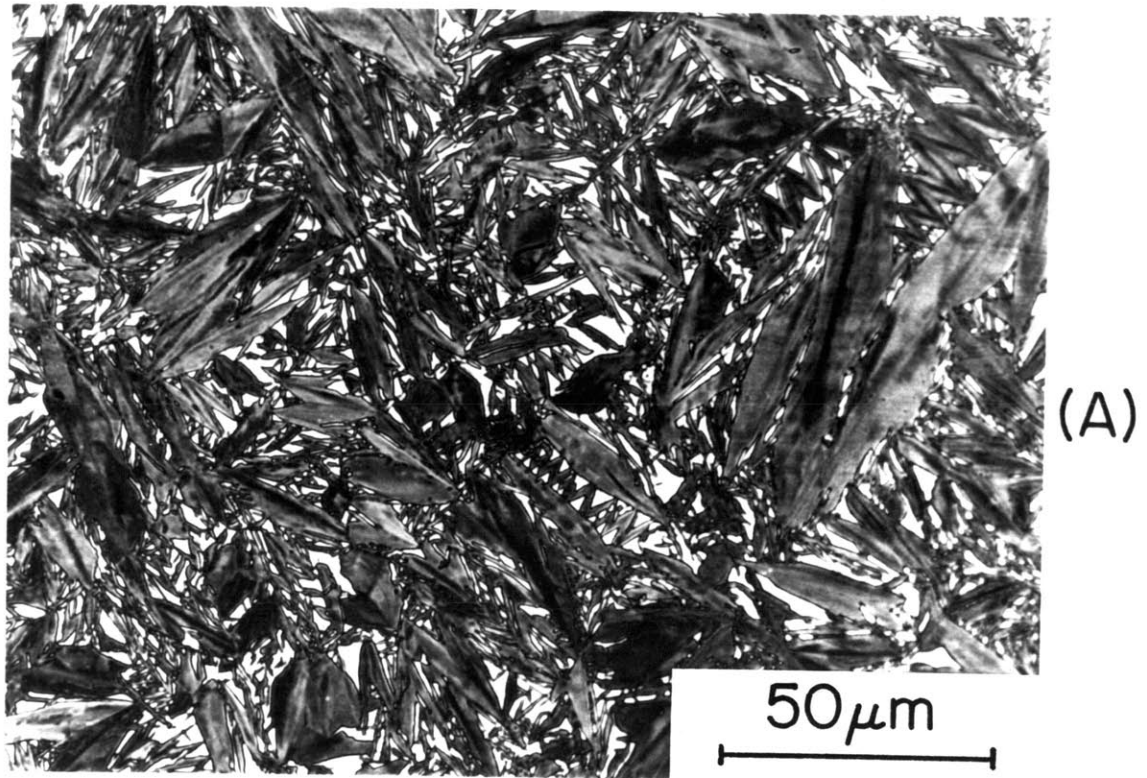
Figure 5-3. Optical micrographs of Fe-25Ni-0.4C (A)
and Fe-15Ni-1C (B) after quenching to -196°C.

(A)

50 nm

(B)

0.5 μm
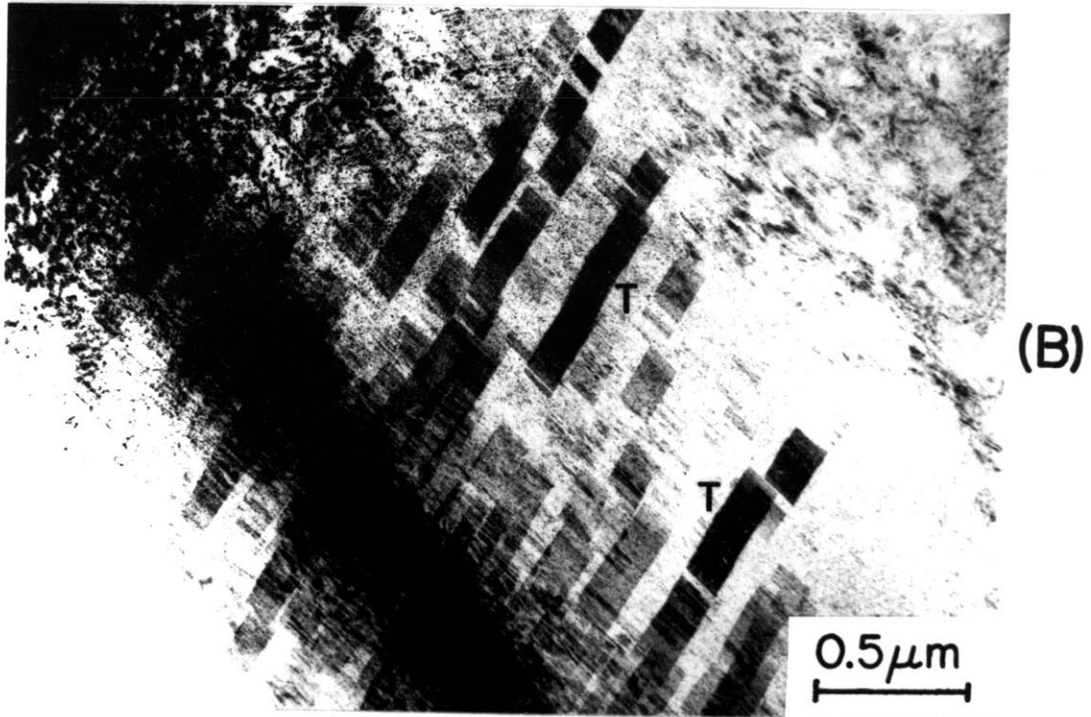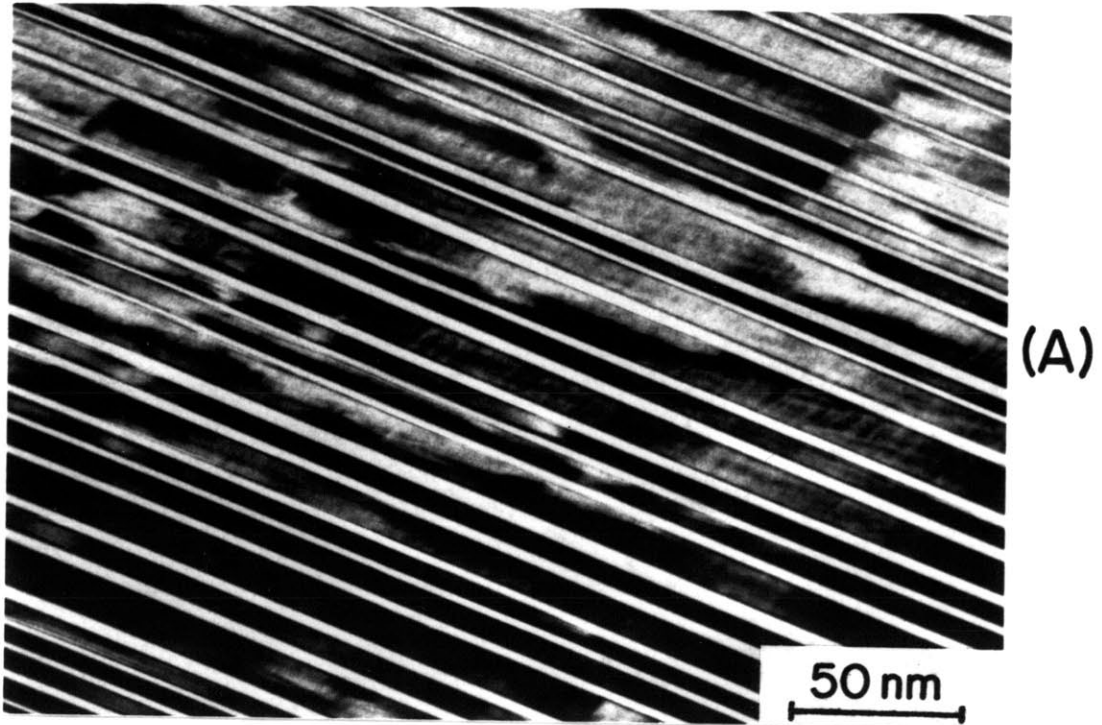
Figure 5-4. Bright-field electron micrographs of the midrib region of martensitic Fe-25Ni-0.4C. The thin {11$\underline{2}$} transformation twins are viewed in an edge-on orientation in (A). A lower magnification view of a different martensitic plate is shown in (B), where the twins, inclined to the electron beam, rapidly decrease in number and become more fragmented in moving away from the midrib (MR) (see text for discussion).

electron beam. In general, the geometry of a twin image is determined by the lateral extent of the plate-like twin, its inclination to the electron beam, and the foil normal. The long axis of a typical twin image ("T" in Figure 5-4(B)) is roughly parallel to the projection of the intersection of the twin with the foil surfaces. Frequently, abrupt changes in contrast are noted in laterally traversing the image of a twin. The contrast change marks either the twin/matrix boundary or an abrupt change in the twin thickness. The twins generally become less numerous as one moves away from the midrib region. The main features of the contrast from the {112} transformation twins are the same as those reported by Patterson and Wayman [33], therefore the reader is referred to their paper for more details.

It was impossible to measure quantitatively the relative volume fraction of "densely-twinned martensite," not only because of the difficulties inherent in such a measurement, but also because of considerable variation in the extent of twinning from plate-to-plate. In fact, some of the smaller martensitic units appeared to be completely twinned, probably attributable to the fact that these units formed at the lowest temperatures during quenching. A very qualitative visual estimate, based on TEM examination of a large number of specimens, places the volume of densely-twinned martensite at about 20 to 30% of the total. Twinning on {11$\underline{2}$} seems to occur to a somewhat greater extent in Fe-25Ni-0.4C, perhaps due to its somewhat lower M_s (M_b) temperature.

5.3 <111> Screw Dislocations

A transition in the dominant substructural feature from {11$\underline{2}$} twins to 1/2<111> lattice dislocations is common in plate-like ferrous martensites. The dislocation morphology often consists of one or several arrays of straight dislocations, as Figure 5-5 clearly demonstrates. These
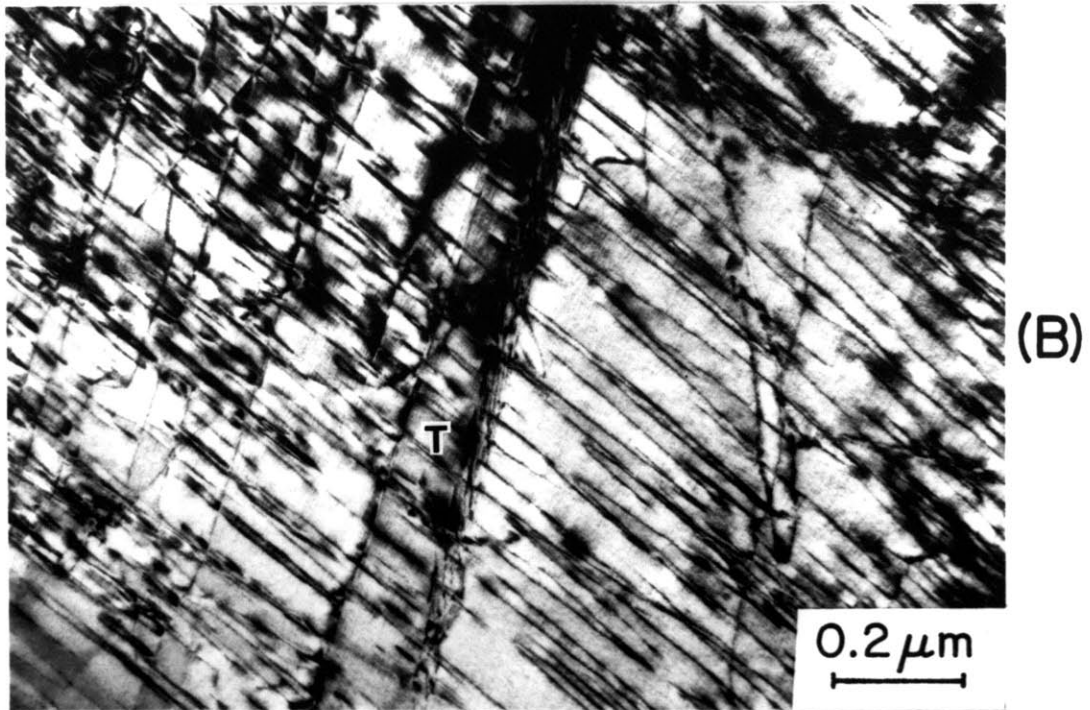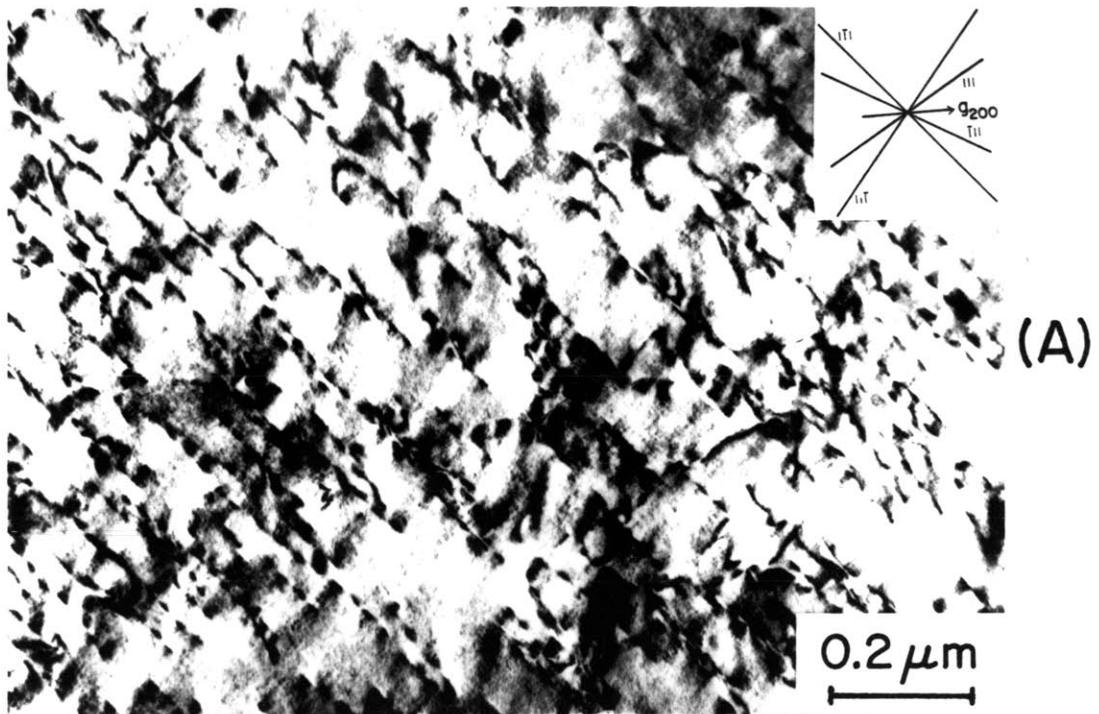
Figure 5-5. Bright-field (**g** = 020) electron micrographs of dislocation
structures in martensitic Fe-25Ni-0.4C and Fe-15Ni-1C (B).
The projections of the four <111> directions are shown in (A).
In (B), the feature marked "T" is a {11$\underline{2}$} twin (see text).

dislocations consistently lie along <111> directions and display the contrast indicative of a parallel 1/2<111> Burgers vector. The parallelism of the Burgers vector, **b**, and the line direction indicates that the dislocations are pure screw in character. Screw dislocations have also been observed (in plate-like martensites) by Patterson and Wayman [33], Oka and Wayman [44], and Sachdev [42].

The operating diffraction vector, **g**, is the same in both of the bright-field images of Figure 5-5 (**g** = 200). Since **g·b** is ±1 for all four of the possible <111> Burgers vector variants, all lattice dislocations are visible in these images. The projections of the four <111> directions are shown in Figure 5-5(A), from which it is apparent that the four Burgers vector variants are not equally populated. The reason for this non-uniform distribution may lie in the relative ease with which the different dislocations can move through twinned volumes; twinning on {112} leaves one <111> direction an invariant line, and a dislocation possessing a Burgers vector of that variant may pass freely through the twinned region [33]. In contrast, Patterson and Wayman concluded that all four screw dislocation variants were about equally populated in their Fe-Ni alloys. However, their observations were made under diffracting conditions such that only two variants were in contrast at the same time. In addition, the presence of carbon in the present alloys may influence the substructural details.

In addition to lattice dislocations, twinning (partial) dislocations possessing Burgers vectors of the type 1/6<111> were also frequently observed in this study. These dislocations provide the shear necessary for twinning on {112} planes. A portion of a {112} deformation twin can be seen in Figure 5-5(B), where the twinning plane is nearly parallel to the electron beam. Twinning dislocations are evident in the right matrix/twin

interface and are associated with the gradual thickening of the twin in going from the top towards the bottom of the micrograph. The twinning dislocations here are closely spaced and make a rather small angle with the electron beam, and hence are difficult to resolve. However, when stereo microscopy was done by tilting the specimen (about 20°) while maintaining the same diffracting conditions, the above interpretation was confirmed.

It was possible to make a quantitative estimate of the total dislocation density, ρ_d, from microgaphs such as those of Figure 5-5. Micrographs taken with g = <200> were preferred for this analysis since all lattice dislocations (with b = 1/2<111>) are then in contrast. The dislocation density was determined by counting the total number of dislocations visible for each <111> family in a given micrograph and dividing this quantity by the area of the micrograph. This procedure yields a result in units of $(area)^{-1}$. This quantity was converted to units of (length)/(volume) by multiplying by an appropriate factor whose value is a function of specimen thickness and orientation. For example, consider the case where the beam is incident normally on the foil surface. If there are N_d straight dislocations (of a given <111> family), each making an angle θ with the beam direction, then the total line length, L, is given by

$$L = N_d \cdot t \cdot \tan(\theta), \tag{5-2}$$

where t is the foil thickness. The dislocation density is then given by

$$\rho_d = L/(At) = \tan(\theta) \cdot \frac{N_d}{A}, \tag{5-3}$$

where A is the area of the region of interest. Note that the foil thickness conveniently drops out of Equation 5-3. An analogous procedure

71

can be followed for the case where the foil normal and beam direction are not parallel; however, the calculations become significantly more complicated [79].

Several different micrographs were analyzed from both Fe-Ni-C alloys. No significant difference in ρ_d was apparent between the two alloys, and the results suggest a typical dislocation density of about 1 to 4 x 10^{10} cm/cm^3. This value is some 1 to 2 orders of magnitude smaller than both measured [80] and calculated [28,58] dislocation densities in low- and medium-carbon lath martensites. The difference in ρ_d can be attributed to the fact that, in plate-like martensites, some or all of the lattice-invariant deformation is accomplished by twinning.

The present value for ρ_d was obtained from micrographs taken away from the midrib region of the martensite plate. Figure 5-6 demonstrates that the dislocation density is not necessarily uniform throughout any given martensitic plate. The density appears to be higher near the midrib, based on qualitative visual examination of Figure 5-6 and similar specimens. The dislocation densities calculated above can thus be taken as conservative estimates. The profusion of fringe contrast in Figure 5-6 suggests, however, that many of the dislocations are partial dislocations, particularly near the midrib. These are probably twinning dislocations (associated with twin boundaries), however the twinning is apparently not always limited to the <111>{112} system. This feature is discussed in more detail in the following section.

5.4 Twinning on {011}

There is, in addition to {112} transformation twins and <111> (lattice and partial) dislocations, a third distinctive feature of the martensitic
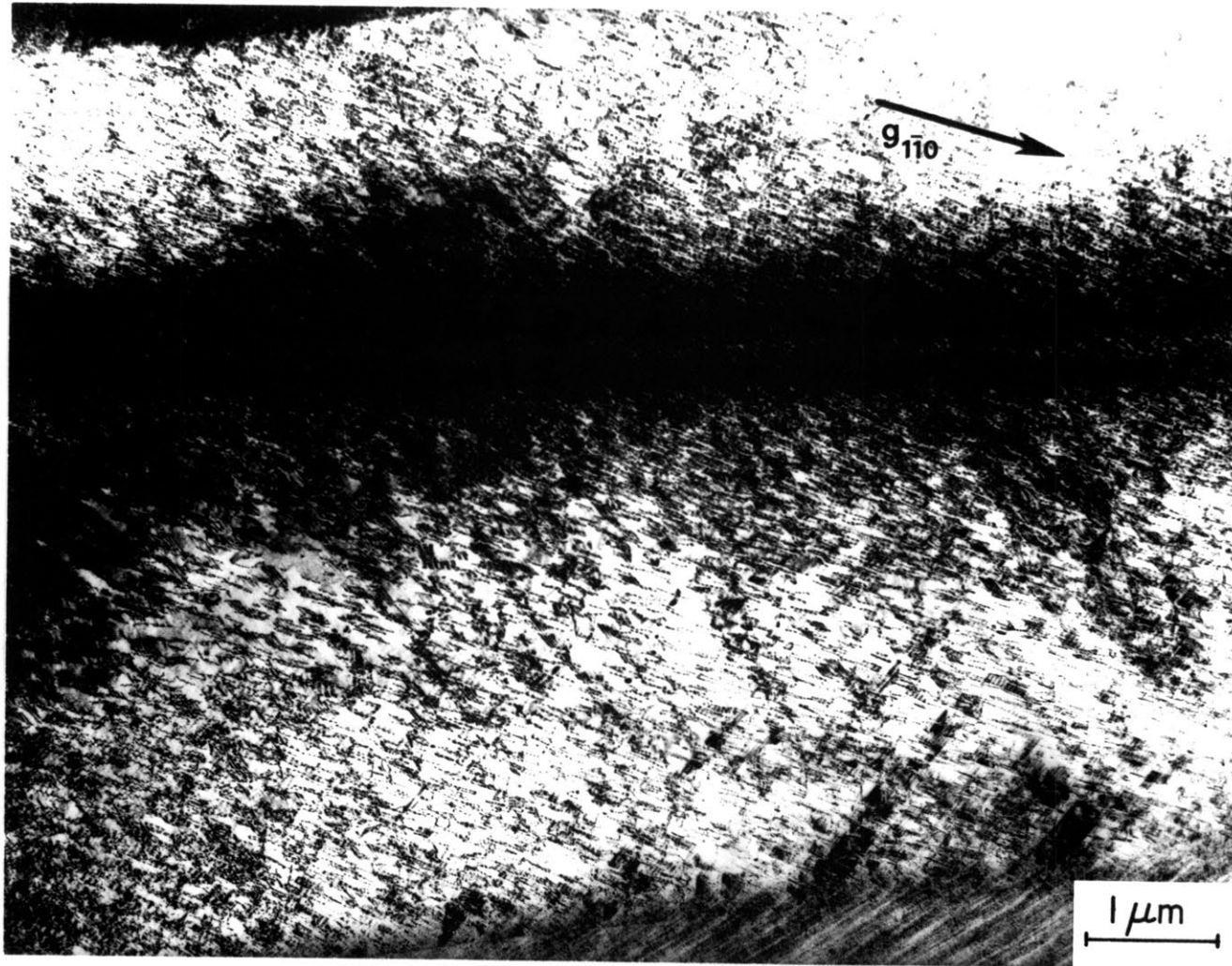
Figure 5-6. Bright-field electron micrograph of dislocation structure in martensitic Fe-25Ni-0.4C. The habit plane is nearly parallel to the beam direction ([115]) in this image. An adjacent martensitic plate appears in the lower portion of the micrograph.

substructure in the Fe-Ni-C alloys of this study. Examples are shown in the bright-field micrographs of Figures 5-7 and 5-8, taken with the electron beam nearly parallel to [001], the c-axis of the martensitic structure. When $g = 110$, fringe contrast is visible, suggesting that the defects are planar in morphology. The fringe contrast is an interference phenomenon, indicating that the atomic arrangement on either side of the defect boundary is related by a displacement vector, R, that is not a lattice vector. Since the specimen of Figure 5-7 is untilted, the habit plane of the defects can be determined from a [001] standard stereographic projection. Here, the traces of the two families of defects are parallel to the [100] and [010] directions. This implies that the defects possess a habit plane of the type {0k$\underline{1}$}. In fact, the trace analysis of numerous images taken at different specimen orientations is always consistent with a habit plane of the type {01$\underline{1}$}. Each of the {01$\underline{1}$} planes makes an angle of $45°$ with [001] (the beam direction in Figures 5-7 and 5-8).

The displacement vector associated with the {01$\underline{1}$} features can be determined by noting the contrast behavior as a function of g. When $g \cdot R$ takes on an integral or nearly-integral value, the phase shift, α (= $\exp[2\pi i g \cdot R]$), associated with the defect is small and no contrast is expected. Thus, restrictions on the form of R can be deduced by noting when the defects are invisible. In Figure 5-7(A), two families of defects (one on {1$\underline{0}$1} and the other on {$\underline{0}$11}, with their traces being [010] and [100], respectively) are visible with $g = 110$. The same area is shown in Figure 5-7(B) after tilting to excite $g = 020$. In this case, the family on {1$\underline{0}$1} becomes invisible, while white-on-black contrast appears for the {$\underline{0}$11} family. Here, $g \cdot R = 0$ requires that R be of the form [h01], and this must be the form of R for the {1$\underline{0}$1} defects. The only vector of this type
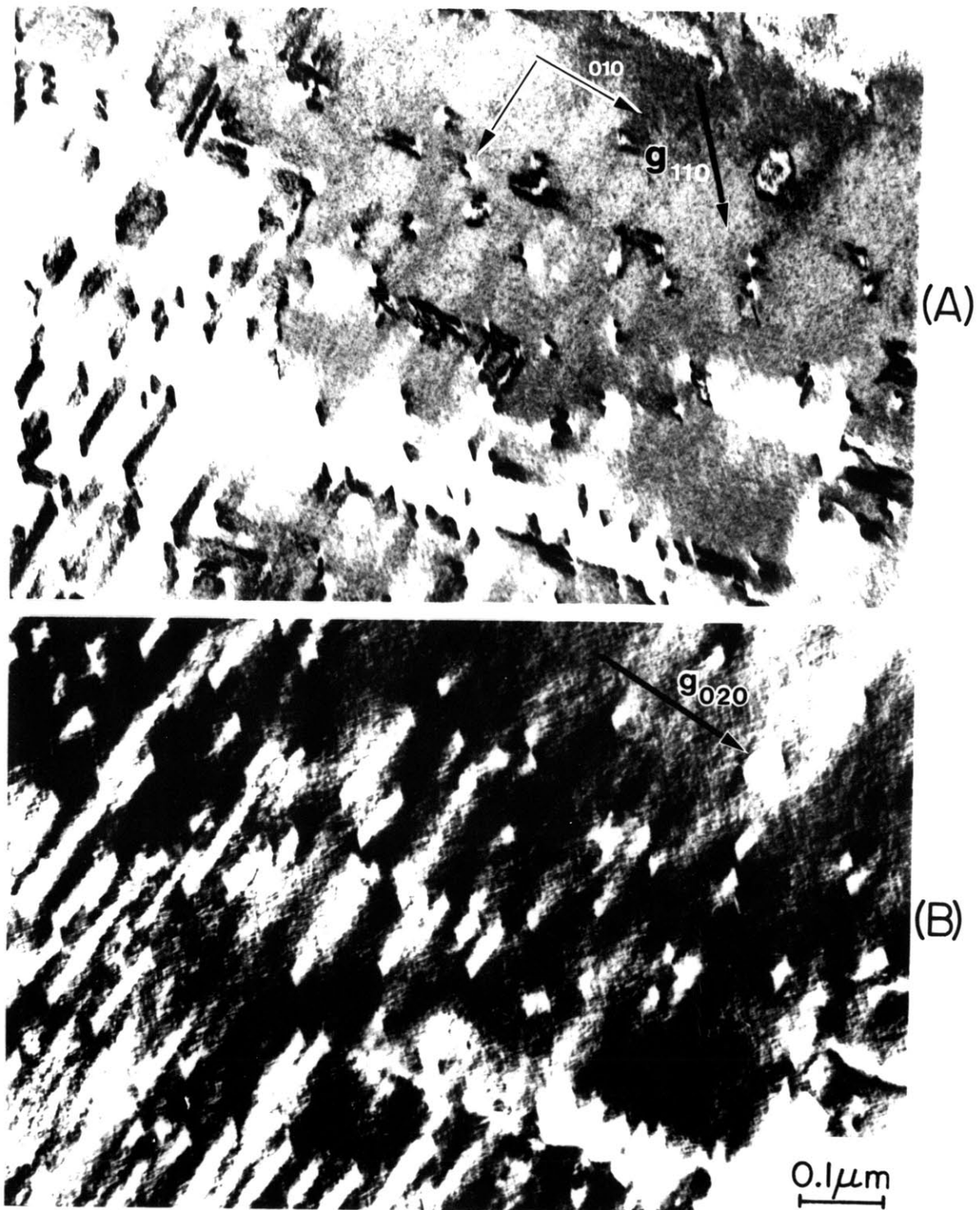
Figure 5-7. Bright-field electron micrographs of {011} planar features in martensitic Fe-25Ni-0.4C. $g = 110$ and $\bar{g} = 020$ in (A) and (B), respectively.
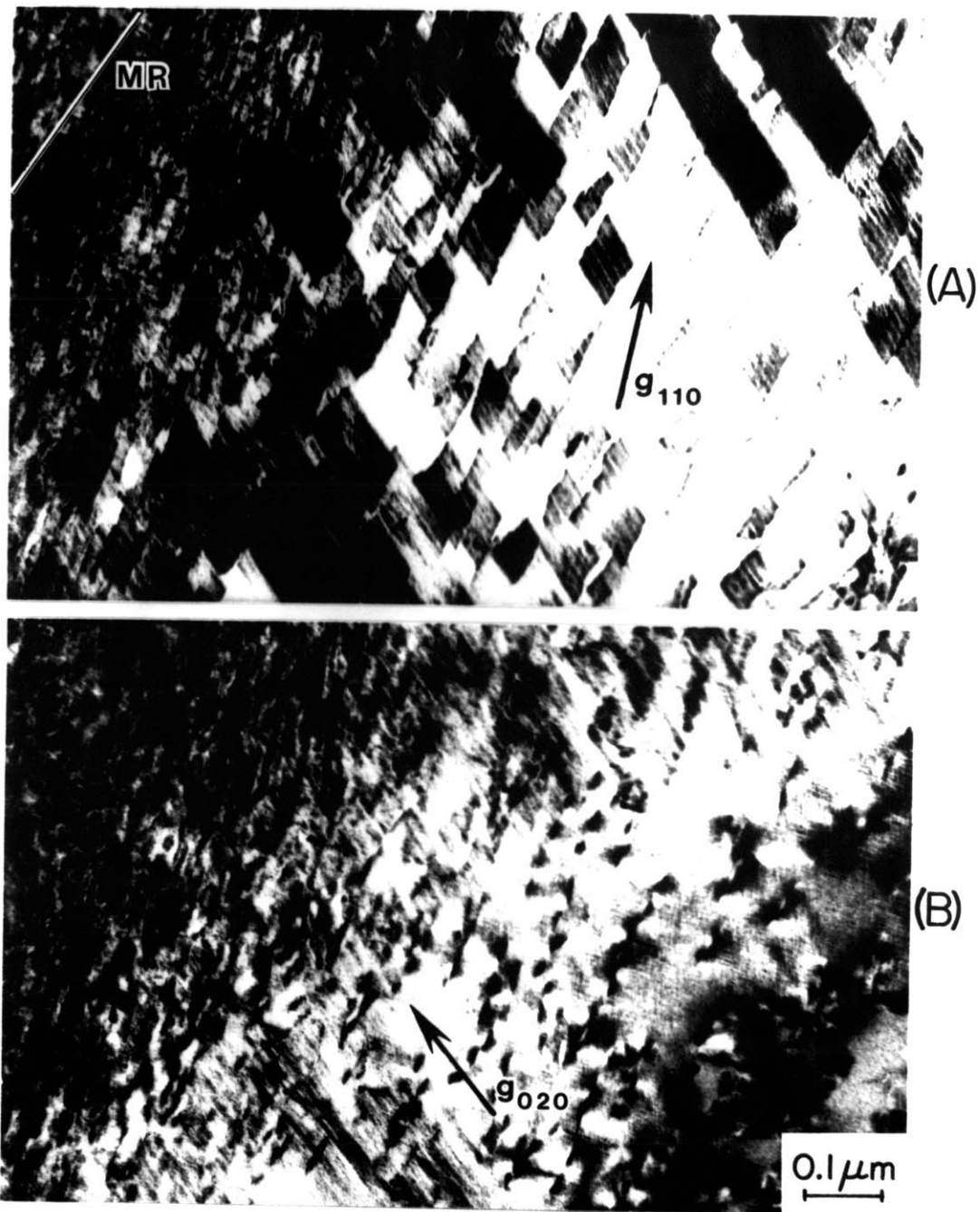
Figure 5-8. Bright-field electron micrographs of {011} planar features in
martensitic Fe-15Ni-1C. g = 110 and g = 020 in (A) and (B),
respectively. The midrib is denoted by "MR." This foil is some
2-3 times thicker as compared with that of Figure 5-7 and
therefore the planar features exhibit more fringes.

which lies in, for example, the (101) plane, is [10$\bar{1}$]. This analysis can
be summarized by saying that the defects exhibit a {01$\underline{1}$}-type habit plane
and possess an associated shear vector parallel to the particular <01$\underline{1}$>
direction lying in the habit plane.

The contrast behavior in Figure 5-8 is also consistent with the above
conclusion. In Figure 5-8(A), **g** = 110 and the {1$\underline{0}$1} defects are visible.
In this case, unlike Figure 5-7(A), the {$\underline{0}$11} defects appear to be absent.
In Figure 5-8(B), **g** = 020 and the {1$\underline{0}$1} defects are invisible, as would be
expected since their shear vector is parallel to [10$\bar{1}$] (or [101]) and **g·R**
is therefore zero.

Some knowledge of the distribution of the {01$\underline{1}$} defects can be gained
from Figure 5-9(A). This is a low-magnification view of the same
martensitic plate shown in Figure 5-7 (the region in Figure 5-7 is at the
lower left of Figure 5-9). The midrib (MR) of the plate can be seen
running nearly vertically along the left side of the micrograph. The
contrast in the midrib itself is due to (112) transformation twins, whose
trace lies along the [$\bar{1}$10] direction. The density of {01$\underline{1}$} defects is
clearly highest in the immediate vicinity of the midrib, and decreases in
moving away from the midrib. In addition, there appears to be a strong
tendency for only one defect variant to be present in the immediate
vicinity of the midrib. This agrees with the fact that only one variant
exists in Figure 5-8(A). A second defect variant, as in Figure 5-9,
frequently appears in moving away from the midrib. No extreme difference
in the number density of the {01$\underline{1}$} defects was apparent between the two Fe-
Ni-C alloys, although this conclusion is, at best, very qualitative.

Further insight into the nature of the {01$\underline{1}$} defects can be gleaned
from Figure 5-9(B). This is a bright-field micrograph of the midrib region
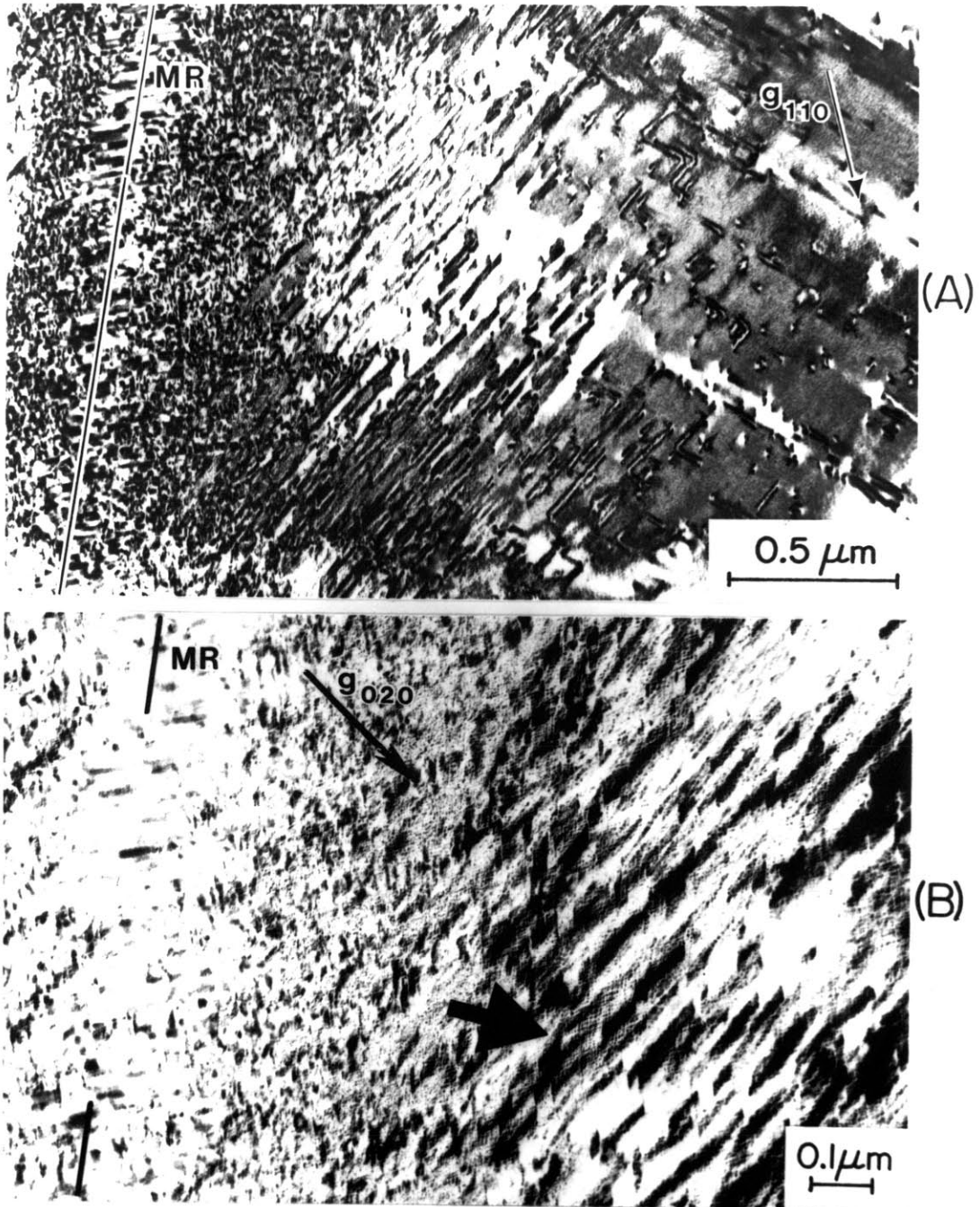
Figure 5-9. Bright-field electron micrographs of {011} planar features in martensitic Fe-25Ni-0.4C. $g = 110$ and $\bar{g} = 020$ in (A) and (B), respectively. The midrib is denoted by "MR."

of Figure 5-9(A), taken with **g** = 020. In the vicinity of the midrib, where the density of (011) defects is high, a peculiar contrast consisting of fine-scale striations is present. The striations tend to lie along two different directions, giving rise to a "basketweave" or "tweed-like" morphology. This type of contrast will be discussed at length in connection with aging phenomena (Chapter 7); for now it is sufficient to say that the c-axis of the martensitic structure lies along the bisector of the larger of the two angles made by the criss-crossing sets of striations. This is quite surprising, since the direction of the electron beam has also been taken to be parallel to the c-axis. How, then, can some regions of the martensitic plate have their c-axis oriented at some 90° with respect to adjacent regions? The most obvious answer is that twinning on $\{01\underline{1}\}$ has occurred. For example, twinning on (011) transforms the b-axis into the c-axis, which is the situation that is seen in Figure 5-9(B).

It will be recalled (from Section 2.4) that twinning on $\{01\underline{1}\}$ has been predicted to occur [39], on the basis of the unusual axial ratios of certain Fe-X-C martensites. Such twinning involves a shear (whose magnitude depends on the axial ratio of the lattice) of the type <0kk> on successive $\{01\underline{1}\}$ planes. This is precisely the type of shear that is indicated from the contrast analysis given above. Thus, it can now be concluded that the $\{01\underline{1}\}$ defects represent the boundary between material which is related by a twinning operation on $\{01\underline{1}\}$.

Roytburd and Khachaturyan [39] originally suggested that $\{01\underline{1}\}$ defects are actually stacking faults (on $\{111\}_{\gamma}$) which are inherited from the parent austenite phase. In the present investigation, however, no faulting was observed in the austenite, even in the severely deformed retained austenite which survives cooling to -196°C. Consequently, one must

conclude that twinning on {01$\underline{1}$} occurs either as a mechanism for post-transformation stress-relief within the martensitic phase, or that it is part of the lattice-invariant deformation of the martensitic transformation itself. The latter conclusion is supported by the inhomogeneous distribution of twins (i.e. the high concentration near the midrib).

Some clues regarding the mechanism of {01$\underline{1}$} twinning can be sought from Figure 5-7(A). Here, two different defect variants often intersect. The only direction which is contained in two different {01$\underline{1}$} planes is of the type <111>. In addition, isolated defects also often appear to be bounded by a <111> direction. This suggests that the {01$\underline{1}$} twins may form by the dissociation of 1/2<111> screw dislocations. An appropriate dissociation reaction, consistent with the necessary twinning shear, can be written as

$$1/2[11\bar{1}] \rightarrow 1/4[21\bar{1}] + 1/4[01\bar{1}]. \tag{5-4}$$
$$(011)$$
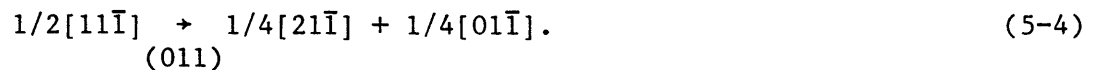
Frank's rule can be invoked to demonstrate that this reaction may be energetically favorable. This rule assumes that the energy of a dislocation is proportional to the square of the magnitude of its Burgers vector. Thus we have:

$$3/4 \rightarrow 3/8 + 1/8 = 1/2,$$

which clearly (neglecting any associated stacking-fault energy) constitutes a net reduction in energy.

The shear, R, necessary for twinning on {01$\underline{1}$} is given by

$$R = f(c/a) \cdot <01\underline{1}>, \tag{5-5}$$

80

where
$$f(c/a) = \frac{(c/a)^2 - 1}{(c/a)^2 + 1}.$$

For a c/a of 1.07 (which may be taken to represent, at least approximately, 100% O_z site occupancy by carbon atoms in an Fe-1.0C alloy), f(c/a) is 0.068. The cumulative displacement produced by a twin which is four {01$\bar{1}$} planes in thickness is then 4 x 0.068<01$\bar{1}$> = 0.27<01$\bar{1}$>. This is very nearly equal to the Burgers vector of the leading partial dislocation produced by the dissociation reaction of Equation 5-4. Thus, a thin {01$\bar{1}$} twin can be formed by allowing the leading 1/4<01$\bar{1}$> partial to spread its displacement over several (the actual number may depend on c/a) {01$\bar{1}$} planes. The extended displacement field of the partial then represents the displacements due to O_y (or O_x) occupancy of carbon atoms within that volume. Whether carbon atoms move from O_z to O_y or O_x sites depends upon the particular twinning variant in operation: for twinning on (011) and (01$\bar{1}$), carbon atoms move into O_y sites; for twinning on (101) and (10$\bar{1}$), carbons move into O_x sites.

As discussed in Section 2.4, the lattice constants of martensite are given by

$$a = a_0[1 + u_{11}(n_2 + n_3) + u_{33}n_1]$$
$$b = a_0[1 + u_{11}(n_3 + n_1) + u_{33}n_2] \qquad (2\text{-}9)$$
$$c = a_0[1 + u_{11}(n_1 + n_2) + u_{33}n_3],$$

where n_1, n_2, and n_3 are the ratios of the number of carbon atoms in O_x, O_y, and O_z sites, respectively, to the number of host atoms, and the u_{ij} are elements of the concentration-dependent lattice expansion tensor. Also appearing in Equations 2-9 is a_0, the lattice constant of the corresponding

carbon-free alloy. In as much as twinning on $\{01\underline{1}\}$ alters the relative values of n_1, n_2, and n_3, this may be invoked to explain differences which exist in the measured axial ratios for different Fe-X-C alloy systems. Equations 2-9 indicate that martensite is only truly tetragonal for the case where $n_1 = n_2$, i.e. for equal O_y and O_x occupancy. When single-crystal x-ray diffraction techniques are employed, it is generally found that the martensite lattice is macroscopically orthorhombic, as would be predicted for the general case where $n_1 \neq n_2 \neq n_3$. In such cases, the orthorhombicity is relatively small, but nonetheless detectable. In any event, variations in the concentration dependence of axial ratios among different alloy systems can now be explained in terms of the differences in the relative volume fractions of the different $\{01\underline{1}\}$ twinning variants. The amount of $\{01\underline{1}\}$ twinning which actually takes place may depend on alloy composition as well as on the elastic properties of the alloy.

It should be emphasized that twinning on $\{01\underline{1}\}$ does not force one to consider the structure of martensite to be orthorhombic. Rather, its structure should be considered tetragonal, but with a domain-like substructure where each domain has its c-axis oriented at nearly right angles to adjacent domains due to a $<01\underline{1}>\{01\underline{1}\}$ twinning operation. As discussed in Section 6.1, the axial ratio for fully tetragonal martensite can be measured when selected micro-area diffraction techniques can be applied to small volumes of crystal which are free of $\{01\underline{1}\}$ twins.

The lattice constants from the study of Chen and Winchell [69] can be applied to Equations 2-9 to calculate the volume fraction of $\{01\underline{1}\}$ twins in Fe-18Ni-1.0C. Note that this composition is similar to the Fe-15Ni-1C alloy of the present study. Since Equations 2-9 consist of three relations involving a total of five unknowns (n_1, n_2, n_3, u_{11}, and u_{33}), some

additional relations are required to specify a solution. First, the requirement that $n_1 + n_2 + n_3 = n_C$ can be imposed (where n_C is the total number of carbon atoms divided by the total number of host atoms).

Secondly, a relationship between u_{11} and u_{33} can be derived by examining an alloy where the distribution of carbon atoms among the OIS is known. Entin et al. [14] examined the structure of martensitic Fe-8Ni-1.5C ($n_C = 0.0711$) via neutron diffraction. Their sample was enriched with ^{57}Fe and ^{62}Ni in order to increase the relative contribution of carbon to the total diffracted intensity (^{57}Fe has a small positive scattering amplitude and ^{62}Ni has a relatively large negative scattering amplitude). In addition to concluding that carbon atoms occupy only OIS sites, they were also able to infer that 20% of the carbon atoms occupy O_x and O_y sites. For simplicity, we will assume that $n_1 = n_2$ for their alloy, whence Equations 2-9 can be written as:

$$a = b = a_0[1 + u_{11}(\frac{n_C + n_3}{2}) + u_{33}(\frac{n_C - n_3}{2})] \qquad (5\text{-}6A)$$

$$c = a_0[1 + u_{11}(n_C - n_3) + u_{33}n_3] \qquad (5\text{-}6B)$$

$$\text{and} \qquad c/a \cong 1 + \frac{(u_{33} - u_{11})}{2} \cdot (3n_3 - n_C), \qquad (5\text{-}6C)$$

where $n_3 = 0.8n_C$. Entin et al. found that c/a was 1.07 for their alloy. Substituting for c/a, n_3, and n_C in Equation 5-6C, one obtains

$$u_{33} - u_{11} = 1.41. \qquad (5\text{-}7)$$

For virgin Fe-18Ni-1.0C ($n_C = 0.0464$), Chen and Winchell report that a = 0.28314, b = 0.28433, and c = 0.29913 nm. Substituting these values into Equations 2-9, and combining with Equation 5-7, one obtains the following:

$$n_1 = 0.0013$$

$$n_2 = 0.0042$$

$$n_3 = 0.0409$$

and
$$V_T\{1\underline{0}1\} = n_1/n_C = 0.028$$

$$V_T\{\underline{0}11\} = n_2/n_C = 0.091,$$

where V_T is the volume fraction of the indicated twin variant. Note that the results indicate that the volume fractions of the two types of twin families differ by about a factor of three, which is qualitatively consistent with the TEM observations described earlier. The total twin volume fraction is 0.119, also qualitatively consistent with the TEM results.

Let us now consider the behavior of Fe-6.2Mn-1.0C ($n_C = 0.0469$), an alloy which exhibits a significant orthorhombic distortion and an unusually small effective tetragonality. Lysak et al. [81] give the following lattice parameters: a = 0.2866, b = 0.2882, and c = 0.2955 nm. From Equations 2-9 and 5-7, one obtains:

$$n_1 = 0.007$$

$$n_2 = 0.011$$

$$n_3 = 0.029$$

and
$$V_T\{1\underline{0}1\} = 0.15$$

$$V_T\{\underline{0}11\} = 0.23.$$

Note that the total volume fraction of twins is significantly larger than for Fe-18Ni-1.0C (0.38 vs. 0.12) and is consistent with Sachdev's [42] observations of extensive $\{01\underline{1}\}$ twinning in Fe-Mn-C alloys.

The above calculations thus demonstrate how anomalies in the lattice

constants of virgin martensites can be explained simply on the basis of carbon movement to O_x and/or O_y sites. This conclusion, when coupled with the TEM observations, indicates that twinning on $\{01\underline{1}\}$ is an important mechanism for transferring carbon atoms to different octahedral interstitial sublattices. Alloys in which no significant $\{01\underline{1}\}$ twinning occurs will have an ideal tetragonal structure with the maximum possible tetragonality. On the other hand, alloys in which appreciable $\{01\underline{1}\}$ twinning occurs will have smaller axial ratios and generally a macroscopically orthorhombic lattice due to differing extents of twinning on $\{1\underline{0}1\}$ and $\{\underline{0}11\}$.

5.5 Summary

In summary, the important substructural features of the martensites of this study include the following:

(1) Twinning on $\{11\underline{2}\}$ planes, limited primarily to the midrib region. The twin thicknesses generally range from about 2 to 20 nm and, of the total volume of the martensitic phase, perhaps 20 to 30% is densely twinned.

(2) Lattice dislocations, primarily pure screw in character, with Burgers vectors of the type $1/2\langle111\rangle$. The total dislocation density is in the range of $1 - 4 \times 10^{10}$ cm/cm^3; however, the four possible $\langle111\rangle$ variants may not be equally populated within any given volume. The dislocation density appears to be highest in the vicinity of the midrib; however, many of these are partial dislocations associated with twin boundaries.

(3) Twinning on $\{01\underline{1}\}$ planes. Such twinning involves the coordinated movement of carbon atoms from O_z to O_y (or O_x) sites, and may be catalyzed by the dissociation of $1/2\langle111\rangle$ lattice dislocations. The $\{01\underline{1}\}$ twins are not uniformly dispersed throughout the martensitic phase, but tend to be more numerous in the vicinity of the midrib. This suggests that $\{01\underline{1}\}$

twinning may be an important lattice-invariant deformation mechanism which operates during the martensitic transformation. In addition, the presence of such twins can explain anomalies in the measured lattice parameters of various Fe-X-C martensites.

CHAPTER 6

ELECTRICAL RESISTIVITY BEHAVIOR

AND THE KINETICS OF AGING AND TEMPERING

A knowledge of the kinetics of aging and tempering has important

implications. Not only may it permit the rate-controlling process(es) to

be deduced, but it may also allow the direct comparison of results obtained

from independent investigations, where combinations of aging/tempering

temperature and time invariably differ. Eldis [75] and Sherman [25] have

systematically measured the variation in activation energy throughout the

aging and tempering processes in a series of Fe-Ni-C alloys. Their

experimental approach was applied to the two Fe-Ni-C alloys of this study.

The present results and analyses are reported in this chapter and are later

used in the interpretation of TEM results. The assumptions implicit in the

kinetic analysis are also briefly described; the reader can find more

detailed discussion in References [75] and [25].

6.1 General Features of the Resistivity Behavior

Both Eldis and Sherman noted that characteristic changes in electrical

resistivity occur during aging and tempering. The general features of the

resistivity behavior were the same in all the alloys they studied, even

when differences in martensitic morphology (lath vs. twinned) occurred.

Figure 6-1 illustrates the behavior schematically, where the curve is

broken into three regimes for the purposes of subsequent discussion. The

work of Eldis and of Sherman (as well as this study) indicates that the

schematic behavior is characteristic of a wide range of isothermal (or

isochronal) treatments, but that the time (or temperature) scale of a

particular treatment may not encompass the entire range of Figure 6-1.
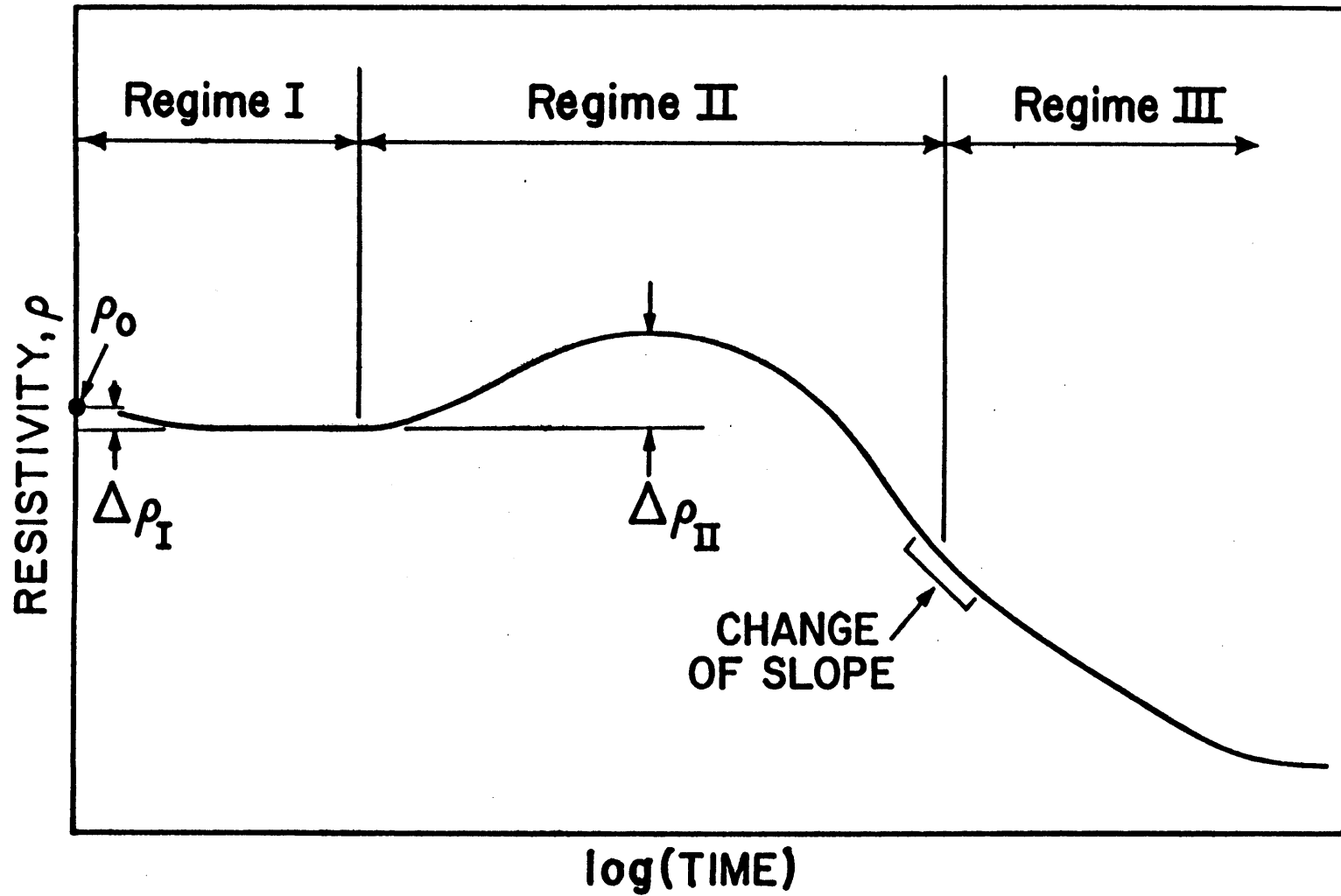
Figure 6-1. Schematic electrical resistivity vs. log(time) behavior (after Sherman et al. [70]).

Regime I is characterized by a slight decrease in resistivity, $\Delta\rho_I$, which is detectable only at low aging temperatures. The cause of this change is discussed in some detail in Appendix B. For now, it suffices to say that regime I is due to the transformation of some retained austenite to martensite. Since this process does not involve the aging or tempering of martensite **per se**, it will not be discussed any further here. In regime II, there is a peak in resistivity which is measured in alloys aged in the vicinity of room temperature. The magnitude of the peak, $\Delta\rho_{II}$, tends to increase with carbon content, at least up to 0.9 wt pct. Regime III consists of a monotonic decrease in resistivity on tempering above about 125°C; above 125°C, the resistivity peak presumably occurs before the first measurement (taken after 15 seconds). Sometimes the transition from regime II to regime III is marked by a noticeable change of slope ("elbow") in the resistivity vs. log(time) curve. This is thought to reflect a change of the rate-controlling step in the tempering process [70].

Figure 6-2 shows the resistivity behavior of Fe-25Ni-0.4C and Fe-15Ni-1C, where each data point represents the relative resistivity (at -196°C) of the two-phase (austenite + aged/tempered martensite) alloy after one hour at the indicated temperature. There are some differences between these curves and the schematic curve of Figure 6-1 which deserve mention. First, regime I is absent in the alloys of this study. Even going to lower aging temperatures would not reveal regime I here because these specimens were given a one-hour preaging treatment at -130°C. This procedure allows any additional formation of martensite to take place before the processes characteristic of aging and tempering ensue at higher temperatures. If this preaging procedure were not followed, the resistivity changes measured during aging would reflect both a change in the resistivity of the
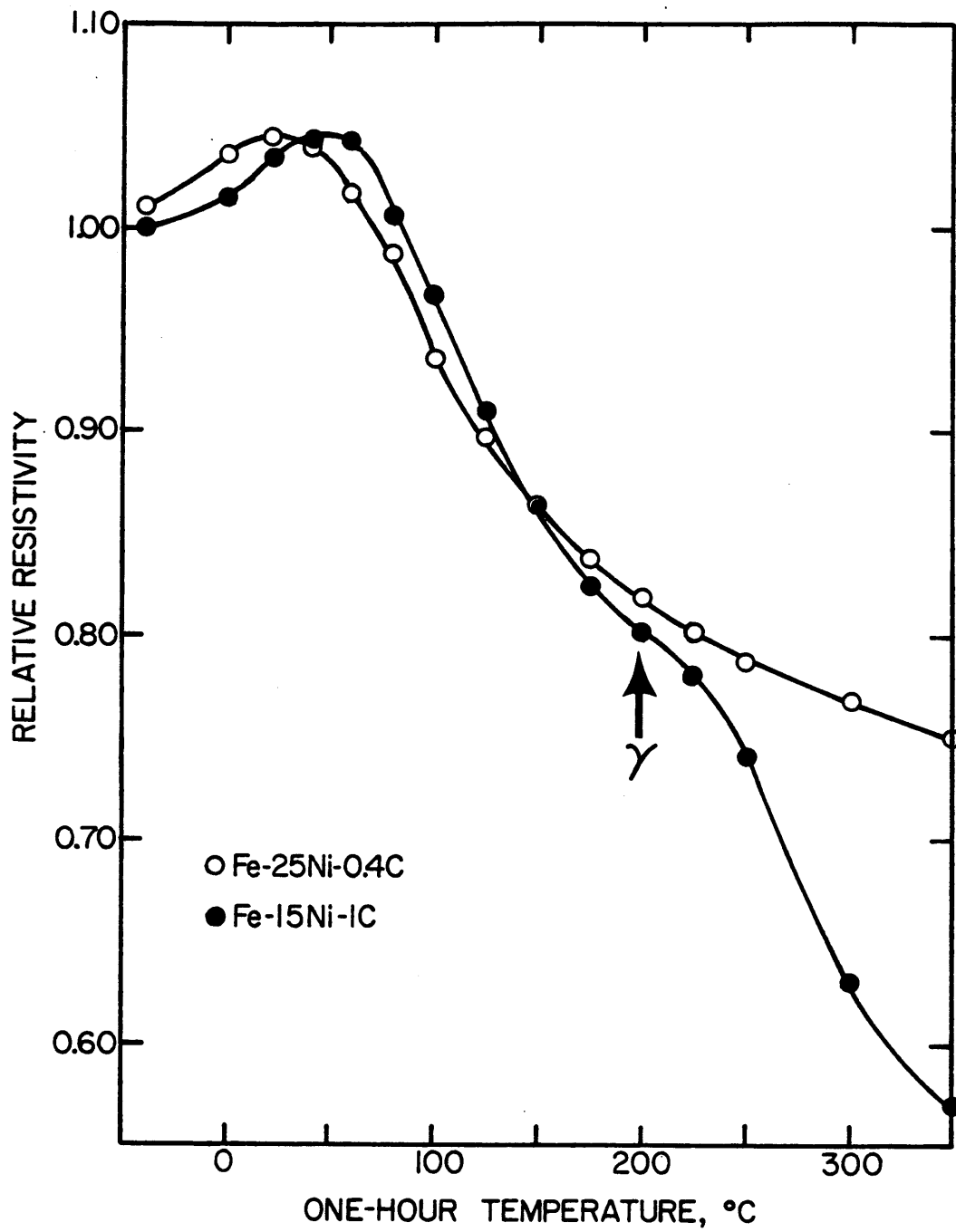
Figure 6-2. Relative resistivity (at -196°C) of two-phase
(austenite + martensite) Fe-Ni-C alloys after
aging/tempering one hour at the indicated temperature.

martensitic phase as well as the volume fraction of this phase, effects which can be difficult to separate. In this investigation, the measured magnitudes of the regime II resistivity peaks were much larger than was anticipated based on the extrapolation of Sherman's [25] data (e.g. 2.4 vs. about 1 $\mu\Omega$-cm for Fe-15Ni-1C). He did not employ a low-temperature preaging treatment for his study, thus probably resulting in an overlap of regimes I and II.

Another difference between the observed and schematic behavior concerns the conspicuous drop in resistivity at high temperatures in Fe-15Ni-1C (indicated by the arrow in Figure 6-2). Metallographic examination revealed that the retained austenite begins to decompose at the onset of this rather large resistivity change. The decomposition product is probably a mixture of ferrite and cementite, which has a resistivity substantially lower than that of the parent austenite.

Complete sets of isothermal resistivity vs. log(time) curves for both alloys are presented in Figure 6-3. Each curve represents a different specimen, with the data being normalized to the initial (preaged) resistivity. Because of the long times required for generating the data, the curves (in most cases) were obtained from a single run; where duplicate runs were made, there was excellent agreement. The general features which characterize the isochronal curves are also indicated here, although no single curve displays the complete behavior due to practical limitations on the time scale of the experiments. A new feature does appear however, in the form of a slight resistivity decrease in Fe-25Ni-0.4C at 300 and 350°C. Metallographic examination of these specimens revealed a (prior austenite) grain-boundary phase which might be ferrite or cementite; the retained austenite appears to survive this high-temperature treatment. Further
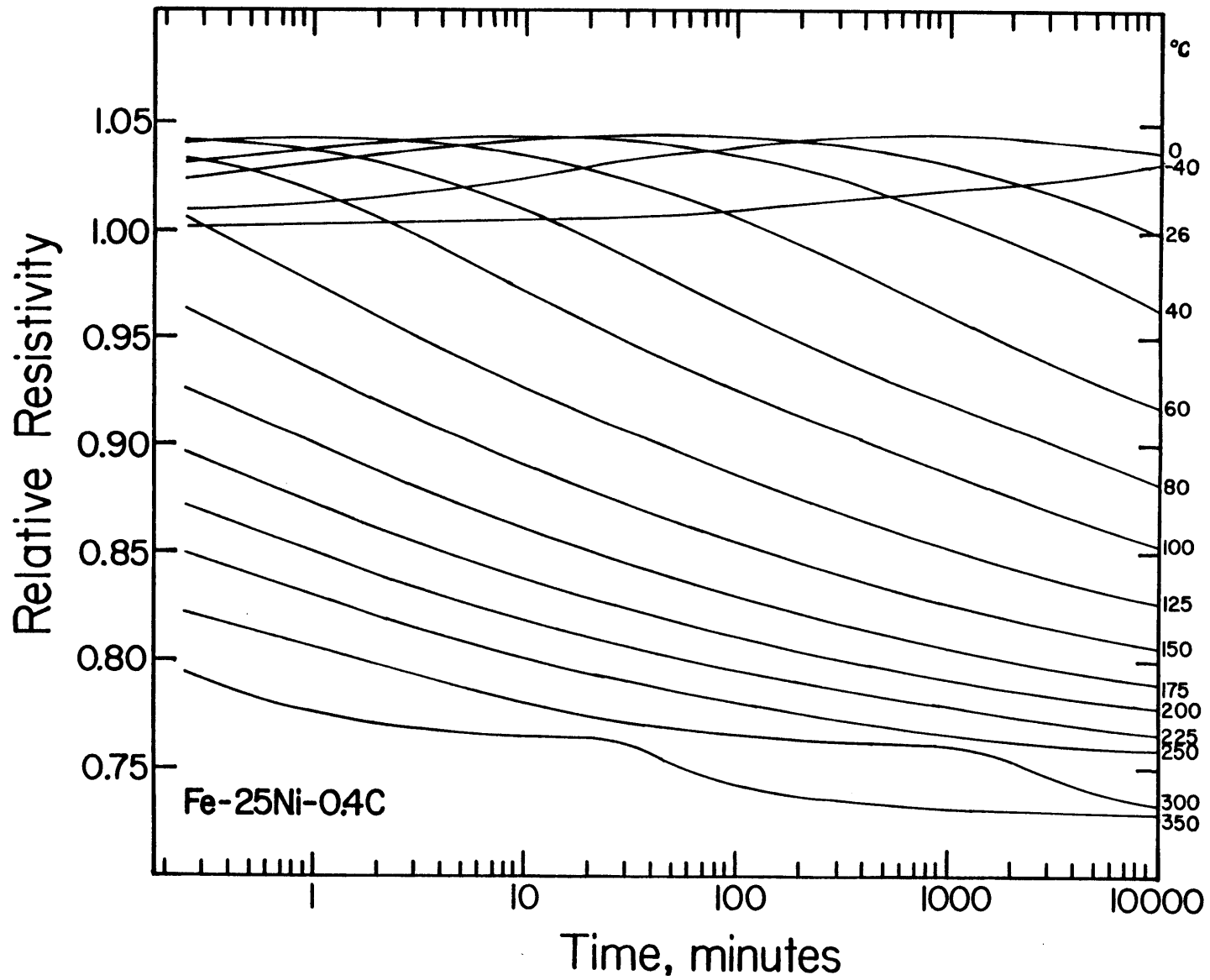
Figure 6-3(A).   Resistivity at -196°C vs. log(time) for Fe-25Ni-0.4C (85% martensite), aged/tempered at the indicated temperatures.
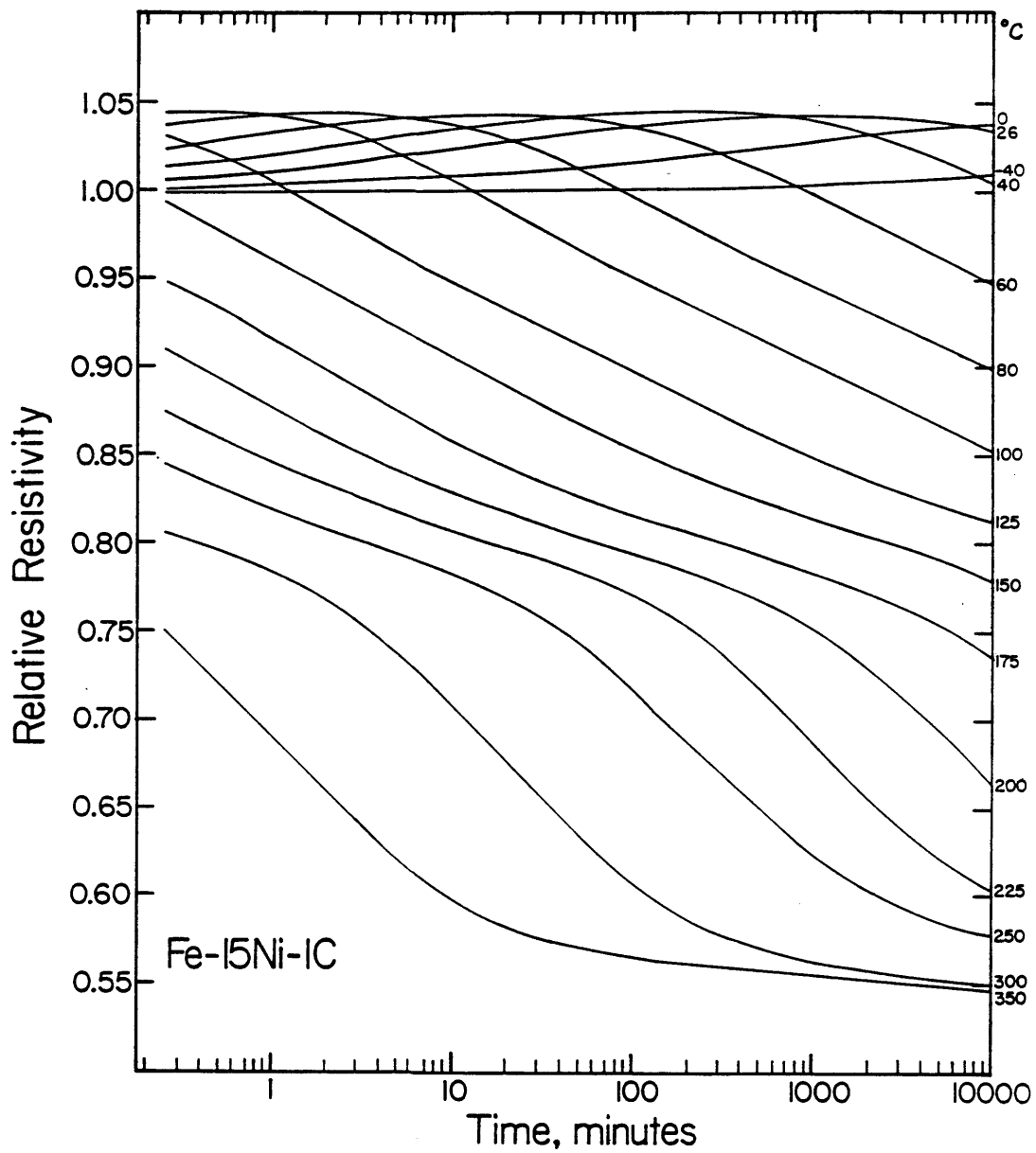
Figure 6-3(B).   Resistivity at -196°C vs. log(time) for Fe-15Ni-1C
(67% martensite), aged/tempered at the indicated temperatures.

study on the nature of the boundary phase is underway [82].

The curves of Figure 6-3 reflect the behavior of two-phase specimens; Fe-25Ni-0.4C contains 15% retained austenite and Fe-15Ni-1C, 33%. Accordingly, a procedure developed by Hoffman [83] (see Appendix A) was followed to correct the measured resistivities for the influence of retained austenite. The corrected curves, shown in Figure 6-4, correspond to the behavior of the martensitic phase itself and form the basis of the kinetic analysis which follows. It should be noted that the Hoffman correction was not applied when the retained austenite began decomposing in Fe-15Ni-1C because then Hoffman's assumption of a constant volume fraction of the martensitic phase becomes invalid.

Table 6-1 lists some resistometric parameters for the two Fe-Ni-C alloys which are mentioned in subsequent discussion. These include the resistivity of the two-phase alloys $(\rho_{\alpha+\gamma})$, the resistivity of pure austenite and martensite $(\rho_\gamma$ and $\rho_\alpha)$, and the resistivity of well-tempered martensite (ρ_e), all at -196°C. Here, ρ_e is taken to be the resistivity where the isothermal curves level-off at high tempering temperatures. For Fe-25Ni-0.4C, this corresponds to a relative resistivity of about 0.7 in Figure 6-4(A). For Fe-15Ni-1C, it corresponds to a relative resistivity of about 0.54 in Figure 6-3(B).

6.2 The Kinetic Analysis

6.2.1 Basic Assumptions

The postulate of a linear dependence of martensite resistivity on dissolved carbon content is the key assumption underlying the kinetic analysis of the resistivity data. The interstitial carbon atoms can be regarded as crystal (point) defects which displace neighboring iron atoms,

94
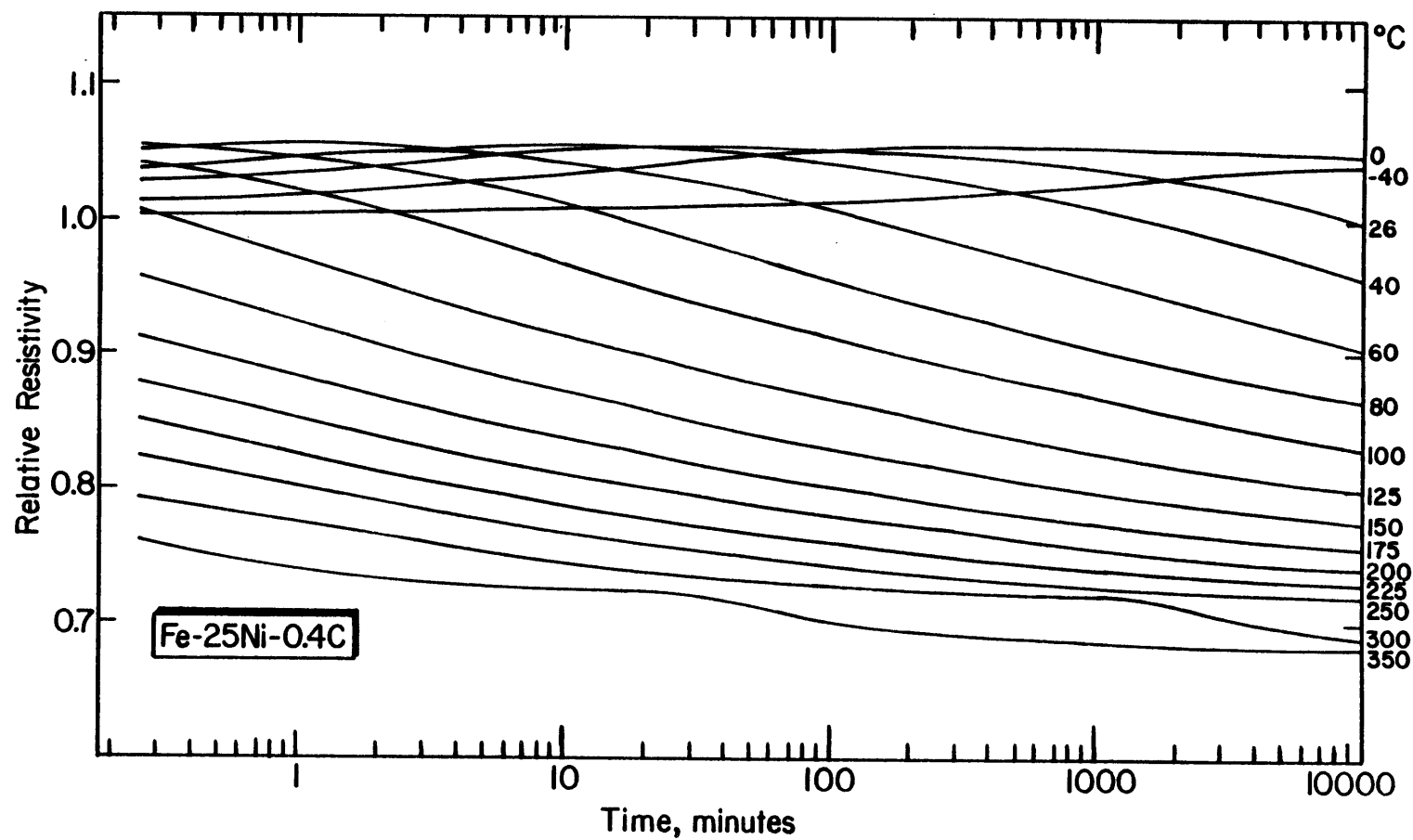
Figure 6-4(A). Resistivity at -196°C (corrected for retained austenite) vs. log(time) for martensitic Fe-25Ni-0.4C, aged/tempered at the indicated temperatures. The resistivity of virgin martensite is 25.3μΩ-cm.
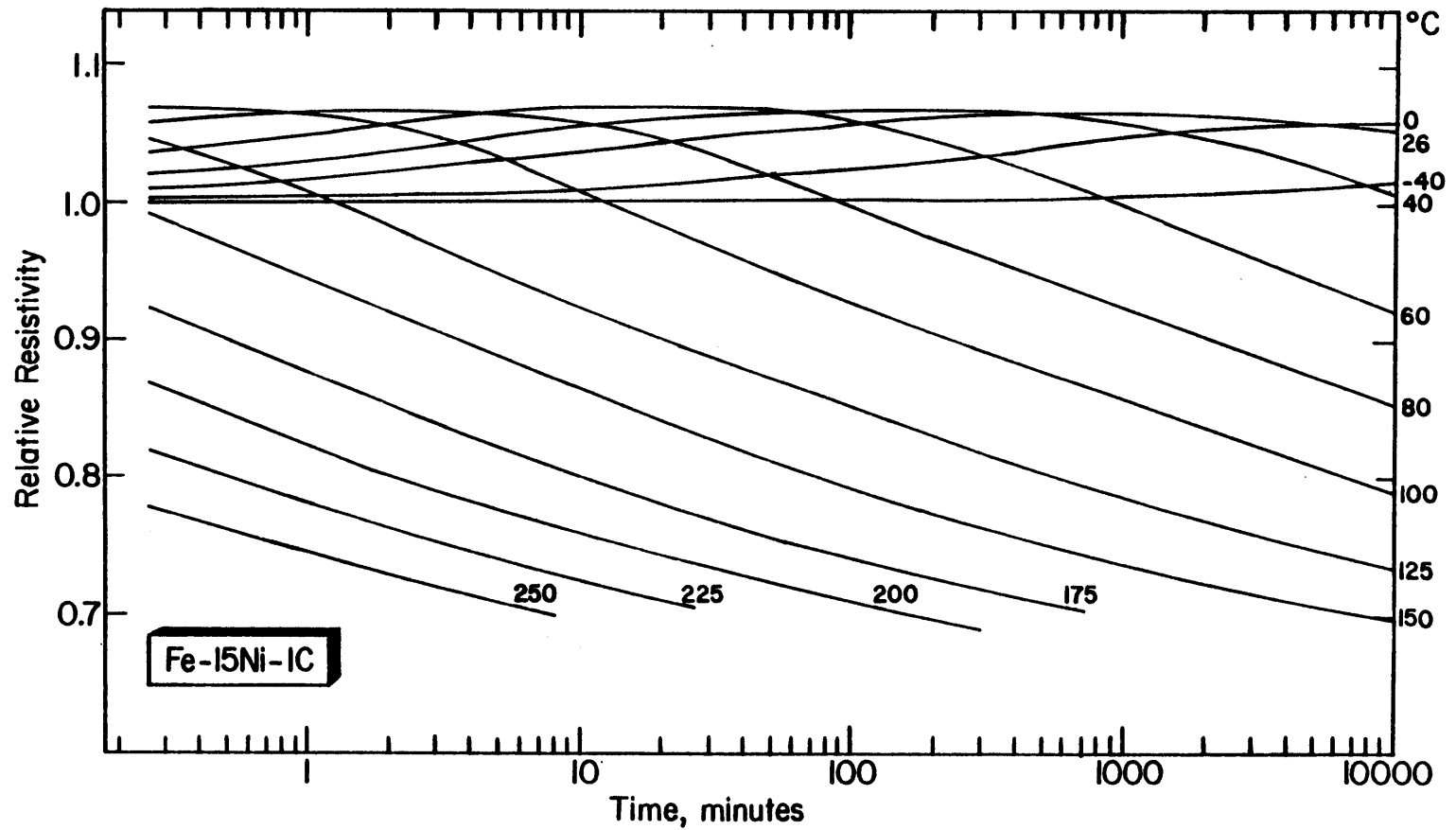
Figure 6-4(B). Resistivity at -196°C (corrected for retained austenite) vs. log(time) for martensitic Fe-15Ni-1C, aged/tempered at the indicated temperatures. The resistivity of virgin martensite is 36.3μΩ-cm.

TABLE 6-1

SELECTED ELECTRICAL RESISTIVITIES FOR THE TWO FE-NI-C ALLOYS
(in $\mu\Omega$-cm; "α" and "γ" designate untempered
martensite and austenite, respectively)

Alloy	$\rho_{\alpha+\gamma}^{-196}$	ρ_{γ}^{-196}	ρ_{γ}^{0}	ρ_{α}^{-196*}	ρ_{e}^{-196**}
Fe-25Ni-0.4C	28.8 (15% γ)	61.3	78.1	25.3	17.7
Fe-15Ni-1C	40.0 (33% γ)	49.5	72.6	36.3	21.6

*The average of the Hoffman-corrected resistivity of four and three
different samples of Fe-25Ni-0.4C and Fe-15Ni-1C, respectively.

**Not corrected for the presence of carbides.

thereby disturbing the lattice potential through which conduction electrons travel. The contribution of defects to resistivity is expressed by Matthiessen's rule

$$\rho = \rho_T + \rho_o, \qquad (6\text{-}1)$$

which separates the resistivity of a metal into a thermal component (ρ_T) whose origins are lattice vibrations, and a defect component (ρ_o). Matthiessen's rule does not take into account the residual resistivity of a pure, defect-free metal at $0^\circ K$. This quantity is generally quite small and has justifiably been ignored here. Since the resistance measurements of this investigation were all made at $-196^\circ C$, variations in resistivity must be attributed primarily to changes in ρ_o rather than in ρ_T. This, in turn, implies that resistivity changes are due primarily to the removal of carbon atoms from solution. Changes in dislocation content may also influence ρ_o, however such changes are very likely to be quite small here, particularly during aging in the vicinity of room temperature where thermally-activated dislocation migration is quite sluggish.

The Fe-Ni-C alloys of this study can, to a first approximation, be considered binary alloys. The solvent is the mixture of iron and nickel atoms while the solute is the interstitial carbon atom. Nordheim's rule gives the resistivity contribution of solute atoms of concentration n:

$$\rho(n) = An(1 - n), \qquad (6\text{-}2)$$

where A is a constant. For martensitic steels, the concentration of carbon is small and Nordheim's rule may be approximated as:

$$\rho(n) = An_C. \qquad (6\text{-}3)$$

98

This implies, as eluded to above, that the resistivity of virgin martensite should increase linearly with carbon content. This expected behavior, despite differences in nickel content, is born out in Figure 6-5, which shows the resistivity of unaged Fe-Ni-C martensites as a function of carbon content. Figure 6-5 includes the two alloys of this study as well as a series of alloys studied by Sherman [25].

Tempering, on the other hand, ultimately results in the removal of carbon atoms from solution and a net decrease in the average rms iron-atom displacement. Figure 6-5 shows that the total resistivity change accompanying complete tempering varies in a linear manner with total carbon content. Here, the total change is given by the the resistivity of "well-tempered" martensite less that of virgin martensite.

In considering the kinetics of a transformation, a major parameter of interest is f, the "fraction transformed" or degree of completion of the reaction. Letting ρ_o be the resistivity of virgin martensite, ρ_e the resistivity at the end of tempering, and ρ the instantaneous value of resistivity, we can define f phenomenologically as follows:

$$f = \frac{\rho_o - \rho}{\rho_o - \rho_e}.$$

(6-4)

Implicit in Equation 6-4 is the assumption that a given normalized resistivity represents the same state of aging or tempering, regardless of the time/temperature path taken to reach that resistivity. Equation 6-4 also signifies that ρ can be substituted for f in the kinetic expressions which follow (by virtue of the linear relationship between the two quantities).

Since aging and tempering permits segregation of carbon atoms, one
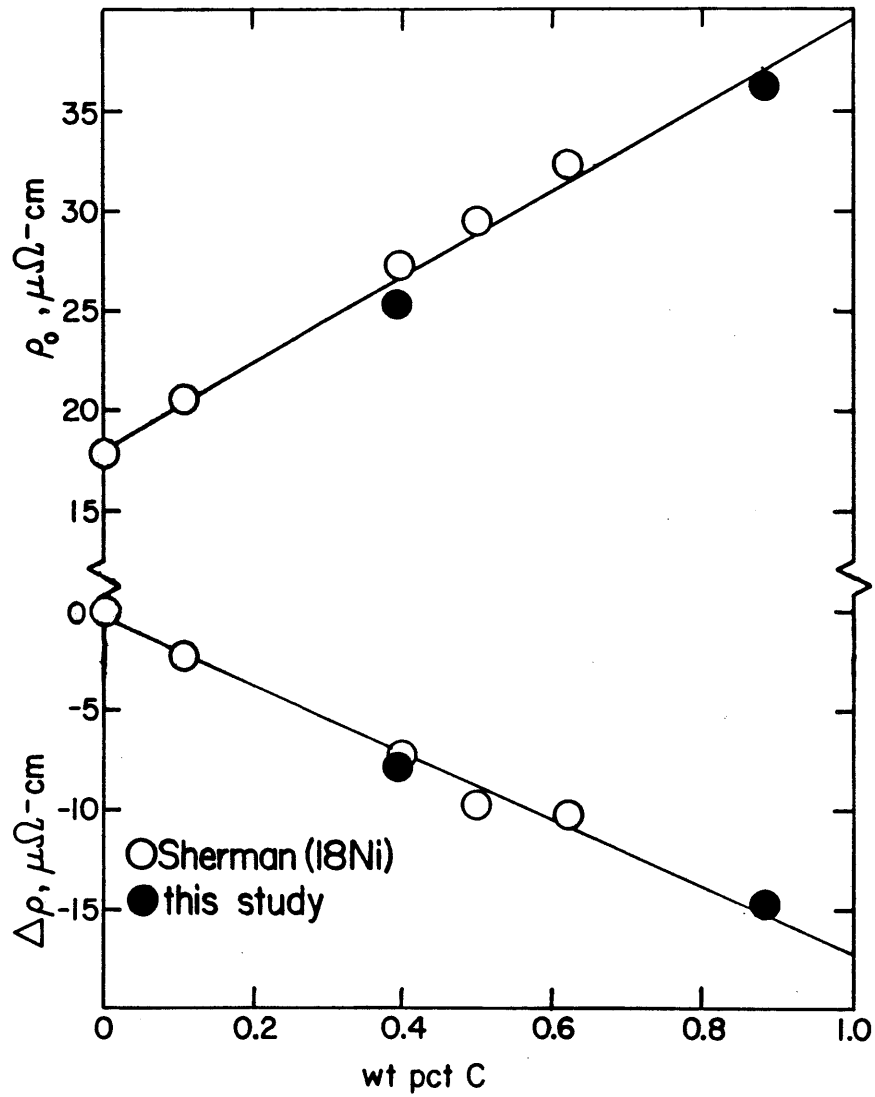
Figure 6-5. Resistivity of virgin martensite (ρ_o) and total resistivity change attending complete tempering ($\Delta\rho = \rho_o - \rho_e$) as a function of carbon concentration for various Fe-Ni-C alloys.

might well ask why an **increase** in resistivity occurs in regime II. The resistivity peak in Fe-Ni-C martensites is not well understood, but it appears to be associated with a redistribution of carbon atoms which causes the rms static displacement of iron atoms to increase. This hypothesis is discussed in more detail by Eldis [75] and by Hoffman and Cohen [84]; more is also said in Chapter 7.

6.2.2 Methods

One procedure for calculating the activation energy of a thermally-activated process is to start with a generalized Avrami equation:

$$f = 1 - \exp[-(kt)^n] \qquad (6-5)$$

in which f = fraction transformed

t = time

n = time exponent

$k = k_0 \exp(-Q/RT)$

k_0 = a constant

Q = activation energy

R = gas constant

and T = absolute temperature.

It is usually assumed that k and n are independent of f, and by taking the natural log of both sides of Equation 6-5 twice:

$$\ln t = -\frac{Q}{R} \cdot (1/T) + C(f), \qquad (6-6)$$

where C is a constant for a given value of f. The slope of a plot of $\ln t$ vs. $1/T$ (for a particular value of f) then gives the activation energy:

$$- \frac{Q}{R} = \frac{\partial \ln t}{\partial (1/T)}\bigg|_{f=f_1}. \tag{6-7}$$

When Q is not a function of f (i.e. the activation energy does not vary during the course of the reaction), the slope of a plot of ln t vs. 1/T is the same for all values of f. However, if the activation energy does vary, then Q represents an average activation energy for the process up to $f = f_1$. Hillert [71] has pointed out that the latter is in fact the case for the tempering of martensite, where several overlapping processes may occur, each perhaps having a different activation energy. He suggested that Q can be more accurately calculated by considering the transformation rate (at a particular f or ρ) rather than only time (to attain a particular f or ρ). Hillert considered the rate of transformation to be a function of both f and T:

$$\frac{\partial f}{\partial t} = G(f,T) = G_o(f) \cdot \exp - \left[\frac{Q(f)}{RT}\right]. \tag{6-8}$$

Taking the natural log of each side:

$$\ln \frac{\partial f}{\partial t}\bigg|_{f=f_1} = \ln G_o(f_1) - \left[\frac{Q(f_1)}{RT}\right]. \tag{6-9}$$

The slope of a plot of $\ln \partial f/\partial t|_{f=f_1}$ vs. 1/T then gives a Q value more closely reflecting the activation energy of the process(es) occurring at $f = f_1$:

$$\frac{Q(f_1)}{R} = - \frac{\partial \ln(\partial f/\partial t)}{\partial (1/T)}\bigg|_{f=f_1}. \tag{6-10}$$

Equation 6-10 can readily be applied to the regime III resistivity behavior of Figure 6-4, where the continuous decrease of resistivity

102

reflects the progressive removal of carbon atoms from solution. However, a problem does arise in applying Equation 6-10 to the regime II resistivity peak. Here the association of a particular resistivity with a particular value of f is not justifiable; not only is ρ not single-valued, but ρ also increases, indicating an unphysical (by Equation 6-4), negative "fraction transformed." To avoid this difficulty, the following simple but reasonable assumption is made: namely, that attainment of a particular fraction of the total **peak height** represents the same state of aging, regardless of the time and temperature required to reach that state (in resistivity). This empirical assumption permits Equation 6-7 to be applied to the resistivity data.

6.2.3 Results and Discussion

The changes in activation energy accompanying aging and tempering are shown in Figure 6-6. The data for Fe-15Ni-1C are somewhat incomplete due to the complications arising from retained austenite transformation. Though there is some scatter in the data, several trends are clear. First, a rather marked increase in Q occurs on traversing the resistivity peak. Throughout this regime the activation energy for Fe-15Ni-1C remains about 8 - 25 kJ/mole (2 - 6 kcal/mole) higher than that for Fe-25Ni-0.4C. A gradual increase in Q takes place over the range $0 < f < 0.6$, but the difference in Q between the two alloys decreases from about 8 kJ/mole (2 kcal/mole) at $f = 0$ to essentially zero at $f = 0.6$. For $f > 0.7$, relatively large values of Q are measured, centered at about 145 kJ/mole (35 kcal/mole) for Fe-25Ni-0.4C.

An increase in activation energy during regime II was also noted by Eldis [75] and Sherman [25]. In passing through the resistivity peak,

103
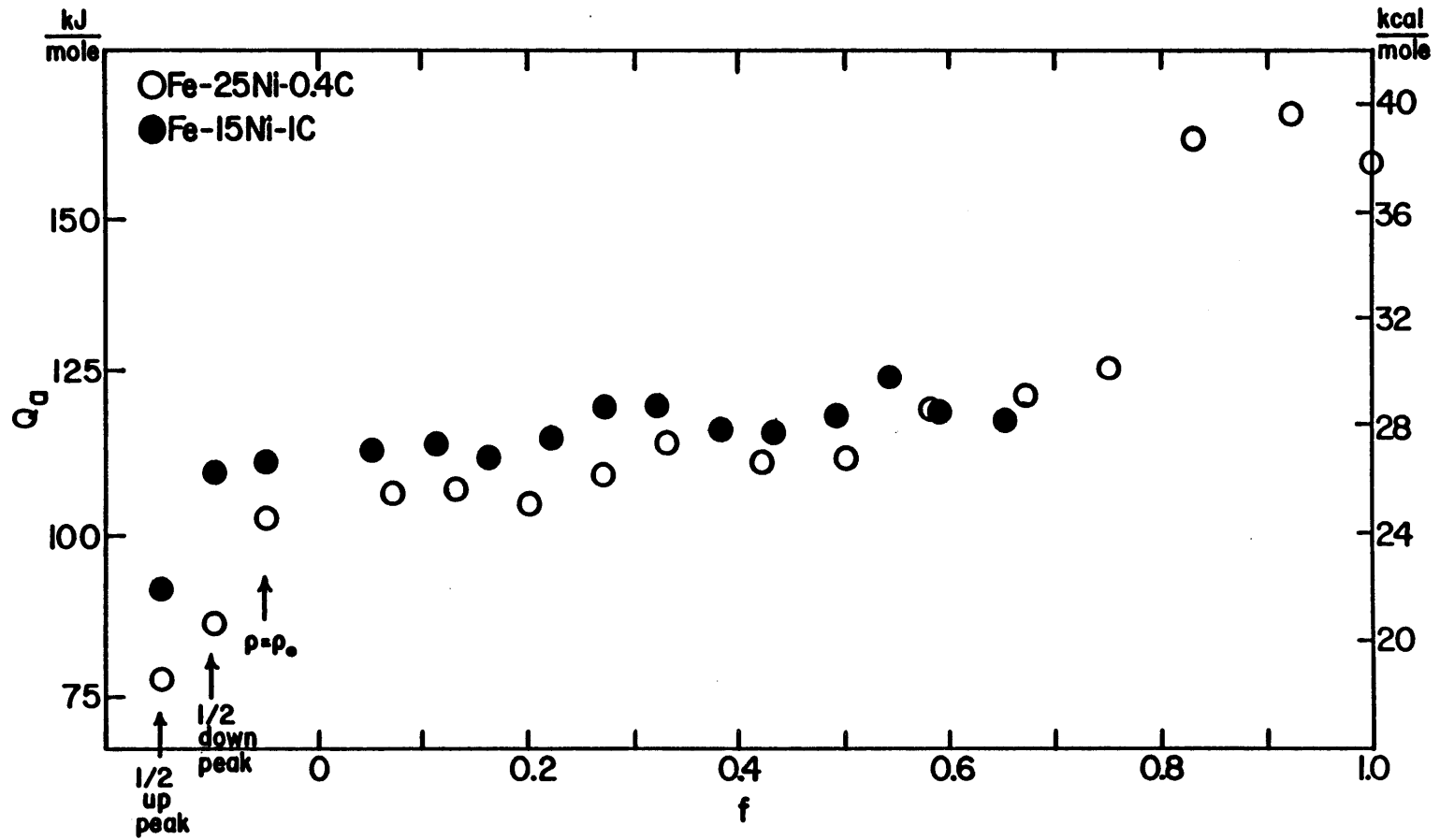
Figure 6-6. Activation energy (Q) vs. fraction transformed (f) for Fe-25Ni-0.4C and Fe-15Ni-1C. Values of Q at various points on the regime II resistivity peak are also shown.

Sherman found that Q increased from 75 to about 100 kJ/mole for alloys containing between 0.11 and 0.62 wt. pct. carbon. The same holds true for the Fe-25Ni-0.4C alloy of this study; however, the corresponding Q's for Fe-15Ni-1C are shifted upward as described above. The "average" Q for regime II and its increase at higher carbon content is in qualitative agreement with Hillert's [71] postulate of a concentration-dependent diffusion coefficient for carbon in martensite (Equation 5-1). This leaves little doubt that the rate-controlling step during aging involves the diffusion of carbon atoms; this process is consistent with the considerable evidence which indicates that a carbon-atom redistribtuion occurs during aging.

No well-defined change of slope, marking the onset of regime III, can be identified in the resistivity curves of Figure 6-4. Instead, only gradual changes of slope are evident beyond the peak, probably a reflection of the gradually increasing activation energy. In contrast, the "elbow" observed by Eldis and Sherman is associated with a more rapid increase in Q. This difference in behavior may be a reflection of slight differences in martensitic substructure and is probably not significant.

The increase in activation energy to 145 kJ/mole for Fe-25Ni-0.4C is encountered well into the conventional first stage of tempering. This value can thus be associated with the coarsening of epsilon carbide and cementite precipitation as well. A Q of 145 kJ/mole is well above that for carbon diffusion and well below that for iron (lattice) diffusion, which is about 250 kJ/mole [85]. However, Eldis and Sherman both point out that the former Q is nearly equal to the calculated activation energy for the short-circuiting diffusion of iron atoms along lattice dislocations [86]. Accordingly, they conclude that carbide precipitation is controlled by dislocation pipe-diffusion of iron, presumably required by the increase in

the molar volume of iron for the carbide phases; this interpretation will be critically evaluated in Chapter 8, in light of the TEM results on transition carbide precipitation.

To summarize, the process of martensite decomposition apparently involves two activation energies; one associated with a carbon-atom redistribution during aging (where the rate-controlling step involves carbon diffusion) and another associated with carbide growth. A considerable regime exists over which the calculated activation energy appears to reflect a mixture of two mechanisms. This "apparent" activation energy may reflect the overlapping nucleation and growth of carbides.

CHAPTER 7

RESULTS AND DISCUSSION: SPINODAL DECOMPOSITION DURING AGING

Virgin martensites undergo significant structural changes during aging at room temperature. The most important TEM results are presented and discussed in this chapter. In addition, a thermodynamic model for the body-centered Fe-C solution is developed and analyzed. The microstructural evolution associated with prolonged aging at room temperature sets the stage for the precipitation of transition carbides; these results are deferred until Chapter 8.

In all subsequent discussion, aging times will refer to time at <u>room temperature</u>, unless otherwise stated. The reported aging time for any given specimen was measured from the time it was quenched to -196°C to form martensite. In most cases, final thinning was carried out just prior to TEM observation in order to minimize any modifications to the aging processes that might be attributed to the small thickness of the TEM foils. Since the jet thinning was carried out at -55°C, it can be safely assumed that no appreciable aging occurred during this process and therefore the time involved was not added to the total aging time.

In the results and discussion which follow, reference is frequently made to certain crystallographic directions of the martensitic structure. To avoid confusion, no distinction is explicitly made between real- and reciprocal-space directions. This should not trouble the reader since, for cubic structures, the [hkl] direction in real space is parallel to the [hkl] direction in reciprocal space; this equivalence is approximately maintained in martensitic crystals because the tetragonality is small in magnitude.

7.1 Formation of a Modulated Structure

7.1.1 Diffuse Electron Scattering and "Tweed" Contrast

Three electron diffraction patterns taken from different Fe-25Ni-0.4C specimens after short-time aging at room temperature are shown in Figure 7-1. A similar set of diffraction patterns from the Fe-15Ni-1C alloy is shown in Figure 7-2. The beam direction for each pattern is different; Figure 7-1(A) is identified as a <100>-type pattern, (B) a <331>, and (C) a <111>. For a "normal" cubic structure, these patterns would exhibit four-fold, two-fold, and three-fold symmetry, respectively. However, the patterns of Figures 7-1 and 7-2 exhibit only the two-fold symmetry characterstic of the conspicuous diffuse scattering (DS) which is present in each. This reduction of symmetry should not come as a complete surprise, for the reader will recall (from the Literature Review chapter) that the lattice of virgin martensite is macroscopically tetragonal due to its "Zener-ordered" nature (where carbon atoms preferentially occupy O_z sites). In fact, the macroscopic tetragonality can actually be measured on <10$\underline{0}$>-type patterns. For example, Figure 7-2(A) is a [100] pattern, where the shorter of the two <200> reciprocal lattice vectors is parallel to the c-axis and the associated diffraction spot is accordingly indexed as 002. The axial ratio (c/a) is given by $|g_{002}|/|g_{020}|$ and is 1.064 in this case. Two other [100] patterns from Fe-15Ni-1C specimens aged for 3 hrs and 5.25 hrs exhibited axial ratios of 1.051 and 1.052, respectively. The scatter in the measured c/a's can be attributed to the fact that the TEM thin foils are always severely bent; when this is the case, the diffraction pattern is distorted and reflections may be displaced from their "normal" locations. The average c/a, 1.056, is in good agreement with that predicted for fully-tetragonal martensite (exclusive O_z occupancy); for Fe-15Ni-1C (n_C =
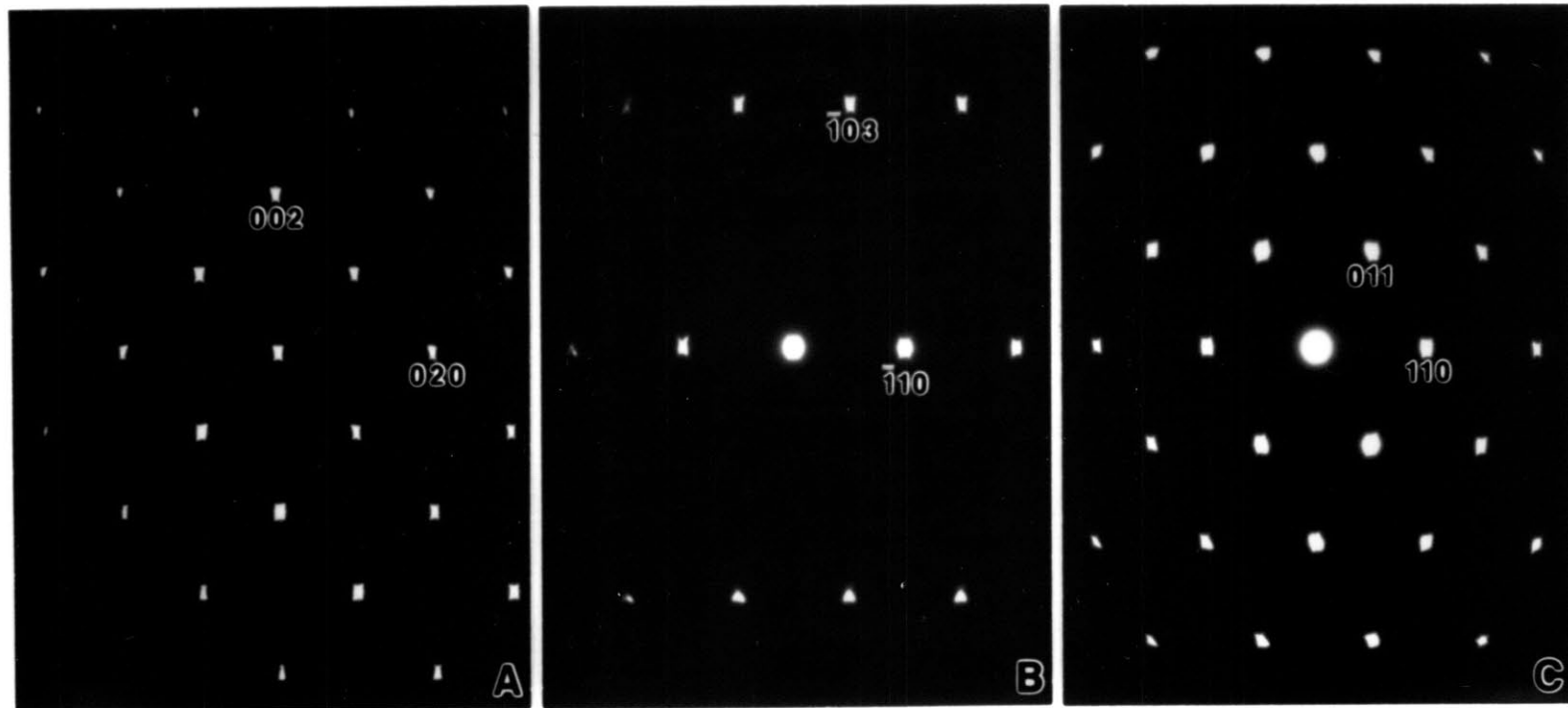
Figure 7-1.   Three electron diffraction patterns from different martensitic Fe-25Ni-0.4C specimens. The beam direction and aging times are [100]/2 hrs, [331]/40 min, and [1$\bar{1}$1]/2.5 hrs in (A), (B), and (C), respectively.
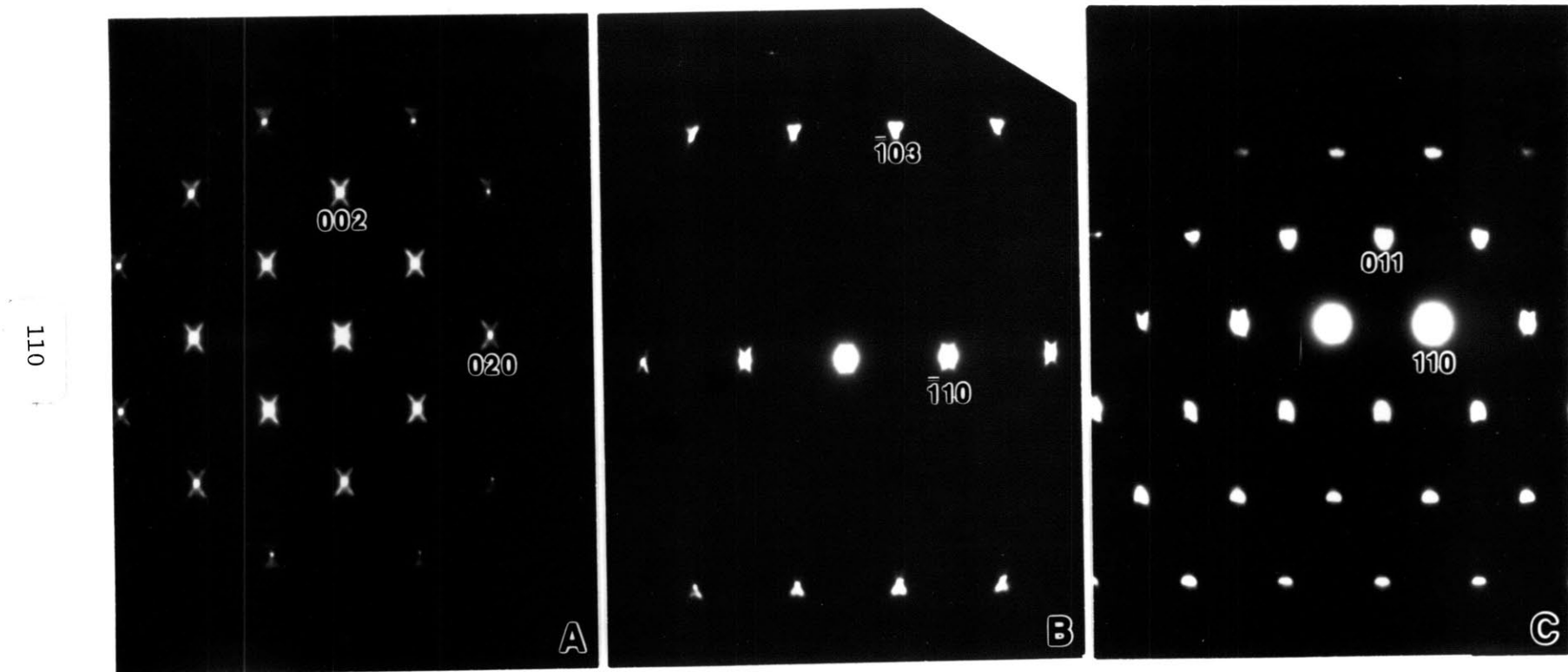
Figure 7-2. Three electron diffraction patterns from different martensitic Fe-15Ni-1C specimens. The beam direction and aging times are [100]/26 min, [331]/1.75 hrs, and [1Ī1]/9.5 hrs in (A), (B), and (C), respectively.

110

0.0416), Equations 2-7 and 5-7 give:

$$c/a \cong 1 + 1.41(0.0416) = 1.059.$$

Similarly, the average c/a measured from three <100> patterns from Fe-25Ni-0.4C (n_C = 0.0184) was 1.025, again in good agreement with the predicted value:

$$c/a \cong 1 + 1.41(0.0184) = 1.026.$$

Thus, it can be concluded that even in aged martensite, carbon atoms occupy O_z sites exclusively. This does not rule out the possible transfer of some carbon atoms to O_x or O_y sites by the process of {01$\underline{1}$} twinning described in Chapter 5, but it does indicate that it is possible to locate regions of the size of the selected area aperture ($\sim$1 μm in diameter) wherein no such twinning occurs.

The pattern of Figure 7-2(B) can be identified as either [331] or [313], depending upon the relative magnitudes of the two shortest reciprocal lattice translations present in the pattern (<110> and <103>). For an axial ratio of 1.056, $|g_{10\underline{3}}|/|g_{11\underline{0}}|$ is 2.130 and $|g_{30\underline{1}}|/|g_{10\underline{1}}|$ is 2.284. The actual value obtained from Figure 7-2(B) is 2.149 and therefore it has been identified as a [331] pattern. Figure 7-2(C) is taken as a [1$\bar{1}$1] pattern, this choice being arbitrary since each <111> direction remains equivalent in the tetragonal system. The projection of the c-axis lies along the vertical direction in each pattern of Figures 7-1 and 7-2.

Figure 7-3 shows diffraction patterns taken with the electron beam nearly parallel to the c-axis, but tilted slightly about [010]. Four distinct spots can be seen about the locations of the fundamental reflections. The spacing between these spots increases in an asymmetric manner as one moves away from the origin of reciprocal space. This behavior can be attributed to the manner in which the reflecting sphere intersects DS streaks which are centered about each fundamental reflection.
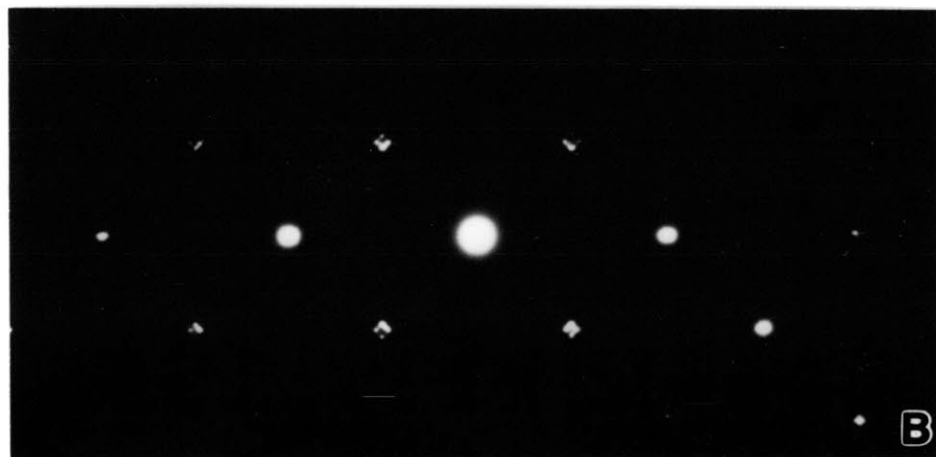
Figure 7-3. Two diffraction patterns with the incident beam
deviating slightly from the [001] direction.
(A) is from martensitic Fe-25Ni-0.4C, aged 4
hrs at room temperature and (B) is from martensitic
Fe-15Ni-1C, aged 6 days at room temperature.

Note that the regions contributing to the diffraction patterns (~ 1 μm in diameter) produce diffuse intensity along four different (but crystallographically-equivalent) directions.

The DS present in the patterns of Figures 7-1 thru 7-3 was observed even after the shortest obtainable aging times in this investigation (about 5 minutes). The DS intensity is highly anisotropic and, based upon the detailed examination of numerous diffraction patterns from different orientations, can be (roughly) characterized as streaks centered about each fundamental reflection. The habit line of the DS was determined from Figures 7-2 and 7-3(B) with the aid of the [001] stereogram of Figure 7-4. Although this stereogram has actually been drawn for a cubic structure, the relatively small tetragonality of the martensite lattice does not introduce any significant error. Here, each great circle segment represents a projection of the diffuse scattering maxima present in the diffraction patterns (where the geometry of the DS for the [100] orientation has been duplicated for the equivalent [010] orientation). The results indicate that the DS tends to lie along <20$\underline{3}$> directions.

A characteristic image contrast arises when a specimen is oriented such that the DS occurs. A typical example is shown in Figure 7-5, where the specimen orientation is near [100] and the g_{020} diffraction vector is strongly excited. The inset diffraction pattern reveals intense DS along the [023] and [02$\bar{3}$] directions. The bright-field and dark-field images exhibit a conspicuous criss-cross or "basketweave" contrast consisting of two sets of fine striations. The spacing between the striations is (on the average) about 1.5 nm, approximately equal to the reciprocal of the lengths of the DS streaks. There is a marked tendency for each set of striations to lie along the directions which are normal to the two DS streaks,
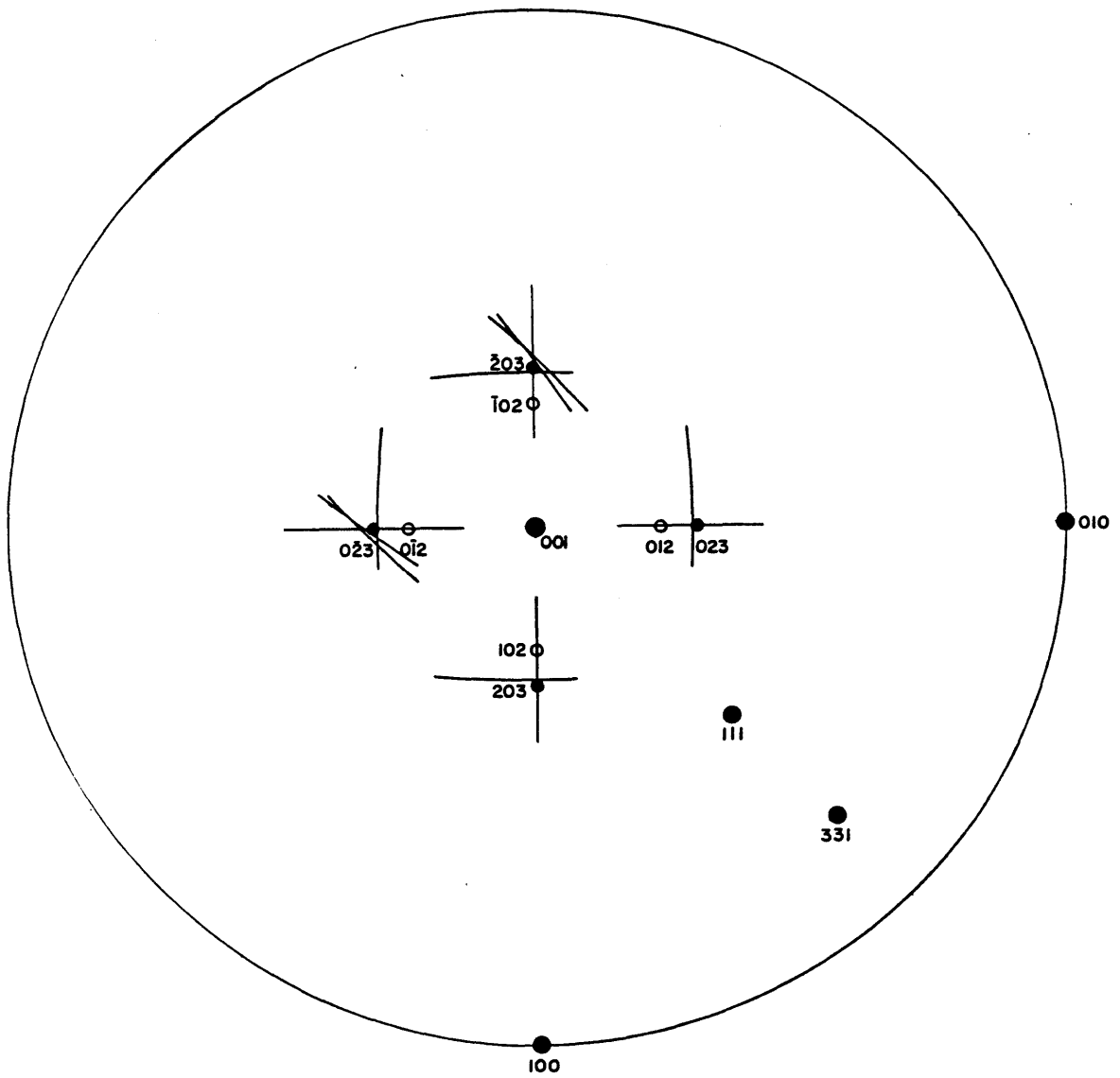
Figure 7-4. Cubic [001] stereogram showing the projected directions of the DS present in the four diffraction patterns of Figures 7-2 and 7-3(B).
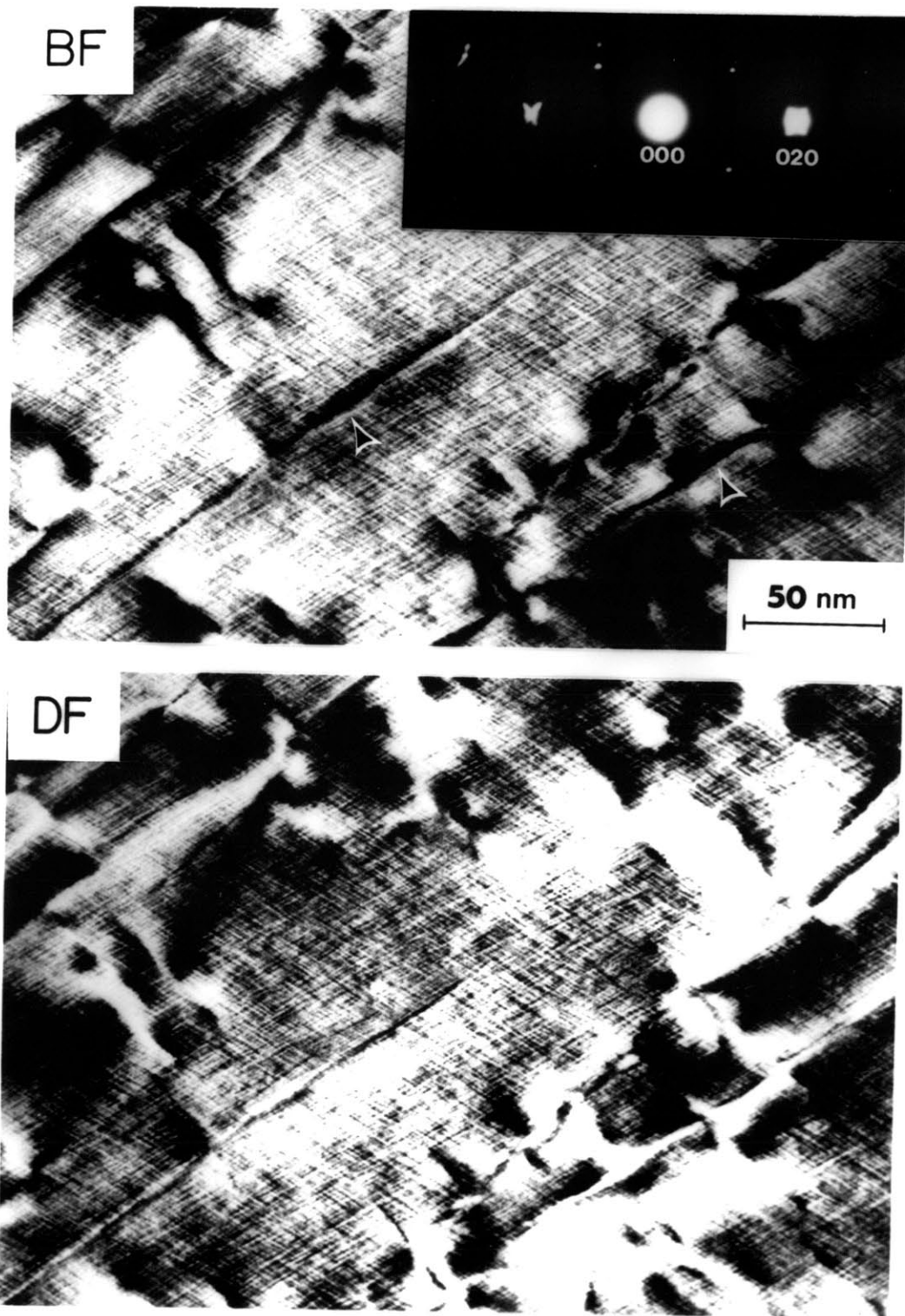
Figure 7-5. Transmission electron micrographs (bright-field/dark-field pair) of martensitic Fe-15Ni-1C, aged 5.5 hrs at room temperature ($\mathbf{g}$ = 020). Arrows indicate strain contrast at dislocations.

although slight local variations in both the spacing and direction of the striations are evident. The image contrast is very similar under the two-beam bright- and dark-field conditions here; the dark-field contrast is somewhat enhanced, however, such behavior being typical when strain contrast is an operating contrast mechanism. The morphology typified by Figure 7-5 will subsequently be referred to as "tweed," however the reader should recognize that this term has already been used in the literature to describe contrast from microstructures whose origins may be different from those of the present study.

Additional dark-field contrast from Fe-15Ni-1C is shown in Figure 7-6, again taken with the 020 spot and its associated DS near the [100] orientation. The bright area (the 020 extinction contour) in this micrograph represents regions which are at a small deviation from the Bragg condition and are therefore in a strongly-diffracting orientation. Within this region, the tweed contrast is similar to the two-beam contrast presented above. The contrast becomes different in character in moving away from the extinction contour, into regions where the deviation from the Bragg condition becomes significant. Here the relatively continuous striations characteristic of the tweed break down into discrete sets of fine dots less than 1 nm in size. Such contrast can be taken to be more characteristic of that produced by the DS since the background intensity has been dramatically reduced here by virtue of the weak-beam condition. The fact that the tweed contrast is intimately associated with the DS in reciprocal space can be demonstrated quite easily by performing an optical transform experiment on the image negative. This was done by using a laser optical system to illuminate a selected area on the negative with a beam of coherent, monochromatic light. Suitable lenses were used to focus the

Figure 7-6. Martensitic Fe-15Ni-1C, aged 3 hrs at room temperature. (A) Dark-field transmission electron micrograph taken with the 020 reflection and its associated diffuse intensity. (B) Diffraction pattern. (C) Optical diffraction pattern from circled region in (A).

resulting diffraction pattern onto a piece of photographic film. The
optical diffraction pattern from the encircled area in Figure 7-6(A) is
shown in Figure 7-6(C), where all of the important features present in the
electron diffraction pattern are seen to be faithfully reproduced. This
implies that all of the information that went into the production of the
electron image is actually present in the recorded image, and that the
tweed contrast is directly related to the DS.

The previous discussion relating to Figures 7-1 thru 7-3 suggests that
the geometry of the DS is very sensitive to specimen orientation and is
determined by the manner in which the reflecting sphere intersects the
distribution of DS in reciprocal space. A similar conclusion regarding the
tweed contrast can also be drawn. In fact, the tweed is only observed when
appreciable DS intensity is present in the diffraction pattern. When two
streaks are present, such as in Figure 7-5, two sets of striations arise,
each normal to one of the DS streaks. When a specimen is oriented such
that only one DS streak occurs, only one set of striations is produced in
the image, Figure 7-7. On the other hand, if no DS is evident in the
diffraction pattern, then no tweed contrast occurs in the image. The
reader can find a more detailed presentation of the tweed contrast in the
recent paper by Sandvik and Wayman [87].

The observations made during the present investigation indicate that
both Fe-Ni-C alloys exhibit completely analogous diffraction and contrast
behavior. A distinct difference can, however, be noted; namely, the DS
streaks tend to be shorter and the tweed correspondingly coarser for the
lower-carbon alloy. Figure 7-8 illustrates the behavior of the DS over a
broad range of carbon content. Four [100] diffraction patterns are shown;
one from each of the two Fe-Ni-C alloys of this study and two others from

118
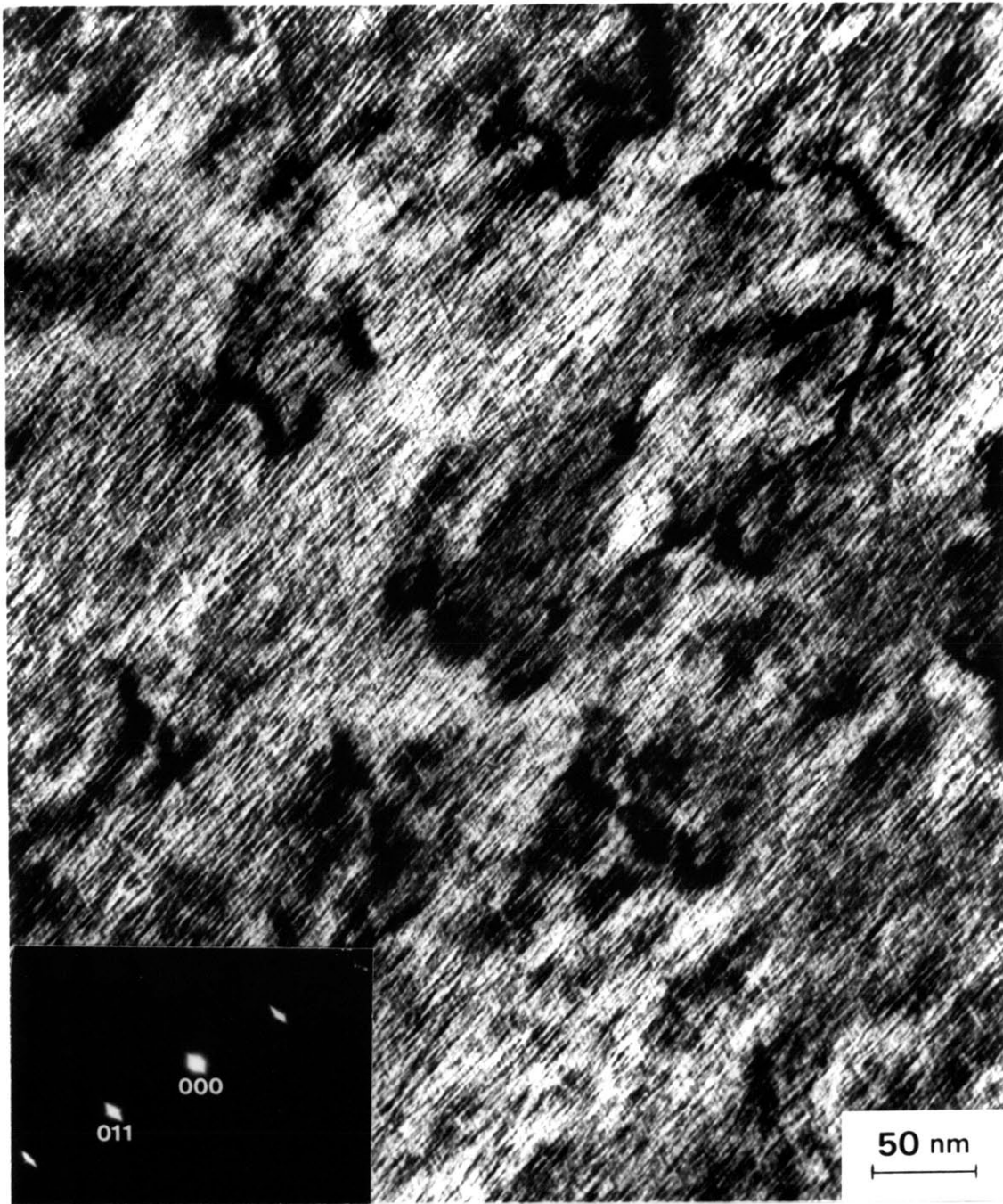
Figure 7-7. Bright-field (**g** = 011) transmission electron micrograph of martensitic Fe-25Ni-0.4C, aged 1.75 hrs at room temperature. The specimen orientation is near [100].
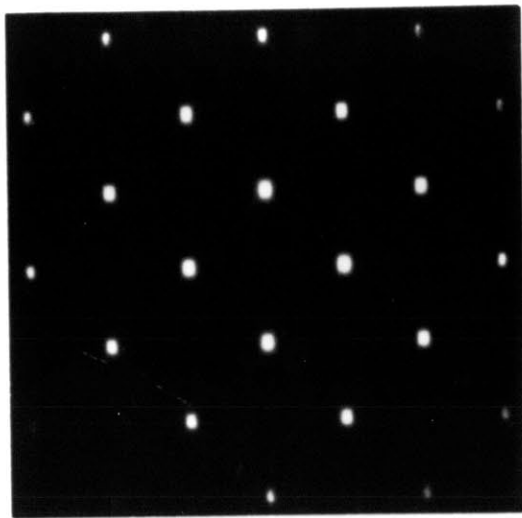
Fe-25Ni-0.2C
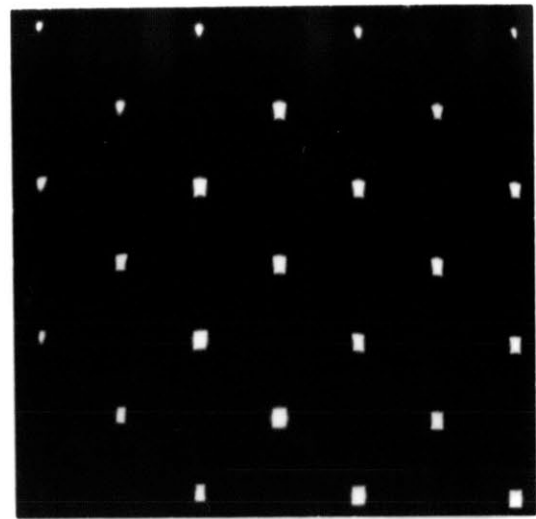
Fe-25Ni-0.4C / 2 hrs
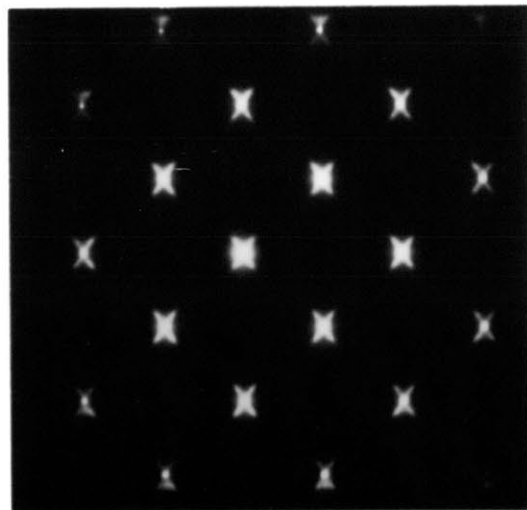
Fe-15Ni-IC / 26 min
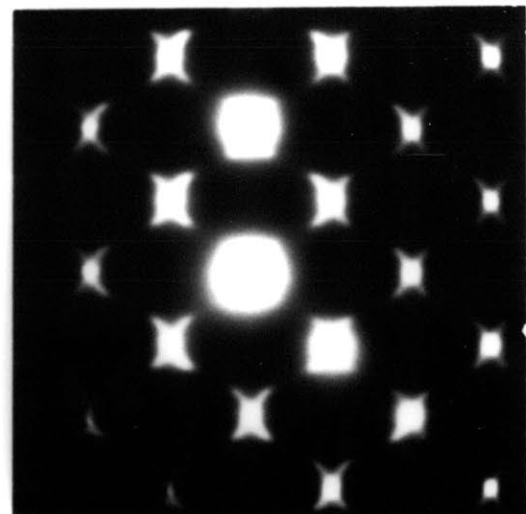
Fe-1.8Mn-1.8C / 3.25 hrs

Figure 7-8. [100] diffraction patterns from four different alloys.

Fe-25Ni-0.2C and Fe-1.8Mn-1.8C alloys. The length of the DS maxima clearly increases with carbon concentration, indicating a corresponding decrease in the tweed wavelength. The variation in initial wavelength with carbon content is shown in Figure 7-9. The present results are in general agreement with those of Kusunoki and Nagakura [88], except at small carbon contents where the present study reports much larger wavelengths. Additional note can be made of how the short wavelength components tend to rotate toward <10$\underline{1}$> directions in the 1.8C alloy. These trends are discussed in Section 7.2.

Aging experiments were conducted above room temperature to determine whether or not a temperature could be reached where tweed formation does not occur. These attempts were unsuccessful because the tweed structure is rapidly converted to a fine dispersion of transition carbides above 175°C. The tweed does indeed form at this temperature, but aging only 2 seconds at 200°C produced carbides. Future attempts to measure the critical temperature at which the tweed becomes unstable will have to employ rapid heating and quenching techniques so that sub-second aging times can be obtained.

7.1.2 Image Contrast Theory

"Weak-beam" contrast from Fe-25Ni-0.4C is shown in Figure 7-10, where, unlike previous images, the specimen orientation is very close to [001] (the c-axis). However, as in Figure 7-3, the specimen has been tilted slightly about [010] such that the DS from the four different <20$\underline{3}$> variants is visible about the four {110} reflections. The weak (110) reflection and its associated DS "spots" were used to form the image of Figure 7-10. The contrast consists essentially of two sets of bright
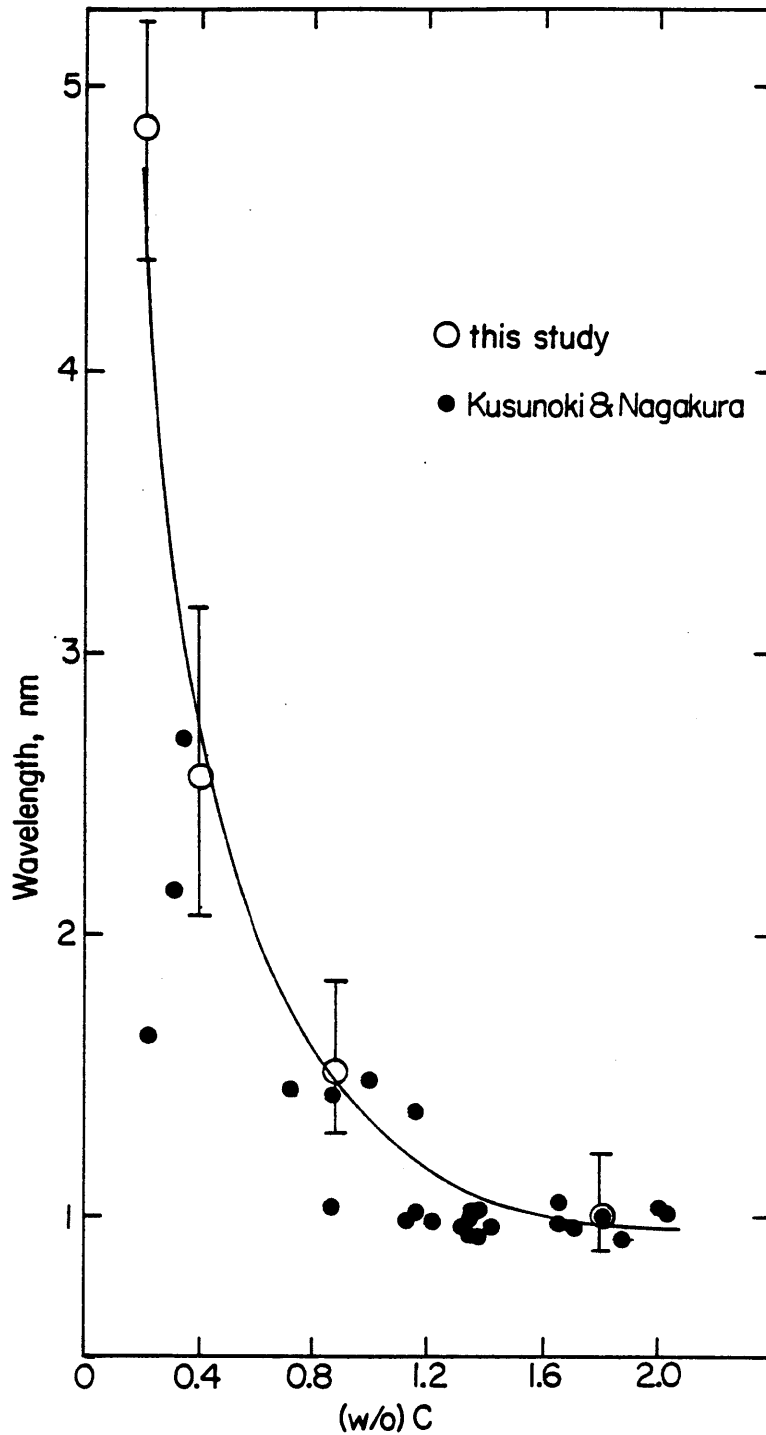
Figure 7-9. Variation of the initial tweed wavelength with carbon content. Solid circles are the data of Kusunoki and Nagakura [88] and open circles are data from the present investigation, obtained after aging several hours at room temperature.
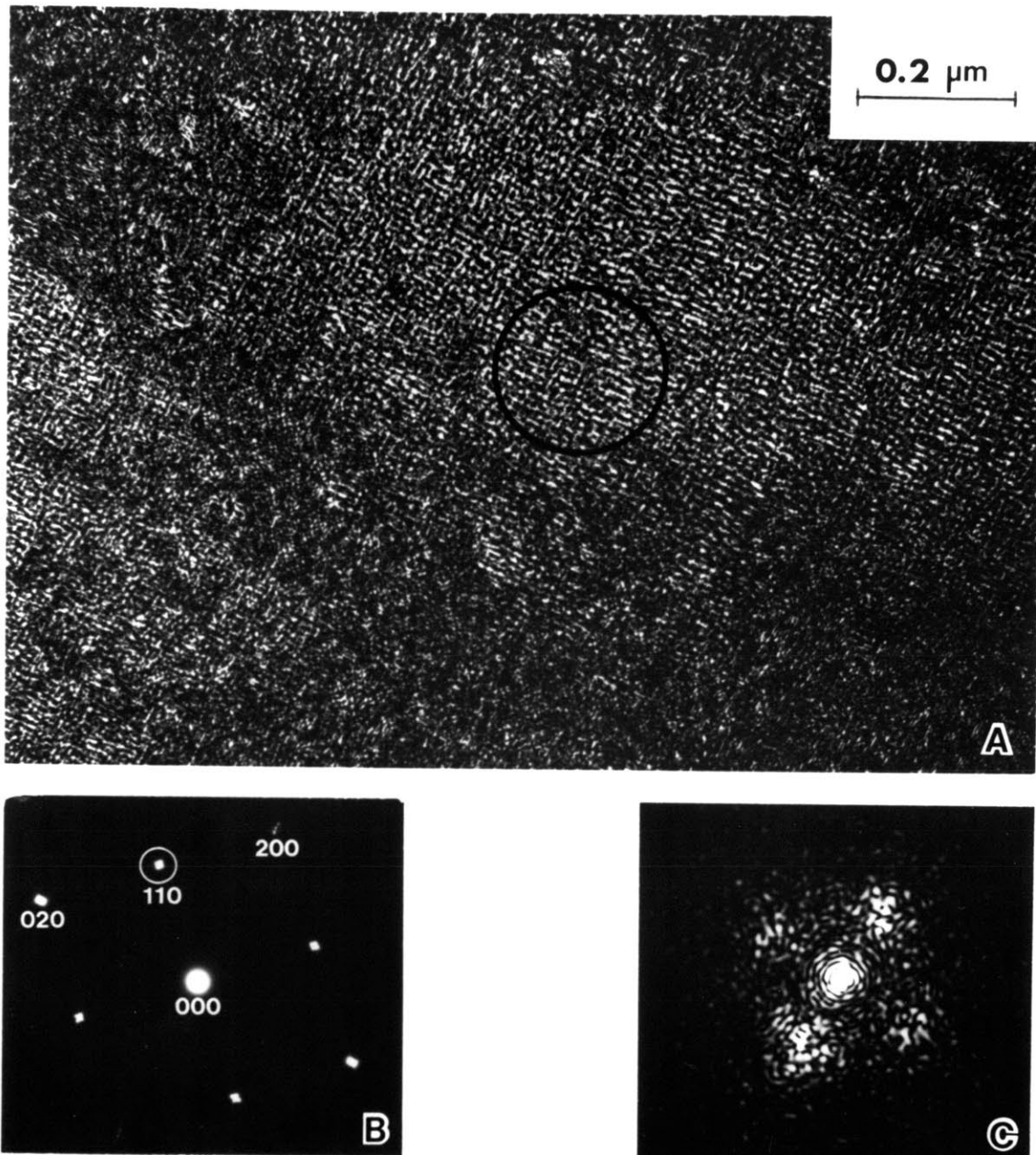
Figure 7-10.   Martensitic Fe-25Ni-0.4C, aged 4 hrs at room temperature.
(A) Dark-field transmission electron micrograph taken with
the 110 reflection and its associated diffuse intensity.
(B) Diffraction pattern.   (C) Optical diffraction pattern
from circled region in (A).

123

striations which together tend to make a square network. The striations are periodically spaced along directions defined by the vectors joining the (110) fundamental reflection and its associated DS "spots." From the diffraction pattern, the length of these vectors is of the order of 1/40th of $|g_{110}|$. This corresponds to a real-space periodicity of $40d_{110}$ (about 8 nm), in good agreement with the observed spacing. In contrast, when the same alloy is oriented along [100] so that the $<20\underline{3}>$ tweed is in contrast (e.g. Figure 7-7), a striation spacing of 2.5 to 4 nm results. Clearly, this contrast behavior cannot be explained simply in terms of, for example, structure factor contrast, since two different characteristic dimensions (sizes) would then be indicated for the microstructural feature giving rise to the contrast. The following paragraphs present a simple theory for qualitatively explaining the important contrast features.

The image contrast presented thusfar can be understood from the simple arguments which follow. First, consider a monochromatic beam of electrons. The well-known de Broglie postulate of quantum physics states that each electron in the beam can be represented by a matter wave (wave function), whose eigenfunction, ψ, can be represented by

$$\psi(\mathbf{k},\mathbf{r}) = \phi(\mathbf{k})\exp(2\pi i \mathbf{k} \cdot \mathbf{r}), \qquad (7-1)$$

where ϕ is the wave amplitude (and is in general a complex number), $\mathbf{k}$ is the wave vector, and $\mathbf{r}$ is a vector which represents a spatial coordinate. The wave vector is parallel to the direction of the electron's motion and has a magnitude given by the reciprocal of the electron wavelength, $|\mathbf{k}| = 1/\lambda_e$. Equation 7-1 describes a unique state and therefore applies only to an electron with a particular momentum and potential energy. When the possibility exists for the electron to interact with its surroundings, then

other eigenfunctions are required in order to represent the different possible states that can arise as a result of the interaction. In other words,

$$\psi_T = \Sigma\phi_j\exp(2\pi i k_j\cdot r), \tag{7-2}$$

where the summation is carried out over all j possible states.

The total eigenfunction is, in general, a complex function and as such has no physical significance in and of itself. However, the probability of finding the electron at position r, $P(r)$, is given by the normalized modulus of ψ_T:

$$P(r) = A\psi\psi^*, \tag{7-3}$$

where A is a constant such that P is unity when integrated over all space. Only relative probabilities are important in most physical situations and therefore the normalization factor will be ignored in subsequent expressions.

Now consider the case where the electron can be in two different states. For this case,

$$\psi_T = \phi_1\exp(2\pi i k_1\cdot r) + \phi_2\exp(2\pi i k_2\cdot r) \tag{7-4}$$

and
$$\begin{aligned}P(r) = &\ \phi_1\phi_1^* + \phi_2\phi_2^* \\ &+ \phi_1\phi_2^*\exp[2\pi i(k_1-k_2)\cdot r] \\ &+ \phi_2\phi_1^*\exp[-2\pi i(k_1-k_2)\cdot r].\end{aligned} \tag{7-5}$$

This equation can be rewritten in the following real form:

$$P(r) = I_1 + I_2 + 2(I_1 I_2)^{1/2}\cos[2\pi(k_1-k_2)\cdot r + \Delta], \tag{7-6}$$

where I_1 and I_2 are the relative probabilities of the electron being in

states 1 and 2, respectively, and Δ is the phase difference between the two wave amplitudes. The intensity at any point r in space, $I(r)$, will be proportional to the number of electrons which strike that point, and hence is proportional to $P(r)$. Thus we can write

$$I(r) \propto I_1 + I_2 + 2(I_1 I_2)^{1/2} \cos[2\pi(k_1 - k_2) \cdot r + \Delta]. \qquad (7-7)$$

This expression is equivalent to that given by Laughlin [89] in his treatment of contrast from spinodally-decomposed microstructures. The important feature of Equation 7-7 lies in the third term on the RHS. The magnitude of this term oscillates over space and therefore gives rise to an intensity which is periodic over space, having a wavelength, λ, given by

$$\lambda = \left| \frac{r}{(k_1 - k_2) \cdot r} \right|. \qquad (7-8)$$

Note that when $(k_1 - k_2)$ is normal to r, λ is infinite and hence no intensity variation occurs along r. Note also that the intensity variation is a maximum when $I_1 = I_2$ and is zero everywhere if either I_1 or I_2 is zero. In general, the values of I_1 and I_2 as well as Δ depend on specimen orientation (deviation parameter) and thickness. In addition, electron-optical parameters (such as defocus and lens aberrations) may have an important influence on image contrast. Treatment of such factors is, however, beyond the scope of this thesis.

Up to this point, we have said nothing about the possible electron-specimen interactions which can result in the total eigenfunction given by Equation 7-4. Nevertheless, the tweed contrast exhibited by ferrous martensites can be qualitatively explained with the aid of Equations 7-7 and 7-8. For the purposes of this discussion, state 1 can be considered to

be either non-interacting (transmitted) electrons in the case of bright-field, or Bragg-diffracted electrons in the case of dark-field microscopy. State 2 can be considered to represent electrons having a wave vector lying within a volume of reciprocal space (surrounding either the transmitted spot or Bragg reflection) where appreciable DS intensity occurs. This amounts to saying that a well-defined satellite is situated about the spot, which is clearly an idealization. The theory then predicts that a periodic image will result. The intensity modulation has its shortest period along a direction parallel to the reciprocal space vector joining the transmitted or Bragg-diffracted spot and its associated satellite and (from Equation 7-8) exhibits a wavelength given by the reciprocal of the magnitude of this vector. This is precisely the nature of the periodic (tweed-like) images of aged martensite presented in Section 7.1.1. However, in the case of aged martensite, the "satellites" situated about the fundamental reflections tend to exhibit radial as well as (to a lesser extent) angular smearing. This arises from the observed local variation in tweed wavelength and direction, respectively.

7.1.3 Effect of Martensitic Substructure on Aging Behavior

Some previous studies of lath martensites have indicated that the martensitic morphology may exert a substantial influence on the aging and tempering behavior [26,28,58]. That is, dislocations and lath boundaries were believed to be potent traps for carbon atoms and could accommodate more than 0.1 wt pct carbon. In this investigation, however, the formation of the tweed was clearly the dominant process occurring in the plate-like martensite during aging. Furthermore, the tweed formed uniformly throughout the martensitic phase of all the alloys studied; it was detected in dislocated as well as finely-twinned regions, Figures 5-9(B)

and 7-11. Weak-beam microscopy was performed in an effort to detect carbon segregation to dislocations, however no clusters or precipitates were directly observed on the dislocations. Furthermore, no carbon-free zones (i.e. tweed-free zones) were observed around the dislocations.

How can this apparent disparity concerning the role of substructure be reconciled? Well, a large fraction of the lattice dislocations in the Fe-Ni-C martensites of this study are nearly pure screw in character. Lath martensites, on the other hand, may contain a larger fraction of edge dislocations, which may be more effective in trapping carbon. Alternatively, the tweed may not form at all in alloys low in carbon. Carbon atoms would then be quite free to diffuse to available low-energy dislocation sites and the effect of substructure would be most pronounced. However, when the tweed does form, it proceeds on a scale much finer than the mean free path between defects and therefore tweed formation can certainly occur much faster than migration to defects. Moreover, carbon atoms may be bound to clusters to the extent that no significant migration to defects occurs.

Some of the most convincing evidence for the trapping of carbon by structural defects comes from Speich's resistometric study of Fe-C martensites [28]. His results are critically reviewed in Appendix C in light of the more recent resistometric results from Sherman et al. [70] and this investigation.

7.1.4 Coarsening of the Tweed

The coarsening of the tweed structure was monitored as a function of time at room temperature. Visual estimates of average wavelengths were made directly from TEM micrographs like Figure 7-12. The results for both
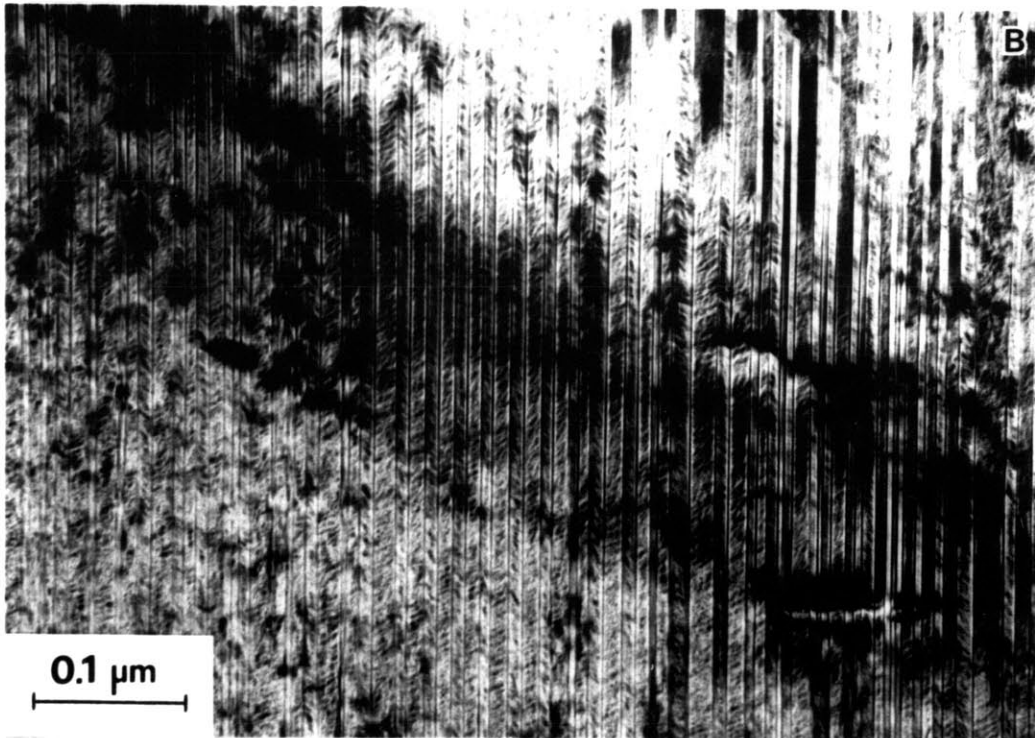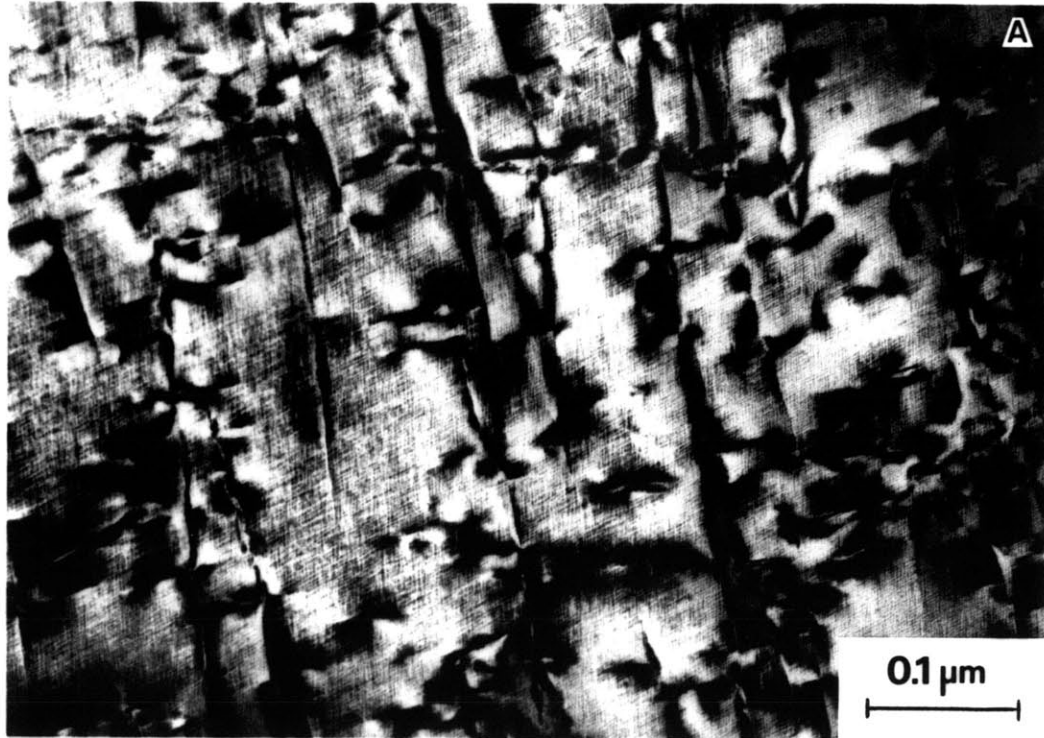
Figure 7-11.   (A) Tweed formation in a dislocated volume of martensitic
Fe-15Ni-1C (aged 5 hours).   (B) Coarse, univariant tweed
contrast in a finely-twinned volume of martensitic
Fe-25Ni-0.4C (aged 2 hours).

5.5 hrs **2 days** **48 days**
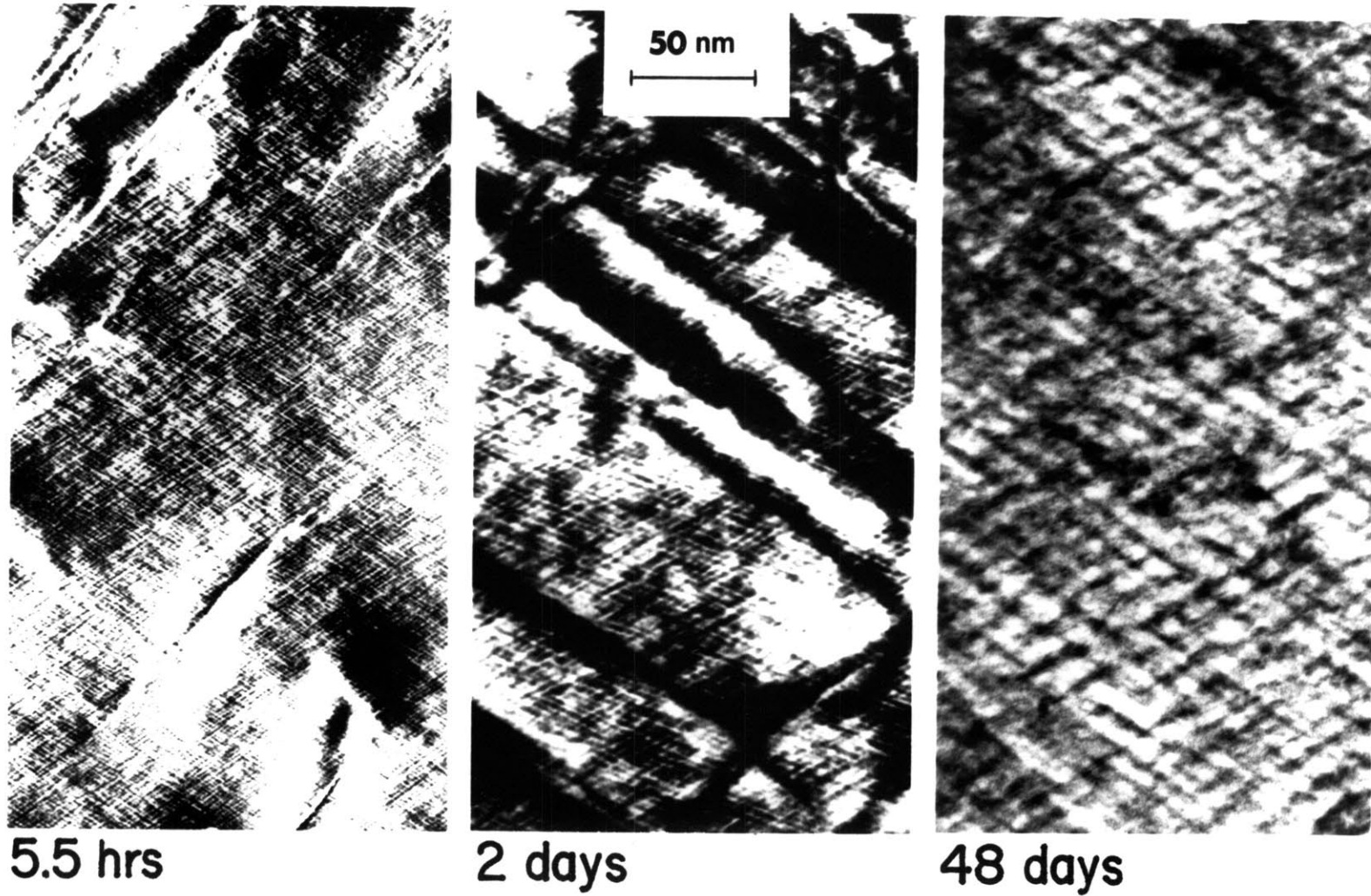
Figure 7-12. TEM micrographs of the tweed structure in martensitic Fe-15Ni-1C. Aging times (at room temperature) are indicated.

Fe-Ni-C alloys are plotted on a log-log scale in Figure 7-13. The rate of coarsening is initially higher in the lower carbon alloy, but the wavelength approaches a similar value (about 10 nm) in both alloys after prolonged aging.

For diffusion-controlled coarsening (with constant diffusivity), one may expect the following relation between wavelength, λ, and aging time, t [90]:

$$\lambda^3 - \lambda_o^3 = k(t - t_o), \tag{7-9}$$

where λ_o is the wavelength at $t = t_o$ and k is a constant. When $\lambda \gg \lambda_o$ (and $t \gg t_o$), Equation 7-9 predicts that a log-log plot of λ vs. t should yield a straight line of slope 1/3. However, neither set of data appears to fit such a line, indicated in Figure 7-13. This apparent discrepancy is discussed in Section 7.2.1.

7.2 Discussion

7.2.1 Concomitant Spinodal Decomposition and Ordering

The electrical resistivity behavior which accompanies the aging of the Fe-Ni-C alloys of this study was presented in Chapter 6; those results can be used in order to gain some insight into the processes which occur during aging. The reader will recall that aging in the vicinity of room temperature results, at least initially, in a net increase in resistivity. Furthermore, the activation energy asssociated with the early stages of aging indicates that carbon-atom diffusion is the rate-controlling step. The extensive discussions which have been put forward by Eldis [75], Sherman [25], Hoffman and Cohen [84], and Sherman et al. [70] all conclude that the increase in resistivity is related to an increase in the mean-square static displacement of iron atoms which results from the carbon-atom

131
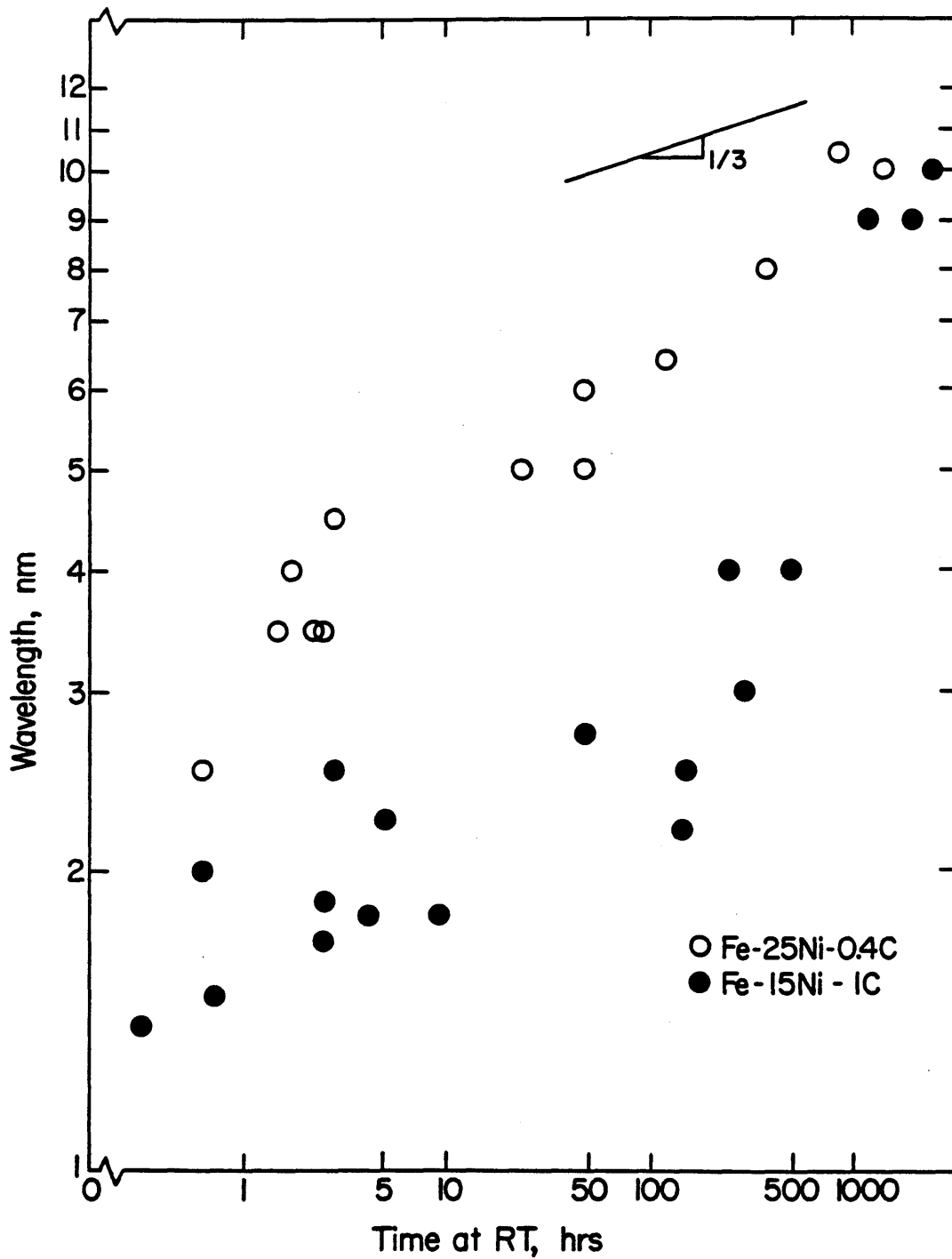
Figure 7-13. Variation of tweed wavelength with aging time (at room temperature).

redistribution. In this interpretation, the mean iron displacement remains essentially unchanged, consistent with the observed preservation of the initial tetragonality. Chen and Winchell [69] have reached the same conlusion on the basis of x-ray diffraction. That is, the broadening of their martensite (002) x-ray peak (without significant change in peak position) was attributed to an increase in the mean-square iron-atom displacement.

The results of Mössbauer investigations provide additional insight into aging processes. Although the details of the interpretations differ somewhat from author-to-author, each concludes that the fraction of iron atoms whose nuclear properties are influenced by neighboring carbon atoms tends to decrease during aging [19]. This, in and of itself, is conclusive evidence of the redistribution of carbon atoms. Moreover, it implies that carbon atoms "cluster" during aging, for only this process can result in a net decrease in the fraction of iron atoms which are perturbed by carbons.

With a carbon-atom redistribution firmly established, the TEM results presented earlier in this chapter can now be more meaningfully interpreted: The periodic tweed structure results from a modulation of carbon concentration along the <203> directions, with the initial wavelength being a decreasing function of the alloy carbon content. The decrease in wavelength signifies that carbon atoms diffuse over shorter distances as the alloy carbon content increases. However, the kinetics of aging clearly decrease with increasing carbon content, as indicated by the longer times required to traverse the regime II electrical resistivity peak (see Figure 6-2). This is surprising because one would normally expect the rate of a diffusion-controlled reaction to increase when the diffusion distance is reduced. Apparently the reduction in the carbon-atom

mobility with increasing carbon content [71] has a more important effect on the overall kinetics than the reduction in diffusion distance.

As indicated in the Literature Review chapter, DS was first observed along <10$\underline{2}$> by Izotov and Utevskiy [64] in the electron diffraction patterns of high-carbon Fe-C and Fe-Cr-C alloys aged at room temperature. They concluded that the DS was a shape effect produced by small, coherent, plate-like carbide particles having a {10$\underline{2}$} habit. Although the present study finds DS primarily along <20$\underline{3}$>, it is undoubtedly the same effect as observed by Izotov and Utevskiy. However, in view of the current results, it is not clear that the DS is simply a shape effect and an alternative explanation of its origin seems warranted.

Nagakura and coworkers [65,88] have examined the problem of aging much more thoroughly via electron microscopy. They observed the same diffraction effects as did Izotov and Utevskiy, however their interpretation differs somewhat from the latter authors. They believe the DS to be composed of two different components. One is a set of diffuse spikes emanating from each fundamental reflection along the <10$\underline{2}$> directions. The other component is a set of satellite spots which develops at the tips of the diffuse spikes and is most intense after aging one hour at about 70°C. The diffuse spikes were attributed to carbon clustering and the satellite spots to the development of a modulated structure. Their calculations indicate that the satellite spots are due to a periodic displacement of iron atoms from their normal BCC lattice positions, presumably caused by a periodic modulation in carbon concentration. A modulated lattice strain will, in general, produce diffuse scattering of similar geometry about each fundamental Bragg reflection [79] and may even produce appreciable intensity about the transmitted beam, consistent with

the fact that the DS described above is always observed about the transmitted beam and does not disappear with slight tilting of the sample (as one might expect of a double diffraction effect).

Nagakura claims that his structural model gives good agreement between calculated and measured satellite intensities; however intensity measurements from electron diffraction patterns are generally very unreliable. His results are further complicated by uncertainties in alloy composition; compositions were determined indirectly from measurements of axial ratios, a procedure which is unreliable for the reasons presented in Chapter 5. Finally, one must presume that his alloys were auto-tempered to some unknown extent, since Fe-C alloys have M_s temperatures above room temperature.

The above interpretation due to Nagakura and coworkers is qualitatively similar to that derived from the current investigation. The former authors do not, however, make any statements regarding the mechanism by which the modulated structure of aged martensite forms. In this investigation, the aging product possessed a periodic and aligned character from the very outset of the reaction. This feature alone is strongly indicative of a spinodal reaction. The periodic nature of the tweed is not, however, conclusive proof that spinodal decomposition has occurred. For example, the nucleation and growth of elastically-interacting particles can also result in a periodic microstructure. Such may be the case in Ni-Al alloys; the alignment of the γ' precipitates was originally attributed to spinodal decomposition, but Ardell and Nicholson [91] later showed that a homogeneous nucleation and growth process operates, followed by alignment during coarsening. However, it is difficult to imagine such a process whereby a structural modulation on the scale of 1-2 nm can result.

New and very important compositional information on aged martensite has been obtained from a collaborative AP/FIM study of the same Fe-15Ni-1C alloy used in this investigation, indicating that a compositional modulation does indeed develop with aging at room temperature [92]. Furthermore, the concentration in the carbon-rich regions increases with aging time; after aging for 64 days, alternating carbon-poor and carbon-rich bands are detected with the averaged concentration varying from roughly 0.2 to 11 at pct [93]. Such an increase in concentration amplitude is consistent with a spinodal mechanism; a nucleation and growth process yields a new phase whose composition remains constant (ignoring capillarity effects). To date, the AP/FIM results provide the most direct evidence of spinodal decomposition. In theory, one should be able to measure an increase in concentration amplitude at constant wavelength during the early stages of decomposition. However, the tweed structure begins to coarsen (albeit rather slowly) early-on during the reaction, precluding such a measurement. Nevertheless, on the basis of the aligned nature of the tweed, the kinetic control by carbon diffusion, and the increase in concentration amplitude with time, it seems clear that spinodal decomposition is occurring during the aging of ferrous martensite.

The expression for the coarsening kinetics, Equation 7-9, assumes that the difference in composition between carbon-rich and carbon-poor bands remains constant. However, this assumption is clearly invalid; this may explain why the data in Figure 7-13 do not follow the predicted $t^{1/3}$ behavior.

Structural information concerning the carbon-rich phase which develops with aging comes from the electron microscopy and Mössbauer spectroscopy studies. Izotov and Utevskiy [64] and Kusunoki and Nagakura [88] report the appearance of superlattice reflections in the electron diffraction

patterns of high-carbon martensites when aged below 90°C. Both studies attribute this effect to ordering of carbon interstitials within the O_z sublattice, producing zones of the Fe_4C superstructure shown in Figure 7-14. Note that this structure is characterized by chains of carbon atoms along the three mutually-orthogonal [001], [110], and [1$\bar{1}$0] BCC directions. The superlattice reflections attributed to this phase usually exhibit a peculiar splitting along the c-direction, as shown in Figure 7-15. Izotov and Utevskiy offer no explanation for the splitting, but Kusunoki and Nagakura attribute it to the presence of stacking faults within the Fe_4C phase.

"Extra" diffraction spots were frequently observed in the present study, often located near the anticipated positions of coherent Fe_4C reflections. Figure 7-16 shows one example, with unsplit reflections near the ($0\underline{0}1$) positions of the [100] zone. Such unsplit, relatively sharp spots were observed on all of the alloys of this study and are due to the presence of a thin film of magnetite on the specimen surfaces; this is discussed in more detail in Appendix D. The split spots which have been previously attributed to Fe_4C were observed only in the highest-carbon alloy, Fe-1.8Mn-1.8C (see Figure 7-15(A)). Though unable to offer a better explanation of their origin, the author believes that the possibility that the split spots are due to a different oxide or other compound cannot be ruled out. In any case, the electron diffraction results should not be taken as positive proof of Fe_4C formation.

While prior evidence of long-range order of the Fe_4C type comes from electron microscopy, short-range order of the same type has also been detected by Choo and Kaplow [12] using Mössbauer spectroscopy. Their spectra from splat-quenched Fe-1.86C contain two components with a

137
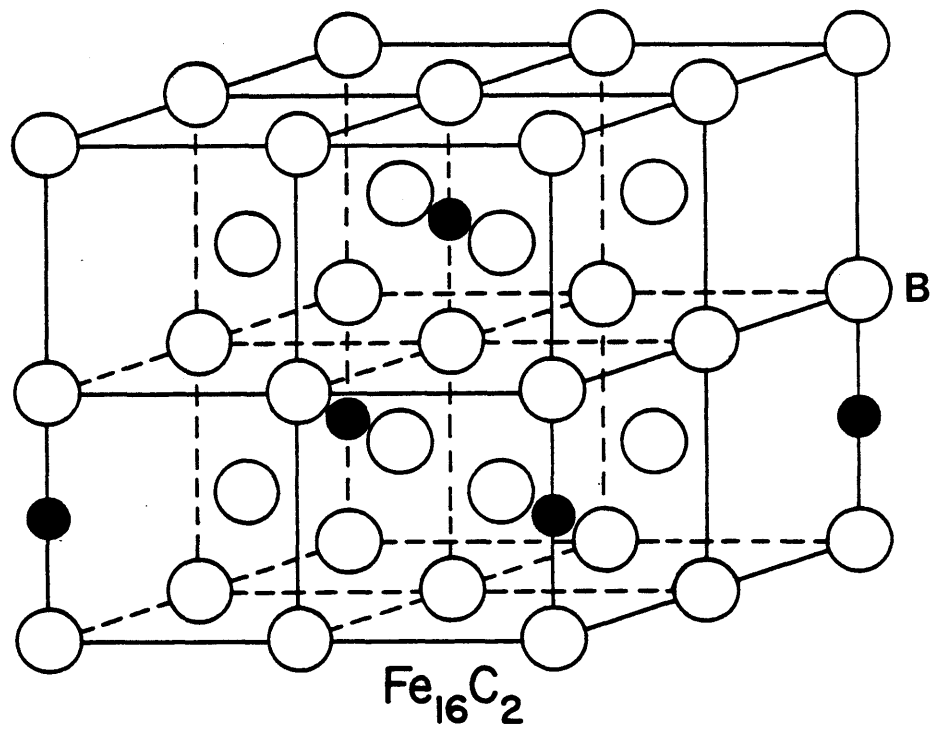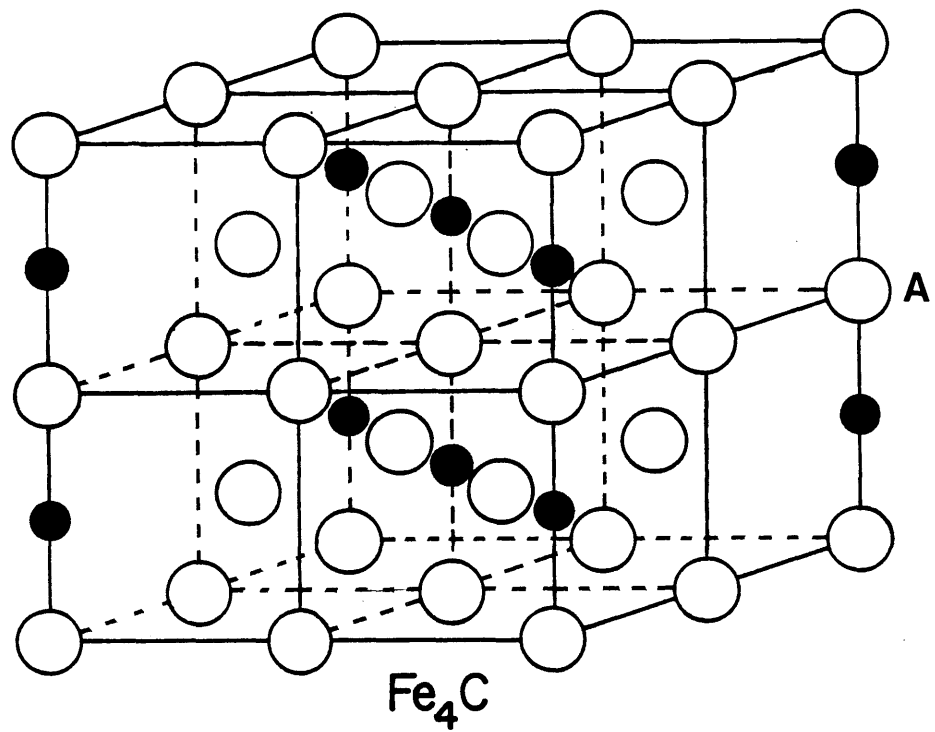
Figure 7-14. Schematic representation of the coherent Fe_4C (A) and $Fe_{16}C_2$ (B) structures. Large open circles represent metal atoms and small solid circles interstitial atoms. The iron atoms in these drawings constitute eight (2x2x2) BCC unit cells.
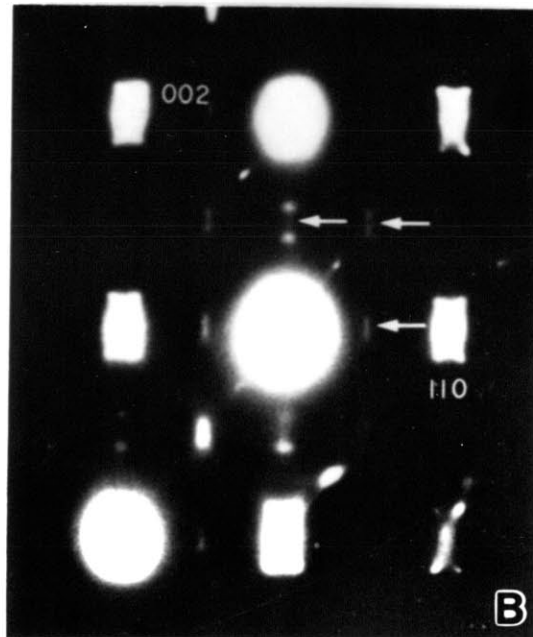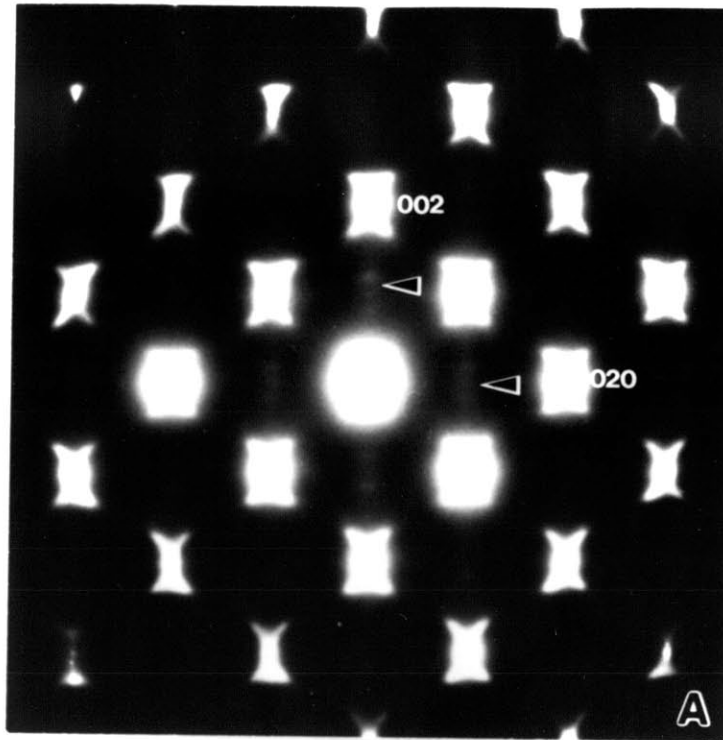
Figure 7-15. Split "superlattice" reflections (arrows) in the diffraction patterns of high-carbon martensites. The [100] pattern (A) is from Fe-1.8Mn-1.8C (aged 8 days at room temperature). The [1$\bar{1}$0] pattern (B) is from Fe-1.62C [65].
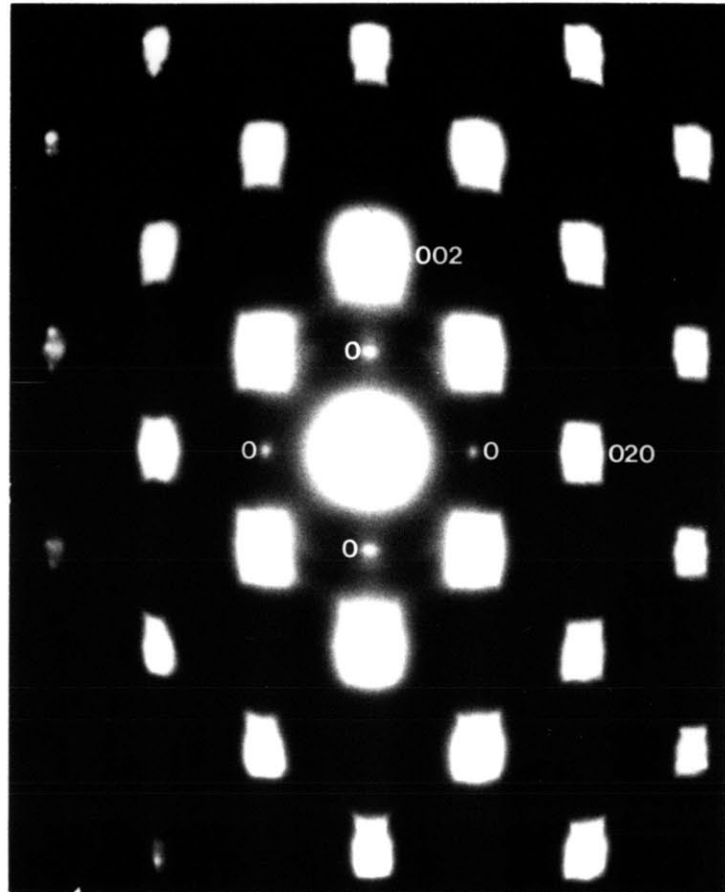
Figure 7-16. [100] diffraction pattern from martensitic Fe-
15Ni-1C (aged 2.5 hrs at room temperature).
The four spots flanking the transmitted beam
and labelled "0" are due to magnetite.

population ratio of 1:3 and a ratio of hyperfine magnetic fields of 3:2. From the similarity of these features to those of the two iron atoms in the γ'-Fe_4N structure, an isomorphous Fe_4C structure has been proposed as a reasonable model for the "decomposed state." Mössbauer spectra from Fe-Ni-C alloys [72] have also been interpreted in terms of Fe_4C precipitation during aging. These interpretations are consistent with the conclusions drawn from the TEM studies, but the breadth of the Mössbauer peaks suggests a distribution of compositions deviating from exact Fe_4C stoichiometry. Ino et al. [21] have published a Mössbauer study of carburized iron foils and propose the formula "Fe_4C_x (x << 1)" for the decomposed state; they identified peaks due to iron atoms located between pairs of carbons (i.e. iron atoms along the carbon chains mentioned above), but with intensities much less than that anticipated for stoichiometric Fe_4C.

The maximum carbon concentration detected by AP/FIM indeed falls far short of that required for Fe_4C (11 vs. 20 at pct). Therefore, the formation of an Fe_4C-based phase highly deficient in carbon [21] does not seem unreasonable. One possibility is that a coherent phase of composition $Fe_{16}C_2$ may form, characterized by a regular absence of 1/2 of the carbon atoms in stoichiometric Fe_4C, Figure 7-14(B). An analogous α'' phase forms from Fe-N martensites, before precipitation of the equilibrium γ'-Fe_4N phase. Ferguson and Jack [94] have studied Fe-N-C alloys and find that the metastable α'' carbonitride, $Fe_{16}(C,N)_2$, precipitates, indicating that carbon behaves to some extent like nitrogen. On the other hand, DeCristofaro and Kaplow [22] have studied the aging of Fe-N martensite using Mössbauer spectroscopy and were indeed able to clearly differentiate between the three different components (due to the $Fe_{16}N_2$ phase) in their spectra. The identification of only two Mössbauer components in Fe-1.86C

141

by Choo and Kaplow does not seem compatible with the hypothetical $Fe_{16}C_2$ structure; nor, to the author's knowledge, has any diffraction evidence ever been presented.

In light of the above discussion, it seems safe to say that carbon atoms undergo at least short-range ordering during aging. The best available evidence suggests that the ordering is of the type exemplified by the Fe_4C structure. An important feature of this type of ordering is that carbon atoms avoid near-neighbor sites of the O_z lattice. This kind of repulsion seems plausible when one considers the large lattice distortion produced by the carbon interstitial.

7.2.2 Rationalizing the Tweed Habit

The next issue which is addressed concerns the observed {20$\underline{3}$} habit of the tweed morphology. Khachaturyan [9] has presented a theory based upon linear anisotropic elasticity which can be applied to the present study. He has treated the case of a coherent phase with tetragonal symmetry residing in an infinite matrix of cubic symmetry. This is applicable to the present study because the occupation of O_z sites by carbon atoms results in a tetragonal distortion of the martensite lattice. An additional restriction imposed by Khachaturyan is that the elastic moduli of both phases are equal. His results indicate that the habit plane of the second phase particle is determined by the elastic anisotropy parameter, A:

$$(hkl)_{habit} = \begin{array}{l} (h0l) \text{ if } A < 0 \\ (hhl) \text{ if } A > 0 \end{array},$$

where A is given by $(c_{11}-c_{12}-2c_{44})/c_{44}$. For pure iron, $c_{11} = 2.42 \times 10^{12}$ dyne/cm^2, $c_{12} = 1.465 \times 10^{12}$, and $c_{44} = 1.12 \times 10^{12}$. The anisotropy parameter is less than zero for iron, implying a habit plane of the type

142

{h0l}. The exact habit plane is determined by the magnitude of the tetragonal distortion of the host lattice and, for given values of the elastic constants, is a function only of the "tetragonality factor," t_1, for the interstitial solution (= u_{11}/u_{33}):

$$(hkl)_{habit} = (\sin\theta_o, 0, \cos\theta_o),$$

where

$$\cos^2\theta_o = 1 + \frac{c_{11} + 2c_{12}}{c_{11} + c_{12}} \frac{t_1}{1 - t_1}.$$

The tetragonality factor applicable to the Fe-Ni-C alloys of this study can be estimated from the precise lattice parameter measurements from the Chen and Winchell study [69]. From the discussion in Chapter 5 and Chen and Winchell's lattice parameters for virgin Fe-18Ni-0.98C martensite, one obtains:

$$u_{11} = -0.302$$

$$u_{33} = 1.108$$

and

$$t_1 = -0.272.$$

Combining these values with the elastic constants for iron yields a habit plane normal of [0.543,0,0.840], which is less than 1° from [203]. The predicted habit plane agrees very well with observed habit plane, even though the Khachaturyan calculation strictly applies only to a second phase particle in an infinite matrix. Furthermore, the result provides better agreement with experiment than the {100} habit predicted from Cahn's theory of spinodal decomposition [95].

7.3 Thermodynamics of Decomposition

7.3.1 Descriptions of the Body-Centered Fe-C Solution

A number of models have been presented to describe the thermodynamics of FCC, BCC, and BCT Fe-C solutions [16,96-104]. These models have been developed primarily to calculate T_o, the temperature at which the FCC and BCC (or BCT) phases (of the same composition) have the same free energy, and $\Delta G^{\gamma \to \alpha}(M_s)$, the chemical driving force at M_s. These are important parameters in any transformation theory and their compositional dependence can provide some insight into the nature of the transformation itself. The application of the models to the thermodynamics of martensite and the martensitic transformation are, however, complicated by at least two factors:

(1) Because of the low solubility of carbon in BCC iron, experimental equilibrium thermochemical data are available only over a very limited compositional range. The behavior of carbon in more concentrated solutions must then be inferred by extrapolating the known behavior at dilute concentrations.

(2) The Fe-C solution is an interstitial solution. The local distortion of the iron lattice about an interstitial carbon leads to an important carbon-carbon interaction energy which is neither easily evaluated nor easily incorporated into the model. Furthermore, it is generally convenient to describe the configurational entropy of the BCC (or BCT) solution by using a sublattice approach, which leads to more complicated calculations.

Khachaturyan has studied the thermodynamics of body-centered Fe-C solutions in detail; most of his results are included in his recent book [9], where an extensive list of references is also provided for the interested reader. His model was examined critically in this investigation

144

because it considers explicitly the effect of Zener ordering on the free energy of the body-centered Fe-C solution. The Khachaturyan model considers only the elastic energy, which he purports is the most important contribution to the thermodynamics of any interstitial solution. His model is formulated within the framework of anisotropic elasticity theory and as such the mathematics are very complicated. His model is now reviewed and assessed; its shortcomings are emphasized and an alternative phenomenological thermodynamic description is presented.

Khachaturyan's treatment of Zener ordering leads to the conclusion that carbon atoms occupy only O_z sites in all but the most dilute Fe-C alloys. The long-range order parameter, η, which describes such ordering is defined by:

$$n(O) = \begin{array}{ll} c - c\eta & \text{for } O_x \text{ sites} \\ c - c\eta & \text{for } O_y \text{ sites} \\ c + 2c\eta & \text{for } O_z \text{ sites,} \end{array} \qquad (7\text{-}10)$$

where $n(O)$ is the occupation probability for octahedral sites and c is the total number of carbon atoms divided by the total number of octahedral sites. Note that when η is zero, each interstitial sublattice is occupied with equal probability, corresponding to the disordered state. When η is unity, all carbon atoms are located in O_z sites. This corresponds to the Zener-ordered state. The temperature dependence of the long-range order parameter (at small c) is defined by:

$$\frac{kT}{\lambda_2(0)c} = \frac{-3\eta}{\ln[(1+2\eta)/(1-\eta)]}, \qquad (7\text{-}11)$$

where k is Boltzmann's constant and $\lambda_2(0)$ is an energy characteristic of the ordered state and is determined by the elastic constants of the host

lattice, the severity of the tetragonal distortion produced by the interstitial atom, and a short-range "contact" repulsion between neighboring interstitials. The contact repulsion was calculated from a potential function which Khachaturyan claims to give good agreement between the calculated and observed structures of organic crystals. Equation 7-11 is illustrated graphically in Figure 7-17. At the ordering temperature, η changes discontinuously from zero to about 0.5, indicating that the ordering is a first-order transition. At room temperature, Equation 7-11 predicts that Zener ordering is stable at all carbon concentrations above about 0.125 at pct. It should be mentioned that the ordering temperature does not change significantly when the estimated elastic constants for Fe-20Ni [25] are substituted for those of pure iron.

According to Khachaturyan, the Helmoltz free energy, F, of the ordered solution is given by:

$$F(c,\eta) = N\lambda_1(0)c/2 + 3N\lambda_2(0)c^2\eta^2$$
$$+ kTN\{2c(1-\eta)\ln[c(1-\eta)] + c(1+2\eta)\ln[c(1+2\eta)]$$
$$+ 2[1-c(1-\eta)]\ln[1-c(1-\eta)]$$
$$+ [1-c(1+2\eta)]\ln[1-c(1+2\eta)]\}, \qquad (7-12)$$

where N is the total number of host atoms, $\lambda_1(0)$ is an energy characteristic of the disordered solution, and the other terms have their previous meanings.

The second term in Equation 7-12, defining the change in internal energy due to the ordering, grows rapidly in magnitude as the carbon concentration increases. The result is an inflection in the free energy curve at a small carbon concentration, i.e. a conditional spinodal decomposition is predicted. At room temperature, the spinodal occurs at
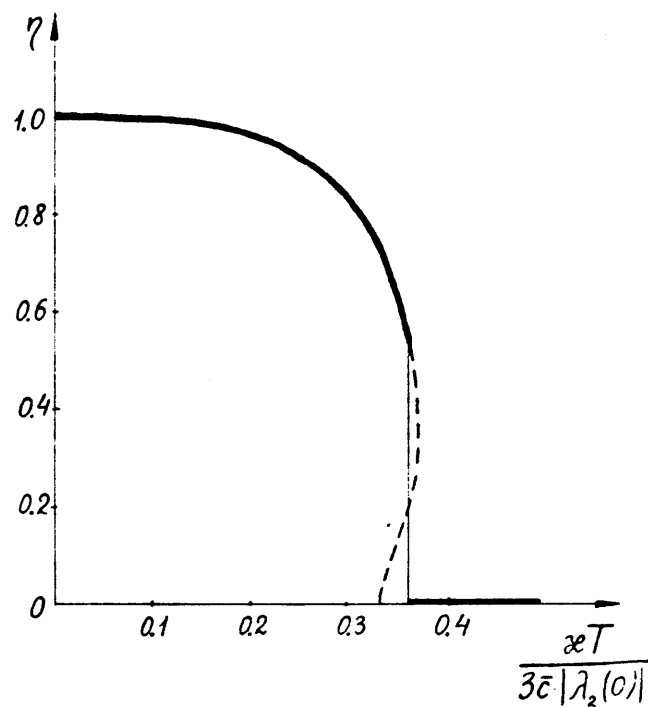
Figure 7-17. The temperature dependence of the long-range order parameter, η (from Khachaturyan [9]).

about 0.2 at pct carbon, irrespective of whether one uses the elastic
constants for pure iron or for Fe-20Ni [25]. Free energy curves for
several values of the order parameter are shown in Figure 7-18. The shape
of the free energy curves indicates that the phases which result from the
decomposition should be essentially pure iron and pure FeC.

Khachaturyan extends his thermodynamic analysis to include a
calculation of the wave vectors which are spontaneously amplified at the
onset of spinodal decomposition. The locus of maximum wave vectors in the
[100] zone at $300^{\circ}K$ is shown as a function of carbon content in Figure 7-19.
These contours define the angular dependence of the minimum spontaneously-
amplified wavelength; one set was calculated with the elastic constants of
pure iron, the other with those for Fe-20Ni. Although the calculated
maximum wave numbers are generally too large, the overall shape of the
contours and the increase in wave number with increasing carbon content are
in qualitative agreement with experiment. The elastic constants of both
alloys favor modulations along <20$\underline{3}$>, again in agreement with experiment.
However, the "softer" elastic constants of Fe-20Ni reduce the maximum
possible elastic energy reduction from decomposition, resulting in a
smaller maximum wave number as compared with pure iron. This agrees with
the fact that the Fe-Ni-C alloys of this study exhibit larger initial
wavelengths than the corresponding Fe-C alloys studied by Kusunoki and
Nagakura [88] (cf Figure 7-9).

Although the Khachaturyan model predicts a spinodal reaction with the
correct habit, it nonetheless has some serious shortcomings. Foremost
among these is the prediction that the compound FeC should form. This is a
direct consequence of the fact that Khachaturyan only considered the
stability of superstructures having a certain subsymmetry of the BCC

148
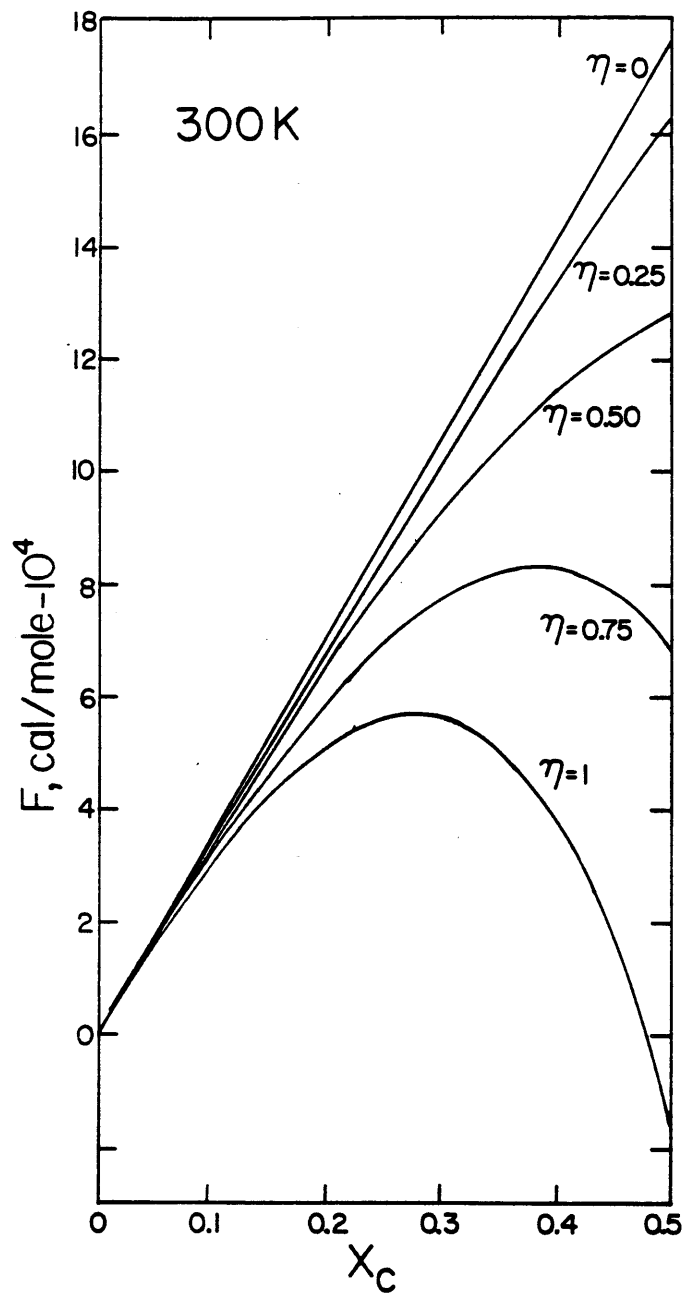
Figure 7-18. The free energy (at 300°K), F, for the
Khachaturyan model as a function of carbon
concentration. Curves for several values
of the order parameter are indicated.
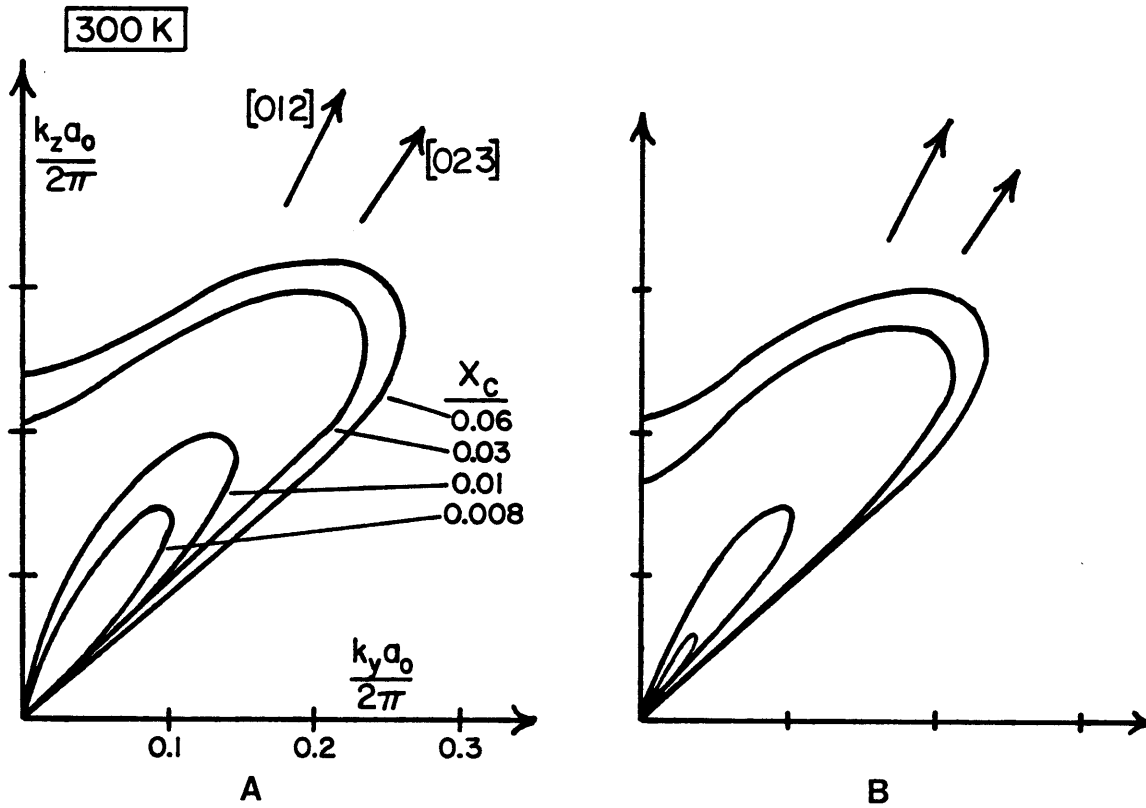
Figure 7-19. Locus of the wave vectors in the [100] zone which are spontaneously amplified during the initial decomposition of Fe-C alloys at 300°K (predicted by Khachaturyan's theory). The axes are numbered in units of dimensionless wave number. The elastic constants for pure iron and for Fe-20Ni were used to calculate (A) and (B), respectively.

structure. His model is not sophisticated enough to treat, for example, the Fe_4C structure, where longer-range atomic interactions are important in determining structural stability. A second shortcoming concerns the calculated spinodal wavelengths, which are generally shorter than those measured experimentally.

7.3.2 An Alternative Thermodynamic Description

An attempt is made in this section to develop a thermodynamic description of the body-centered Fe-C solution which provides better agreement with the experimental results on spinodal decomposition than Khachaturyan's model. Because of the complexities inherent in treating carbon ordering, it was decided that a phenomenological approach to the problem might be most fruitful. The proposed description is based on that presented by Kaufman and Nesor [105]. They considered the behavior of both the FCC and BCC phases; their thermodynamic description of the BCC phase was derived from the well-established behavior of austenite (out to relatively high carbon concentrations) and the behavior of T_o (the temperature at which the two phases have the same free energy). The Kaufman-Nesor (K-N) formulation can be classified as a "subregular" solution model according to the definition provided by Hardy [106]. The K-N model, however, contains a non-zero excess entropy of mixing term because their ideal entropy of mixing appears in the same form as that for a substitutional solution. Their description was chosen as a starting point because it provides fairly good agreement with experimental thermochemical measurements on dilute Fe-C solutions and also because of its simple analytical form. In the K-N formulation, the Gibb's free energy of the BCC Fe-C solution is given as:

$$G^{BCC}(\text{J/mole}) = (1-X)G_{Fe}^{BCC} + XG_C^{BCC}$$
$$+ RT[(1-X)\ln(1-X) + X\ln X]$$
$$+ (1-X)X[(1-X)(-35146-37.823T)$$
$$+ X(-95814-29.079T)], \qquad (7\text{-}13)$$

where X is the atomic fraction of carbon in solution, G_{Fe}^{BCC} is the free energy of pure BCC iron, G_C^{BCC} is the free energy of pure BCC carbon, R is the gas constant, and T is the temperature in degrees Kelvin. Kaufman and Nesor give the following difference between the free energy of pure BCC carbon and graphite (the stable form of carbon at room temperature):

$$G_C^{BCC} - G_C^{graphite} = 146858 - 14.644T \qquad (300 < T).$$

Surprisingly, the K-N model predicts a miscibility gap in the BCC solution at temperatures below about 125°K. Nevertheless, this prediction is not in good agreement with the experimental observation of a miscibility gap (spinodal decomposition) at and above room temperature and for this reason the model must be modified.

The indications of Fe_4C-type ordering described earlier suggest that an additional term which describes this kind of ordering may be incorporated in the free energy function of Equation 7-13. Saunders and Miodownik [107] have provided an empirical expression which can be used to introduce an extra term to the free energy function over a limited composition range. Such a term may be warranted when ordering or some other contribution to the free energy occurs over a certain composition range. The extra free energy term is of the following form:

$$\Delta G^{order} = C[(X-X_1)(X_2-X)/(X_1-X_2)^2]^2, \qquad (7\text{-}14)$$

152

where X_1 and X_2 are the composition limits within which the additional stability is operative and C is a temperature-dependent constant. Saunders and Miodownik state that the temperature dependence which achieves the best experimental fit often requires a strong T^2 term. X_1 and X_2 were taken as 0 and 0.4, respectively, thereby centering the free energy minimum associated with this extra term at the Fe_4C composition (20 at pct carbon).

The carbon-ordering energy was incorporated into the K-N model by the following procedure. First, the K-N formulation was reduced to a regular solution description by neglecting the excess free energy of mixing term which dominates on the carbon-rich side of the phase diagram (i.e. the last term in Equation 7-13). This leaves the free energy function essentially unchanged at iron-rich compositions (where it already agrees with experiment). An ordering energy identical in form to that suggested by Saunders and Miodownik (S-M) was substituted in a manner (i.e. by appropriate choice of "C") such that the T_o temperature remained consistent with that predicted by the previous models. The above procedure yields a free energy function which contains a regular solution term, plus an additional S-M term describing the tendency towards ordering about the Fe_4C stoichiometry:

$$G^{BCC}(J/mole) = (1-X)G_{Fe}^{BCC} + XG_C^{BCC}$$
$$+ RT[(1-X)\ln(1-X) + X\ln X]$$
$$+ (1-X)X(-35146-37.823T)$$
$$+ (C_0 + C_2T^2)[(X)(0.4-X)/(-0.4)^2]^2, \qquad (7-15)$$

where C_0 and C_2 are taken as -106670 J/mole and 0.1393 J/mole-$^\circ K^2$, respectively. For these particular values of C_0 and C_2, the S-M ordering term takes on positive values above about 875°K, and therefore above this

153

temperature it should be omitted from the free energy function. Figure 7-20 depicts the free energy function at 300°K. The dashed curve represents the regular solution component of Equation 7-15. The ordering term produces a slight bump in the curve near the Fe_4C composition, as well as inflections on either side of this composition.

The fit of the phenomenological model to the known FCC-BCC phase equilibria will now be quantitatively assessed. First, the compositional dependence of the T_o temperature will be compared with the predictions of other models. This requires an expression for the free energy of the austenitic phase, G^{FCC}. Kaufman and Nesor suggest the following function:

$$
\begin{aligned}
G^{FCC}(J/mole) = \ & (1-X)G_{Fe}^{FCC} + XG_C^{FCC} \\
& + RT[(1-X)\ln(1-X) + X\ln X)] \\
& + (1-X)X[(1-X)(-94558-2.929T) \\
& + X(-155226+5.816T)],
\end{aligned}
\qquad (7\text{-}16)
$$

where G_{Fe}^{FCC} and G_C^{FCC} are the free energies of pure FCC iron and carbon, respectively. Kaufman and Nesor [105,108] give

$$
G_C^{BCC} - G_C^{FCC} = 8368 \text{ J/mole} \qquad (300 < T)
$$

and

$$
\begin{aligned}
G_{Fe}^{BCC} - G_{Fe}^{FCC} = \ & -6108.64 + 3.4618T + 0.7472\times10^{-2}T^2 \\
& - 0.51254\times10^{-5}T^3 \qquad (300 < T < 1100).
\end{aligned}
$$

Equations 7-15 and 7-16 were used to calculate the T_o curve which appears in Figure 7-21. Included in this plot are several sets of T_o temperatures from other studies which Kaufman et al. [99] tabulate in their paper. The current T_o curve lies between the $\alpha+\gamma/\gamma$ phase boundary and the M_s curve (as is required) and also lies within the range of those values reported previously.
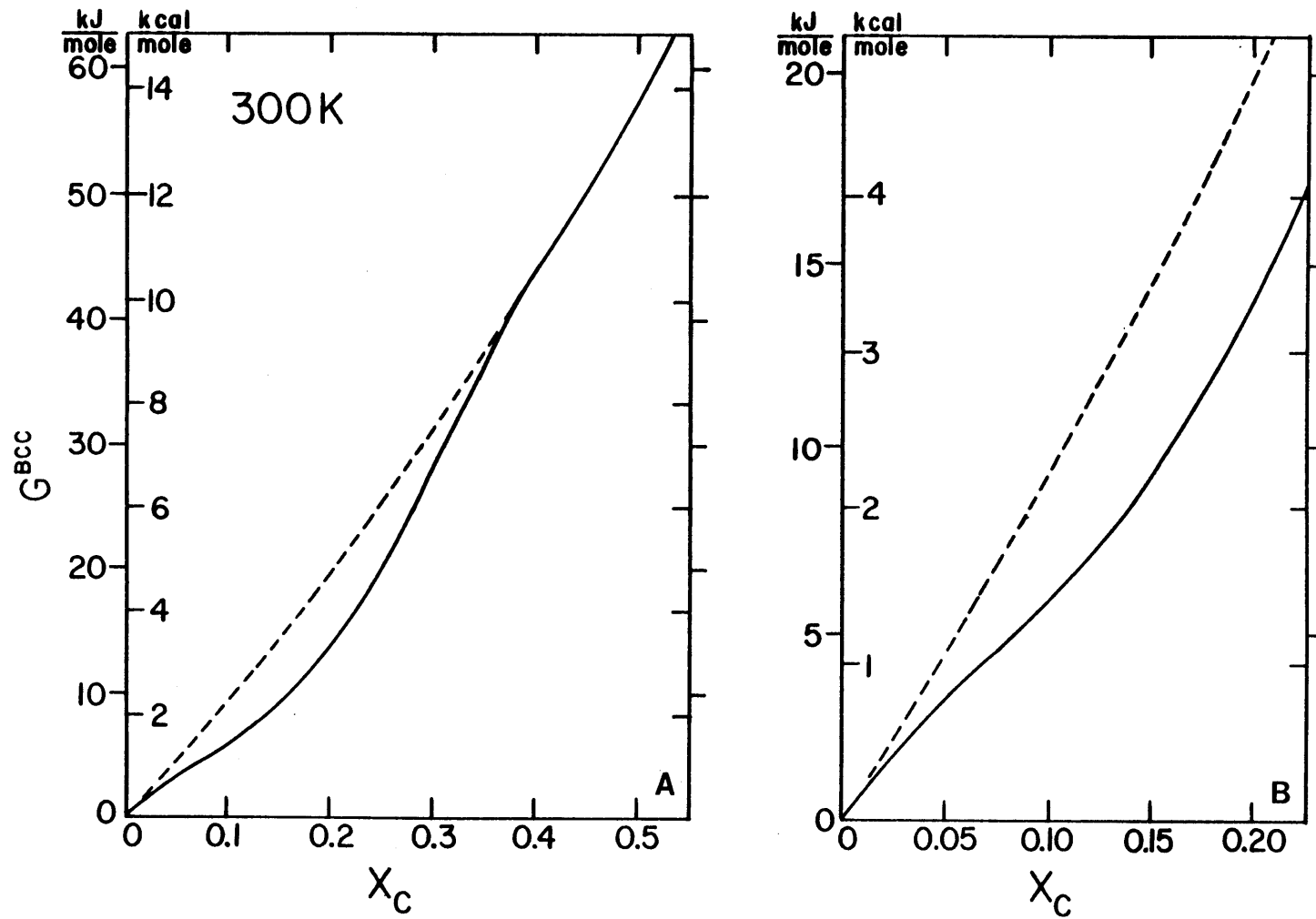
Figure 7-20. The free energy (at 300°K) of the body-centered Fe-C solution according to the S-M model. The reference state for both pure iron and pure carbon is taken as BCC and the standard states are taken as BCC and graphite, respectively. An enlargement of the iron-rich side of (A) is shown in (B).
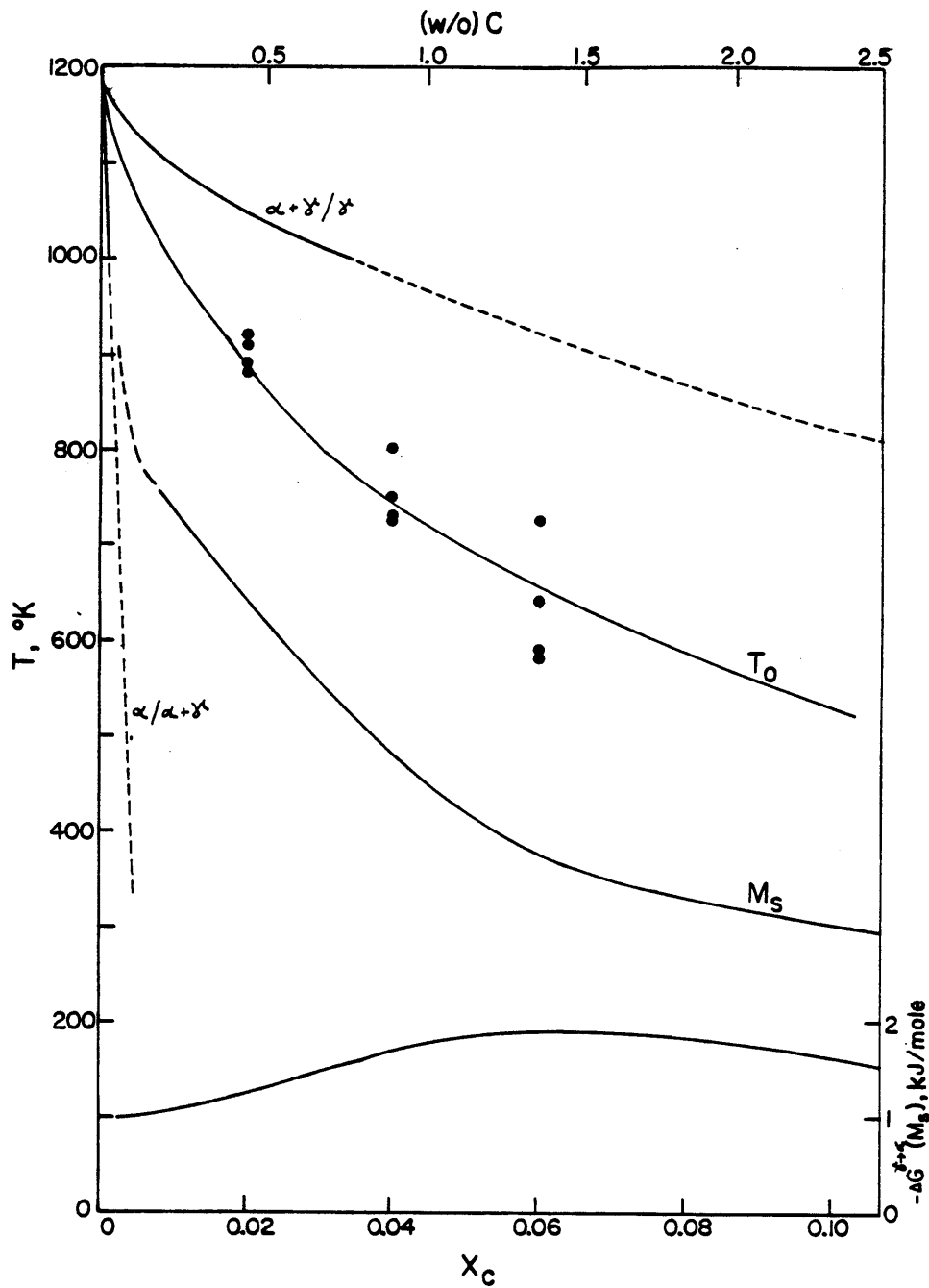
Figure 7-21. Portion of the Fe-C phase diagram showing: The $\alpha/\alpha+\gamma$ phase
boundaries (from Chipman [3]); the variation of M_s with
composition (from Sachdev [42]); the T_0 curve for the
present model and several sets of previously calculated
values [99]; and the chemical driving force at M_s, $\Delta G^{\gamma \rightarrow \alpha}(M_s)$.

156

Equations 7-15 and 7-16 were also used to calculate $\Delta G^{\gamma \to \alpha}$ at M_s as a function of carbon concentration. The results, again shown in Figure 7-21, fall within the range of values tabulated by Kaufman et al. However, the driving force varies in neither a linear nor a monotonic manner with carbon content. Instead, the curve exhibits a maximum near 6 at pct carbon. Bhadeshia [109] has recently calculated the chemical driving forces predicted by several models and also found similar behavior. He attributed this to the reduction in the free energy of martensite relative to austenite by the Zener ordering (preferential occupation of O_z sites) effect. This interpretation cannot be correct, however, because a reduction in the free energy of the martensite phase should result in a net increase in the driving force, other factors being constant. The decrease in driving force above 6 at pct carbon is directly related to the tendency for the M_s curve to flatten above this concentration. This, in turn, may be related to a "solute drag" effect [110] of carbon which should become less important at lower temperatures as the diffusivity of carbon decreases to the point where carbon can no longer exert a drag effect on the austenite/martensite interface.

7.3.3 Predictions of the Current Model

The free energy function of Equation 7-15 (S-M model) does indeed predict a miscibility gap, one which is in better agreement with experiment than that predicted by the K-N and Khachaturyan models. The coherent spinodal predicted by Equation 7-15 is a "conditional spinodal" [111] since prior ordering is required before decomposition can occur (this term was originally coined by Allen and Cahn [112] in their study of spinodal decomposition in Fe-Al alloys). The results of both models are depicted in

157
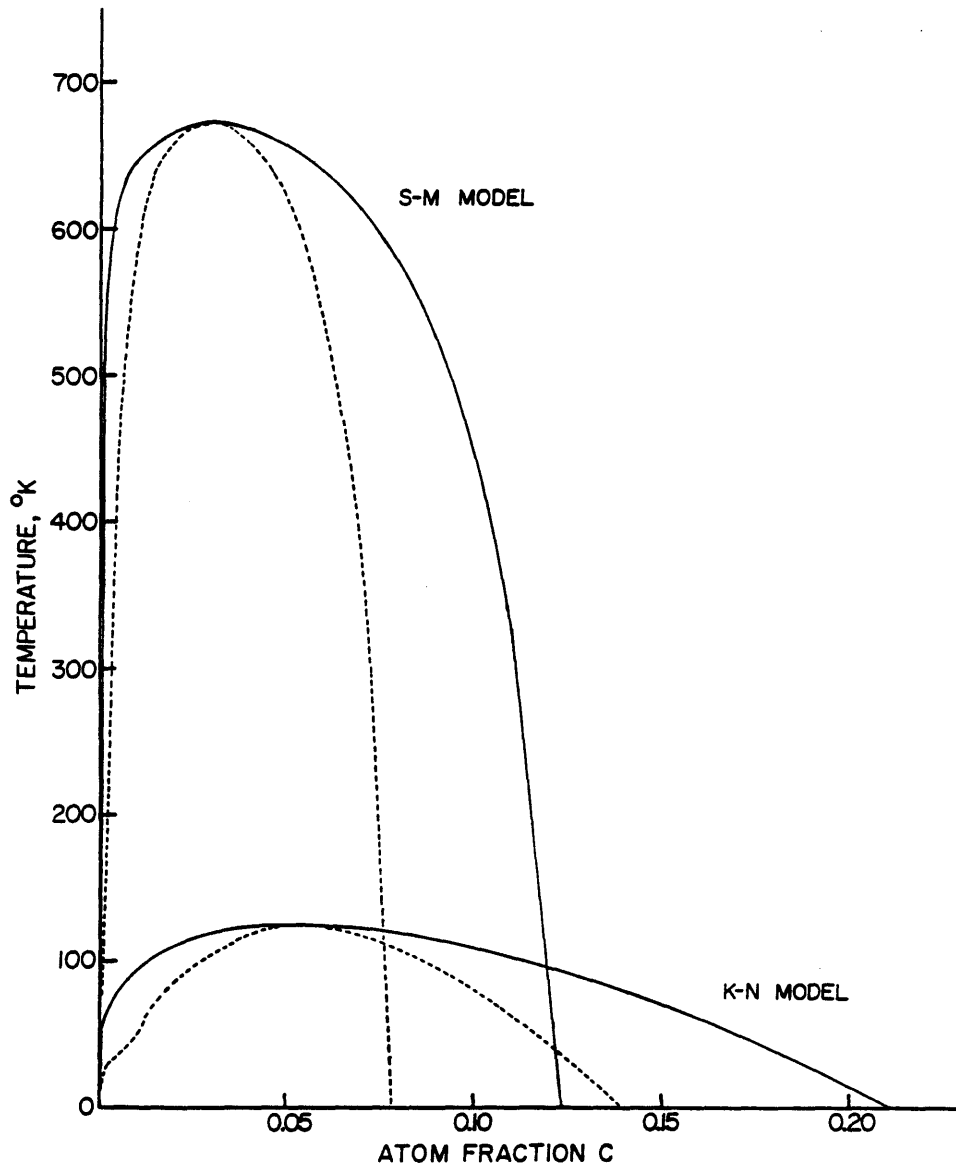
Figure 7-22. Calculated (metastable) miscibility gaps in the Fe-C system. Solid lines represent the phase boundaries; dashed lines represent the spinodals.

Figure 7-22. The critical temperature (T_c) and composition (X_c) for the K-N model are 124°K and 0.053, respectively. On the other hand, the S-M model predicts that T_c = 675°K and X_c = 0.029. At 300°K, the spinodals for the S-M model are located at X = 0.0025 and X = 0.0723 and the corresponding phase boundaries are located at X ≅ 0 and X = 0.111. This places both of the Fe-Ni-C alloys of this study well within the instability region and is consistent with the fact that both alloys decompose spinodally at room temperature. Moreover, the calculated phase boundaries are in excellent agreement with atom probe results, which indicate compositional fluctuations between 0.2 and 11 at pct carbon.

Experimentally-measured heat effects due to aging, ΔH_a, can be compared with the enthalpy of decomposition predicted by Equation 7-15. There are several published papers which report calorimetry results on Fe-C martensites aged above and below room temperature [62,113]. Generally, heat evolution is measured well before the heat effect associated with transition carbide precipitation. Differential scanning calorimetry (DSC) results on the two Fe-Ni-C alloys of this study are shown in Figure 7-23. The "as-quenched" curves represent the heat capacity of freshly-quenched martensite during heating at 5°K/min. The "tempered" curves represent the heat capacity of the same samples after holding at 400°C for 15 minutes and rerunning the scans. The difference between each set of curves represents the (negative) enthalpy contribution due to aging and tempering. The difference is small at the beginning of the scans because the samples were held for a short period of time at 0°C before starting. Separate peaks associated with aging and the three stages of tempering have been indicated. Graphical integration of the area defined by the aging peaks yield values of 140 and 365 J/mole (33 and 88 cal/mole) for Fe-25Ni-0.4C
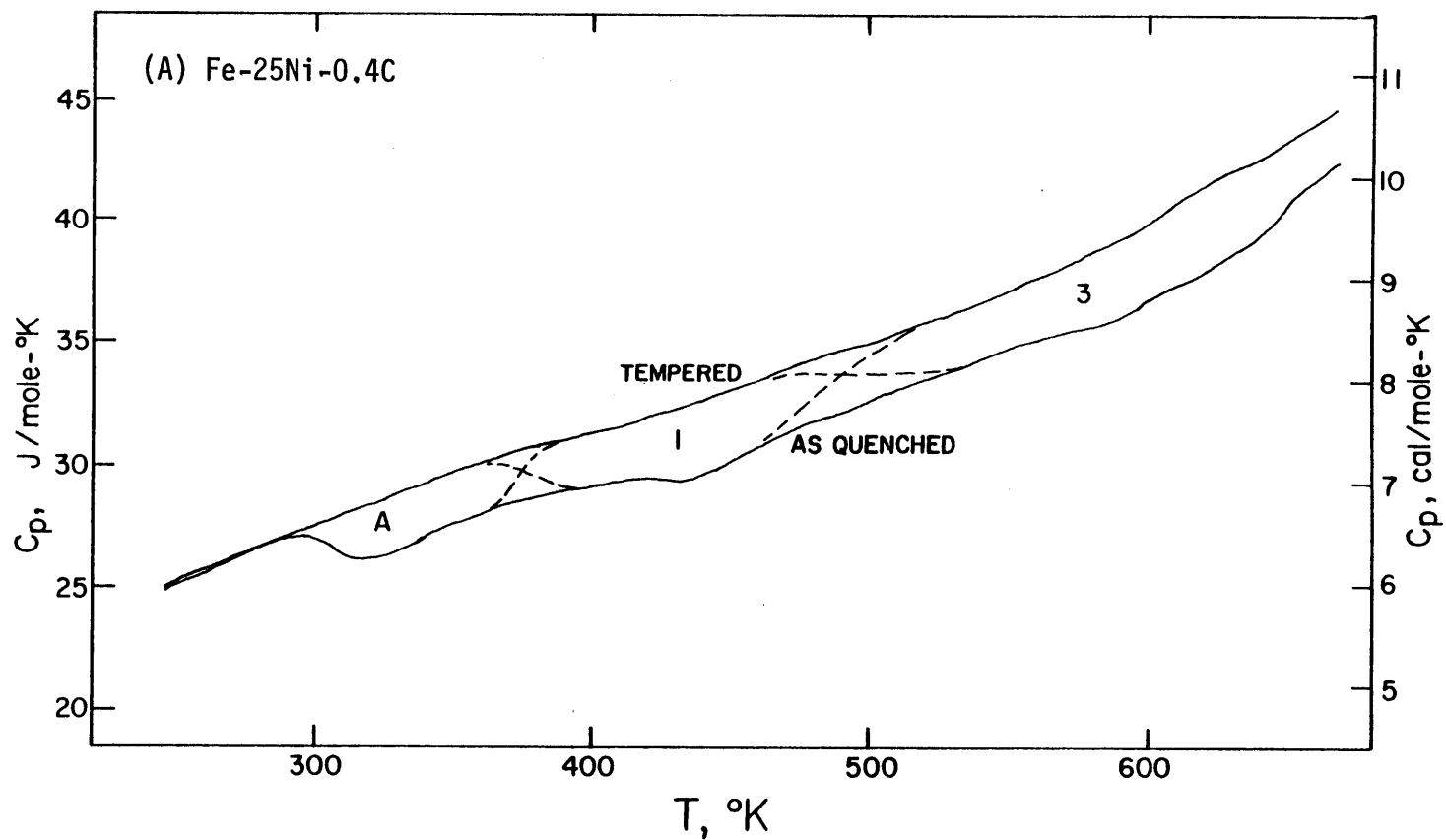
Figure 7-23. DSC results from Fe-25Ni-0.4C (A) and Fe-15Ni-1C (B). The heating rate was 5°K/min. The heat effects due to aging and the three stages of tempering are designated by "A", "1", "2", and "3", respectively.
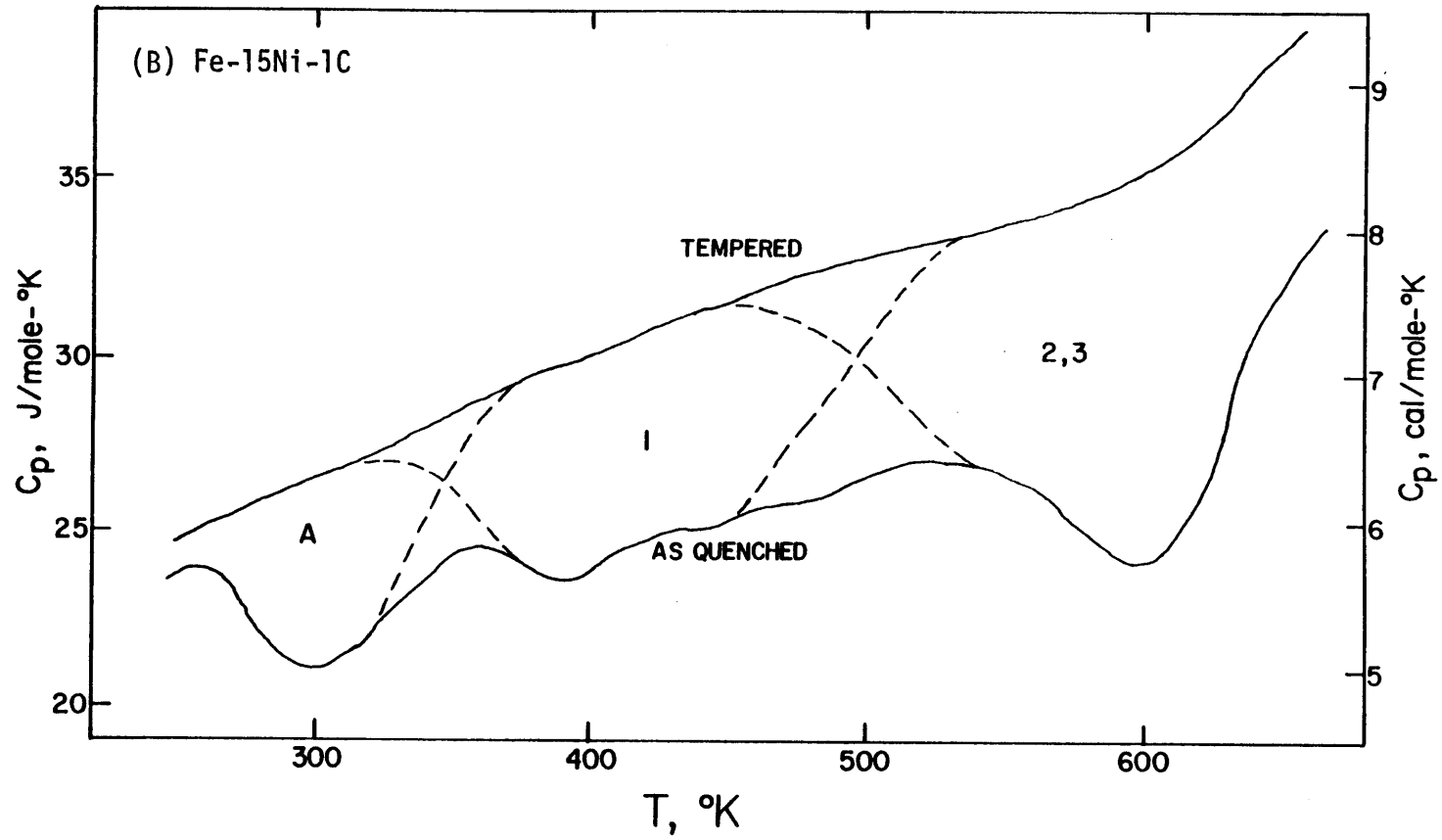
Figure 7-23 (cont.)

and Fe-15Ni-1C, respectively. These values are considered to be conservative estimates of ΔH_a since some enthalpy was released before the DSC scan, during the short hold at 0°C. The calculated variation in ΔH_a with carbon content is shown in Figure 7-24, along with the measured values from this study and a curve which Mittemeijer and van Doorn [114] claim is a good fit to the previous literature data. The measured values are consistently less than the calculated values. This can be attributed to the fact that the literature values were obtained from auto-tempered Fe-C martensites, while the current values are underestimates for the reasons mentioned above.

The spinodal is the point where the second composition derivative of the free energy function, G'' (= $\partial^2 G / \partial X^2$), vanishes. Within the spinodal points G'' is negative, as is required in order for compositional fluctuations to result in a net decrease in free energy. Cahn [95,115] has presented a quantitative, phenomenological theory of spinodal decomposition which is based on solving the diffusion equation for an inhomogeneous system. In its most simple form, the diffusion equation is linearized and therefore this theory only applies to the early stages of decomposition when concentration fluctuations are small. His theory predicts that the compositional modulations can be represented by a series of plane waves with wavelength-dependent amplitudes. The "amplification factor," $R(\beta)$, for any given wave is given by (neglecting strain energy):

$$R(\beta) = -M\beta^2(G'' + 2K\beta^2), \tag{7-17}$$

where β is the wave number (= $2\pi/\lambda$), M is the diffusional mobility, and K is the "gradient energy coefficient." The gradient energy term in Equation 7-17 is always positive and tends to stabilize the homogeneous solution.
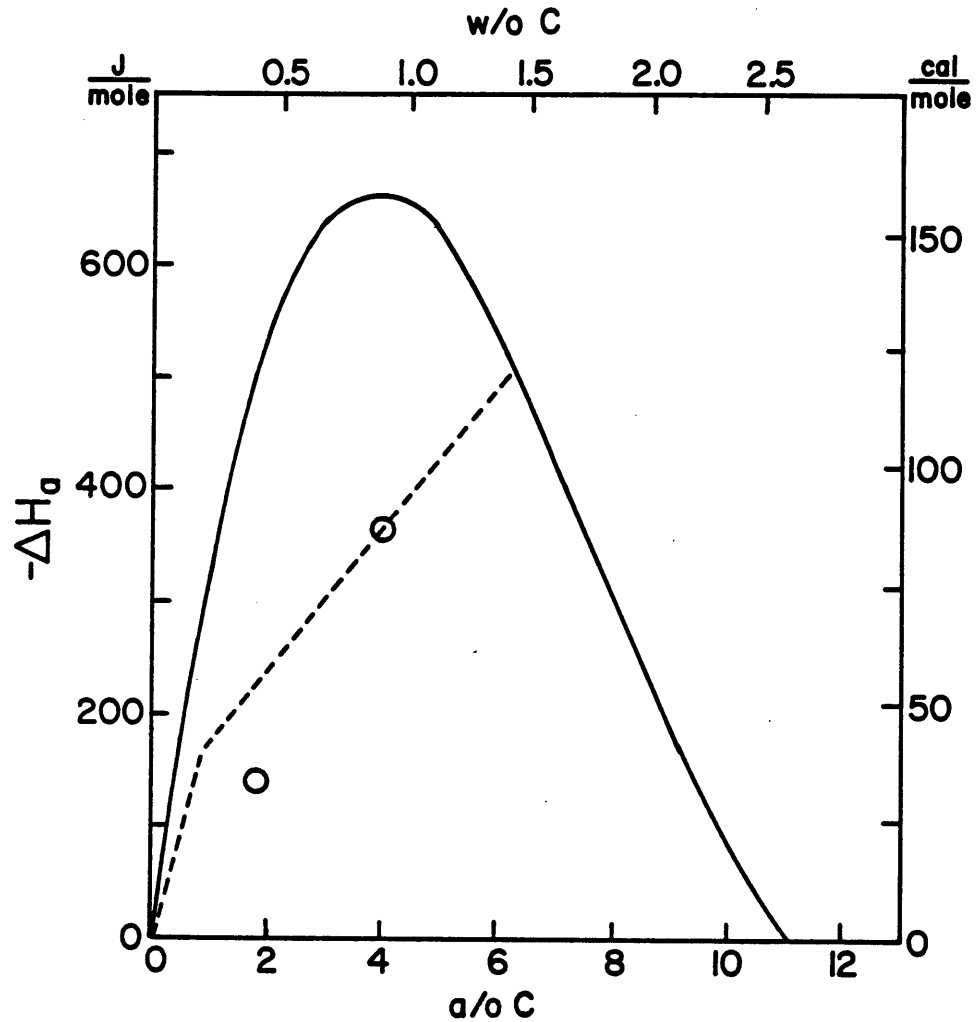
Figure 7-24. Heat effects due to aging. The solid curve
represents the calculated S-M enthalpy change
due to spinodal decomposition. The
open circles represent current DSC data and
the dashed curve has been proposed by
Mittemeijer and van Doorn [114] as a good fit
to previous experimental data.

Equation 7-17 reveals that the amplification factor is negative for all

wavelengths when G" > 0, i.e. only the homogeneous solution is stable.

The wave number receiving maximum amplification, β_m, can be obtained

by differentiating Equation 7-17 with respect to β:

$$\beta_m = 2\pi/\lambda_m = [-(G''/K)^{1/2}]/2. \tag{7-18}$$

Equation 7-18 indicates that the wavelength receiving maximum

amplification, λ_m, varies inversely with the square root of G". Returning

to the free energy function of Equation 7-15, the minimum value of G"

occurs (at 300°K) at about 1.25 at pct carbon ($\sim$0.27 wt pct). At this

composition the linear theory predicts a minimum spinodal wavelength.

However, the TEM results presented in section 7.1 show that the wavelength

decreases continuously with carbon concentration all the way out to at

least 8.5 at pct. This discrepency in the current phenomenological

solution model illustrates that, while it may provide qualitative agreement

with experiment, it cannot be used to predict the solution behavior in a

rigorous, quantitative manner. This is not at all surprising considering

the simple nature of the model and the meager experimental data which are

available for quantifying the behavior of concentrated Fe-C solutions.

7.4 Summary

At this point it is worth reflecting a little on the results and

interpretation which have been presented in this chapter. The dominant

process which occurs during martensite aging involves a diffusion-

controlled redistribution of carbon atoms. The mechanism appears to be a

conditional spinodal reaction which occurs over a wide range of alloy

composition.

A phenomenological thermodynamic description of the body-centered Fe-C

solution has been developed which predicts a conditional spinodal reaction over a wide range of temperature and composition. Whether ordering beyond the Zener type (intrinsic to virgin martensite) is actually required for decomposition is a matter which can be debated; no evidence of any long-range secondary ordering was detected in this study, but short-range order has been previously detected by Mössbauer spectroscopy.

The current model is very simple in form and makes no explicit assumptions regarding the nature of the carbon-carbon interaction. Some of the more sophisticated models assume an explicit interaction [99,100,102,104] or Fe-C superstructure [9]. Although the framework of these models is structured on better theoretical grounds, none accurately predict the behavior actually observed and therefore certainly cannot be regarded as any better (than the current model) for describing the behavior of supersaturated Fe-C martensites.

Much work remains to be done in modelling the behavior of body-centered Fe-C solutions. The aligned nature of the product of the spinodal decomposition indicates that Khachaturyan's treatment of the elastic energy of Zener-ordered martensite may be a good starting point for future refinement. By properly considering secondary ordering (of the Fe_4C type, for example), it may be possible to derive a metastable miscibility gap which provides better agreement with experiment than Khachaturyan's model alone.

CHAPTER 8

RESULTS AND DISCUSSION: TRANSITION CARBIDE PRECIPITATION

After a month or so at room temperature, diffraction effects from a distinct, new phase begin to appear in patterns taken from aged martensite. In terms of a one-hour treatment, general precipitation is detectable at temperatures greater than about 80°C. Later, it will be shown that this phase is epsilon-carbide; its appearance marks the beginning of the so-called "first stage of tempering." Before analyzing the structure of this phase, however, we will first examine its morphology.

8.1 Carbide Morphology

Figure 8-1 shows an Fe-25Ni-0.4C crystal at the [100] orientation. Inspection of the diffraction pattern reveals streaking which is different from the diffuse scattering (along <20$\underline{3}$> directions) associated with the tweed structure (presented in Chapter 7). In the initial stages of aging, spinodal decomposition gives rise to diffuse scattering which is located about each fundamental reflection in a _symmetric_ manner. That is, the diffuse "streaks" are _centered_ about the fundamentals. However, the streaking in Figure 8-1 is asymmetric (except at the origin of reciprocal space), tending to emanate from only one side of any given fundamental reflection. The streaks at the (0$\bar{1}\bar{1}$) reflection were used to form the dark-field image of Figure 8-1. Two families (variants) of thin particles can be seen, each with their short dimension parallel to one of the streaks. The streaking may thus be a shape effect due to the small particle size (along the streak direction), a strain effect due to lattice mismatch between the martensitic matrix and the new phase, or a combination of the two. The streaks at the origin are indicative of a shape effect;
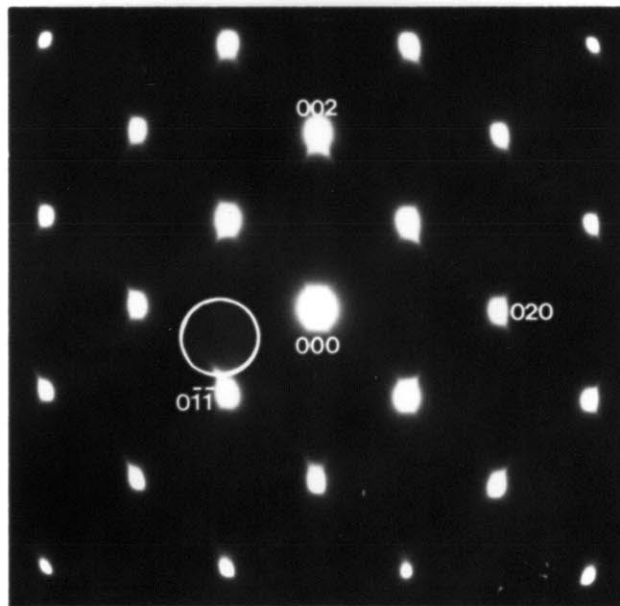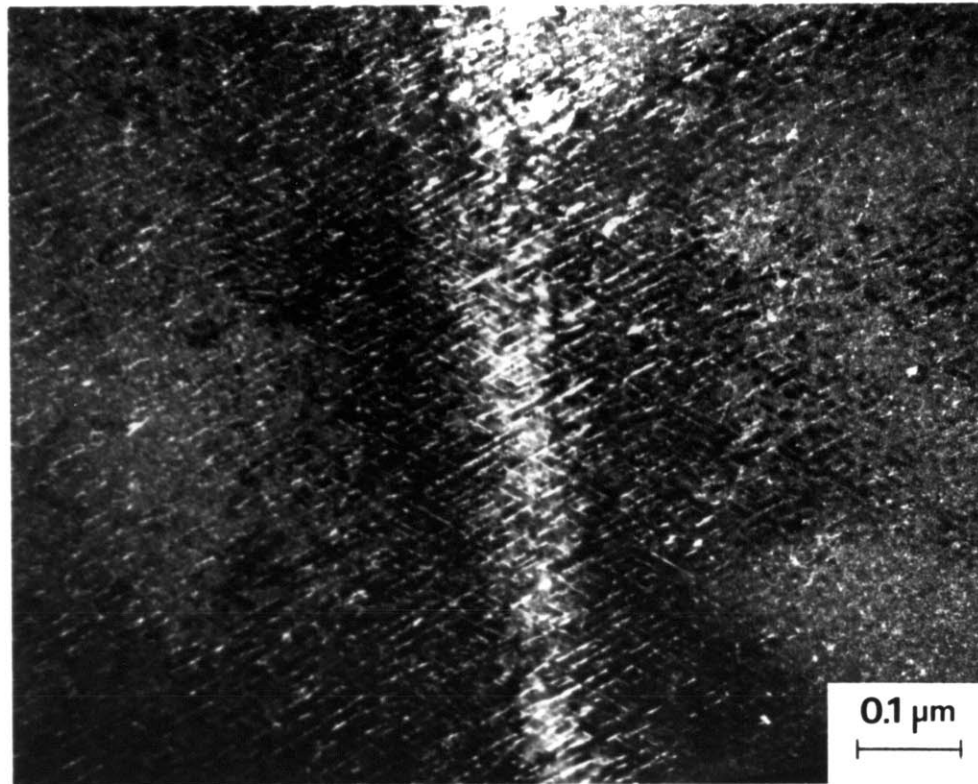
Figure 8-1. Dark-field transmission electron micrograph of Fe-25Ni-0.4C after aging 58 days. Two families of second phase particles give rise to the relrods or streaks along [012] and [01$\bar{2}$]. The objective aperture (indicated by the circle on the diffraction pattern) was located so as to include primarily the two streaks near the (0$\bar{1}\bar{1}$) reflection. The schematic pattern depicts only the streaks along [01$\bar{2}$].

the projected image of the particles in Figure 8-1 is consistent with either a plate- or rod-like shape.

The same features described above were observed in Fe-15Ni-1C. Contrast from thin particles after a one-hour treatment at 100°C is shown in Figure 8-2. Here, the two families of particles are better defined and appear to comprise a larger volume fraction (as compared with Fe-25Ni-0.4C), consistent with the higher carbon content of the alloy.

The morphological features of precipitates can often be more easily analyzed by increasing the precipitate size and reducing the number density, i.e. by allowing them to coarsen. The volume fraction of carbides can be further reduced by going to alloys with lower carbon content. A one-hour treatment of Fe-25Ni-0.4C at 150°C produces the microstructure shown in Figure 8-3. The sample orientation (near $[711]_{\alpha}$) is similar to Figure 8-1, but in addition to the two carbide variants which are rod-like in projection, at least one other variant appears (at the arrow) which has an irregular projected shape. The latter particles undoubtedly represent an additional crystallographic variant of the former "rod-like" precipitates. Their larger projected width suggests that the carbide particles are actually plate-like in shape.

It is quite common to observe more than one carbide variant within any given martensitic volume, particularly during the early stages of precipitation. The same crystal shown in Figure 8-3 is shown again in Figure 8-4, but after slight tilting. Four different carbide habit variants are now indicated within this martensitic unit; this represents the maximum number of variants which were detected within a single crystal. The symmetry operations which relate crystallographically-equivalent variants reflect the orientation relation between the parent and

168
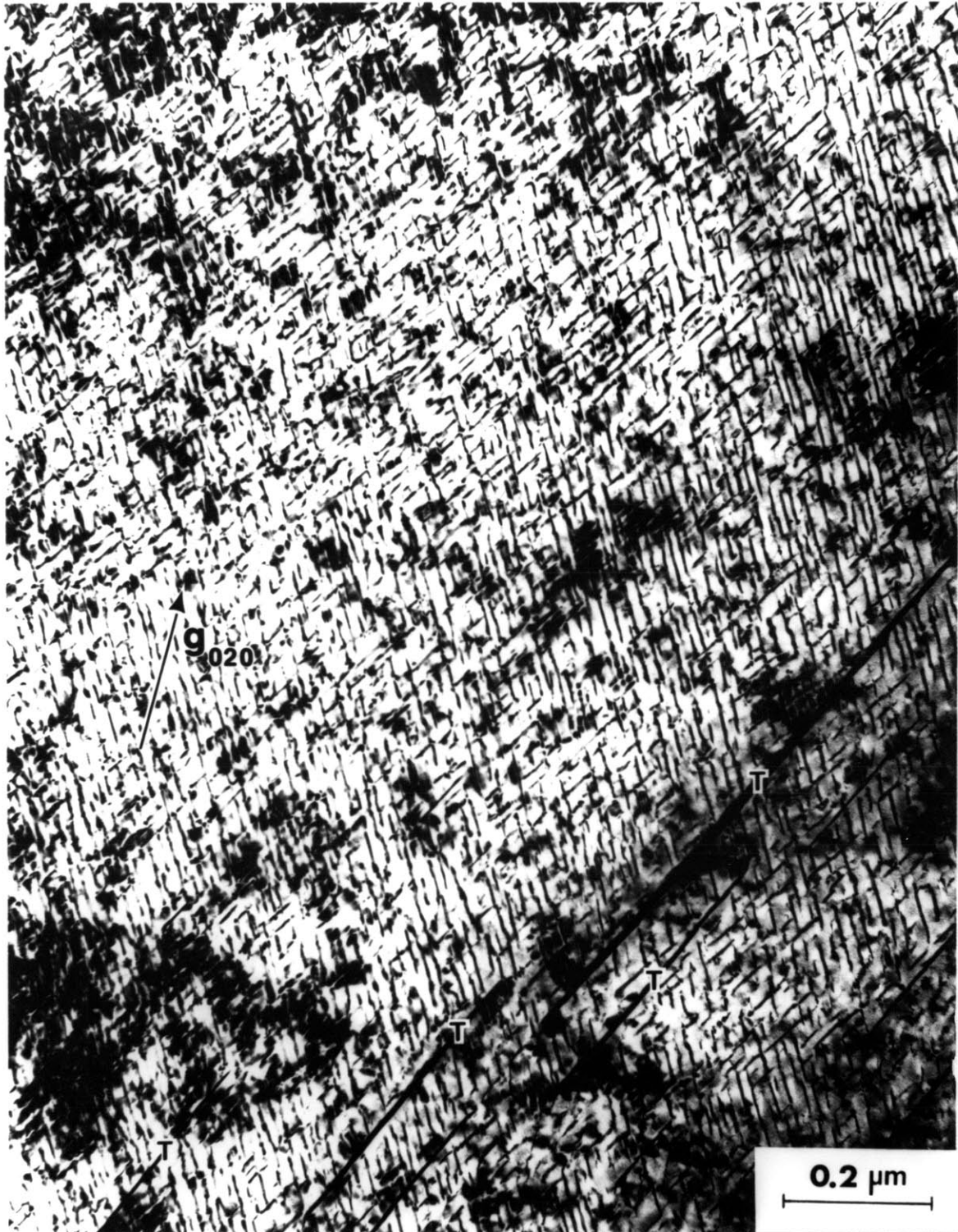
Figure 8-2. Dark-field transmission electron micrograph of Fe-15Ni-1C after one hour at 100°C + 146 days at room temperature. Several {11$\underline{2}$} transformation twins are indicated by "T".
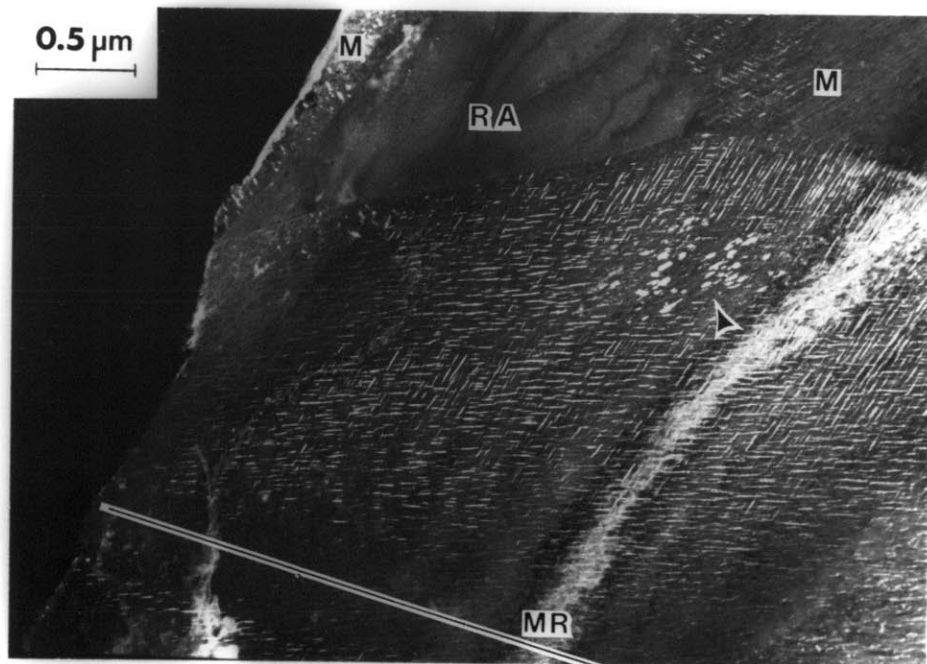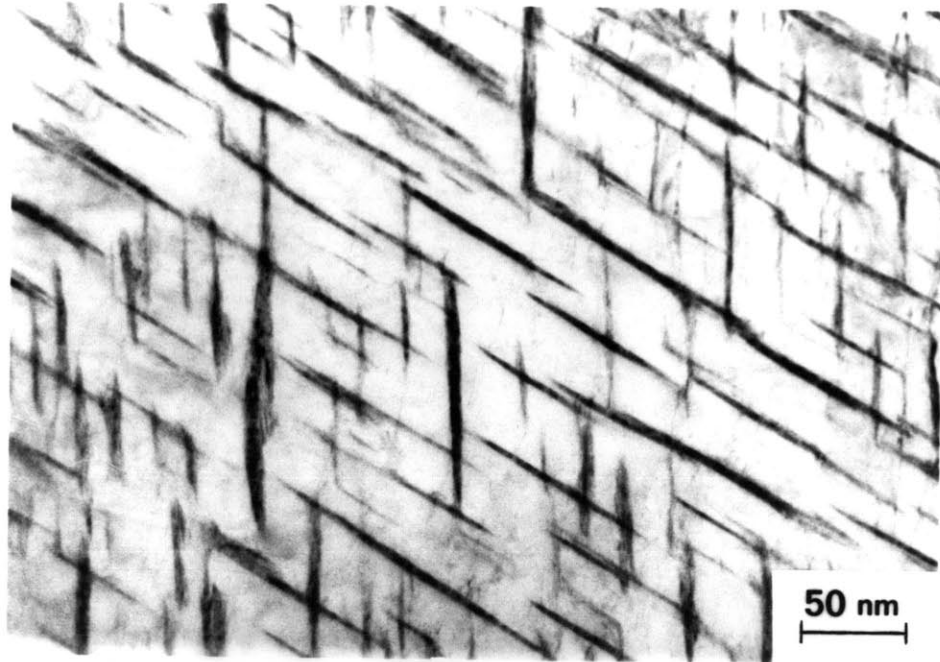
Figure 8-3. TEM micrographs showing transition carbides in Fe-25Ni-0.4C after tempering one hour at 150°C. (A) and (B) are bright- and dark-field images (respectively) of the same crystal. "MR", "M", and "RA" denote the midrib, adjacent martensite plates, and adjacent retained austenite, respectively.

Figure 8-4.   Dark-field micrograph of the same crystal as in Figure 8-3, but after slight tilting. The particles of irregular shape represent two additional orientation variants (see Figure 8-8). The positioning of the objective aperture is indicated by the circle in the diffraction pattern.

precipitate lattices; this point is exploited in Section 8.5. Generally, it seems easier to locate volumes of monovariant precipitation in samples tempered well into stage one. This suggests that some variants may coarsen at the expense of others, perhaps being influenced by local states of internal stress.

Single-surface trace analysis was performed on a number of micrographs in order to determine the habit plane of the carbides. Measurements were restricted to cases where the particles were near an edge-on orientation so that their trace was well-defined. The results are shown in the stereogram of Figure 8-5. Here, each great circle segment represents the projection of a line normal to the trace of a carbide habit plane. The c-axis of the parent martensitic phase was determined unambiguously for all micrographs. In all cases, the projected habit plane normal is close to the projection of one of the four <10$\underline{2}$> matrix directions. This near parallelism between the carbide habit plane and a {10$\underline{2}$}$_\alpha$ plane was alluded to above. No carbides were identified with a {12$\underline{0}$}-type habit plane, at least in non-twinned martensitic volumes.

8.2 Carbide Crystallography and Substructure

Electron diffraction was employed to study the crystal structure of the carbides. Patterns taken along several low-index zone axes of the martensitic structure are depicted in Figure 8-6. Within the limits of error, the carbide spot patterns can be indexed as ε-carbide; the accurate measurement of the deviation from the epsilon symmetry is precluded because the martensitic crystals do not exhibit the Kikuchi lines which are required to accurately orient a sample.

The reader will recall that the ε-carbide structure proposed by Jack [1] has iron atoms in a hexagonal configuration. Although the positions of

172
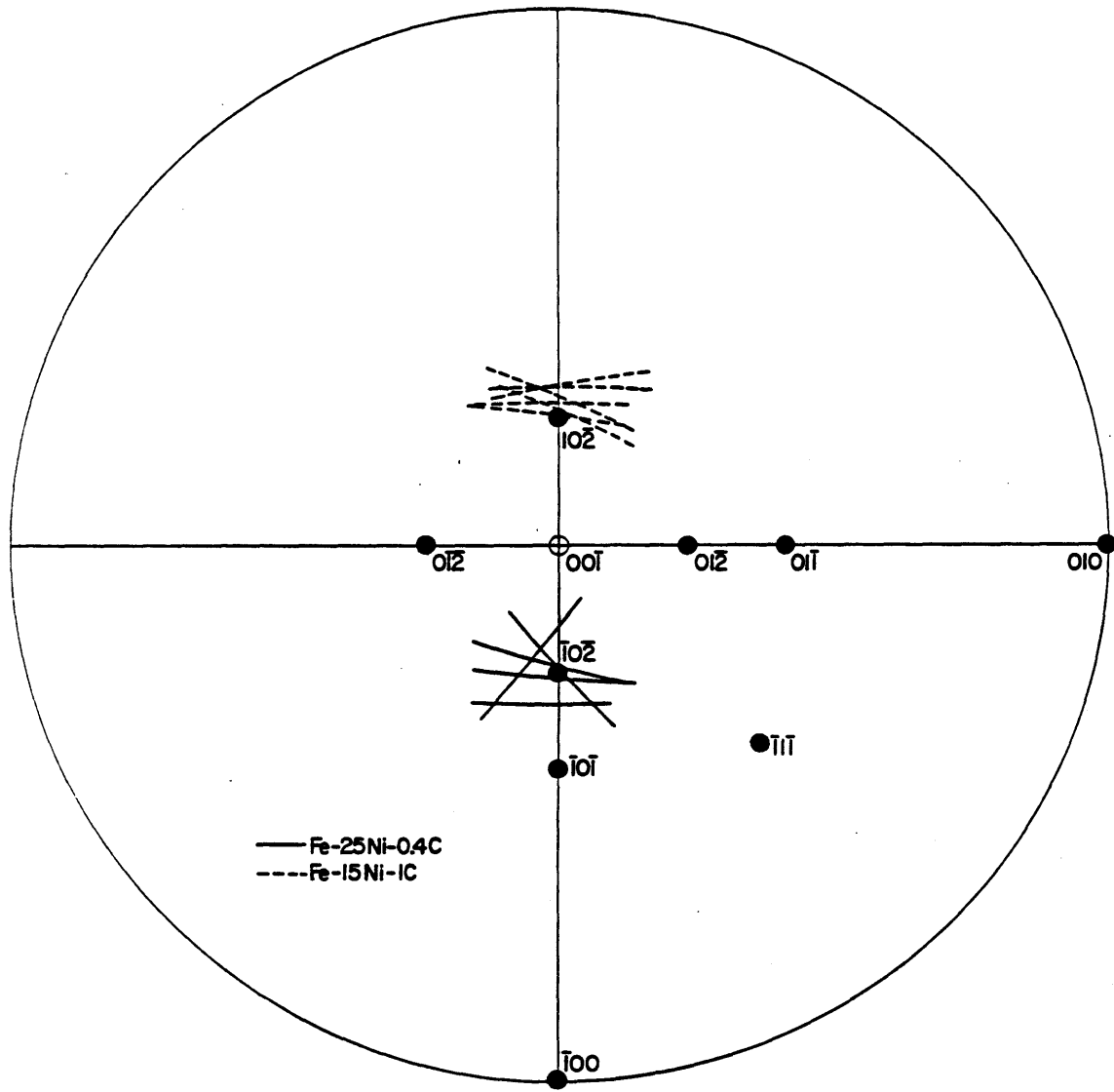
Figure 8-5. Cubic [001] stereogram showing projected carbide habit plane normals, as measured from a number of TEM micrographs. The four-fold rotational symmetry of the martensite c-axis was invoked to produce traces for each alloy which cluster about a single habit variant.

173
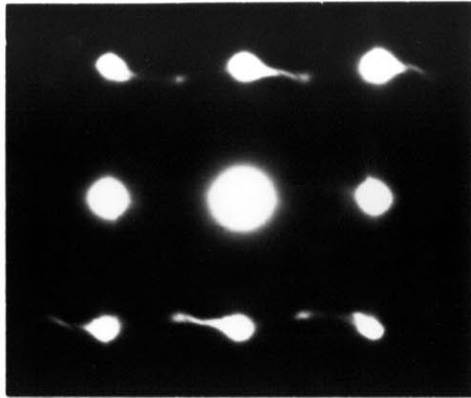
Fe-25Ni-0.4C
1 hr @ 100C + 118 days @ RT
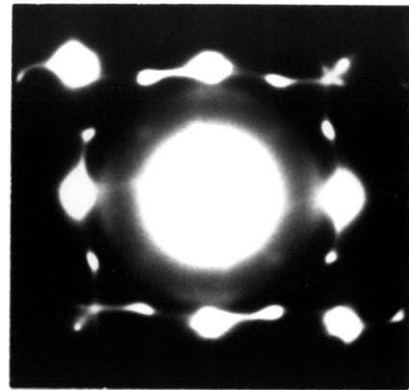
Fe-15Ni-1C
1 hr @ 150C + 15 months @ RT

$[100]_\alpha$

$[\bar{1}00]_\eta$
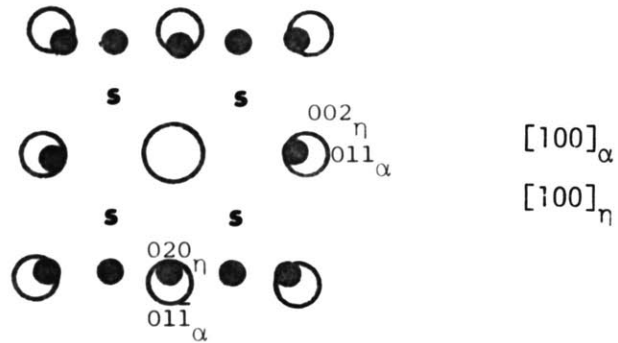
Figure 8-6. Indexed diffraction patterns from samples tempered into stage one. Open circles denote matrix reflections, small solid circles fundamental eta-carbide reflections, and "s" the positions of eta superlattice reflections. Beam directions and tempering treatments are indicated. Note that two carbide variants appear at a right angle in the $[100]_\alpha$ pattern for Fe-15Ni-1C.
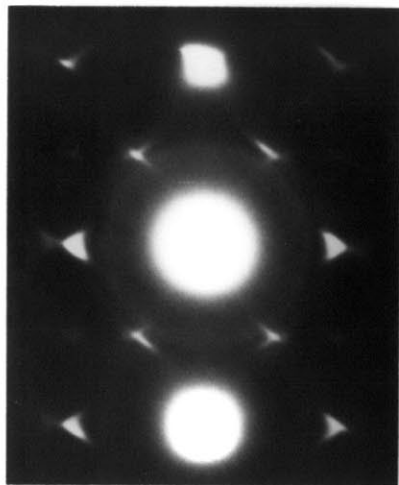
Fe-25Ni-0.4C
2 seconds at 175C
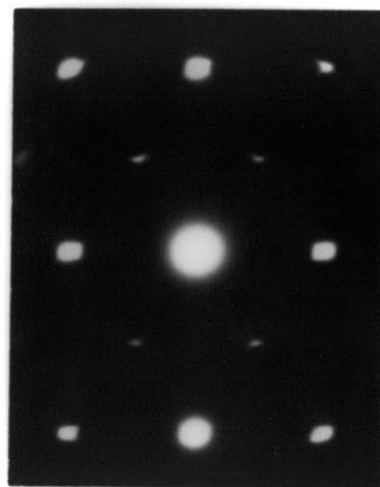
Fe-15Ni-1C
1 hr @ 90C + 25 days @ RT

200_α

$Pr[10\bar{2}]_\alpha$

$1\bar{1}0_\eta$

$Pr[\bar{1}0\bar{2}]_\alpha$

$o\bar{1}1_\alpha$

$[011]_\alpha$

$[001]_\eta$

$\bar{1}\bar{1}0_\eta$
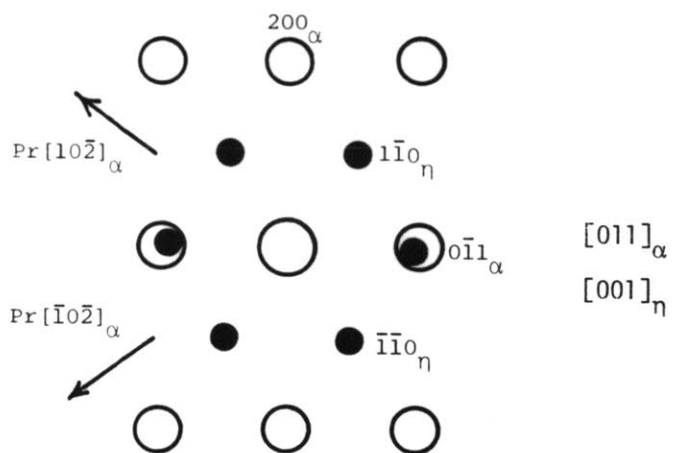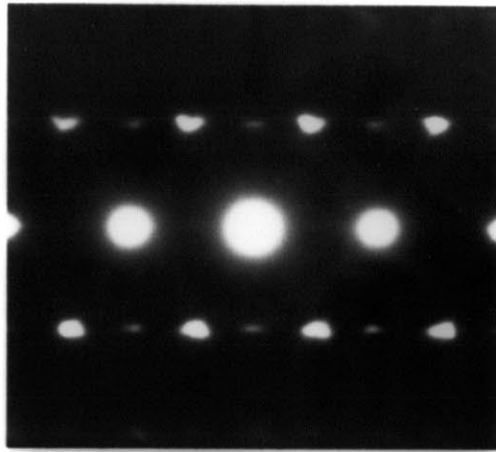
Figure 8-6 (cont.)

Fe-15Ni-1C/83 days at RT

$[111]_\alpha$
$[110]_\eta$
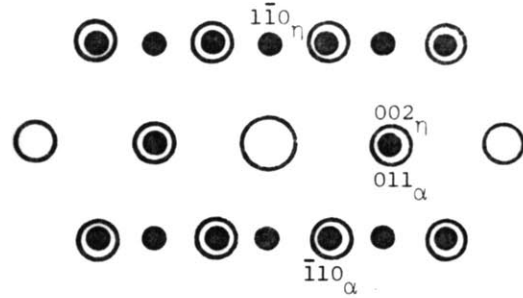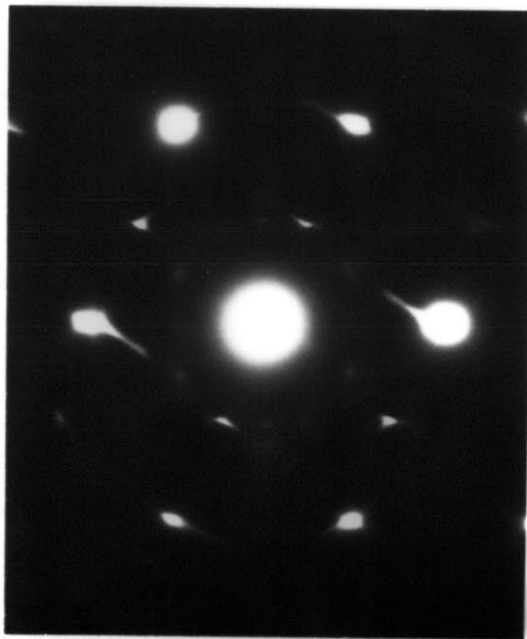
Fe-15Ni-1C/1 hr @ 125C + 30 days @ RT

$[1\bar{2}0]_\alpha$
$[1\bar{1}\bar{1}]_\eta$
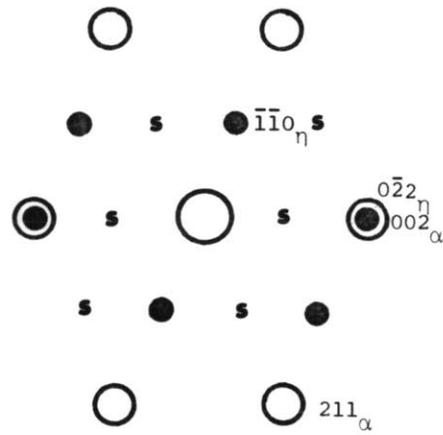
Figure 8-6 (cont.)

carbon atoms were not determined, Jack suggested that the carbide may exist

over a range of composition from Fe_2C to Fe_3C. A more recent structure

analysis by Hirotsu and Nagakura [52] indicates that the carbon atoms in

this phase may take on an ordered arrangement; they call the ordered phase

η-carbide in order to distinguish it from Jack's carbide. The structure of

η-carbide is shown schematically in Figure 8-7. The carbon-atom chains

along the $[100]_\eta$ direction produce a distortion which reduces the symmetry

of the iron-atom arrangement from hexagonal to orthorhombic. The ratio

b_η/a_η and its deviation from $\sqrt{3}$ (= 1.732) provide a measure of the

magnitude of the orthorhombic distortion. Previously measured lattice

constants of η-carbides [52,116-118] indicate that this distortion is

rather small in magnitude ($b_\eta/a_\eta \sim 1.64 - 1.72$) and therefore diffraction

patterns from η- and ε-carbide look very similar.

The preceding paragraph indicates that the structures of ε- and η-

carbide differ only in that the carbon interstitials are ordered in the

latter phase. The present author feels that this structural similarity

would be better emphasized by referring to the ordered phase as ε'-carbide,

rather than η-carbide. This is the convention which is followed in the

remainder of this thesis.

Note that in Figure 8-7 the c-axis for the ε'-carbide unit cell is

normal to the "basal"[*] plane. This choice of crystal axes differs from

previous investigations [52,116,117], but has the advantage of corresponding

directly to the orthohexagonal crystal axes for ε-carbide. Thus, the

Miller indices given in Figure 8-6 apply to both ε' and ε as long as one

remembers that the ε unit cell is taken to be orthorhombic (with $b_\varepsilon = \sqrt{3}a_\varepsilon$).

Basal is used in quotes to indicate that the $(001)_{\varepsilon'}$ plane is not a close-
packed plane having hexagonal symmetry, as is the case for the (001) plane
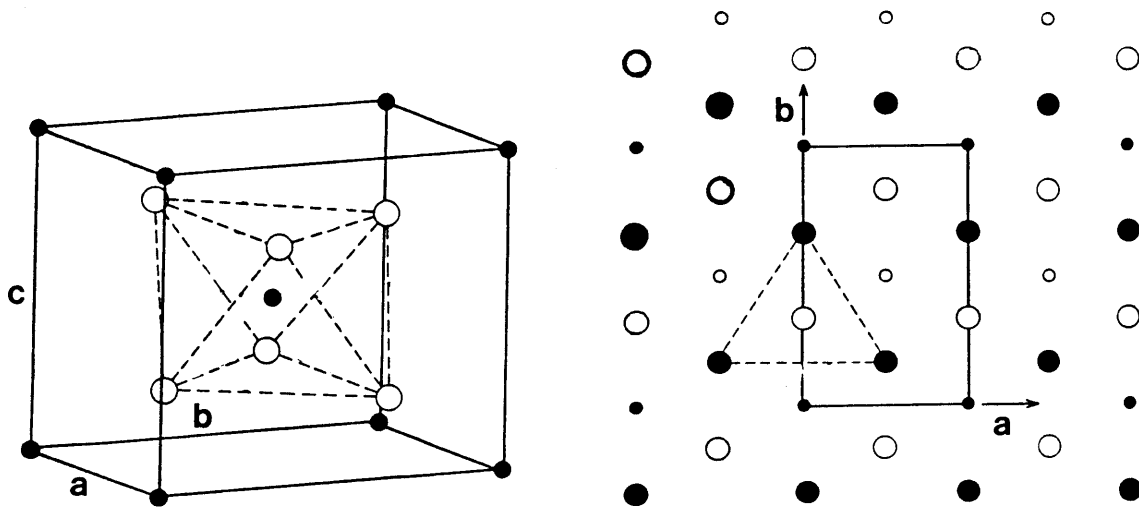
Figure 8-7. Schematic representation of the eta-carbide
structure, including a projection along c_η. Atom
positions are Fe: 1/2,1/6,1/4; 0,2/3,1/4; 0,1/3,3/4;
1/2,5/6,3/4; C: 0,0,0; 1/2,1/2,1/2 (from Hirotsu and
Nagakura [52]).

of a hexagonal lattice.
_____

In this investigation, lattice constants were calculated from the diffraction patterns of coarsened carbides. Since carbide and matrix spot patterns invariably overlapped, the camera constant could be calculated for each pattern from the known interplanar spacings of the low-carbon martensitic matrix. For carbides precipitated in Fe-25Ni-0.4C, a = 0.273 nm, b = 0.457 nm, c = 0.437 nm (and b/a = 1.674). For Fe-15Ni-1C, a = 0.276 nm, b = 0.463 nm, c = 0.438 nm (and b/a = 1.678). The accuracy is estimated to be ±0.003 nm. The current lattice constants are in good agreement with those measured by Hirotsu et al. [119] on similar alloys, except the b parameter for Fe-25Ni-0.4C is about 2% smaller than the value reported by Hirotsu et al. for Fe-24Ni-0.33C.

The measured b/a is about 3% smaller (in both alloys) than the ideal value ($\sqrt{3}$) for a hexagonal structure. Therefore, the transition carbide will be referred to as ε'-carbide in subsequent discussion, recognizing that the carbides exhibit an orthorhombic distortion which is presumably produced by carbon ordering. However, no superlattice reflections attributable to carbon ordering were detected in any diffraction patterns. This indicates that the carbides may not be fully-ordered. Interplanar spacings and structure factors for a number of low-index ε'-carbide reflections are listed in Table 8-1.

Tanaka and Shimizu (T-S) [117] report the following orientation relation between the martensitic matrix and ε'-carbide:

$$(001)_{\varepsilon'} \ || \ (011)_{\alpha}$$
and $\qquad [100]_{\varepsilon'} \ || \ [100]_{\alpha}.$

This is analogous to that proposed by Jack for the hexagonal ε-carbide. It

TABLE 8-1

INTERPLANAR SPACINGS AND STRUCTURE FACTORS FOR THE ε'-CARBIDE PHASE
IN FE-15NI-1C

hkl*	d(nm)	$\lvert F \rvert^{2**}$	hkl*	d(nm)	$\lvert F \rvert^{2**}$
011(s)	.318	22.3	220(f)	.119	10.6
110(f)	.237	32.1	202(f)	.117	62.9
101(s)	.234	14.1	040(f)	.116	10.1
020(f)	.231	31.0	132(f)	.115	60.6
002(f)	.219	201.3	221(f)	.114	63.9
111(f)	.208	214.6	123(s)	.113	2.1
021(f)	.205	206.7	041(f)	.112	60.7
121(s)	.164	6.3	004(f)	.110	102.5
112(f)	.161	82.2	033(s)	.106	1.7
022(f)	.159	80.4	222(f)	.104	28.6
031(s)	.146	4.5	141(s)	.104	1.5
013(s)	.139	3.9	042(f)	.102	27.0
200(f)	.138	177.4	231(s)	.100	1.3
130(f)	.135	167.8	114(s)	.099	7.3
103(s)	.129	3.1	024(s)	.099	7.2
211(s)	.127	2.9	213(s)	.098	1.2
113(f)	.124	76.0	223(f)	.092	36.7
023(f)	.123	75.0	043(f)	.091	35.3

*Superlattice reflections are denoted by "s," fundamentals by "f."

**The units are (Angstrom)^2. Atomic scattering amplitudes were
interpolated from the tabulated values in Reference [79],
based on relativistic 200 kV electrons.

is also closely related to the relations proposed by Hirotsu and Nagakura [52] and by Shimizu and Okamoto [116] (for ε'-carbide) by slight rotations about the [100] axis. The T-S relation features parallelism between the carbide "basal" plane and the densely-packed $(011)_\alpha$ plane. The diffraction patterns of Figure 8-6 are consistent with the T-S orientation relation, although the similarity between the T-S, H-N, and S-O relations and the inability to accurately orient samples made a discrimination between the three relations impossible.

Figure 8-8, an enlargement of part of the area shown in Figure 8-4, reveals a peculiar contrast from the carbide particles of irregular projected shape. These particles, oriented such that their "basal" plane is nearly parallel to the electron beam, exhibit striations along the trace of the basal plane. The striations are spaced about 1.0 to 1.5 nm apart in both Fe-Ni-C alloys and probably represent faulting on the carbide basal plane. Diffraction patterns from striated carbides exhibit streaking along the $[001]_{\varepsilon'}$ direction. This was also noted in the early TEM study done by Tekin and Kelly [120]; they too suggested that faulting had occurred, but were not able to resolve the substructure. For the two variants of Figure 8-8, the basal planes are nearly parallel to $(011)_\alpha$ and $(01\bar{1})_\alpha$. In fact, the carbide basal plane was always found to be nearly parallel to a martensitic $\{01\underline{1}\}$ plane; none in this study was identified as having a basal plane parallel to a $\{11\underline{0}\}_\alpha$ plane. This feature undoubtedly reflects the tetragonal symmetry of the parent aged martensite, where the $\{01\underline{1}\}$ and $\{11\underline{0}\}$ planes are not equivalent.

8.3 Effect of Martensitic Substructure on Precipitation Behavior

Just as spinodal decomposition occurs throughout the martensitic phase
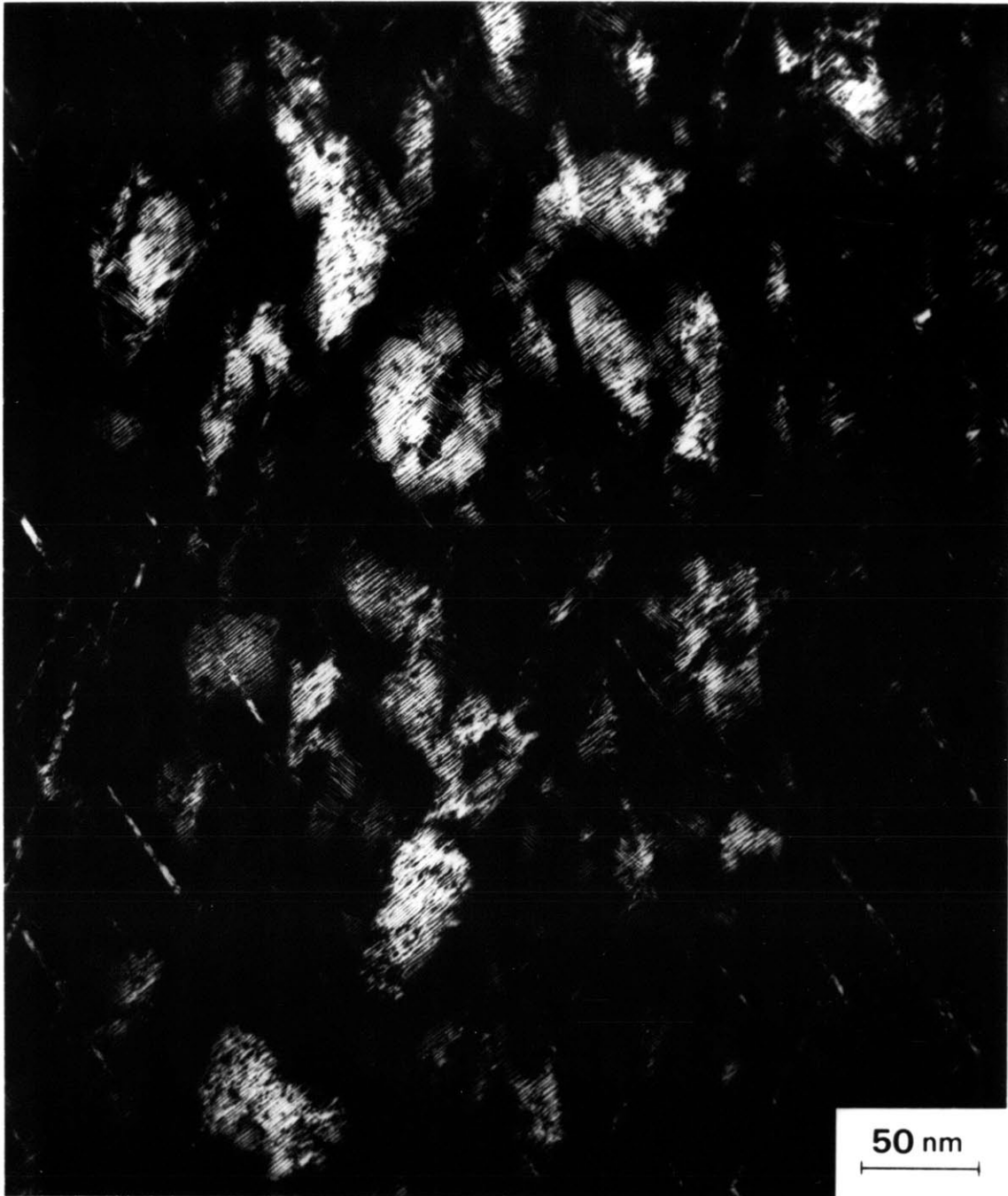
Figure 8-8. Enlargement of Figure 8-4 showing the two carbide variants with their "basal" planes nearly parallel to the electron beam.

during the early stages of aging, so too does subsequent precipitation of the transition carbide. This statement applies to all of the alloys of the present study. Figure 8-9 shows that precipitation even occurs in the finely-twinned volumes comprising the midrib. In volumes twinned on $\{11\underline{2}\}_\alpha$, two carbide variants which appear to be related by the correspondence dictated by the matrix (martensite) twinning operation can often be identified, Figure 8-10.

Figure 8-11 shows at least two carbide variants at the [100] orientation. The diffraction pattern reveals two $\{100\}_{\varepsilon'}$ spot patterns which lie at nearly a right angle and represent two variants of the T-S orientation relation. Surprisingly, two variants light up in each of the dark-field micrographs, even though only a single reflection appears to contribute to each image. Each dark-field image apparently includes two variants which have parallel basal planes (and overlapping spot patterns) and habit plane normals which lie roughly at right angles in the projected image. This morphology suggests that the two variants in each dark-field micrograph are related by (011) twinning in the parent phase. Such twinning leaves the carbide basal plane essentially invariant; however, the projected $\{10\underline{2}\}_\alpha$ habit plane normal (which lies at 45° to the twinning plane) is rotated by 90°.

There are some indications that $\{11\underline{2}\}$ twin boundaries may provide sites for the early (heterogeneous) nucleation of transition carbides. In fact a previous AP/FIM study [74] detected some carbon segregation to such boundaries during aging at room temperature. A [111] diffraction pattern from a twinned volume of Fe-15Ni-1C after aging one hour at 60°C is shown in Figure 8-12. The twin reflections overlap with the matrix reflections, but other spots also appear. These lie roughly midway between the
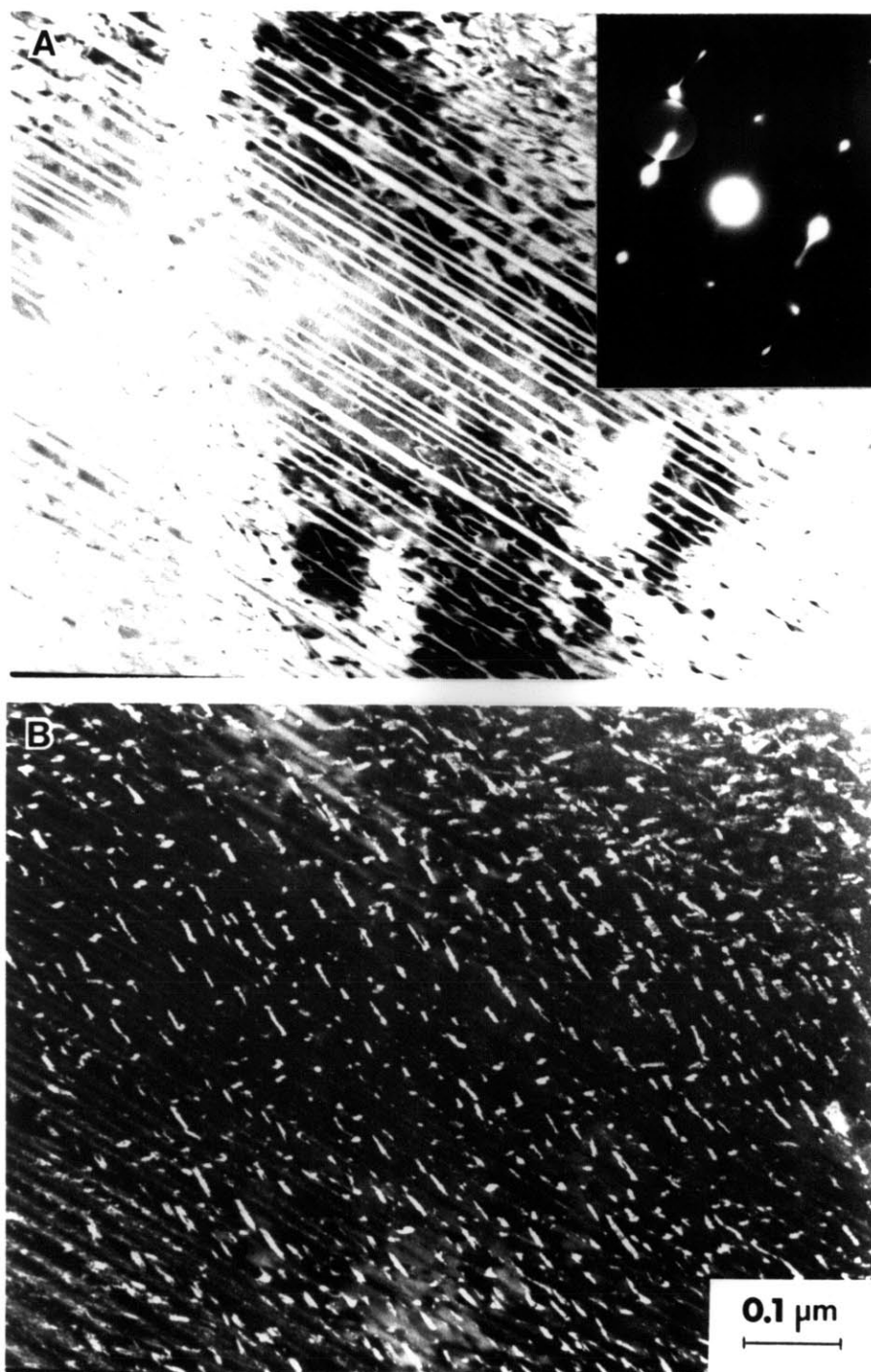
Figure 8-9. Carbide precipitation in the midrib of martensitic
Fe-25Ni-0.4C. This bright-field (A)/dark-field (B)
pair was taken after tempering one hour at 100°C,
plus 118 days at room temperature. The positioning
of the objective aperture is indicated by the circle
in the diffraction pattern.
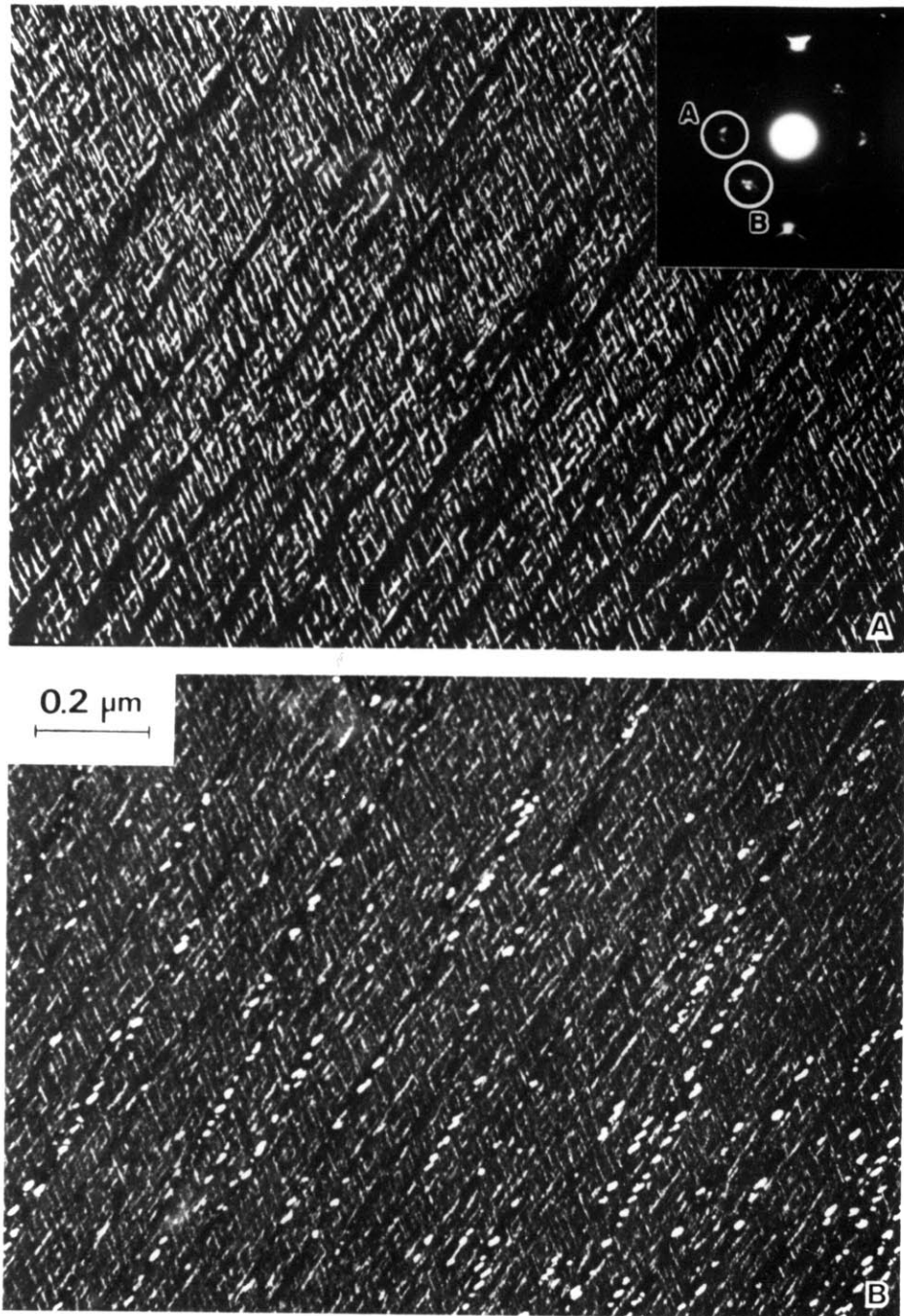
Figure 8-10. Carbide precipitation in a twinned volume of the Fe-15Ni-1C alloy, after one-hour at 100°C plus 500 days at room temperature. Families in a Widmanstatten pattern (A) and (B) and/or "blocky" carbides in {11$\underline{2}$} transformation twins (B) can be imaged, depending on the reflections used to form the image (indicated in the diffraction pattern).
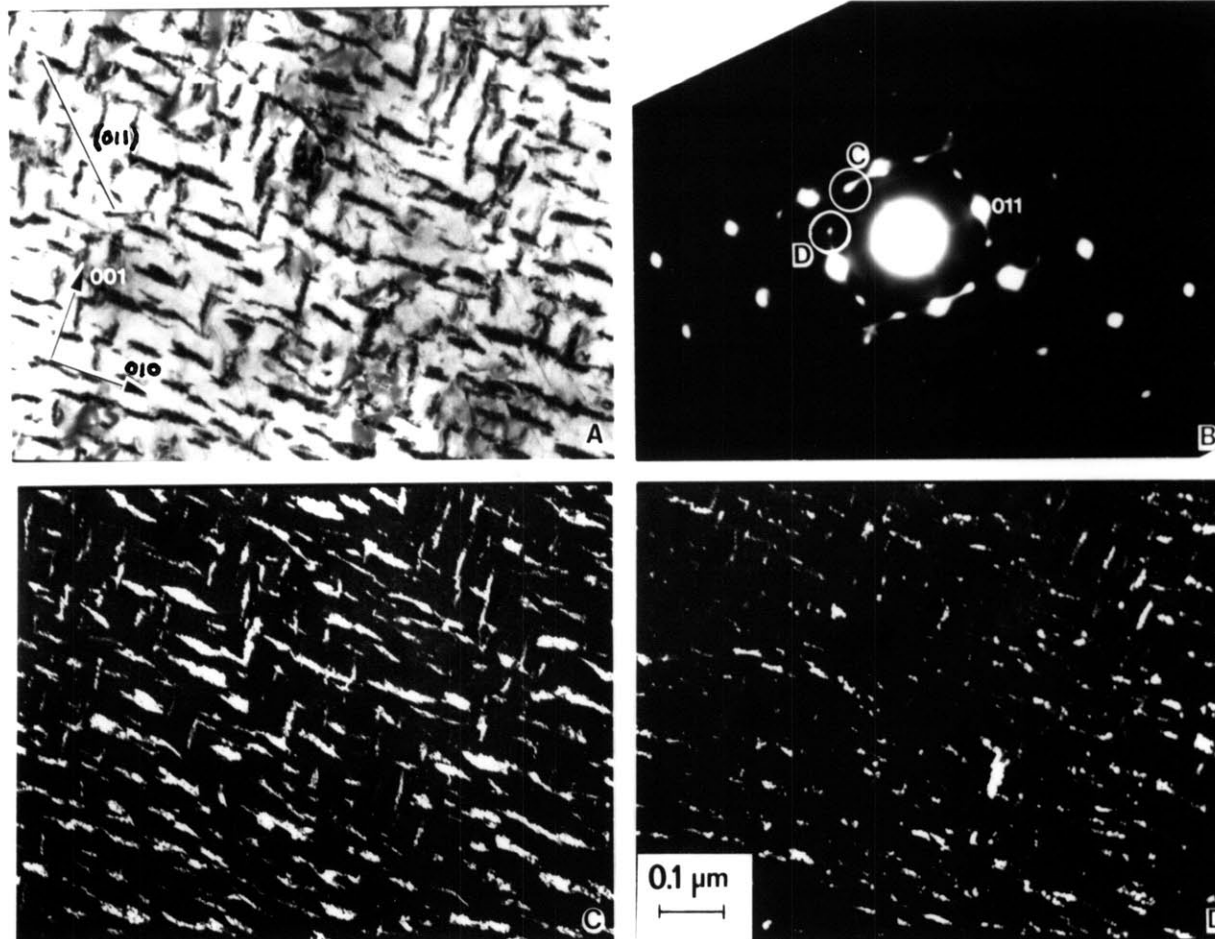
Figure 8-11. Carbides in Fe-15Ni-1C which appear to be related by (BCT) twinning on $(011)_\alpha$. The specimen was tempered one hour at 150°C, plus 15 months at room temperature; the beam direction is near $[100]_\alpha$. The circled reflections in the diffraction pattern (B) were used to form the dark-field images (C) and (D). The particles along $[010]_\alpha$ have the $(10\bar{2})$ habit, while those along $[001]_\alpha$ have the (120) habit, related to the former by the twinning on (011).
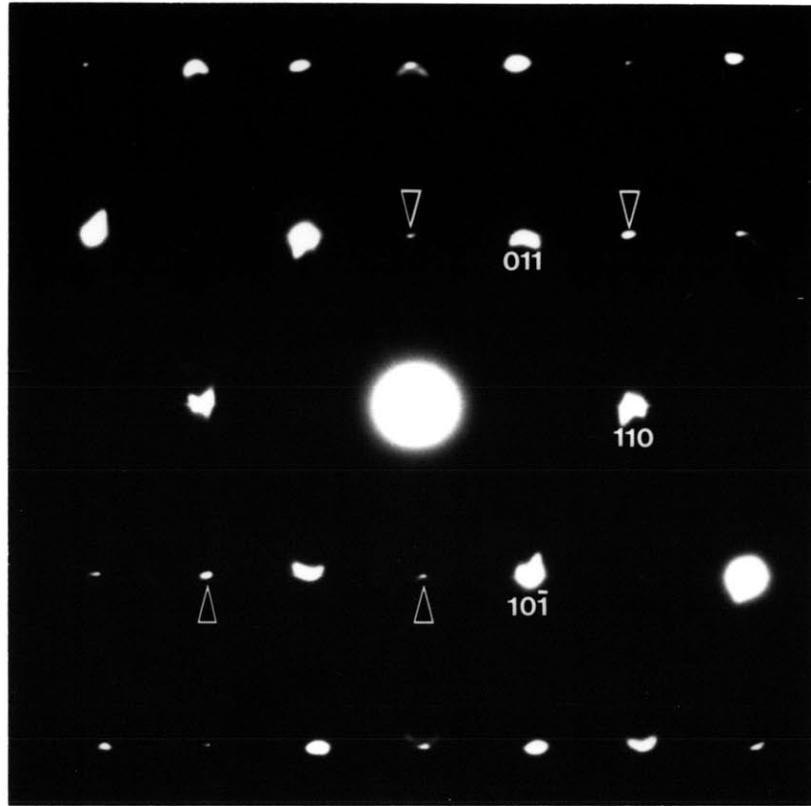
Figure 8-12. [111] diffraction pattern from Fe-15Ni-1C after aging
one hour at 60°C. Spots indicated by arrows cannot
be explained by twinning and may be due to epsilon-
martensite or epsilon-carbide.

matrix/twin spots along the [110] direction, at the positions where spots should appear for the transition carbide. Diffraction patterns like Figure 8-12 were even observed from freshly-quenched samples, which suggests that the "extra" spots may be due to the presence of some HCP epsilon-martensite in the midrib. Such a defect can be looked upon as low-carbon ε-carbide. However, direct attempts to detect the early carbide particles or films by dark-field microscopy were unsuccessful.

The $\{112\}_\alpha$ twin boundaries frequently appear to act as barriers to carbide growth. For example, the twin-related carbides in Figure 8-10 do not cross the twin boundaries. This indicates that the coherency between ε'-carbide and the martensite is difficult to maintain if growth proceeds across such twin boundaries.

Line defects do not appear to play a significant role in the nucleation of transition carbides; no nucleation was directly observed on dislocations, although in practice it is difficult to deduce where a particle was nucleated once it has grown to a size detectable by microscopy. Also, no precipitation was observed at the martensite/austenite interface.

8.4 Application of the Bowles-MacKenzie Crystallographic Theory to ε'-Carbide

The plate-like shape of the transition carbide indicates that the transformational strain energy may play an important role in its growth. In general, the strain energy for a plate-like particle is a minimum when its habit plane is an invariant plane [38]. Several mathematical procedures have been developed to analyze the crystallography of invariant-plane strain (IPS) transformations [35-37]. The approach put forth by Bowles and MacKenzie [36] was applied to the ε'-carbide in order to make

detailed predictions of the crystallographic observables of this phase. First, the principles behind the crystallographic analysis are briefly discussed. The assumptions, input, and results for the present BCC → orthorhombic transformation are then presented. The results of the analysis will prove to be consistent with experiment and have important implications regarding the heterogeneous carbide nucleation as well as the growth kinetics. These aspects are covered later in Section 8.5.

In describing a structural change in which some degree of interfacial coherency is maintained, one can always relate the parent and product lattices by a homogeneous deformation, or lattice deformation. However, there is generally no plane in the product lattice which contains exactly the same distribution of lattice points as any plane in the parent lattice. An IPS is therefore not realizable under such a circumstance, unless an inhomogeneous deformation (such as slip or twinning) occurs in order to maintain some plane at least macroscopically invariant. This is a key assumption upon which the crystallographic theories rest. The fundamental equation which the theories exploit can be expressed (in matrix form) as

$$\mathbf{E} = \mathbf{RBP}, \tag{8-1}$$

where $\mathbf{E}$ is the shape deformation, $\mathbf{R}$ is a rigid body rotation, $\mathbf{B}$ is the lattice deformation, and $\mathbf{P}$ is the inhomogeneous shear. That some kind of shear operation occurs during the first stage of tempering is convincingly demonstrated by the surface upheavals produced on pre-polished specimen surfaces, Figure 8-13.

The striations in TEM images of the ε'-carbide indicates an internal shear deformation which makes an IPS possible. In the present case, the shear occurs on the $(001)_{\varepsilon'}$ plane, which is apparently derived from a

189

100 μm
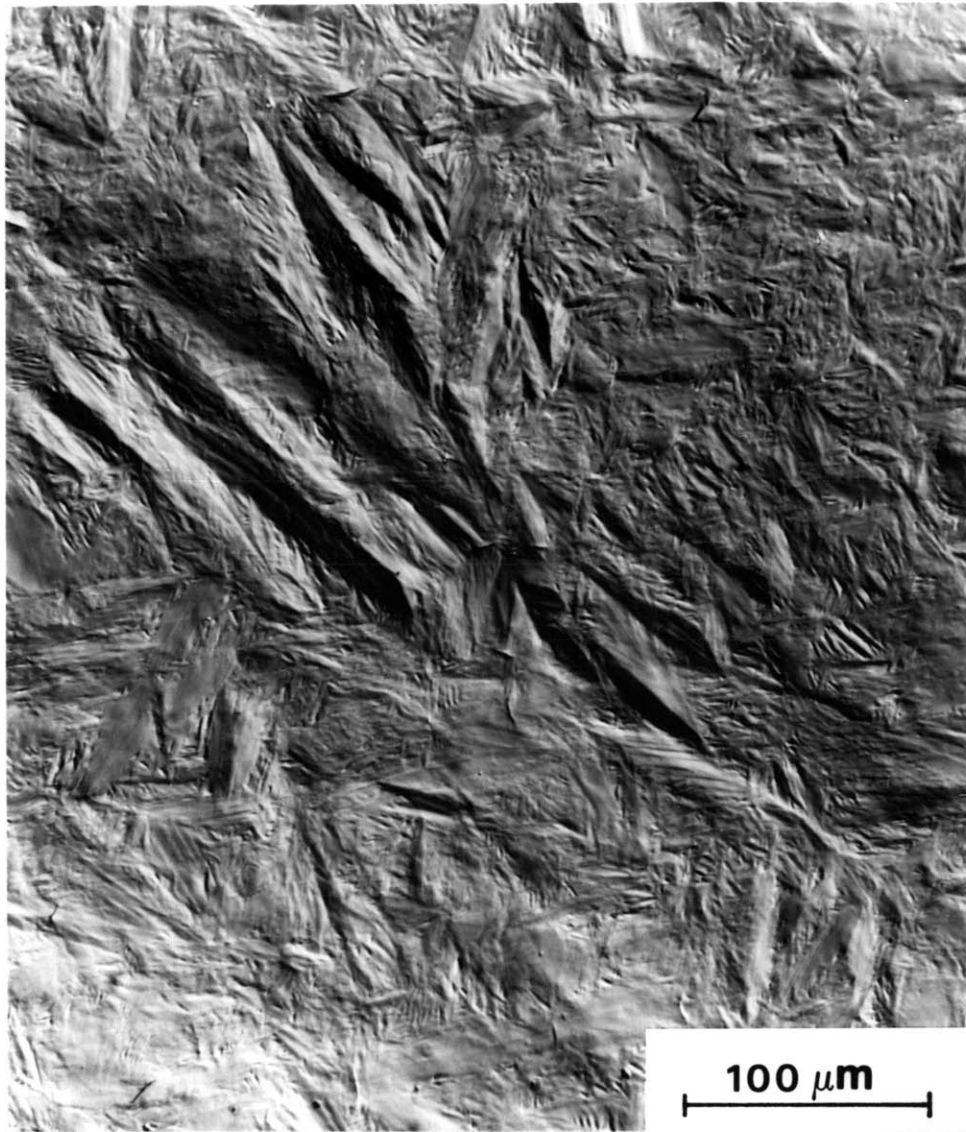
Figure 8-13. Surface relief (interference contrast) on a
sample of Fe-15Ni-1C which was polished before
tempering 24 hours at 150°C.

$\{01\underline{1}\}_\alpha$ plane. The defect contrast within the carbide particles indicates that the shear vector is not a lattice vector, and therefore the accommodation mechanism is not a true lattice-invariant deformation. Accordingly, such faulting will be referred to as an "internal accommodation deformation."

A detailed discussion of the principles behind the crystallographic theories is not possible in this thesis. The reader is referred to Cohen and Wayman [8] for an excellent overview. The Bowles-MacKenzie (B-M) method is described in detail, with a numerical example, by both Wayman [121] and Nishiyama [7]. Since the B-M analysis involves a long series of matrix algebra calculations, a computer program described by Ledbetter and Wayman [122] was used here to eliminate human error. The input required by the program and the results for ε'-carbide are reported in the following sections.

8.4.1 Lattice Deformation

A lattice deformation can be visualized most easily by considering how a general distortion deforms a sphere of unit radius, Figure 8-14. The general case distorts the sphere into an ellipsoid with three unequal semi-axes. When at least one of the semi-axes is greater than unity and at least one other is less than unity, the sphere and the ellipsoid then intersect, defining a right elliptic cone with its apex at the origin. This cone is referred to as the "final cone of unextended lines," since vectors on the cone remain at unit length after the lattice deformation. An additional cone is defined by the same vectors when the ellipsoid is allowed to relax back into the shape of a sphere. This latter cone represents the initial positions of the vectors which define the final cone and, not surprisingly, is called the "initial cone of unextended lines."
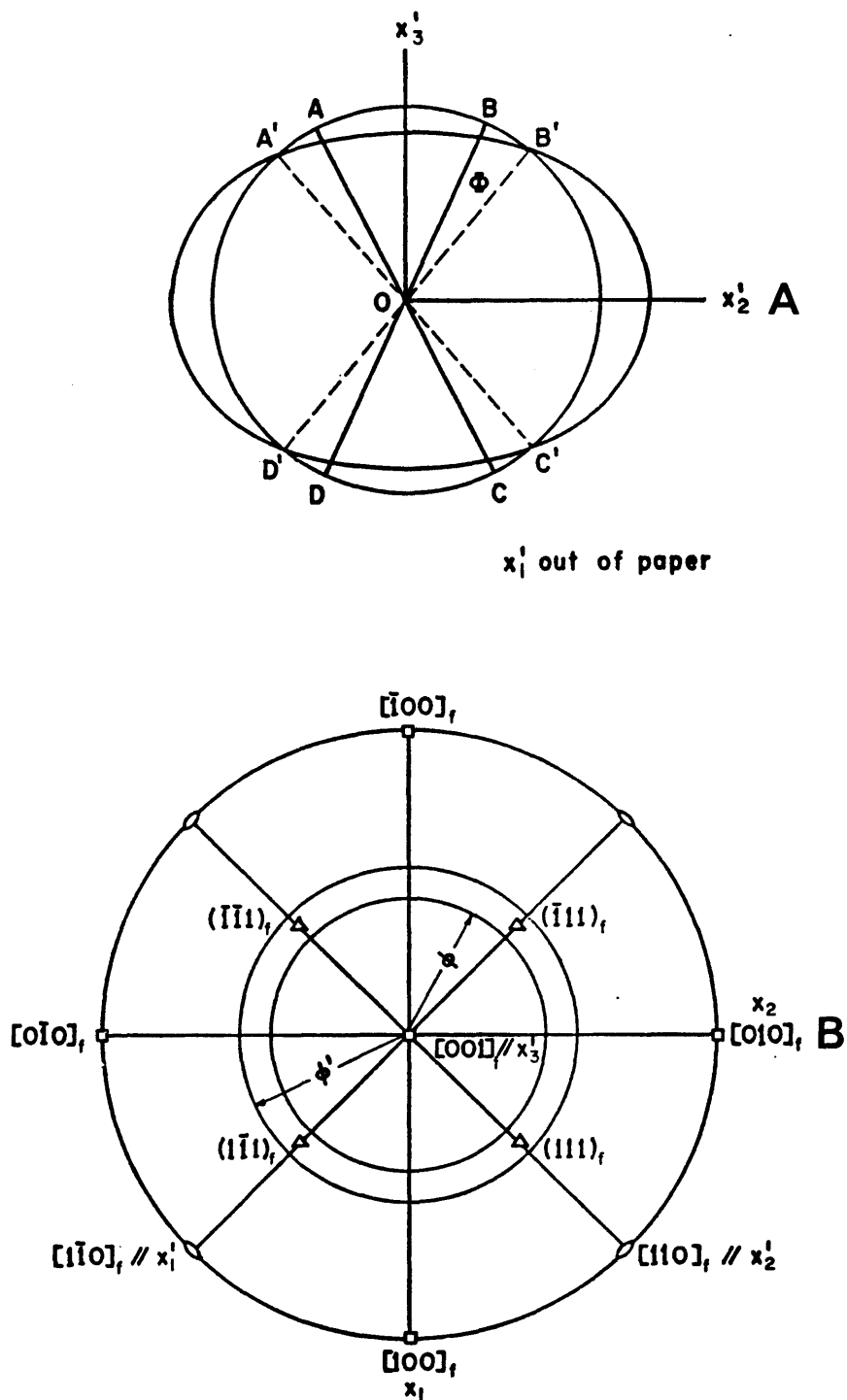
Figure 8-14. Illustration of how a distortion deforms a sphere. Referred to the principal axes of the distortion (x_i'), the sphere becomes an ellipsoid. In (A) the cones of unextended lines and plane normals are indicated (in projection) by AC/BD and A'C'/B'D', respectively. The initial and final cones of unextended lines for the FCC → BCC lattice deformation in an Fe-Ni-C alloy are shown in (B). The cones are circular here because of the tetragonal lattice deformation. Both figures are from Reference [121].

192

The initial and final cones may be viewed in an alternative way: the initial cone defines the final locus of vectors which are normal to planes whose spacing is unaltered by the lattice deformation. Similarly, the final cone represents the initial position of these plane normals. Thus, the initial and final cones of unextended lines are also referred to as the final and initial "cones of unextended plane normals," respectively.

The B-M and other crystallographic theories assume that a lattice correspondence exists between the parent and product phases. In other words, any direction or plane of the product lattice is derived from a uniquely determined direction or plane of the parent lattice. This can be stated formally by the matrix expression

$$\mathbf{b} = (bCo)\mathbf{o}, \qquad (8-2)$$

where $\mathbf{b}$ is a vector of the parent lattice, $\mathbf{o}$ is a vector of the product lattice, and (bCo) is a 3x3 matrix which describes the lattice correspondence. The choice of a specific lattice correspendence is the important first step in the crystallographic analysis. Experimentally determined orientation relations and/or structural features of the two phases frequently make the choice rather obvious. As indicated in Figure 8-15, the distortion which converts the parent BCC lattice into an orthorhombic ε'-carbide lattice (the "b" and "o" lattices, respectively) can be described simply by expansions along the $[011]_\alpha$ and $[01\bar{1}]_\alpha$ directions and a contraction along $[100]_\alpha$. The following correspondence matrix then relates directions between the two structures:

$$(bCo) = \begin{bmatrix} 1 & 0 & 0 \\ 0 & 1 & 1 \\ 0 & \bar{1} & 1 \end{bmatrix}. \qquad (8-3)$$
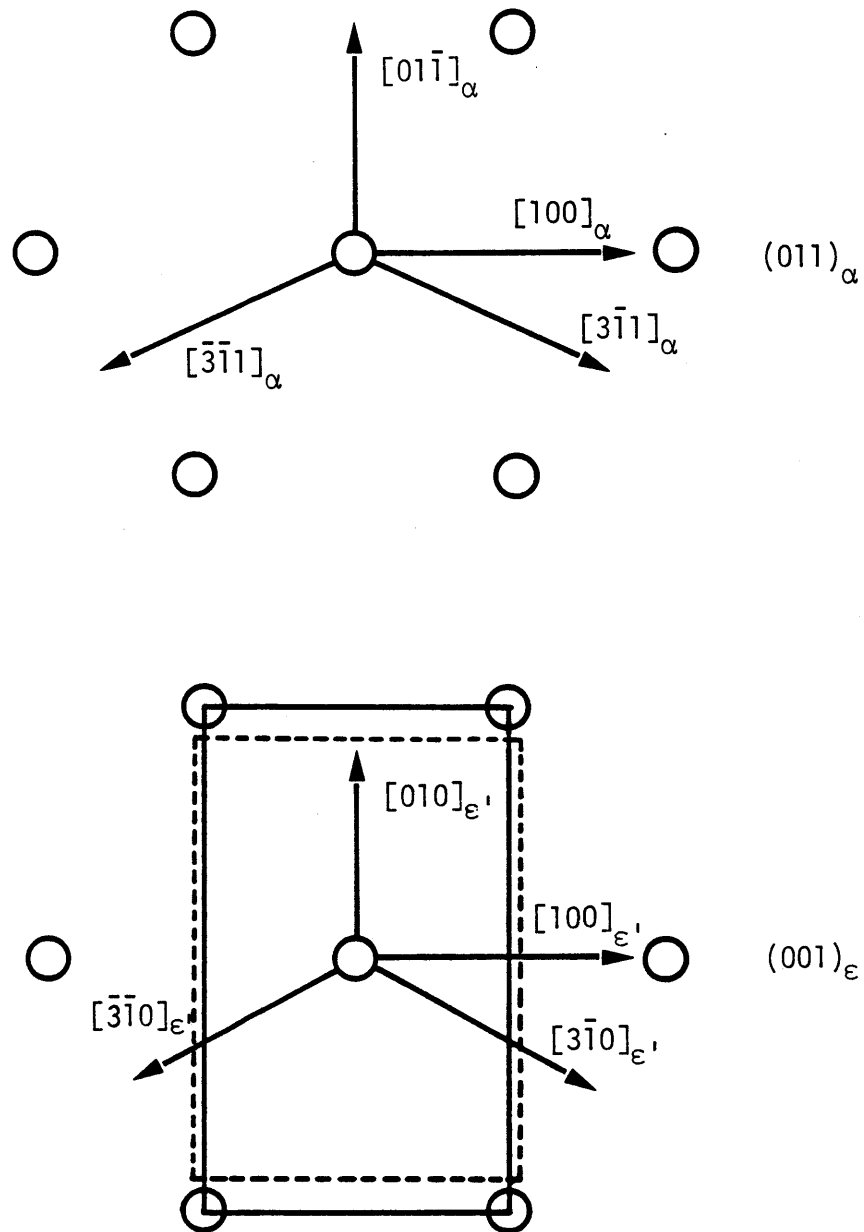
Figure 8-15. Metal-atom arrangement on $(011)_\alpha$ and $(001)_{\epsilon'}$ indicating the correspondence between the two lattices. The distortions which convert the BCC lattice constants into those for the orthorhombic carbide consist of expansions along $[011]_\alpha$ (normal to the paper) and $[01\bar{1}]_\alpha$, and a contraction along $[100]_\alpha$. These transform the dashed rectangle into the solid rectangle (lower figure). The magnitudes of the distortions are given in Table 8-2.

This lattice correspondence is consistent with the T-S orientation relation and intuitively seems to involve the smallest principle strains. Note, however, that shuffling of metal atoms is required on alternate $(011)_\alpha$ planes in order to achieve the kind of stacking described by the ε' structure.

The normalized vectors parallel to the principal axes of the distortion define the eigenvectors of the lattice deformation. These are essential ingredients in the crystallographic analysis; the eigenvectors are parallel to the $[100]_\alpha$, $[01\bar{1}]_\alpha$, and $[011]_\alpha$ directions in the present case. One must also input the magnitude of the principal distortions, η_i (the eigenvalues). These represent the ratio of the final to the inital length of each eigenvector (i.e. the semi-axes of the ellipsoid) and are calculated directly from the measured lattice constants for the two phases. The eigenvalues which apply for the two Fe-Ni-C alloys of this study are given in Table 8-2. These are based on the measured lattice constants for ε'-carbide and for tempered (cubic) martensite.

8.4.2 Internal Accommodation Deformation

The cones for the lattice deformation define two ellipses on the stereograms of Figure 8-16. The trace of a possible accommodation shear plane, $(011)_\alpha$, is also included. The intersection of the shear plane (p_2) with the initial cone of unextended lines defines two invariant lines, x_1 and x_2. Similarly, two invariant plane normals are defined by the intersection of the plane normal to the shear direction (d_2) and the final cone of unextended lines. If a chosen shear direction produces no such intersection, then an IPS cannot be realized under such a shear operation.

The real displacement vector which describes the faulting in ε'-carbide could not be readily determined because of the difficulties

195

TABLE 8-2

EIGENVALUES FOR THE BCC → ε'-CARBIDE LATTICE DEFORMATION

Alloy	Lattice Constants (nm)		Eigenvalues		
	BCC[*]	ε'	η_1	η_2	η_3
Fe-25Ni-0.4C	$a_o=0.2867$	a=0.273	0.952215	1.127129	1.077801
		b=0.457			
		c=0.437	$= \dfrac{a}{a_o}$	$= \dfrac{b}{\sqrt{2}a_o}$	$= \dfrac{c}{\sqrt{2}a_o}$
Fe-15Ni-1C	$a_o=0.2870$	a=0.276	0.961672	1.140733	1.079139
		b=0.463			
		c=0.438			

[*]Based on the BCC x-ray pattern produced after tempering 110 hours at 125°C.

196
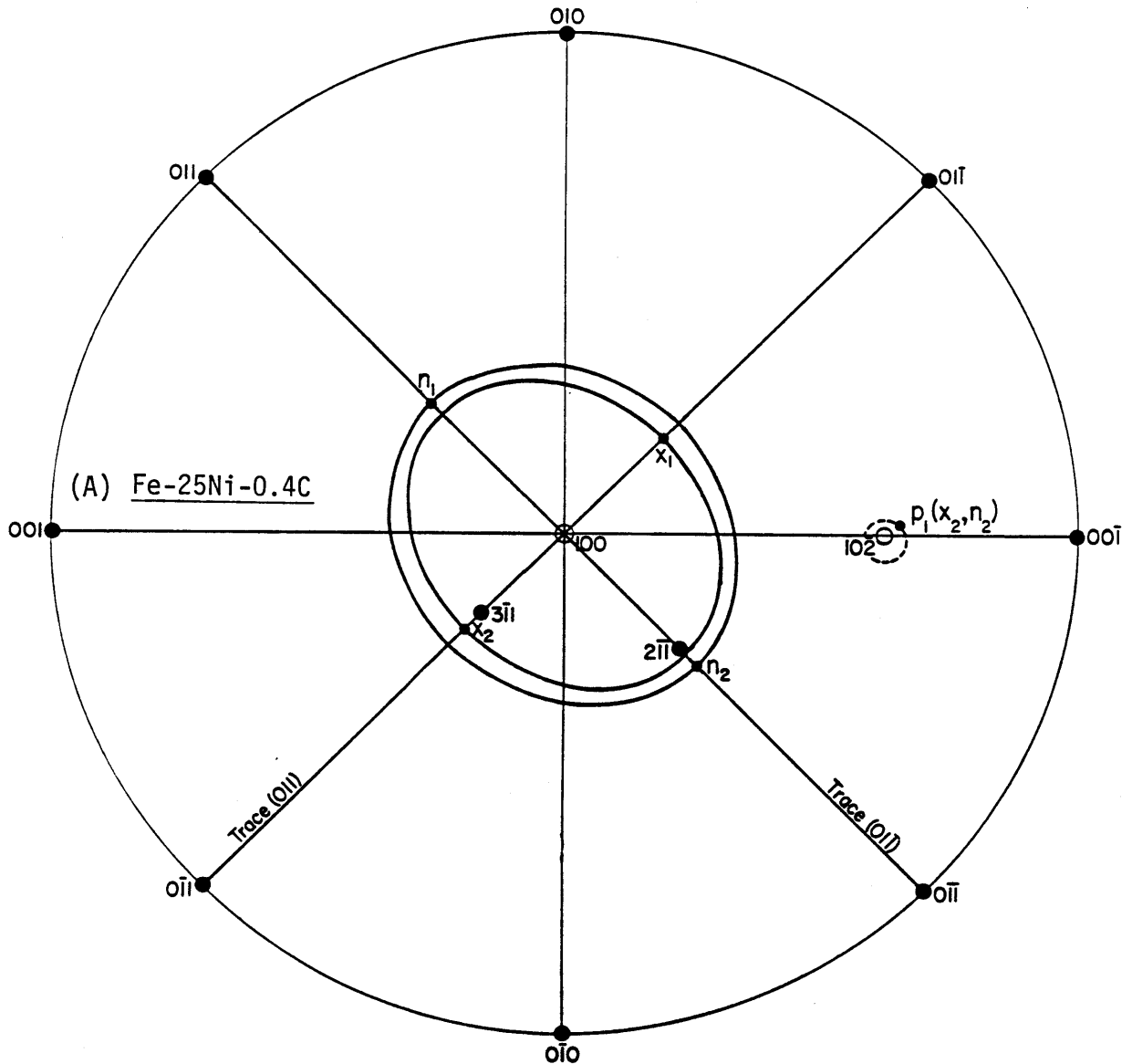
Figure 8-16. Cubic [100] stereogram depicting the initial and final cones
for the BCC → ε'-carbide lattice deformation in Fe–25Ni–0.4C
(A) and Fe–15Ni–1C (B). The intersection of the internal
shear plane and the initial cone defines the invariant lines
(x_i). The intersection of the plane normal to the internal
shear direction and the final cone defines the invariant
normals (n_i). The habit plane normal corresponding to the
$[3\bar{1}1]$ invariant-line and $[2\bar{1}\bar{1}]$ invariant-normal is designated
by "$p_1(x_2,n_2)$".

(B) Fe-15Ni-1C

Figure 8-16 (cont.)

198
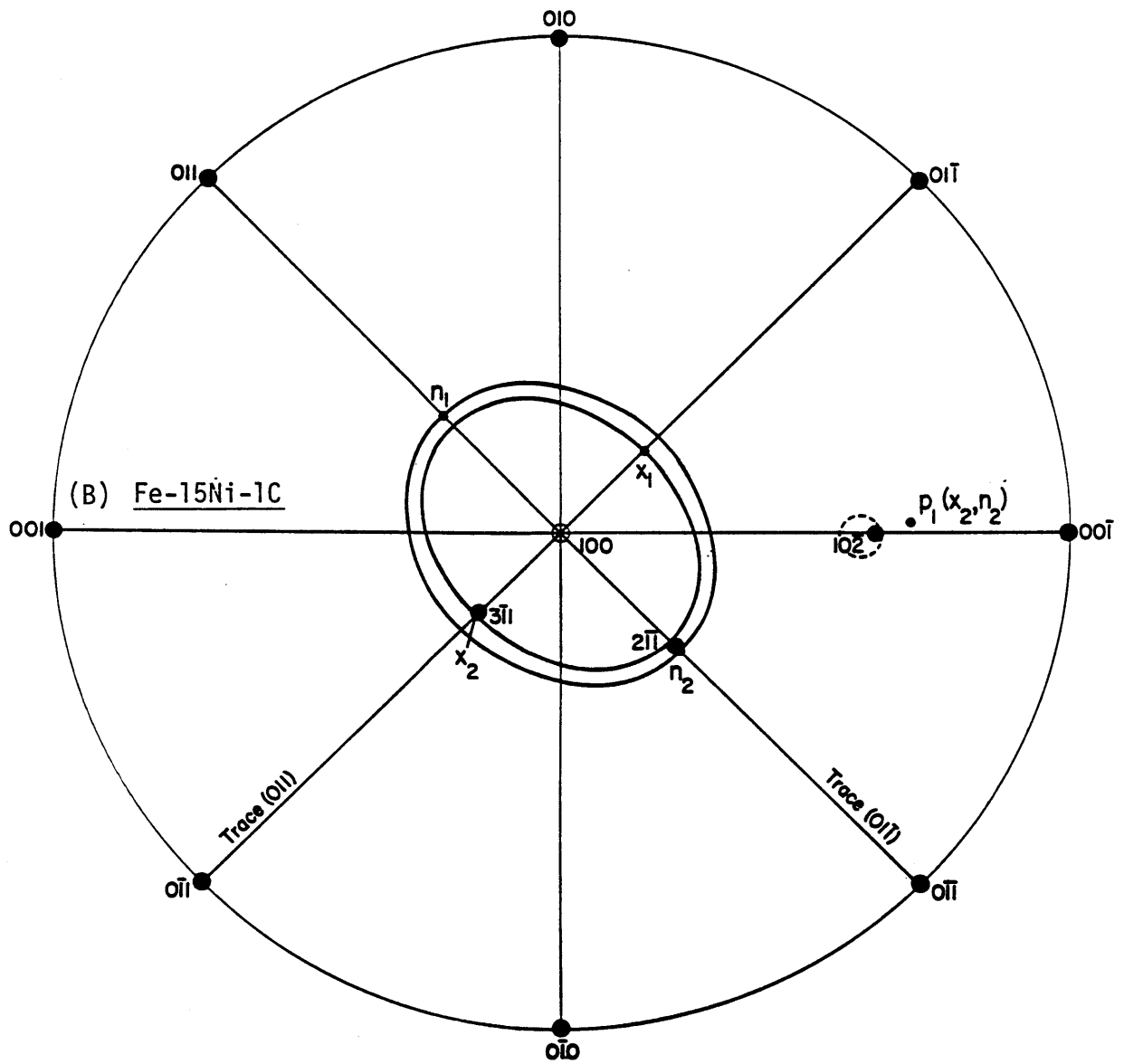
encountered in this investigation in doing tilting experiments, as well as the high density of these defects within any given particle. Attempts to observe dislocations in the martensite/carbide interface were also unsuccessful. However, the shear direction likely coincides with a Shockley-type displacement on the carbide "basal" plane. Six such directions exist: $\pm[3\bar{1}0]_{\epsilon'}$, $\pm[\bar{3}\bar{1}0]_{\epsilon'}$, and $\pm[010]_{\epsilon'}$. Formally, the shear is taken to occur in the parent phase; Equation 8-3 and Figure 8-15 indicate that these directions are derived from $\pm[3\bar{1}1]_{\alpha}$, $\pm[\bar{3}\bar{1}1]_{\alpha}$, and $\pm[01\bar{1}]_{\alpha}$, respectively. Of the three planes which are normal to these sets of directions, only one intersects the final cone. The other two planes have normals that are so close to the cone that their great circles miss the cone altogether. Thus, of the three possible sets of accommodation shear directions only $\pm[01\bar{1}]_{\alpha}$ permit a solution to the IPS problem. The great circle for the $(01\bar{1})_{\alpha}$ plane normal to these directions is included in Figure 8-16. Its intersection with the final cone defines the invariant normals n_1 and n_2.

8.4.3 Predictions of the Analysis

All of the information necessary for the B-M analysis is now at hand. Two cases with slightly different eigenvalues were run on the computer since the ϵ'-carbide lattice constants for the two Fe-Ni-C alloys differ slightly. The same shear system was used for each case: $[01\bar{1}](011)_{\alpha}$. The output is shown in its entirety in Appendix E and is referred to the parent BCC lattice. Four different solutions arise from each case, each defined by one of the four possible invariant line/invariant normal combinations. However, additional solutions arise when one considers the symmetry of the parent lattice. For example, in a cubic parent lattice the carbide basal plane could equivalently be derived from (101), (10$\bar{1}$), (110), (1$\bar{1}$0), or

199

($01\bar{1}$) instead of the chosen (011). When all possibilities are considered,

a total of 4x6 = 24 solutions (not counting variants which differ only in

signs) arise. These can be directly derived from the one complete solution

set in Appendix E by systematically permuting the Miller indices of the output.

The orientation relationship between BCC and ε'-carbide can be

inferred from the B-M output. The reader is referred to Wayman's book

[121] for the procedure. For the lattice correspondence of Equation 8-2,

the angle between the $(001)_{\varepsilon'}$ and $(011)_{\alpha}$ planes is about 6.5° and the angle

between $[100]_{\varepsilon'}$ and $[100]_{\alpha}$ is about 5.4° (in both alloys). This is in

reasonable agreement with the T-S orientation relation and is (within

experimental error) consistent with the diffraction patterns of Figure 8-6.

The B-M analysis predicts the following for the invariant lines and

normals (x_i and n_i), habit plane normal (p_1), and shape deformation (d_1)

for the BCC $\rightarrow$ ε'-carbide IPS in Fe-25Ni-0.4C:

$$x_1 = <0.862271,0.358112,-0.358112>$$
$$x_2 = <0.862271,-0.358112,0.358112>$$

$$n_1 = <0.758244,0.461013,0.461013>$$
$$n_2 = <0.758244,-0.461013,-0.461013>$$

$$p_1 = <0.404878,0.062654,-0.912222>$$

$$d_1 = <-0.491855,0.059660,-0.868631>.$$

The corresponding values for Fe-15Ni-1C are not significantly different.

Here, p_1 is only 4.5° from $<10\bar{2}>$, the approximate observed habit plane

normal (see Figure 8-16). In subsequent discussion, p_1 will be defined to

be of the type $<1,\overline{+}0,2>$ in order to recognize that it is nearly parallel to

$<102>$ and has one small component (designated by "±0") which is not

identically zero. The other parameters that appear above can likewise be

approximated by low-index, integral Miller indices. This leads to the

following approximations (which will prove to be a convenient notation when discussing the distinct variants predicted by the theory):

$$x_1 \cong <31\bar{1}>$$
$$x_2 \cong <3\bar{1}1>$$

$$n_1 \cong <211>$$
$$n_2 \cong <2\bar{1}\bar{1}>$$

$$p_1 \cong <1,+0,\bar{2}>$$

$$d_1 \cong <\bar{1},+0,\bar{2}>.$$

A complete listing of the 24 different variants can be found in Table 8-3. The table has been broken into subsets of eight variants. The first eight represent variants having a $\{1,+0,\underline{2}\}$ habit plane and simple shear on $\{01\underline{1}\}$. The second set represents variants having a $\{01\underline{1}\}$ shear plane but not a $\{1,+0,\underline{2}\}$ habit. The third set contains variants having neither a $\{1,+0,\underline{2}\}$ habit nor a $\{01\underline{1}\}$ shear plane. Within each subset, the variants are grouped into pairs having approximately the same habit plane. In such pairs, the indices for the habit plane differ only in the sign of the smallest component, but the simple shear occurs on orthogonal $\{01\underline{1}\}$ planes.

The magnitude of the accommodation shear, m_2, is also an important output parameter and is about 0.19 for both alloys. This, however, is referred to the parent BCC lattice. Crocker and Bilby [123] have provided expressions for referring m_2 to the product lattice. When this is done, one obtains:

$$|m_2(\varepsilon',Fe-25Ni-0.4C)| = 0.193988$$

and
$$|m_2(\varepsilon',Fe-15Ni-1C)| = 0.206319.$$

Knowing m_2 and the displacement vector of the faulting, **R**, one can calculate the average spacing, s, between faults in the product phase. The

TABLE 8-3

THE DIFFERENT ε'-CARBIDE VARIANTS PREDICTED BY THE B-M ANALYSIS
(planes and directions refer to BCC)

p_2,x	d_2,n	d_1	p_1
$(0\bar{1}\bar{1})[3\bar{1}1]$	$[0\bar{1}1](2\bar{1}\bar{1})$	$[\bar{1},-0,2]$	$(1,-0,2)$
$(01\bar{1})[3\bar{1}\bar{1}]$	$[011](2\bar{1}1)$	$[\bar{1},+0,2]$	$(1,+0,2)$
$(011)[3\bar{1}1]$	$[01\bar{1}](2\bar{1}\bar{1})$	$[\bar{1},+0,\bar{2}]$	$(1,+0,\bar{2})$
$(0\bar{1}1)[3\bar{1}\bar{1}]$	$[0\bar{1}\bar{1}](2\bar{1}1)$	$[\bar{1},-0,\bar{2}]$	$(1,-0,\bar{2})$
$(\bar{1}0\bar{1})[\bar{1}31]$	$[\bar{1}01](\bar{1}2\bar{1})$	$[-0,\bar{1},2]$	$(-0,1,2)$
$(10\bar{1})[\bar{1}3\bar{1}]$	$[101](\bar{1}21)$	$[+0,\bar{1},2]$	$(+0,1,2)$
$(101)[\bar{1}31]$	$[10\bar{1}](\bar{1}2\bar{1})$	$[+0,\bar{1},\bar{2}]$	$(+0,1,\bar{2})$
$(\bar{1}01)[\bar{1}3\bar{1}]$	$[\bar{1}0\bar{1}](\bar{1}\bar{2}1)$	$[-0,\bar{1},\bar{2}]$	$(-0,1,\bar{2})$
$(011)[31\bar{1}]$	$[01\bar{1}](2\bar{1}\bar{1})$	$[\bar{1},\bar{2},+0]$	$(1,\bar{2},+0)$
$(01\bar{1})[311]$	$[011](2\bar{1}1)$	$[\bar{1},\bar{2},-0]$	$(1,\bar{2},-0)$
$(0\bar{1}1)[311]$	$[0\bar{1}\bar{1}](2\bar{1}1)$	$[\bar{1},2,+0]$	$(1,2,+0)$
$(0\bar{1}\bar{1})[31\bar{1}]$	$[0\bar{1}1](2\bar{1}\bar{1})$	$[\bar{1},2,-0]$	$(1,2,-0)$
$(\bar{1}01)[1\bar{3}1]$	$[\bar{1}0\bar{1}](\bar{1}\bar{2}1)$	$[2,\bar{1},+0]$	$(2,1,+0)$
$(\bar{1}0\bar{1})[1\bar{3}\bar{1}]$	$[\bar{1}01](\bar{1}\bar{2}\bar{1})$	$[2,\bar{1},-0]$	$(2,1,-0)$
$(101)[13\bar{1}]$	$[10\bar{1}](\bar{1}2\bar{1})$	$[\bar{2},\bar{1},+0]$	$(\bar{2},1,+0)$
$(10\bar{1})[131]$	$[101](\bar{1}21)$	$[\bar{2},\bar{1},-0]$	$(\bar{2},1,-0)$
$(\bar{1}10)[11\bar{3}]$	$[110](\bar{1}1\bar{2})$	$[2,+0,\bar{1}]$	$(2,+0,1)$
$(\bar{1}\bar{1}0)[1\bar{1}\bar{3}]$	$[1\bar{1}0](\bar{1}\bar{1}\bar{2})$	$[2,-0,\bar{1}]$	$(2,-0,1)$
$(\bar{1}10)[\bar{1}\bar{1}\bar{3}]$	$[110](1\bar{1}\bar{2})$	$[2,+0,1]$	$(2,+0,\bar{1})$
$(\bar{1}\bar{1}0)[\bar{1}1\bar{3}]$	$[1\bar{1}0](11\bar{2})$	$[2,-0,1]$	$(2,-0,\bar{1})$
$(1\bar{1}0)[113]$	$[\bar{1}\bar{1}0](1\bar{1}2)$	$[+0,2,1]$	$(+0,2,\bar{1})$
$(\bar{1}\bar{1}0)[1\bar{1}\bar{3}]$	$[1\bar{1}0](11\bar{2})$	$[-0,2,1]$	$(-0,2,\bar{1})$
$(1\bar{1}0)[\bar{1}\bar{1}3]$	$[\bar{1}\bar{1}0](\bar{1}12)$	$[+0,2,\bar{1}]$	$(+0,2,1)$
$(\bar{1}\bar{1}0)[\bar{1}13]$	$[1\bar{1}0](\bar{1}\bar{1}\bar{2})$	$[-0,2,\bar{1}]$	$(-0,2,1)$

displacment vector is assumed to be the Shockley-like $1/3[010]_{\epsilon'}$. The spacing is then

$$s = \frac{|R|}{m_2} \cong \frac{1.53}{0.20} \cong 0.8 \text{ nm.} \tag{8-4}$$

The predicted value of 0.8 nm is not far from the measured spacing of about 1.0 to about 1.5 nm. In fact, the crystallographic analysis has thusfar given surprisingly good agreement with the experimental observables, especially the habit plane.

For any IPS, the shape deformation which converts one lattice into another can be decomposed into a pure dilatation (normal to the habit plane) and a pure shear (on the habit plane). Referring to Appendix E, the magnitude of the pure shear (γ) is related to the magnitudes of the shape deformation (M1) and the dilatation (ϵ = 1 − DETE) as follows:

$$\gamma = \sqrt{M1^2 - \epsilon^2}. \tag{8-5}$$

When the values appropriate for Fe-25Ni-0.4C are substituted into Equation 8-5, one obtains

$$\gamma = 0.211.$$

Note that γ is actually larger than ϵ ($\cong$ 0.19); i.e. the shear component is larger than the dilatational component.

The wealth of information provided by the crystallographic analysis can be of enormous utility in trying to identify experimentally different carbide variants. However, it should be stressed that Table 8-3 has been derived by considering the parent phase to have cubic symmetry. One can expect the tetragonal symmetry of aged martensite to preclude some of the

203

variants; subsequent discussion will illustrate this by considering which variants might be favored under certain symmetry constraints or conditions of stress.

8.5 Discussion

8.5.1 Carbide Morphology and Structure

A variety of morphologies have been reported for the transition carbide which forms in martensitic steels. Early TEM studies of Fe-Ni-C [49,120] and Fe-C [26,52] alloys reported a plate-like carbide with a $\{100\}_\alpha$-type habit plane. Later studies of Fe-Mn-C [42,117] alloys found that the carbide may also adopt a rod-like shape along $<100>_\alpha$. To complicate this issue further, recent studies of Fe-Ni-C [119] and Fe-Si-C [51] alloys find the carbide particles to be rod-like, but with a long axis nearly parallel to a $<211>_\alpha$-type direction. In this investigation, however, the transition carbides were clearly plate-like in shape. The habit plane is not of the $\{100\}_\alpha$ type reported previously. This is clearly demonstrated in Figures 8-1 and 8-2; if the carbides are on $\{100\}$ planes, then the two variants in each figure should lie at right angles. This is clearly not the case in either figure. Furthermore, the four different morphological variants of Figure 8-4 are not consistent with the three possible $\{100\}$ habits.

The authors of References [116-119] report that the rod-shaped particles are actually composed of aggregates of smaller particles (less than 10 nm in size). Their findings (based on dark-field TEM) are not consistent with those of this study. The present author believes that any dark-field micrographs which indicate that the particles are not continuous can probably be explained in terms of contrast from faulting on the basal

plane or by contrast effects which arise when the particles are in an inclined orientation with respect to the beam direction.

The apparent disparity among the present and previous results regarding the shape of carbides in Fe-Ni-C alloys might be attributable to an inadvertent bias in the previous work. In this study, the author found that the carbide particles were generally most easily visible when they were in a near edge-on orientation and suspects that a good deal of the previous work was unintentionally limited to such cases. In such a situation, the particles have a rod-like projected shape. In fact, the present author initially concluded that the particles were indeed rods or laths and proceeded to measure a long axis which appeared to be near $<211>_\alpha$, in agreement with Murphy and Whiteman [51]. However, subsequent stereo microscopy and TEM micrographs such as Figure 8-4 lead the author to revise his conclusion. As indicated in Section 8.1, the carbides are plate-like with a $\{10\underline{2}\}_\alpha$ habit plane, although deviations of several degrees from this plane appear to be common.

In some cases, morphologies other than the $\{10\underline{2}\}$ plate may be predicted by the crystallographic analysis. For example, as the magnitude of the contraction along $[100]_\alpha$ decreases, the invariant lines move closer to $[100]$. The lattice constants reported by Hirotsu et al. [119] for ε'-carbide in Fe-1.13C ($a_{\varepsilon'}=0.284$ nm vs. $a_{Fe}=0.2866$ nm) suggest that the contraction might be smaller in Fe-C alloys as compared with the current Fe-Ni-C alloys. When their lattice constants were used in the Ledbetter-Wayman program, a habit plane closer to $\{001\}_\alpha$ was predicted. For the limiting case where η_1 equals unity, an IPS is no longer possible. However, an invariant- or near-invariant-line strain may still be realizable, presumably resulting in a rod-shaped particle along $[100]_\alpha$.

Such a situation appears to exist for precipitation of Mo_2C in steels [124], even though there is a slight expansion along [100].

A question still exists as to whether carbon is ordered in the transition carbides observed here. The ordered carbon arrangement of ε'-carbide should, in principle, lead to superlattice reflections which can then be taken as positive proof of ε' precipitation. However, the relatively weak scattering power of carbon atoms implies that these reflections may be quite weak. Such reflections were nonetheless reported by Hirotsu and Nagakura [52] in an Fe-1.13C alloy. On the other hand, no superlattice reflections were observed in the Fe-Ni-C alloys of the present study, even when long exposure times were employed for recording the diffraction patterns. The issue of where carbon atoms reside in the transition carbide is further complicated when one closely examines the spot patterns presented by Hirotsu and Nagakura. They identified superlattice reflections nearly midway between the origin of reciprocal space and the martensite (020) reflection, i.e. near the (010) martensite reciprocal lattice point. However, the magnetite which frequently forms epitaxially on sample surfaces also produces a {022} reflection near this location (see Figure 7-14). If the oxide layer is thin, its weak diffraction spots could be mistakenly identified as ε' superlattice spots.

Hirotsu and Nagakura also observed surprisingly intense superlattice spots in the [$\bar{1}$20] martensite zone. These were later shown by Shimizu and Okamoto [116] to be due to the presence of a second carbide variant. In light of the complications associated with oxide formation and the presence of multiple carbide variants, the diffraction evidence for carbon ordering in the transition carbide is quite dubious. Nonetheless, the slight orthorhombic distortion of the carbide lattice indicates that there is

indeed some tendency for carbon atoms to order, but the long-range order may not be sufficient to produce superlattice spots.

8.5.2 Orientation Variants

Since aged martensite possesses tetragonal symmetry, it is proposed that only the first eight crystallographic variants predicted by the B-M analysis need be considered in analyzing TEM micrographs. These are the only variants which exhibit a habit plane near $\{10\underline{2}\}_\alpha$ and also have a basal plane which is derived from a $\{01\underline{1}\}_\alpha$, two features which are consistent with all of the experimental observations. If all eight proposed variants occur with equal probability, then each $\{01\underline{1}\}_\alpha$ plane should be nearly parallel to the basal plane of two carbide variants. This hypothesis can be verified directly by closely examining the $[011]_\alpha$ diffraction patterns of Figure 8-6. Here, two $[001]_{\varepsilon'}$ patterns from different variants overlap, as indicated by the two different directions along which the carbide reflections are streaked. The streaking is undoubtedly a shape effect, occurring along a direction parallel to the projected habit plane normal. Of the eight proposed, the two variants which have basal planes derived from $(01\underline{1})_\alpha$ should have habit planes near $(102)_\alpha$ and $(10\overline{2})_\alpha$. The observed streaking along $[102]_\alpha$ and $[10\overline{2}]_\alpha$ is consistent with this. This analysis convincingly confirms the hypothesis put forward above. Namely, that symmetry considerations lead to eight possible ε'-carbide orientation variants.

The eight "allowed" carbide variants all have different habit planes, and yet only four different habits are indicated experimentally. The apparent discrepancy can be explained with reference to Table 8-3. The reader will note that each pair of allowed variants has habit plane normals

which are very similar; for Fe-25Ni-0.4C they are only 7.2° apart. In practice, particles whose habits are only several degrees apart cannot be readily distinguished and this may explain why only four variants are readily detected by TEM.

8.5.3 Heterogeneous Nucleation

We know that spinodal decomposition is the first process to occur during aging, even at temperatures as high as 200°C. If a new phase nucleates with continued aging, it is natural to expect the crystallography of the "decomposed state" to exert some influence on this process. Two features of the precipitate morphology suggest that the influence is a strong one. First, the habit plane tends to be parallel to a {10$\underline{2}$} plane in both alloys, close to the {20$\underline{3}$} habit of the product of spinodal decomposition. Second, in the early stages of nucleation and growth the interparticle spacing (10 to 20 nm in Figures 8-1 and 8-2) is similar to the wavelength of the coarsened tweed structure. These observations suggest that nucleation occurs heterogeneously at favorable locations within the tweed structure.

The preferential nucleation along the carbon-rich bands of the tweed can be understood by examining the coupling between metal-atom displacements in the high-carbon bands and the shape strain which converts the BCC martensite phase to the orthorhombic ε'-carbide phase. The carbon-rich band is approximately Fe$_8$C in composition and is distorted from BCC symmetry because of the occupation of O_z sites by the carbon atoms. Formally, a tetragonal lattice distortion can be represented by (neglecting any volume change) shears on {01$\underline{1}$}$_\alpha$ planes. There is an increasing body of evidence which indicates that a number of FCC and BCC alloy systems accommodate centers of tetragonal distortion by shear displacements of the

208

surrounding atoms. In fact, the recent structure analysis by Kusunoki and

Nagakura [88] of the (012) tweed variant in BCT Fe-1.78C martensite

indicates that carbon atoms displace their near-neighbor iron atoms along a

direction whose component in the (100) plane is inclined relative to the c-

axis, Figure 8-17. Surprisingly, this direction is similar to the shape

deformation direction (d_1) indicated for certain ϵ'-carbide variants in

Table 8-3. Thus, the overall shape strain which relates low- to high-

carbon bands of the tweed has an appreciable component parallel to the

shape strain which converts BCC to ϵ'-carbide. The net transformational

strain energy is therefore smaller if nucleation of ϵ'-carbide takes place

in the distorted, high-carbon band. Furthermore, nucleation and growth of

the particle may be more favorable along the boundary between bands because

then interfacial energy is available to help drive the transformation.

These concepts are illustrated schematically in Figure 8-18. This figure

includes a (023) Fe_8C band and a carbide particle with a (012) habit

(representing variant six in Table 8-3). The metal atoms within the Fe_8C

band are displaced along a direction indicated by the arrows. For the

particular carbide particle shown, d_1 is approximately parallel to $[0\bar{1}2]$

and clearly has a significant component parallel to the metal atom

displacements in the tweed. The good coupling between these particular

tweed and carbide habits ensures that the growing carbide can maintain good

contact with the interface between high- and low-carbon bands of the tweed.

8.5.4 Growth Kinetics

Some previous investigations indicate that the local volume change

associated with carbide precipitation may be accommodated plastically by

the surrounding low-carbon matrix [125]. Brown, Rack, and Cohen [126]

209
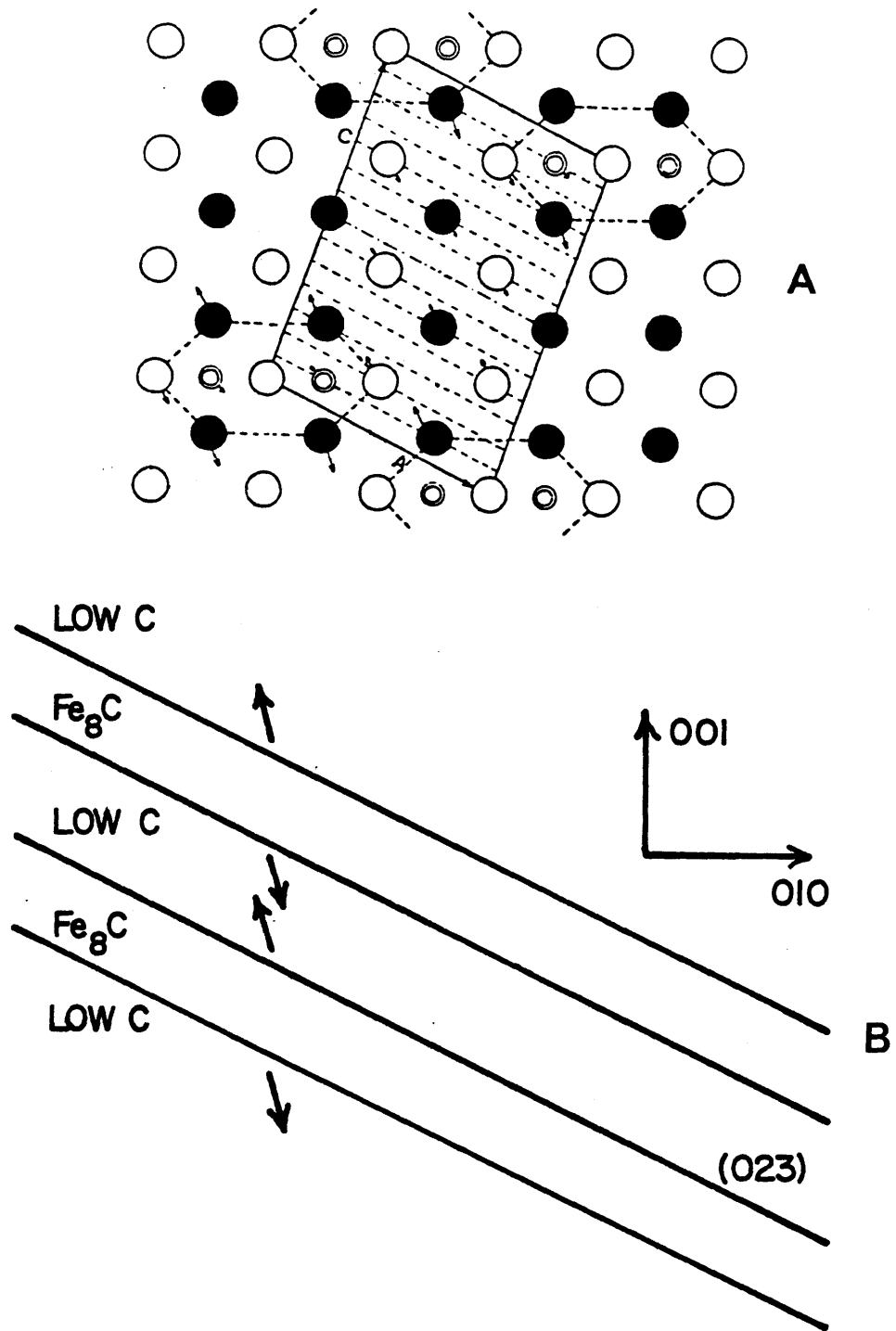
Figure 8-17. Kusunoki and Nagakura's depiction of the (012) modulated
structure in Fe-1.78C martensite, as projected along [100],
(A). Large open and solid circles represent iron atoms on
different (100) planes. Medium double circles indicate
positions which carbon atoms are likely to occupy, based on
the displacements of neighboring iron atoms (indicated by
arrows). Their results indicate that iron atoms in the Fe_8C
bands are, on average, displaced along the directions
indicated in (B).
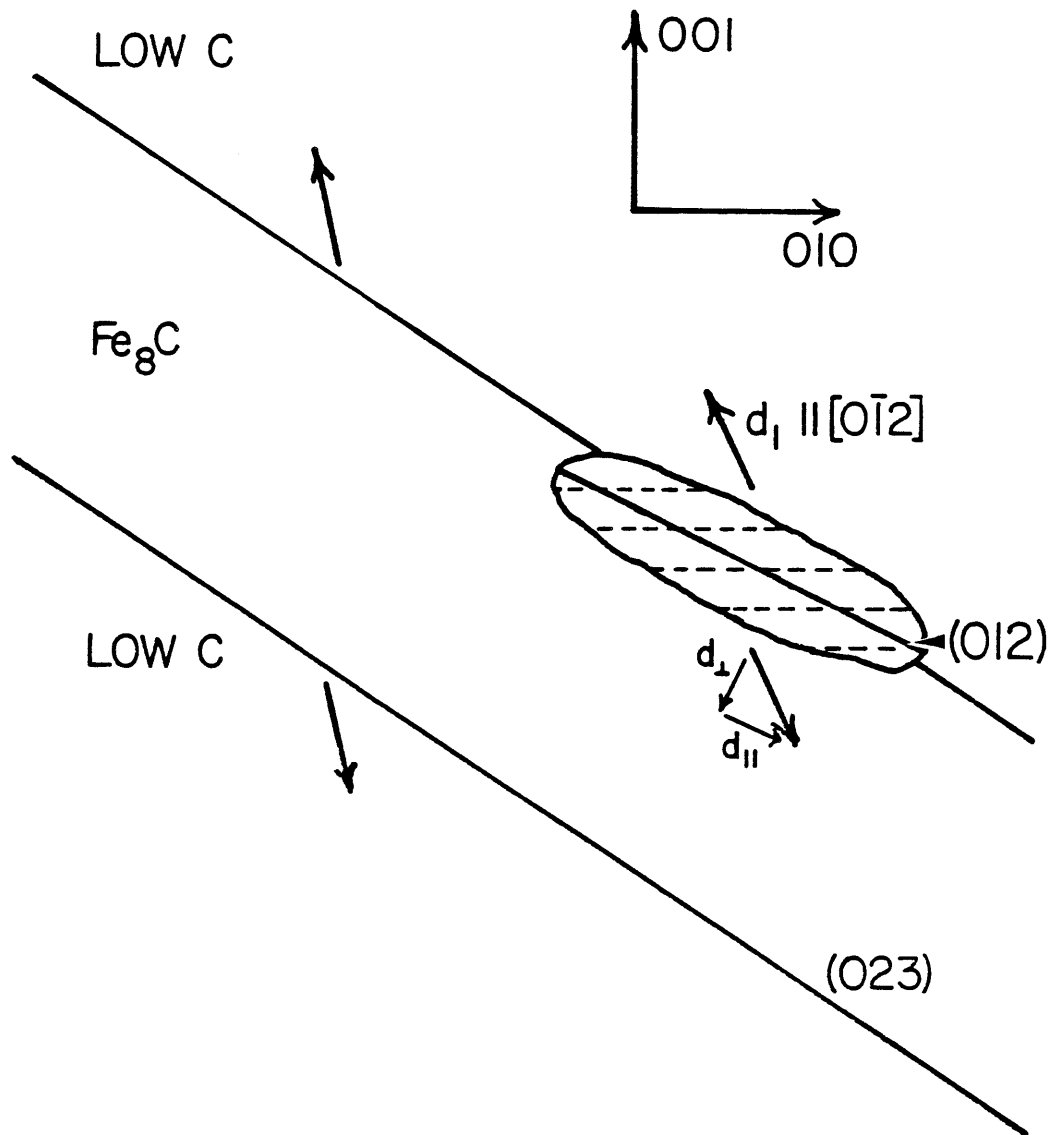
Figure 8-18. Schematic representation of carbide nucleation along
carbon-rich bands of the tweed. Dashed lines in the
carbide represent the trace of the internal shear
plane. See text for discussion.

studied the phenomenon of stress relaxation, mainly in plain-carbon steels, and found that the relaxation kinetics followed the kinetics of tempering. Furthermore, the total relaxation increased with carbon content, but was reduced when samples were tempered into stage one prior to stressing. The x-ray study of Chen and Winchell [69] documents some significant changes in the populations of orientation variants of the martensitic phase during stage one tempering. They conclude that shearing (specifically twinning) in the martensite can be an important stress relaxation mechanism. There is little doubt that stage one precipitation can provide an important stress-relief mechanism. However, the present crystallographic analysis reveals that plasticity intrinsic to the IPS itself may also provide a significant component of the stress-relief.

Sherman et al. [70] found that the apparent activation energy associated with carbide growth and coarsening agreed with that for pipe diffusion of iron along dislocations and, on this basis, suggest that such diffusion is an essential part of the transformation. However, the proposed IPS nature of the ε'-carbide formation has some important implications regarding the growth mechanism. Since the IPS itself is a conservative deformation, there is no intrinsic requirement for diffusive metal-atom transport during the reaction. Therefore, any diffusion of iron can only be rationalized by assuming that dislocation climb occurs as an accommodation mechanism in the surrounding matrix. However, it is difficult to imagine that such a process can be important at the temperatures where nucleation and growth was detected in this study (e.g. as low as room temperature). The author believes that the increase in the apparent activation energy to that representative of iron pipe-diffusion may be fortuitous, and that an alternative rate-limiting mechanism(s)

should be sought. The transformation obviously requires carbon diffusion, but it also requires the propagation of an interface. The interface will contain coherency and anticoherency dislocations, and therefore its motion requires the propagation of the strain field associated with these dislocations. If the interfacial motion is thermally assisted, one can expect it to influence the apparent activation energy. Such thermal activation may be required in order to propagate the interface through obstacles in the matrix. Potential obstacles might include substitutional solute atoms, forest dislocations, and twin boundaries. It is beyond the scope of the present investigation to assess which barriers might require the thermal assistance that is actually measured, but it provides an interesting issue for future work to address.

The processes of carbon diffusion and interfacial motion are viewed as occurring in series and therefore the activation energies for the two processes are additive in determining the overall kinetics. This can explain why the activation energy increases above that required for carbon diffusion alone. The continued increase into the carbide coarsening regime may reflect a variation in interface mobility with particle size. Here, the possibility that cumulative plastic accommodation in the matrix retards the interfacial motion seems attractive.

8.6 Summary

The results in this chapter show that the transition carbide which forms in martensitic Fe-Ni-C alloys has a plate-like shape with a habit near $\{10\underline{2}\}_\alpha$. Although the positions of carbon atoms could not be determined, the orthorhombic symmetry of the carbide suggests that it may be $\varepsilon'-$ rather than ε-carbide. The carbides exhibit extensive faulting on their "basal" plane that appears to be an internal accommodation mechanism

213

necessary to achieve an IPS which minimizes the total strain energy.

The TEM and crystallographic analyses of the carbide strongly suggest that it nucleates heterogeneously along carbon-rich bands which develop during the pre-precipitation spinodal decomposition. The favorable shape strain which relates low- to high-carbon bands and available interfacial energy undoubtedly aid the nucleation process. The continuous increase in activation energy during aging and tempering indicates that no single rate-controlling step operates; it is proposed that carbon diffusion and thermally assisted interfacial motion operate concurrently in determining the overall reaction kinetics.

Regarding the role of the martensitic substructure in stage one, no direct evidence of nucleation on dislocations was found in this study. However, there is evidence that some carbides nucleate on $\{11\underline{2}\}$ twin boundaries, but such particles probably constitute a small fraction of the total.

CHAPTER 9

SUMMARIZING DISCUSSION

The experimental results reported in this thesis are divided into four separate "Results and Discussion" chapters; such partitioning seems appropriate given the varied nature of the results themselves. Herein an attempt is made, for the benefit of the reader, to briefly unify the concepts which have been put forward in somewhat piece-meal fashion in the preceeding four chapters.

9.1 Martensitic Crystallography and Substructure

This study, as well as a number of previous investigations, indicates that the lattice of virgin martensite is tetragonally distorted due to a thermodynamic preference for carbon atoms to occupy only one of the three octahedral interstitial sublattices. However, planar defects exist wherein interstitial carbon atoms are related to those in their surroundings by a twinning operation on one of the four equivalent $\{01\underline{1}\}_\alpha$ planes. Such twinning may represent a lattice-invariant deformation mechanism intrinsic to the martensitic transformation, although the possibility that it also provides post-transformation stress relief cannot be ruled out. The existence of $\{01\underline{1}\}$ twins has been previously postulated on the basis of the macroscopic orthorhombic lattice distortion frequently measured in martensitic steels. The present calculations show that the volume fraction of twinning required to account for the distortion is not out of line with the TEM observations. The $\{01\underline{1}\}$ twinning apparently occurs over a wide range of alloy composition, but differences in the amount of twinning lead to the observed differences in the variation of axial ratios with alloy carbon content among different alloy classes.

In addition to {01$\underline{1}$} twins, the usual substructural features found in

plate-like Fe-Ni and Fe-Ni-C alloys were also observed, namely {11$\underline{2}$}

transformation and deformation twins and <111> lattice screw dislocations.

Attention was paid here to the role which the substructure plays in

subsequent aging and tempering reactions.

9.2 Aging Behavior

The Fe-Ni-C alloys of this study develop a modulated structure (tweed

structure) throughout the martensitic phase upon aging at temperatures

below 175°C. The reaction likely proceeds at even higher temperatures, but

occurs so rapidly that its direct detection requires extremely short-time

aging treatments. Other investigations indicate that modulations occur in

a variety of alloys, including the Fe-C, Fe-Cr-C, and Fe-Mn-C systems. The

structural modulation occurs along directions nearly parallel to the four

<10$\underline{2}$> directions and on a very fine scale (~1 nm in high-carbon alloys).

The four modulation variants are related by the symmetry of the tetragonal

parent phase. It appears that the elastic properties of the metal lattice

determine the exact modulation direction and therfore slight deviations may

be expected among different alloys; modulations along <20$\underline{3}$> are indicated

in the two Fe-Ni-C alloys of this study. The calculated modulation

direction, based on elastic strain energy considerations, agrees very well

with the measured direction.

Direct compositional analysis of Fe-15Ni-1C martensite by AP/FIM

shows that alternating carbon-rich and carbon-poor bands form with aging at

room temperature. Furthermore, the composition amplitude increases with

aging time, indicating that "uphill" diffusion is occurring. This fact,

coupled with the aligned nature of the aging product, provides convincing

evidence that the reaction is a spinodal decomposition. Furthermore, the Zener-ordered nature of virgin martensite suggests that the reaction may be a conditional spinodal decomposition (where prior ordering leads to the compositional instability). Geometrically, the elastic properties of martensite are such that a net free energy decrease results when the tetragonal distortion due to carbon is concentrated in planar bands along $\{20\underline{3}\}_\alpha$.

The electrical resistivity behavior accompanying aging has been analyzed in order to determine the kinetics of aging. The results indicate that aging is controlled simply by carbon-atom diffusion. The apparent decrease in the rate of aging as one goes to higher carbon content agrees with previous suggestions that the diffusivity of carbon in body-centered iron decreases as the lattice becomes more tetragonal.

Attempts to characterize the structure of the carbon-rich bands by electron and x-ray diffraction techniques were not entirely successful in this study. In the early stages of decomposition (before any significant coarsening occurs) the martensitic lattice retains the macroscopic tetragonal distortion characteristic of virgin martensite. Therefore, it can be concluded that carbon atoms remain in a single sublattice. However, as the structure coarsens, the carbon-rich domains no longer diffract coherently, resulting in an apparent loss of tetragonality. Unfortunately, attempts to detect a superstructure within the carbon-rich domains were inconclusive; no superlattice reflections were detected on electron diffraction patterns. On the other hand, other structure investigations, particularly those using Mössbauer spectroscopy, indicate at least short-range order among carbon atoms. Such studies generally propose an Fe_4C-type structure, but considerably deficient in carbon. The AP/FIM results indicate that the actual stoichiometry may be closer to Fe_8C. The

possibility that an $Fe_{16}C_2$ phase forms, perhaps analogous to the α'' iron nitride $(Fe_{16}N_2)$ which precipitates from Fe-N martensites, seems plausible, although no such superlattice reflections have been reported.

The literature contains several models for the body-centered Fe-C solution thermodynamics which predict a compositional instability at room temperature. Those models which explicitly treat the tetragonal (Zener-ordered) nature of virgin martensite predict low-carbon martensite and FeC to be the product phases of the decomposition reaction. However, the AP/FIM results show that the composition reaches only Fe_8C during decomposition. An attempt was therefore made here to develop a simple phenomenological description which is more consistent with the experimental results. It was found that a miscibility gap with phase boundaries consistent with the AP/FIM results could be obtained when a carbon-ordering energy was included, having a maximum value at the Fe_4C composition instead of FeC.

Freshly-quenched martensitic steels are notorious for being very brittle. Tempering is a simple but important process for increasing the ductility and toughness of such alloys. However, the rapidity with which steels age at room temperature makes it difficult to assess, by conventional mechanical testing, whether ferrous martensite is inherently brittle or whether such brittleness is related to the spinodal decomposition which occurs during aging. A recent metallographic investigation [127] has shown that micro-cracking, a reflection of brittleness, occurs in Fe-15Ni-1C martensite when it is allowed to warm up from low temperatures (i.e. $-196^\circ C$). This important finding suggests that the brittleness of nominally untempered martensite may be a reflection of severe internal stresses generated by the coherent mixture of high- and

low-carbon bands which forms during spinodal decomposition (to a first approximation, the Fe_8C bands which form during aging should have a c/a of 1.176 [from Equations 2-7 and 5-7] if they maintain the BCT structure). Much more work needs to be done in characterizing the mechanical behavior of virgin and aged martensites.

9.3 Transition Carbide Precipitation

Electron diffraction indications of carbide precipitation were noted after about a month at room temperature; for a one-hour treatment, carbides were detected at about 80°C. Precipitation occurs on a fine scale, apparently throughout the martensitic phase. However, careful TEM dark-field imaging revealed that nucleation was ocurring along the Fe_8C bands formed by previous spinodal decomposition. There were also some indications that nucleation occurs along $\{112\}_\alpha$ twin boundaries. On the other hand, particles frequently appeared to have their radial growth arrested when impingement onto such a twin boundary occurred during growth.

Diffraction patterns from coarsened particles were consistent with the structure and orientation relation of the ε-carbide commonly found in a variety of martensitic steels. However, slight distortions of the structure from the ideal hexagonal indicate that some ordering of carbon interstitials may occur in the carbides of the present alloys. Similar distortions have been noted by other investigators; they distinguish such carbides from the ε-carbide by referring to them as η-carbide. However, it is suggested here that the distorted carbides be referred to as ε'-carbide, since the two structures are related simply by the ordering of the carbon interstitials.

The ε'-carbide adopts a plate-like shape with a habit plane near $\{10\underline{2}\}_\alpha$. The particles exhibit a fine substructure which consists of

stacking faults on the "basal" plane spaced at intervals of about 1.5 nm. The crystallography of the carbides was analyzed by using a computerized version of the procedure developed by Bowles and MacKenzie (originally to analyze the crystallography of the martensitic transformation in steels). A BCC → orthorhombic lattice deformation was assumed, together with a specific simple shear on $\{01\underline{1}\}_\alpha$ (the type of plane from which the carbide "basal" plane is derived). The crytallographic observables predicted by the analysis are in good agreement with the experimental results.

The crystallographic analysis also explains why ε'-carbides nucleate heterogeneously on the Fe_8C bands of the coarsened tweed structure; the good coupling between the shape strain which converts BCC to ε' and the displacements of metal atoms in the Fe_8C bands implies that the net transformation strain energy is lower if nucleation occurs on such bands rather than in the adjacent low-carbon volumes. Moreover, the good coupling between the carbide and tweed habits ($\{10\underline{2}\}_\alpha$ vs. $\{20\underline{3}\}_\alpha$) suggests that nucleation and growth is favored near the Fe_8C/low-carbon interface, where the available interfacial energy can be used to help drive the transformation.

The kinetics of ε'-carbide precipitation were measured by conducting a series of electrical resistivity experiments at different tempering temperatures. The apparent activation energy (Q_a) is about 109 – 113 kJ/mole (26 – 27 kcal/mole) at the onset of precipitation, but slowly increases to about 121 – 126 kJ/mole (29 – 30 kcal/mole) during carbide coarsening. Previous resistometric studies of the kinetics of the first stage of tempering have concluded that the increase in Q_a is related to a gradual transfer of rate-control from carbon-atom diffusion to dislocation-pipe diffusion of metal atoms. Dislocation climb in the matrix surrounding

the carbides was viewed as necessary in order to accommodate the transformational volume change. However, in view of the low temperatures over which precipitation occurs (where creep rates would be expected to be negligible) and the conservative IPS nature of the transformation (which requires no intrinsic diffusive metal-atom transport), one must seek an alternative rate-limiting process(es). It seems most reasonable to view the precipitation reaction as involving a conservative displacement of metal atoms and a concomitant diffusive flux of interstitial carbon atoms. The increase in Q_a during precipitation and coarsening may then reflect a thermal assistance to the propagation of the carbide/matrix interface; this component would be superimposed on the activation energy for carbon diffusion. The motion of the interface requires the propagation of sets of coherency and anti-coherency dislocations. Since the crystallographic analysis specifies the interfacial structure, a detailed analysis of the interaction of the interface with various obstacles could be undertaken. This is proposed for future research.

The successful application of the Bowles-MacKenzie crystallographic theory to the precipitation of ε'-carbide serves to underscore the fact that it can be applied to any phase transformation where a lattice correspondence can be defined. Its use need not be restricted to purely displacive transformations, such as the martensitic reaction in steels. Indeed, Wayman [128] has applied the Bowles-MacKenzie analysis to hydride precipitation in vanadium and zirconium, where diffusion of hydrogen atoms is involved. Thus, the crystallographic theory may well prove to be a powerful tool for analyzing the crystallography of a variety of coupled displacive-diffusive transformations.

To summarize, the results of the present study of Fe-Ni-C martensites,

221

correlated with other experiments, lead to a refined description of the phenomena which take place as virgin martensite is aged or tempered. At subambient temperatures, a small amount of retained austenite is converted to martensite. Coherent, ordered spinodal decompositon occurs at temperatures above about $-40^{\circ}C$ and produces a peak ($\Delta\rho_{II}$) in the electrical resistivity vs. time or temperature curve. This reaction sets the stage for subsequent ϵ'-carbide precipitation (T1). Although it was not extensively studied in the alloys of this investigation, cementite precipitation (T3) also occurs at temperatures above about $200^{\circ}C$. Figure 9-1 summarizes the temperature range over which each of the above reactions are observed, as typified by the Fe-15Ni-1C alloy. The retained austenite in this alloy also undergoes decomposition (T2) within the investigated temperature range.
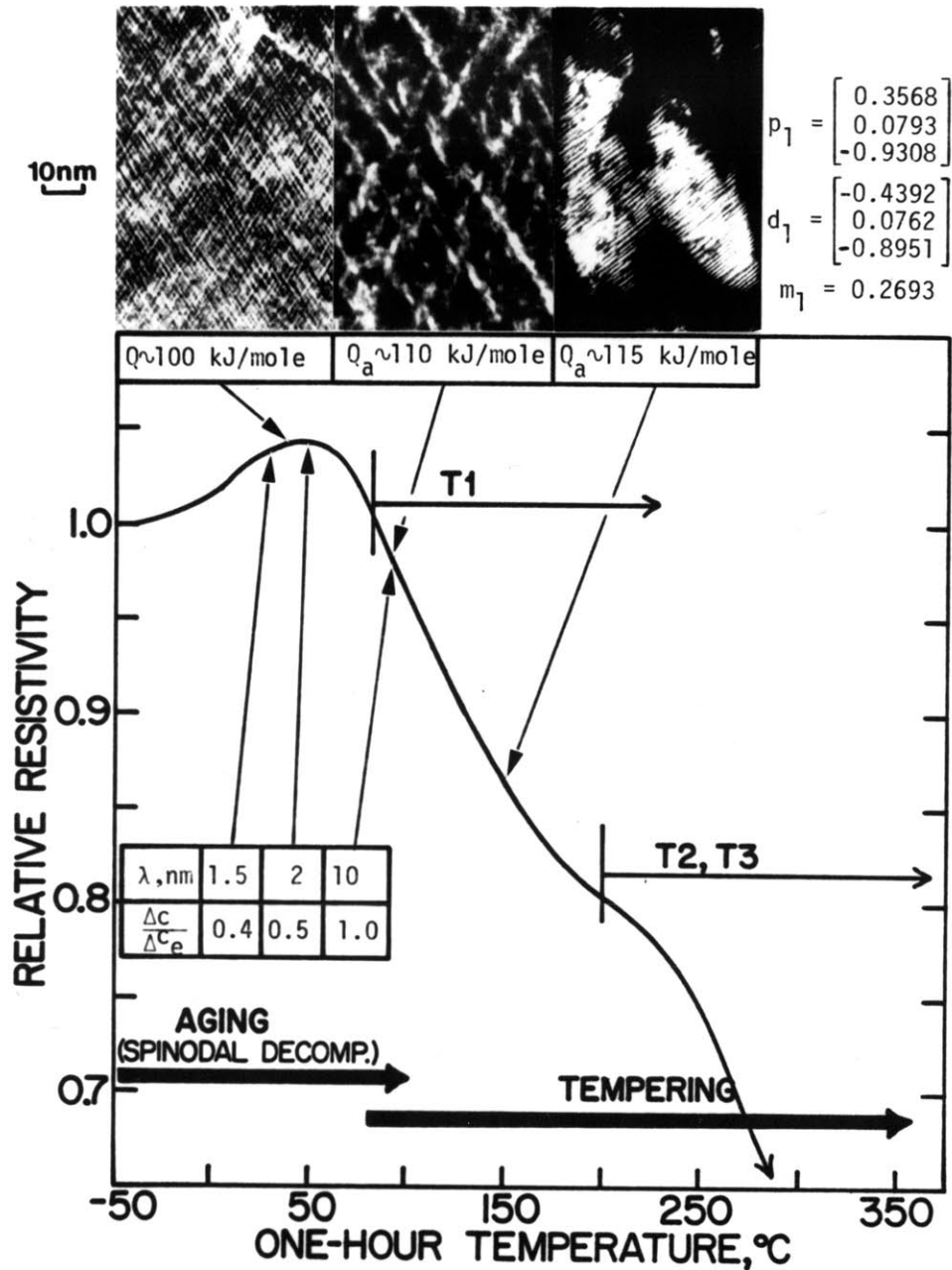
Figure 9-1. Summary of the structural changes which take place during the aging and tempering of an Fe-15Ni-1C alloy, correlated with accompanying resistivity changes. The alloy initially contains 67% virgin martensite and 33% retained austenite. "λ" refers to the wavelength of the tweed structure and "$\Delta c/\Delta c_e$" represents the difference in carbon concentration between high- and low- carbon bands, normalized to the difference at the onset of carbide precipitation (T1).

CHAPTER 10

CONCLUSIONS

The results reported in this thesis lead to the following conclusions with regards to aging phenomena in ferrous martensites:

(1) Carbon atoms tend to occupy a single octahedral interstitial sublattice (O_z) in virgin martensite; however, planar defects exist wherein carbon atoms are related to those in their surroundings by a twinning operation on $\{01\underline{1}\}$. Such defects can account for the orthorhombic lattice distortion frequently measured in virgin martensites.

(2) A small amount of the retained austenite transforms to martensite when the alloys of this study are warmed from liquid nitrogen temperature.

(3) A fine-scale modulation in carbon concentration along $\langle 20\underline{3}\rangle$ directions develops first during the aging of the martensitic phase; it produces the tweed structure detected by transmission electron microscopy. The initial compositional wavelength depends on the alloy carbon content; it is about 2.5 and 1.5 nm in Fe-25Ni-0.4C and Fe-15Ni-1C, respectively. The increase in composition amplitude with aging time and the aligned nature of the tweed indicate a spinodal decomposition mechanism. The Zener-ordered structure of virgin martensite suggests that the decomposition is a conditional spinodal reaction.

(4) Carbon atoms remain in O_z sites during aging. Secondary ordering may also occur, leading to a carbon-rich phase of composition near Fe_8C.

(5) Spinodal decomposition proceeds very rapidly at room temperature. The decomposition requires only carbon diffusion, therefore its kinetics are limited only by this process. The activation energy (Q) increases with alloy carbon content, consistent with predictions of a concentration-dependent diffusion coefficient for carbon in tetragonal martensite. Q is initially about 80 kJ/mole, but, for reasons not well understood, increases by about 10 – 15 kJ/mole as decomposition proceeds.

(6) The transition carbide nucleates after the tweed structure has coarsened. The nucleation appears to be heterogeneous, occurring at the interface between carbon-rich and carbon-poor bands.

(7) The carbides do not exhibit the ideal hexagonal structure. They are probably a partially-ordered version of the ϵ-carbide structure and are designated as ϵ'-carbide.

(8) The ϵ'-carbides in the Fe-Ni-C alloys of this study adopt a $\{10\underline{2}\}_\alpha$ planar habit and exhibit profuse faulting on the "basal" plane. These features are consistent with an invariant-plane strain on $\{10\underline{2}\}_\alpha$-type planes. The crystallographic analysis of the ϵ'-carbide yields the following (referred to BCC) for the habit plane normal (p_1), shape deformation (d_1), and magnitude of the faulting shear (m_1):

Alloy	Fe-25Ni-0.4C	Fe-15Ni-1C
p_1	$\begin{bmatrix} 0.404878 \\ 0.062654 \\ -0.912222 \end{bmatrix}$	$\begin{bmatrix} 0.356808 \\ 0.079278 \\ -0.930808 \end{bmatrix}$
d_1	$\begin{bmatrix} -0.491855 \\ 0.059660 \\ -0.868631 \end{bmatrix}$	$\begin{bmatrix} -0.439235 \\ 0.076239 \\ -0.895132 \end{bmatrix}$
m_1	0.262606	0.269337

(9) The apparent activation energy increases gradually during the first stage of tempering (to about 125 kJ/mole). It is suggested that the motion of the carbide/martensite interface and concurrent carbon diffusion are the two thermally-activated processes which influence the growth rate. The conservative nature of the IPS does not require any intrinsic diffusional transport of metal atoms for sustained growth.

(10) The martensitic substructure does not appear to exert any substantial influence on the aging (spinodal decomposition) behavior. On the other hand, {112} twin boundaries can in some instances catalyze carbide nucleation and in other cases halt carbide growth.

CHAPTER 11

SUGGESTIONS FOR FURTHER STUDY

(1) Experiments should be done to map out the metastable
    miscibility gap in the Fe-C system. It may be possible to map
    out the coherent spinodal by monitoring the electrical
    resistivity behavior **in situ** over a range of temperature.

(2) Uncertainty still exists regarding the nature of the carbon
    ordering in both the tweed structure and the transition carbide.
    Neutron diffraction studies may prove to be more fruitful
    (particularly if alloys can be isotopically enriched in order to
    increase the relative scattering amplitude of the carbon atoms)
    than conventional x-ray and electron diffraction techniques for
    structure determination. A rotating anode x-ray technique (with
    high beam brightness) would also provide a good alternative.

(3) Much work remains in modelling the thermodynamics of body-
    centered Fe-C solutions. The model of this study represents a
    very crude attempt. A thermodynamic description which
    incorporates more details of the interstitial interaction is
    required; Khachaturyan's description provides a good starting
    point for future refinement.

(4) Mechanical testing should be done (in conjunction with TEM) to
    more completely evaluate the influence of spinodal decompostion
    on the mechanical behavior of aged martensite.

(5) The present crystallographic analyses predict a specific ε'-
    carbide/martensite interfacial structure; high resolution TEM

should be done in order to confirm the predictions. In addition, the motion of the interface should be modelled in order to explain the growth kinetics.

(6) An effort should be made to detect spinodal decomposition in a low-carbon lath martensite. Such work would shed more light on the role of substructure, if any, on the aging process. At issue here is whether or not the dense dislocation substructure provides enough low-energy sites for carbon that spinodal decomposition is inhibited. An Fe-Ni-C alloy could be chosen with an M_s temperature high enough to produce a lath-type morphology, yet low enough to prevent any significant carbon segregation during quenching.

(7) High resolution cold stage TEM should be done to document the development of the tweed structure from its earliest stages. A lack of appropriate facilities precluded this in the current investigation.

(8) In-situ heating experiments could be done to observe more directly (via TEM) the coarsening of the tweed and subsequent precipitation of transition carbides.

(9) A more detailed theory of the electrical resistivity behavior of aged and tempered martensites needs to be developed. This would lead to a more meaningful interpretation of the kinetic analyses. Also, the variation (with carbon content) in the magnitude of the increase in resistivity during aging needs to be explained more quantitatively.

APPENDIX A

CALCULATING THE ELECTRICAL RESISTIVITY OF MARTENSITE

The electrical resistivity of the martensites of this study could not be measured directly due to the presence of retained austenite. However, a procedure for correcting for the influence of retained austenite was adopted for this study. It was originally suggested by Hoffman [83] and its description follows that given recently by Sherman et al. [70].

In general, the resistivity of a two-phase mixture will depend on the resistivities of the two phases (here ρ_γ and ρ_α), the relative volume fractions (V_γ and V_α), and on the distribution of the two phases. Two extremes in distribution can be imagined. At one extreme the phases are completely separated from one another, at opposite ends of the specimen. For this case of two resistances in series, the resistivities add, giving:

$$\rho_{\alpha+\gamma} = \rho_\alpha V_\alpha + \rho_\gamma (1 - V_\alpha). \tag{A-1}$$

At the other extreme, the phases are again completely separated, but run continuously from one end of the specimen to the other. For this case of two resistances in parallel, the conductivities add to give:

$$\rho_{\alpha+\gamma} = \left[\frac{V_\alpha}{\rho_\alpha} + \frac{(1 - V_\alpha)}{\rho_\gamma}\right]^{-1}. \tag{A-2}$$

The most general case lies somewhere between these two extremes and can be written:

$$\rho_{\alpha+\gamma} = Z\left[\frac{V_\alpha}{\rho_\alpha} + \frac{(1 - V_\alpha)}{\rho_\gamma}\right]^{-1} + (1 - Z)[\rho_\alpha V_\alpha + \rho_\gamma (1 - V_\alpha)] , \tag{A-3}$$

where Z represents the "fractional parallel character" of the two-phase

mixture, and (1 - Z) the "fractional series character." Equation A-3 can

be solved for ρ_α numerically, when the values of the other variables are

known. Hoffman empirically determined that Z was about 0.65 for an Fe-

23Ni-0.4C alloy and that value was adopted for this work. Although ρ_γ

could not be directly measured at -196°C, it could be estimated by

measuring the temperature dependence of the austenite resistivity over the

range 250°C to just above M_s, and extrapolating this behavior to -196°C.

Figure A-1 illustrates this procedure graphically, where the resistivites

(at -196°C) are seen to be 61.3 and 49.5 $\mu\Omega$-cm for Fe-25Ni-0.4C and Fe-

15Ni-1C, respectively.

Implicit in this entire analysis is the assumption that ρ_γ remains

constant. This, as demonstrated by Eldis [75], turns out to be a valid

assumption.
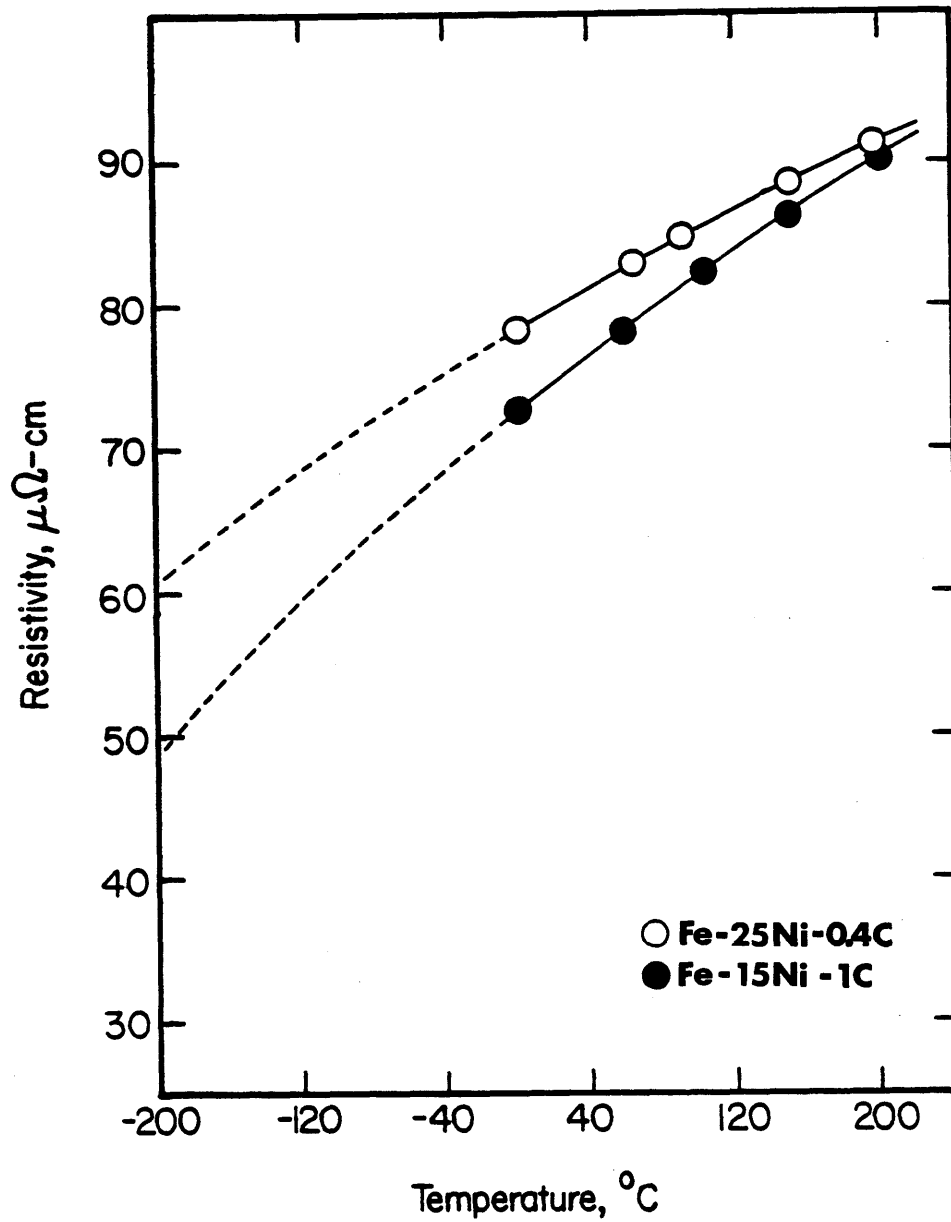
Figure A-1. The temperature dependence of the electrical
resistivity of austenitic Fe-25Ni-0.4C and
Fe-15Ni-1C.

APPENDIX B

TRANSFORMATION OF AUSTENITE TO MARTENSITE

DURING LOW-TEMPERATURE AGING

B.1 Introduction

Previous studies here at MIT [25,75] have shown that when two-phase austenite + virgin martensite Fe-Ni-C alloys are aged below about -40°C, a small but measurable decrease in electrical resistivity takes place ($\Delta\rho_I$). The total change increases with decreasing aging temperature, at least to the lower limit studied, -95°C. In addition, most of the total change occurs after very short times, i.e. less than one minute. Two possible explanations for the observed behavior were originally put forth:

(1) isothermal transformation of retained austenite

to martensite, and

(2) dislocation rearrangements.

Either explanation is plausible since both result in a decrease in resistivity: Over the range of alloy compositions studied, the electrical resistivity of virgin martensite at -196°C is less than that of austenite; also, dislocation rearrangements (which presumably reduce the internal strain energy) reduce the athermal component of electrical resistivity [129].

Eldis [75] rejected explanation (1) after finding no measurable increase in the room-temperature saturation magnetization of samples after low-temperature aging (LTA). Accordingly, both Eldis and Sherman [25] favored explanation (2), although neither presented any substantial direct evidence in support. Evidence is presented here from magnetic and resistometric measurements which supports explanation (1) and hopefully puts this issue to rest. Results on the behavior of samples aged in the vicinity of -130°C are reported. This temperature is close to that found

for the maximum rate of formation of isothermal martensite in various high-alloy steels [7].

B.2 Electrical Resistivity Measurements

The procedure for measuring electrical resistivity is described in Chapter 4. The total change in resistivity due to LTA was determined as follows: Each sample was immersed in liquid nitrogen and held there for 15 minutes, after which its resistance was measured. Each sample was then quickly transferred to a bath of isopentane maintained at $-130\pm5^{\circ}C$ for a period of one hour and then re-immersed in the liquid nitrogen. The electrical resistance was measured again and the percent change noted. The relative change in resistivity is equal to the relative change in resistance here, because the geometric factor (which arises because of the small volume change associated with the martensitic transformation) relating the two relative changes is very nearly unity and can be ignored.

B.3 Saturation Magnetization Measurements

Specimens for magnetic measurements were prepared from both Fe-Ni-C alloys. Discs about 1 mm in thickness were cut from austenitized 3 mm-diameter rods on a low-speed diamond saw. A vibrating-sample magnetometer equipped with a cryostat was used for making the measurements. A simple description of this apparatus may be found in Reference [130]. A Hall probe was inserted between the pole pieces of the electromagnet to measure the applied field, the signal from which drove the x-input to an x-y recorder. The magnetic sample at the end of the vibrating sample rod induced an alternating emf in pick-up coils located near each pole piece. The magnitude of the emf was proportional to the magnetic moment, σ, of the sample and drove the y-input of the x-y recorder. Emf values were

233

converted to magnetic moments using a pure nickel sphere as a calibration standard.

By continuously varying the applied field, H_{app}, plots of σ vs. H_{app} were obtained for all samples including the nickel standard over the range $0 \leq H_{app} \leq 6$ kOe. A typical plot is shown in Figure B-1, obtained from Fe-15Ni-1C. Although the 6 kOe field is not large enough to saturate the sample, it was desirable to estimate the saturation magnetic moment, σ_s, since its magnitude is independent of sample geometry and grain structure. σ_s was estimated by making a plot of σ vs. $1/H_{app}$ using several data points in the 5 kOe $\leq H_{app} \leq 6$ kOe range and extrapolating the least-squares fit to infinite applied field ($1/H_{app} = 0$).

The total change in the saturation moment due to LTA was determined as follows: Completely austenitic samples were placed in a sample cup located at the end of the screw-on extender of the sample rod. The samples were cooled to -196°C to produce ferromagnetic martensite by inserting the rod into the liquid nitrogen-filled cryostat centered between the pole pieces of the magnet. After 15 minutes, a plot of σ (at -196°C) vs. H_{app} was obtained, typically taking about 5 minutes. Immediately afterward, the sample rod was removed from the cryostat and the extender removed and placed in a small dewar containing liquid nitrogen. The extender/sample cup assembly was transported to a bath of isopentane maintained at -130±5°C and immersed in it for one hour. After the aging, the extender was transferred back to the dewar and taken back to the magnetometer whence a new σ vs. H_{app} curve was generated. The saturation moment was calculated for each run and the percent change noted.
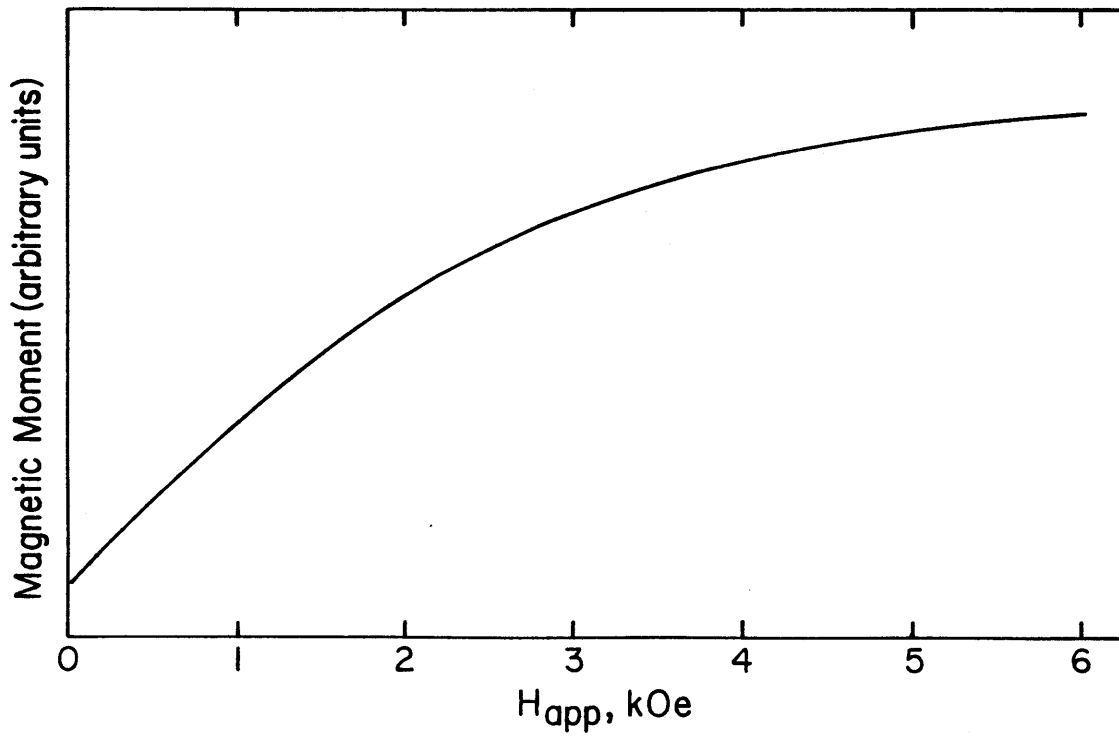
Figure B-1. Magnetic moment (at -196°C) vs. applied field for two-phase Fe-15Ni-1C after quenching to -196°C for 15 minutes.

B.4 Results and Discussion

Table B-1 shows the saturation moment and specific saturation moment for the two Fe-Ni-C alloys both before and after LTA, as well as the percent change. Table B-1 also shows the percent change in electrical resistivity which occurs as a result of LTA, where each value represents the average of thirteen different specimens. In order to get some idea of the kinetics of the process(es) occurring, the electrical resistance (at -196°C) of Fe-15Ni-1C was monitored as a function of aging time at -120°C. The results of this experiment are shown in Figure B-2; it reveals that most of whatever happens occurs very quickly, i.e. within one minute.

The most interesting result of this investigation concerns the measureable increase in the saturation moment of aged samples. Eldis [75] found no such increase; however, his measurements were conducted at room temperature. Now the significance of Figure B-2 becomes clear; the bulk of the low-temperature transformation could have occurred before Eldis made his measurements, while his samples were warming to room temperature. Furthermore, room-temperature aging may have influenced his results. In either case, the only obvious explanation for the increase in magnetic moment is a corresponding increase in the amount of ferromagnetic phase, and since the austenites studied are paramagnetic, some austenite must be transforming to martensite. It is unlikely that LTA processes involve the redistribution of carbon atoms because their diffusivity is negligibly small below about -40°C [2].

The crucial difference between this investigation and that of Eldis is that here the magnetic moments were measured at -196°C. Eldis' results were confirmed, however, when additional **room-temperature** magnetic measurements were done on Fe-15Ni-1C. Here, **no change** in saturation moment

236

TABLE B-1

CHANGES IN SATURATION MOMENT AND ELECTRICAL
RESISTIVITY (AT -196°C) DUE TO LTA

Alloy	Mass (mgr)	Saturation Moment (emu)		Specific Saturation Moment (emu/gr)		Percent Change	Percent Change in Resistivity
		b/4 LTA	after LTA	b/4 LTA	after LTA		
Fe-25Ni-0.4C	69.9	12.49	12.95	178.7	185.3	+3.7	-2.03
Fe-15Ni-1C	62.4	8.51	9.39	136.3	150.6	+10.5	-1.57
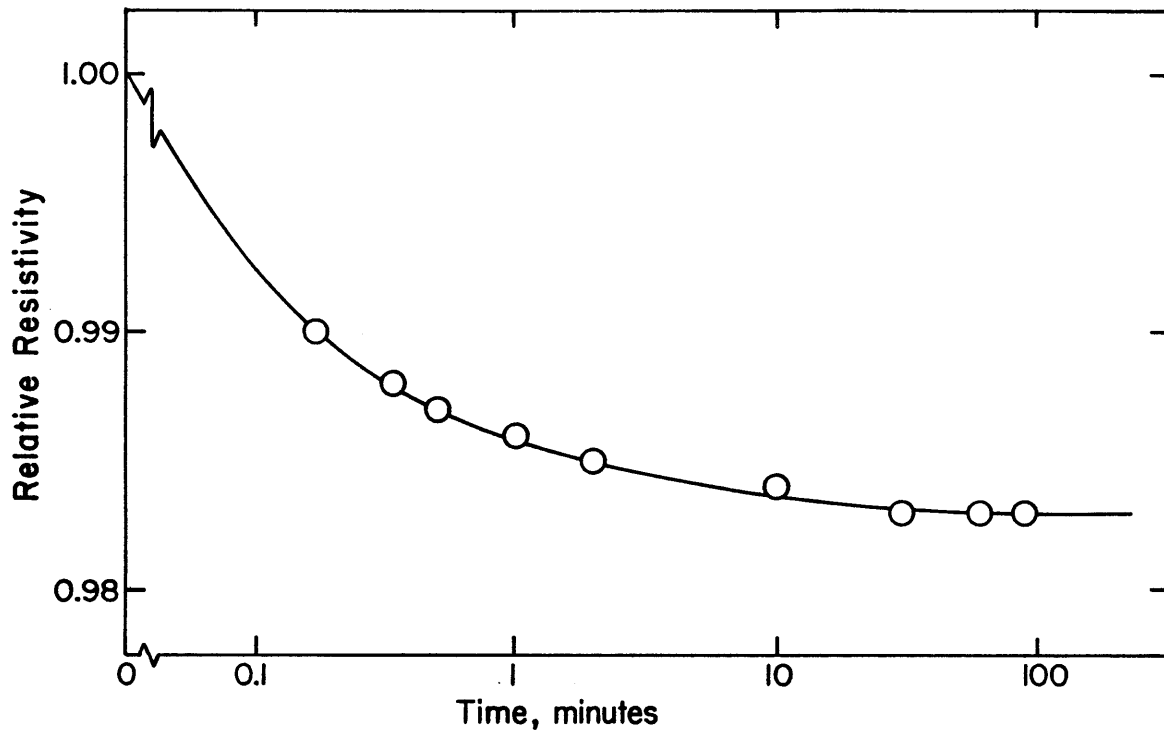
Figure B-2.   Relative resistivity (at -196°C) of Fe-15Ni-1C as a
function of aging time at -120°C.

was found after LTA, presumably because the additional transformation occurred before the first measurement, during the initial warm-up from -196°C to room temperature.

If we assume that the LTA behavior is due to the transformation of retained austenite, then the amount of such transformation can be estimated by starting with Equation A-3, developed by Hoffman [83] to correct measured electrical resistivities for the influence of retained austenite. That expression can be re-written as follows:

$$\frac{R_{\alpha+\gamma}^{-196}}{R_\gamma^0} = Z \left[\frac{V_\alpha}{R_\alpha^{-196}/R_\gamma^0} + \frac{(1-V_\alpha)}{R_\gamma^{-196}/R_\gamma^0}\right]^{-1} + (1-Z)\left[V_\alpha \cdot \frac{R_\alpha^{-196}}{R_\gamma^0} + (1-V_\alpha) \cdot \frac{R_\gamma^{-196}}{R_\gamma^0}\right] \quad \text{(B-1)}$$

Here R represents resistance, with the superscript denoting temperature in degrees Centigrade and the subscript the appropriate phase, martensite (α) or austenite (γ). The "fractional parallel character" of the two-phase mixture is denoted by Z and V_α is the volume fraction of martensite. The resistance of pure austenite at 0°C, R_γ^0, was incorporated in Equation B-1 because this quantity was measured for all resistivity samples and provides a convenient basis for normalizing the other resistances appearing in Equation B-1. This procedure eliminates the need to convert resistances to resistivities[*], where an accurate measure of sample geometry is otherwise required. Equation B-1 can be differentiated with respect to V_α to yield:

$$\frac{\partial\left(\frac{R_{\alpha+\gamma}^{-196}}{R_\gamma^0}\right)}{\partial V_\alpha} = \Delta R_{\gamma\to\alpha} \cdot \left[1 + Z\left(\frac{P'}{\underset{\sim}{S'}} - 1\right)\right], \quad \text{(B-2)}$$

where $\quad \Delta R_{\gamma\to\alpha} = (R_\alpha^{-196} - R_\gamma^{-196})/R_\gamma^0$

---

[*] Transformational and thermal expansions have been neglected.

$$P' = \left[\frac{V_\alpha}{R_\alpha^{-196}/R_\gamma^0} + \frac{(1-V_\alpha)}{R_\gamma^{-196}/R_\gamma^0}\right]^{-1}$$

and $$\tilde{S}' = V_\alpha \cdot (R_\gamma^{-196}/R_\gamma^0) + (1-V_\alpha) \cdot (R_\alpha^{-196}/R_\gamma^0).$$

In the limit of small changes in V_α,

$$\Delta V_\alpha = \frac{\Delta\left(\frac{R_{\alpha+\gamma}^{-196}}{R_\gamma^0}\right)}{\Delta R_{\gamma\to\alpha} \cdot \left[1 + Z\left(\frac{P'}{\tilde{S}'} - 1\right)\right]}. \tag{B-3}$$

Equation B-3 gives the change in the volume fraction of martensite, ΔV_α, in terms of known or measureable quantities. The change in resistance, normalized to the resistance of pure austenite at 0°C, $\Delta(R_{\alpha+\gamma}^{-196}/R_\gamma^0)$, was found to be -7.60×10^{-3} and -9.07×10^{-3} for Fe-25Ni-0.4C and Fe-15Ni-1C, respectively. The remaining quantities are given in Table 6-1 and Appendix A.

Table B-2 shows the calculated ΔV_α for each alloy. Included in the table is the corresponding value based on the magnetization change, where the increase in moment is assumed to reflect a proportional increase in V_α. The two independently-calculated values agree rather well and leave little doubt that the dominant process occurring during LTA involves the conversion of some retained austenite to martensite. In fact, the results imply that, of the austenite which survives the initial quench to -196°C, 16.2% and 15.4% later transforms to martensite (during aging at -130°C) in Fe-25Ni-0.4C and Fe-15Ni-1C, respectively.

Before leaving this issue, it should be mentioned that LTA does not always result in a decrease in electrical resistivity. An **increase** in resistivity is actually measured in very-high-carbon alloys (wt pct carbon > 1.4). This reversal of behavior can be understood by referring to

240

TABLE B-2

INCREASE IN THE VOLUME FRACTION OF MARTENSITE (ΔV_α)
DUE TO LTA

$$\Delta V_\alpha$$

Alloy	Based on Resistivity Change	Based on Magnetization Change
Fe-25Ni-0.4C	0.029	0.030
Fe-15Ni-1C	0.057	0.064

Figure B-3, where the resistivities (at -196°C) of the austenitic and

virgin martensitic phases of several different Fe-(Ni,Mn)-C alloys are

plotted.   Even though these alloys contain substantial substitutional

solutes, a clear trend emerges from the plot: namely, that the resistivity

of virgin martensite tends to increase with carbon content while that of

austenite decreases.   Both variations appear to be linear with carbon

content.   The resistivity of the two phases are equal at about 1.4 wt pct

carbon.   Therefore, below this carbon level the transformation of austenite

to martensite produces a net **decrease** in resistivity;   a net **increase**

results above 1.4 wt pct carbon.
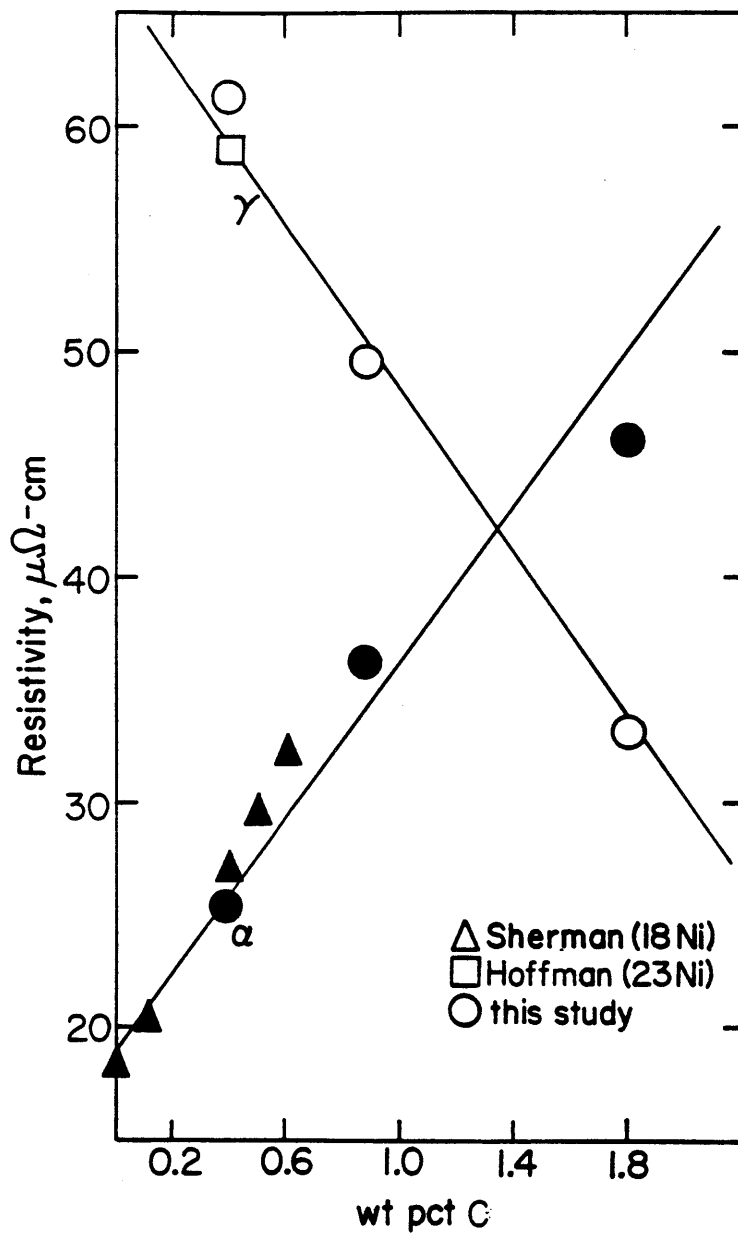
Figure B-3. Electrical resistivity of austenitic
(open figures) and virgin martensitic
(solid figures) Fe-Ni-C and Fe-Mn-C
alloys at -196°C.

APPENDIX C

THE ROLE OF SUBSTRUCTURE IN AUTOTEMPERING

Alloys with subambient M_s temperatures were deliberately chosen for the present study of aging and tempering in order to eliminate autotempering (the redistribution of carbon atoms) during the actual formation of the martensitic phase. In contrast, the M_s temperatures of binary iron-low- and medium-carbon alloys are so high that some degree of carbon-atom redistribution must be expected in all cases where conventional quenching methods are employed.

The phenomenon of autotempering was recognized by Speich [28] in his well-known study of the electrical resistivity of freshly-quenched Fe-C alloys. He examined alloys containing between 0.026 and 0.57 wt pct carbon and reported the behavior (at $-196^{\circ}C$) shown in Figure C-1. The important feature of Figure C-1 is the occurrence of two regimes where the carbon-concentration dependence of the resistivity is different. From zero to about 0.2 wt pct carbon, the resistivity increases with a slope of 10 $\mu\Omega$-cm/(w/oC). Above 0.2 wt pct, the resistivity increases at a rate of about 29.5 $\mu\Omega$-cm/(w/oC). Speich took this behavior to imply that some fraction of the carbon atoms (in a given alloy) move to low-energy sites during quenching, and that the contribution of such carbon atoms to the total resistivity is less than for carbon atoms occupying "normal" interstitial sites. He postulated that the low-energy sites are located near dislocations and lath boundaries, where the strain fields of such defects produce sites which can more easily accommodate carbon atoms. The breakpoint at 0.2 wt pct carbon in Figure C-1 was taken to reflect the saturation of low-energy sites by carbon. Speich noted that this is also the concentration where the tetragonality of iron-carbon martensite can

244
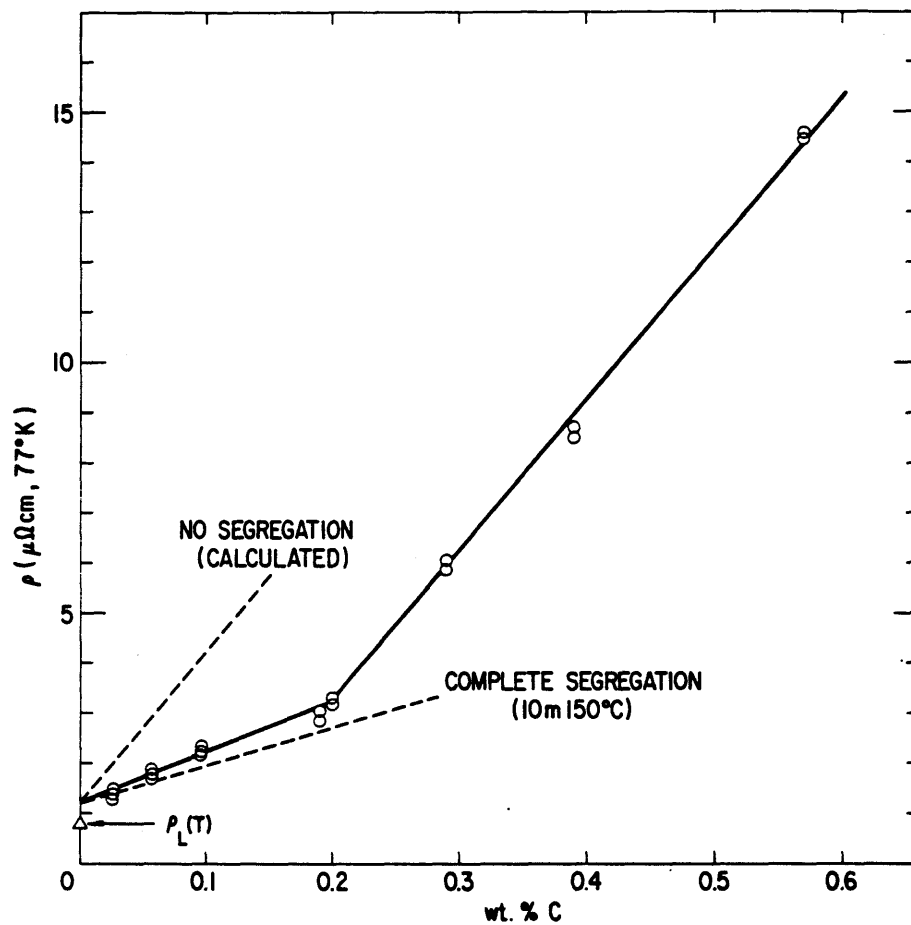
Figure C-1. Electrical resistivity of as-quenched Fe-C
            martensites at -196°C (from Speich [28]).

first be detected (by x-ray diffraction).

To lend further support for his interpretation of the resistivity behavior, Speich calculated the distance which carbon atoms could diffuse during quenching. For this analysis, he used the carbon diffusivity (in α-iron) data of Smith [131] and assumed that his quenching procedure could be approximated as a Newtonian cooling process. He further assumed that all of the martensite formed effectively at $1/2(M_s + M_f)$. His results suggest that below about 0.3 wt pct carbon, the M_s is high enough that all carbon atoms can move to lath boundaries during quenching (although there may not be enough total boundary sites to accommodate all carbon atoms). Furthermore, for his estimated interlath dislocation density of the martensite (0.15×10^{12} cm^{-2}), the results also indicated that complete segregation to dislocations occurs for all of the compositions he studied. This analysis was taken as firm support of the notion that lath boundaries and dislocations can "dissolve" some 0.2 wt pct carbon in lath martensites.

The results of Speich, as well as those of a number of studies undertaken over the years [26,58], have provided some convincing evidence of the trapping of carbon atoms by substructural defects. This implies that the role of substructure during aging and tempering may be significant, particularly for lath martensites, where the defect content is regarded to be much higher than in martensites of the plate-type morphology. More recently, however, the electrical resistivity study conducted by Sherman [25] has cast some doubt on this conclusion. Sherman found, perhaps surprisingly, that the resistivity behavior which accompanies the aging and tempering of initially-virgin Fe-Ni-C martensites was qualitatively the same over a wide range of carbon contents, in spite of differences in the martensitic morphology. In the remainder of this

246

Appendix, it will be demonstrated that the resistivity behavior observed by Speich can be explained in terms of the resistivity behavior intrinsic to the aging and tempering processes and that no special significance need be associated with the breakpoint in resistivity observed by Speich at 0.2 wt pct carbon.

Consider the resistivity behavior (as a function of carbon content) of virgin Fe-18Ni-C martensites as reported by Sherman. The reader will recall that these data were presented in Figure 6-5, where the resistivity increases linearly (with no breakpoint) with carbon over the range studied, indicating that all carbon atoms are in solution in virgin martensite. Sherman's data are replotted along with Speich's data for Fe-C alloys in Figure C-2. Included with Sherman's data is the resistivity for the Fe-15Ni-1C alloy of the present investigation. The rather large offset in absolute resistivity for the two sets of data is not important for the present purposes and can be attributed to the presence of nickel in Sherman's alloys. One may now pose the question: What would the resistivity behavior (as a function of carbon content) look like for the Fe-18Ni-C alloys if they were aged and tempered to the same extent as the corresponding autotempered Fe-C alloys studied by Speich? This question can be answered by following the procedure described in the next paragraph.

One of the key parameters in Speich's resistivity analysis is $(Dt)_q$, the effective product of the carbon diffusivity and time characteristic of his quenching procedure. Here, D represents the diffusivity of carbon and t is time. Thus, $2(Dt)_q^{1/2}$ provides a measure of the distance which carbon atoms can diffuse during quenching and therefore $(Dt)_q$ can be taken as a parameter which describes the extent of autotempering. Accordingly, a (Dt) scale can also be constructed for an isothermal aging/tempering experiment

247
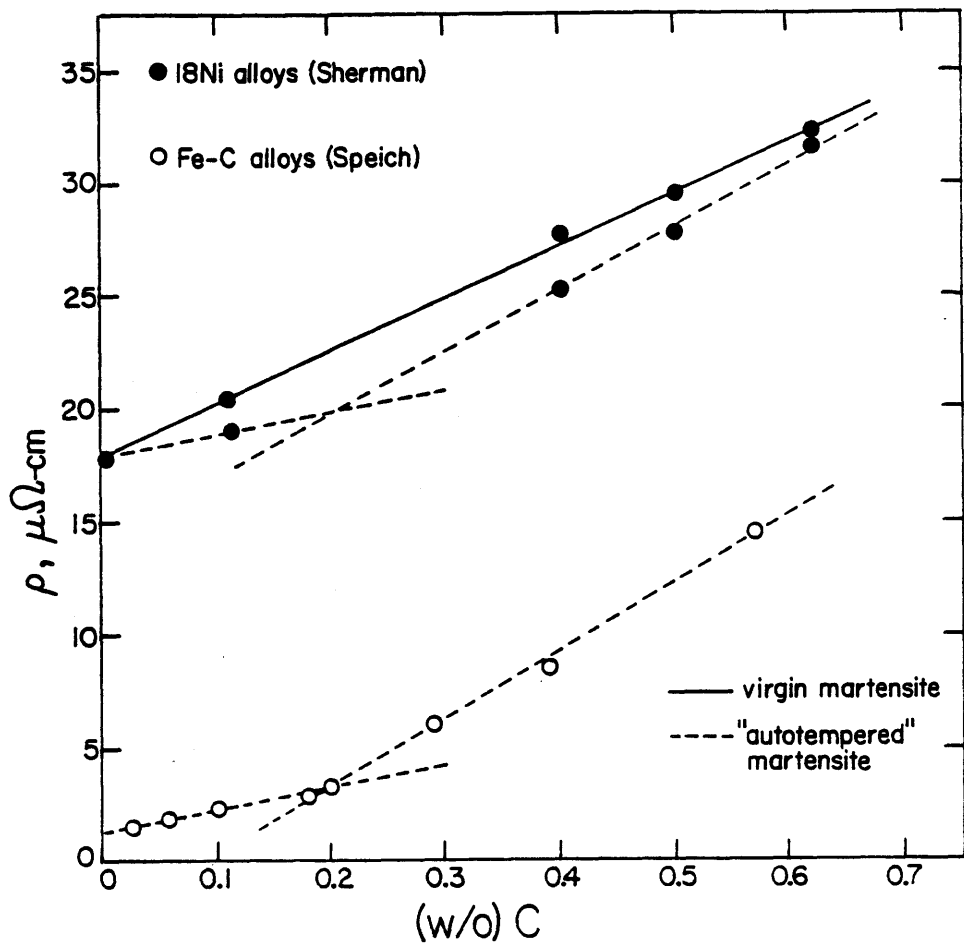
Figure C-2. Electrical resistivity of virgin and "autotempered" Fe-18Ni-C martensites and as-quenched (autotempered) Fe-C martensites at -196°C. Each data point for the Fe-18Ni-C alloys represents the average of several (slightly) different resistivities obtained from experiments run at different temperatures. See text for discussion.

where the electrical resistivity is monitored as a function of time. Such scales were constructed for the Fe-18Ni-C alloys using the concentration-dependent diffusivity of carbon in martensite proposed by Hillert (Equation 5-1). A plot of the resistivity of "autotempered" Fe-18Ni-C martensites analogous to Speich's plot for Fe-C alloys can then be constructed by:

(1) Calculating $(Dt)_q$ for each of the Fe-18Ni-C alloys in a manner completely analogous to that of Speich (see [28]), i.e. under the assumption that the transformation to martensite occurs at the same temperature as given by $1/2(M_s + M_f)$ for the corresponding Fe-C alloy, and that Newtonian cooling prevails. This procedure yields $(Dt)_q$'s for hypothetical Fe-Ni-C alloys which transform at the same temperature as the corresponding Fe-C alloys.

(2) With a calculated $(Dt)_q$ for each Fe-18Ni-C alloy in hand, reference is then made to the resistivity curves obtained from the isothermal aging/tempering experiments. Since a (Dt) scale can be constructed for any given experiment, the resistivity characteristic of $(Dt)_q$ can be obtained directly from the resistivity curves for each alloy.

This two-step procedure provides a means for incorporating the effects of autotempering into the as-quenched resistivity of the martensite, even for alloys where true autotempering does not occur (such as in the Fe-Ni-C alloys of this study). The results for the alloys studied by Sherman are denoted by the dashed line in Figure C-2. The similarity of the resistivity behavior (ignoring the vertical offset) between the Fe-18Ni-C and the Fe-C alloys is striking. The breakpoint in the behavior of the Fe-C alloys is also evident in the behavior of the Fe-18Ni-C alloys, and occurs at about the same composition. Moreover, the slopes of the two line

segments are about the same for each alloy class, namely 10.0 $\mu\Omega$-cm/(w/oC)

vs. 10.3 $\mu\Omega$-cm/(w/oC) and 29.5 $\mu\Omega$-cm/(w/oC) vs. 29.6 $\mu\Omega$-cm/(w/oC) for the

Fe-C and Fe-18Ni-C alloys, respectively. This close quantitative agreement

may be somewhat fortuitous since one set of alloys contains an appreciable

amount of nickel.

The similarity of the "autotempered" resistivity behavior between the

Fe-C and Fe-Ni-C alloys suggests that the processes of aging and tempering

are similar in the two alloy classes. This result does not, however,

permit any a priori conclusions to be drawn from the anomalous behavior at

0.2 wt pct carbon. If anything, Sherman's study suggests that the

substructural differences among ferrous martensites do not lead to any

significant differences in their resistivity behavior during aging and

tempering. This conclusion does not necessarily rule out carbon

segregation to defects, but it does indicate that any such segregation does

not substantially affect the resistivity.

APPENDIX D

OXIDATION OF TEM THIN FOILS

Thin oxide films were frequently observed on specimen surfaces during the course of the present TEM study of aging and tempering. Figure D-1 is a typical example of an oxide-contaminated foil. In this image, the fine cross-hatched striations are due to the modulated structure of aged martensite; the oxide causes a coarse mottling of the image, particularly in the strongly-diffracting (dark) regions.

At least two different oxide morphologies were detected on the alloys under investigation here. Oxide sometimes grew on the alloy substrate epitaxially, giving rise to single-crystal "spot-type" electron diffraction patterns. On the other hand, "ring-type" electron diffraction patterns were frequently observed, indicating the presence of a fine-grained oxide which apparently exhibits no specific orientation relationship with the martensite.

D.1 Oxide Crystallography

The analysis of numerous electron diffraction patterns has revealed that the epitaxial oxide is magnetite (Fe_3O_4) or perhaps trevorite ($NiFe_2O_4$). These two compounds have the same crystal structure and differ only in that nickel substitutes for ferrous iron in trevorite. X-ray diffraction data for these two cubic, spinel-like phases are given in Table D-1.

Figure D-2(A) is an electron diffraction pattern taken from Fe-15Ni-1C with the beam incident along the martensite [001] direction. Flanking the transmitted beam are the four $\{220\}_0^*$ reflections of the magnetite [001] zone. Further evidence of magnetite formation is shown in the diffraction

251

* The subscript "0" refers to the magnetite (or trevorite) lattice.

Figure D-1. Bright field (**g** = 020) image of martensitic Fe-15Ni-1C aged
2.75 hrs at room temperature. The beam direction is near
[100], but tilted slightly about [010]. In the inset
diffraction pattern, spots denoted by arrows are due to
epitaxial oxide.

TABLE D-1

INTERPLANAR SPACINGS AND INTENSITIES FOR MAGNETITE AND TREVORITE[*]

	Magnetite (Fe_3O_4) (a = 0.83963 nm)		Trevorite ($NiFe_2O_4$) (a = 0.8339 nm)	
hkl	d, nm	I/I_1	d, nm	I/I_1
111	0.485	40	0.482	20
220	0.2966	70	0.2948	30
311	0.2530	100	0.2513	100
222	0.2419	10	0.2408	8
400	0.2096	70	0.2085	25
422	0.1712	60	0.1703	8
333,511	0.1614	85	0.1605	30
440	0.1483	85	0.1476	40
620	0.1327	20	0.1319	6
533	0.1279	30	0.1271	10
622	0.1264	10	0.1257	4
444	0.1211	20	0.1204	6
642	0.1121	30	0.1115	6
553,731	0.1092	60	0.1086	16
800	0.1049	40	0.1042	6
660,822	0.0989	10	0.0983	2
555,751	0.0969	40	0.0963	10
840	0.0939	30	0.0932	8
931	0.0879	40		
844	0.0857	50		
951	0.0811	40		

[*] From the Powder Diffraction File.

253

020

004 022 011
040

022 200

◯ hkl BCC
● hkl magnetite

254
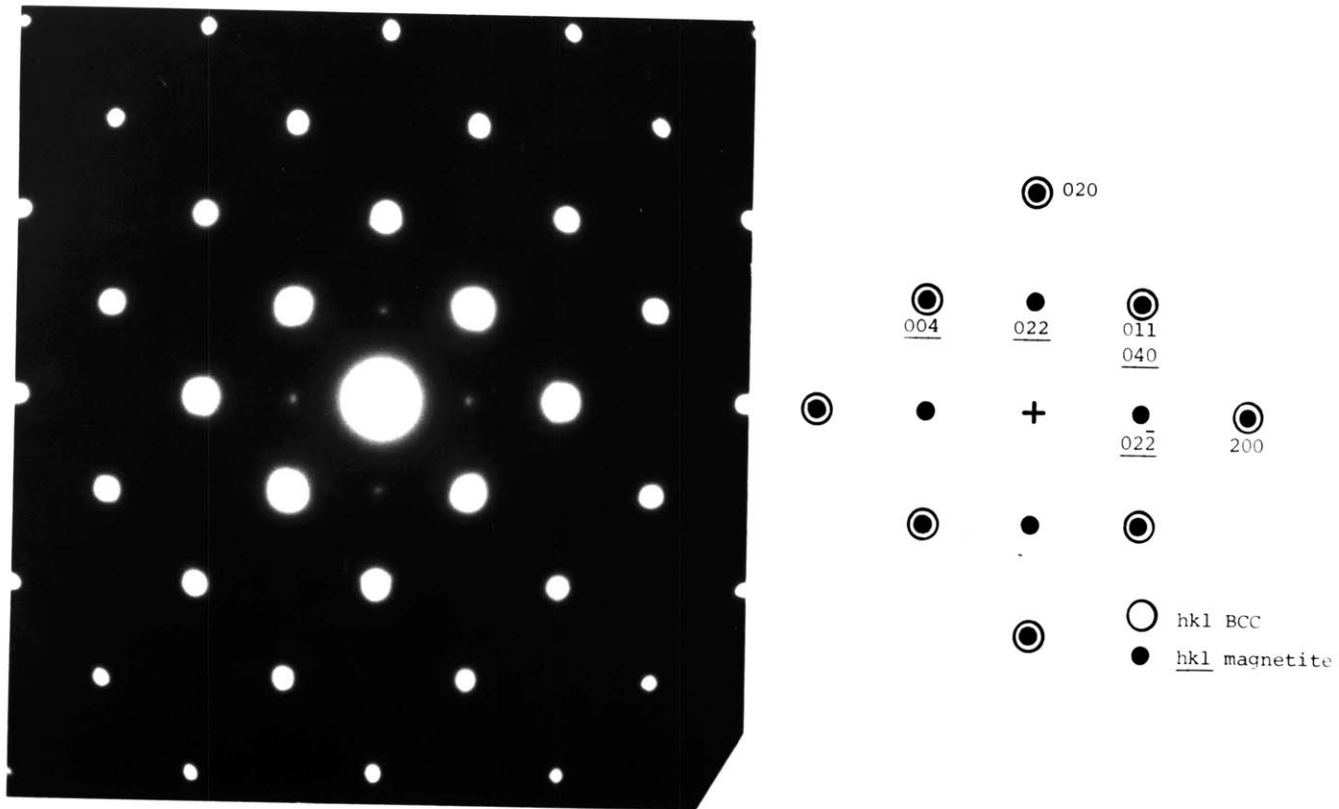
Figure D-2(A).   [001] diffraction pattern (and its indexed schematic diagram) from martensitic Fe-15Ni-1C, aged 2.5 hours at room temperature. The diffraction pattern was exposed to the extent that the martensite {200} and magnetite {044} reflections are not resolvable and have, for simplicity, been illustrated as coinciding.
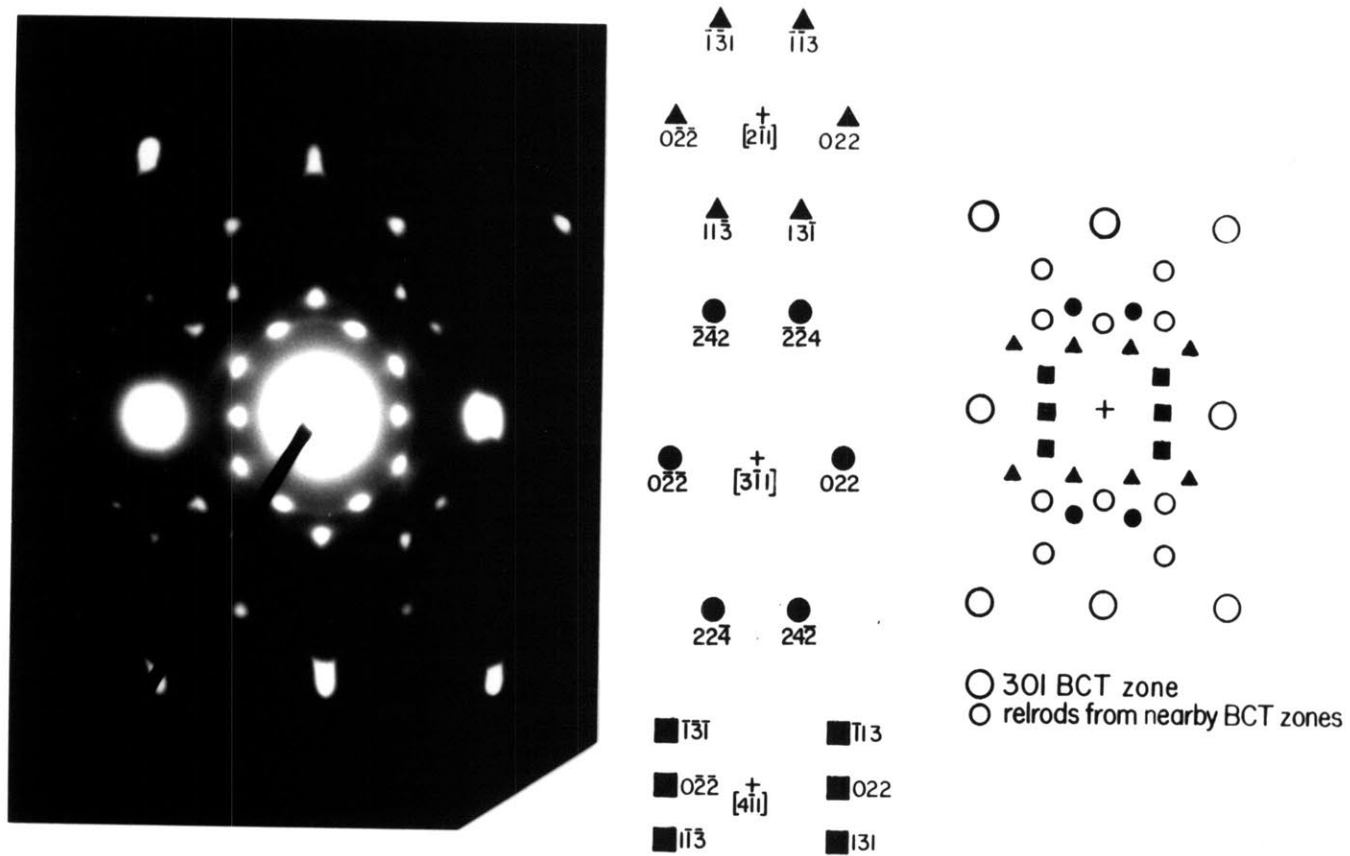
Figure D-2(B). Diffraction pattern from martensitic Fe-15Ni-1C, aged 10 days at room temperature. The specimen orientation is similar to Figure D-1, except tilted further about [010] such that the beam direction is actually near $[301]_\alpha$. Also shown are schematic diagrams of the magnetite $[2\bar{1}1]$, $[3\bar{1}1]$, and $[4\bar{1}1]$ zones, as well as a composite diagram.

pattern of Figure D-2(B), where the beam direction is near $[301]_\alpha$.

Numerous "extra" spots occur, which can be indexed as belonging to the

$[2\bar{1}1]_O$, $[3\bar{1}1]_O$, and $[4\bar{1}1]_O$ zones. Though these zone axes span some 16°,

their simultaneous presence can be rationalized on the basis that the

thickness of the oxide film is very small and leads to appreciable

lengthening of relrods along the incident beam direction.

Several sets of interplanar spacings were measured from Figure D-2 and

are included in Table D-2. The agreement between the measured values and

those for magnetite and trevorite is quite good.

The diffraction patterns of Figure D-2 are consistent with the

following Bain-type orientation relationship between martensite and

magnetite:

$$(0\bar{1}1)_O \; \| \; (001)_\alpha$$
$$\text{and } [100]_O \; \| \; [100]_\alpha \; .$$

This relationship is identical to that reported in both room-temperature

[132] and higher-temperature [133] oxidation studies of pure iron and

represents an optimum matching of iron atoms in both phases [134]. The

Bain orientation relationship was also observed by Chen and Morris [135] in

their study of room-temperature oxidized Fe-Ni and Fe-Ni-Mn,Ti thin foils.

When the foil normal deviated significantly from $\{100\}_\alpha$, Chen and Morris

noted a different orientation relationship, the Nishiyama-Wasserman (N-W)

relationship [136,137]:

$$(0\bar{1}1)_O \; \| \; (001)_\alpha$$
$$\text{and } [211]_O \; \| \; [110]_\alpha \; .$$

Both the Bain and N-W relationships are shown in the stereographic

TABLE D-2

MEASURED OXIDE INTERPLANAR SPACINGS

	MAGNETITE	FINE-GRAINED OXIDE (magnetite or maghemite)	
h,k,l	spacing, nm	spacing, nm	visual intensity*
111	0.487	0.251	vs
220	0.296	0.207	s
311	0.256	0.163	w
		0.147	s
		0.126	vw
		0.120	w
		0.109	vw
		0.102	w
		0.092	w
		0.084	w

* vs-very strong, s-strong, w-weak, vw-very weak

projections of Figure D-3. The two are closely related in that the N-W

relationship can be brought into coincidence with that of Bain by a slight

rotation ($\sim 9^\circ$) about $[0\bar{1}1]_0$. Arguments based upon strain energy have been

presented to explain the transition from the Bain to the N-W orientation

relationship [134,135]. The similarity between the Bain and N-W

relationships make the discrimination between the two very difficult in

this investigation.

Evidence is presented in Figure D-4(A) of the fine-grained oxide,

which produces a ring pattern. At least two and sometimes three distinct

rings appear in diffraction patterns. In Figure D-4(B), these correspond

to interplanar spacings of 0.251, 0.207, and 0.147 nm. Higher-index rings

also appear on patterns taken with a long exposure; however, they are so

weak and diffuse that their accurate measurement is difficult. Measured

interplanar spacings for the fine-grained oxide are included in Table D-2.

Sometimes distinct spots were found embedded in the rings, suggesting that

there may be some tendency toward preferred orientation. This oxide is

probably magnetite or some form of Fe_2O_3. Ring patterns from Fe_2O_3 were

reported by Ali and Wood [132] when pure iron was oxidized in air at room

temperature. The two forms of Fe_2O_3 found in the Powder Diffraction File

are α-Fe_2O_3, hematite, and γ-Fe_2O_3, maghemite. Data for these compounds

can be found in Table D-3. The measured interplanar spacings agree about

equally well with those for maghemite and for magnetite, and therefore the

fine-grained oxide cannot be unambiguously identified. It seems unlikely

that the ring patterns are due to hematite since the two most intense rings

for hematite are absent.

D.2 Oxide Occurrence and Morphology

The information on oxide films reported here is a by-product of the
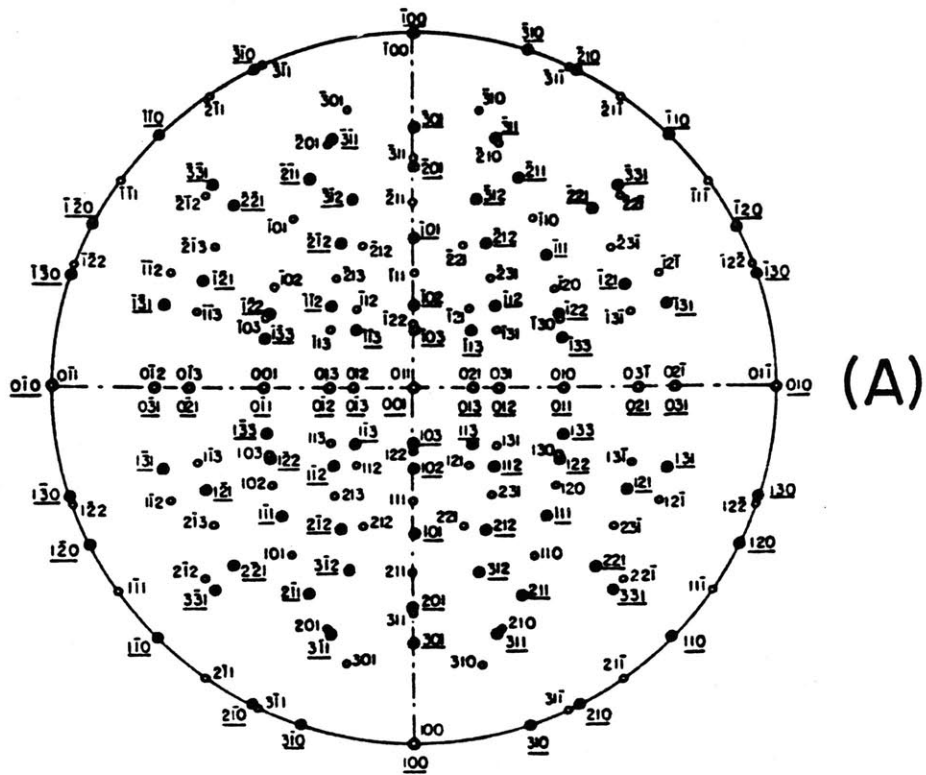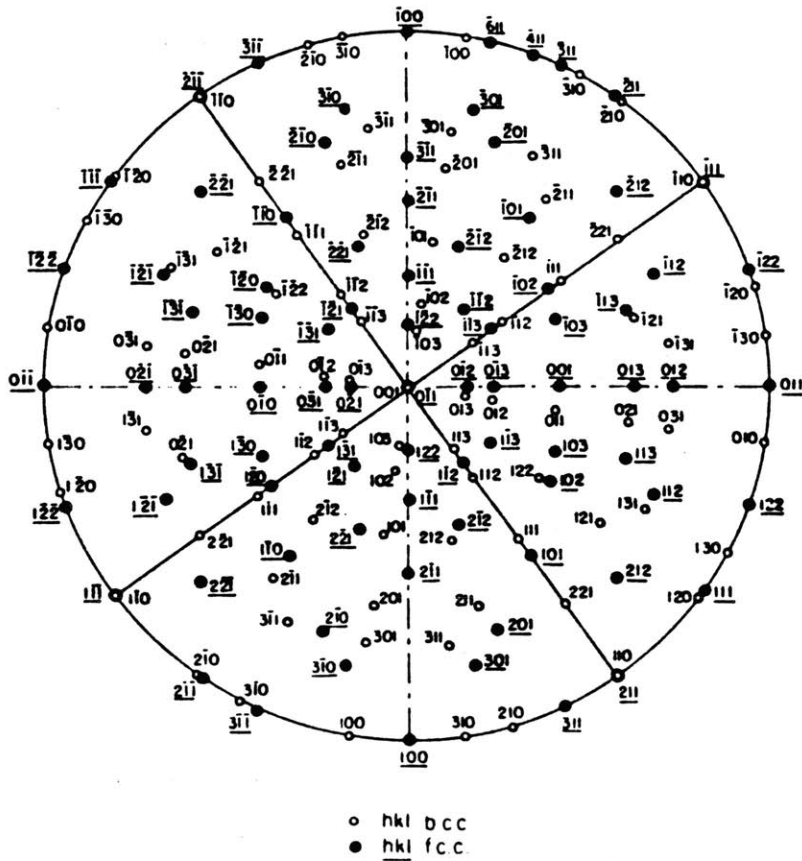
Figure D-3. Stereographic projections representing the Bain relationship between body- and face-centered cubic structures (A) and the Nishiyama-Wasserman (N-W) relationship (B) (from Chen and Morris [135]).
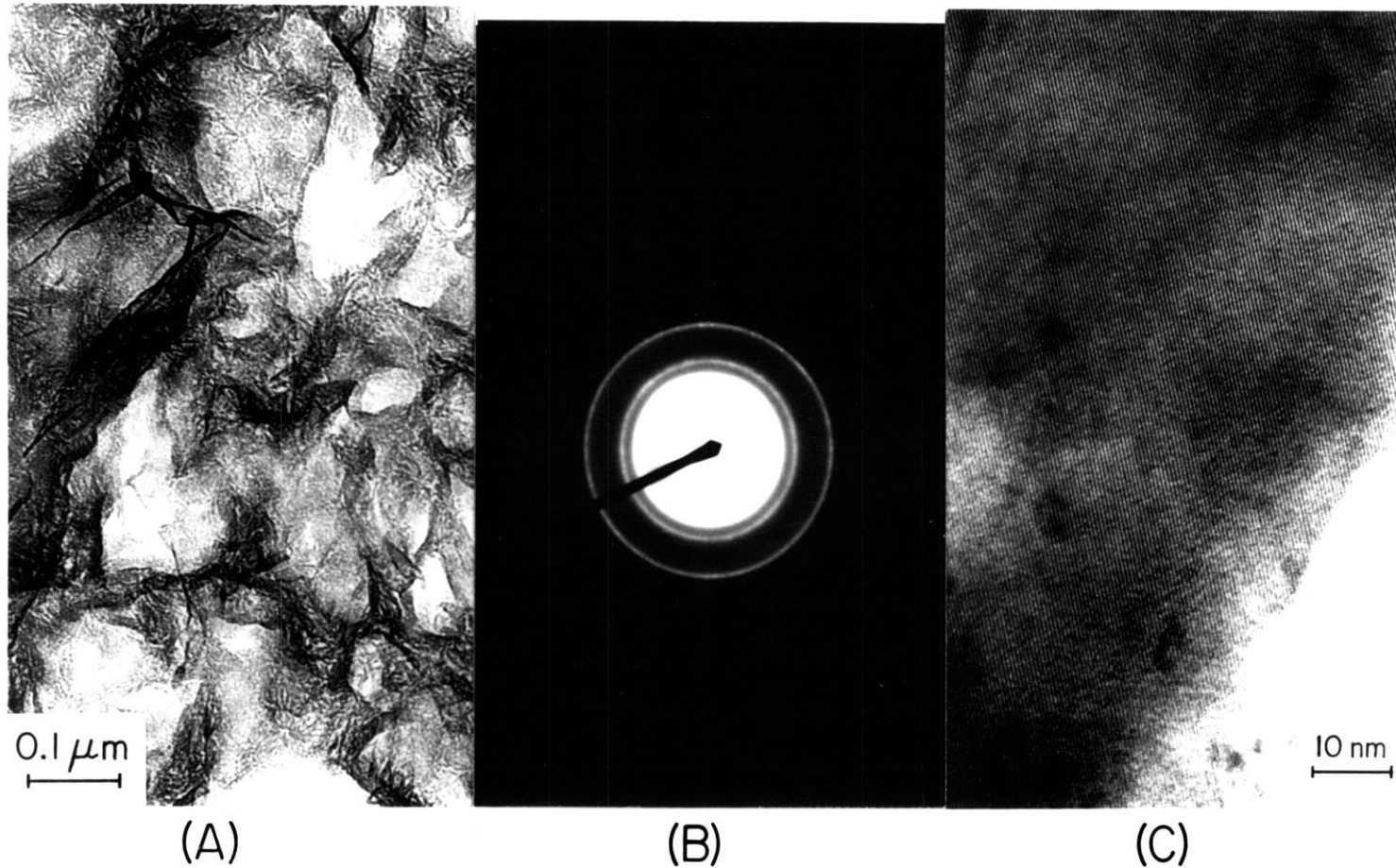
Figure D-4.   Bright-field image of polycrystalline, randomly-oriented oxide (A), and (B), its associated diffraction pattern (from Fe-15Ni-1C, aged 6 hours at room temperature). Note the wrinkled texture of the oxide. This oxide is most likely maghemite. (C) is a lattice fringe image of a single-crystal surface phase (on martensitic Fe-25Ni-0.4C), probably magnetite. The fringe spacing is 0.484 nm.

TABLE D-3

INTERPLANAR SPACINGS AND INTENSITIES
FOR HEMATITE AND MAGHEMITE[*]

Hematite (α-Fe$_2$O$_3$)			Maghemite (γ-Fe$_2$O$_3$)		
hkl	d,nm	I/I$_1$	hkl	d,nm	I/I$_1$
012	0.366	25	101	0.791	1
104	0.269	100	102	0.694	2
110	0.251	50	110	0.590	6
006	0.2285	2	113	0.482	6
113	0.2201	30	114	0.429	2
202	0.2070	2	210	0.373	6
024	0.1838	40	213	0.340	7
116	0.1690	60	214	0.320	3
211	0.1634	4	220	0.295	30
018	0.1596	16	300	0.278	3
214	0.1484	35	310	0.2638	4
300	0.1452	35	313	0.2514	100
208	0.1349	4	226	0.2408	2
119	0.1310	20	323	0.2230	2
220	0.1258	8	400	0.2086	15
036	0.1226	2	420	0.1865	1
223	0.1213	4	423	0.1820	3
128	0.1189	8	426	0.1701	9
02$\underline{10}$	0.1162	10	430	0.1670	2
13$\overline{4}$	0.1141	12	513	0.1604	20
226	0.1102	14	520	0.1550	2
042	0.1076	2	523	0.1525	3
21$\underline{10}$	0.1055	18	440	0.1474	40
11$\overline{12}$	0.1042	2	620	0.1318	6
$\overline{4}$04	0.1038	2	539	0.1272	8
232,318	0.0989	10	626	0.1258	3
229	0.0972	2	44$\underline{12}$	0.1204	5
324	0.0960	18	6$\overline{46}$	0.1115	6
011$\overline{4}$	0.0958	6	733	0.1086	10
140,0$\overline{21}$3	0.0951	12	800	0.1043	7
413^{-}	0.0931	6	826	0.0983	5
048	0.0920	6	753	0.0963	8
13$\underline{10}$	0.0908	25	840	0.0932	4

[*] From the Powder Diffraction File.

261

current study of aging and tempering, and as such neither the kinetics nor the conditions favoring oxidation were extensively studied. The following facts were, however, noted:

(1) Both oxides formed on each of the alloys studied.

(2) Oxide was found on freshly thinned samples as well as samples stored for long periods of time at room temperature.

(3) Oxide formed on tempered samples bearing carbides as well as on nominally untempered samples.

The formation of oxide on the TEM foils of this study is difficult to avoid; oxidation occurred in spite of the fact that specimens were stored in an evacuated dessicator. Indeed, as noted above, even freshly-thinned specimens exhibited oxide. Chen and Morris also found the formation of oxide unavoidable, even when specimens were prepared by different procedures.

In this investigation, most of the evidence of epitaxial magnetite comes from diffraction patterns taken near a $\{100\}_\alpha$ orientation. The fact that comparatively less oxide was detected at higher-index orientations suggests that the rate of magnetite formation is anisotropic (sensitive to the specimen surface orientation). Chen and Morris also observed that the rate of oxidation was greatest for $\{100\}_\alpha$ orientations; the rate for more closely-packed orientations (such as $\{110\}_\alpha$) was much lower.

Evidence is presented in Figure D-5 which suggests that the magnetite layers consist of extremely fine (1-5 nm) oxide particles. The corresponding dark-field image, taken with an $\{220\}_0$ reflection, reveals small bright spots which may be individual magnetite crystallites (all having the same orientation). Chen and Morris also derived this conclusion
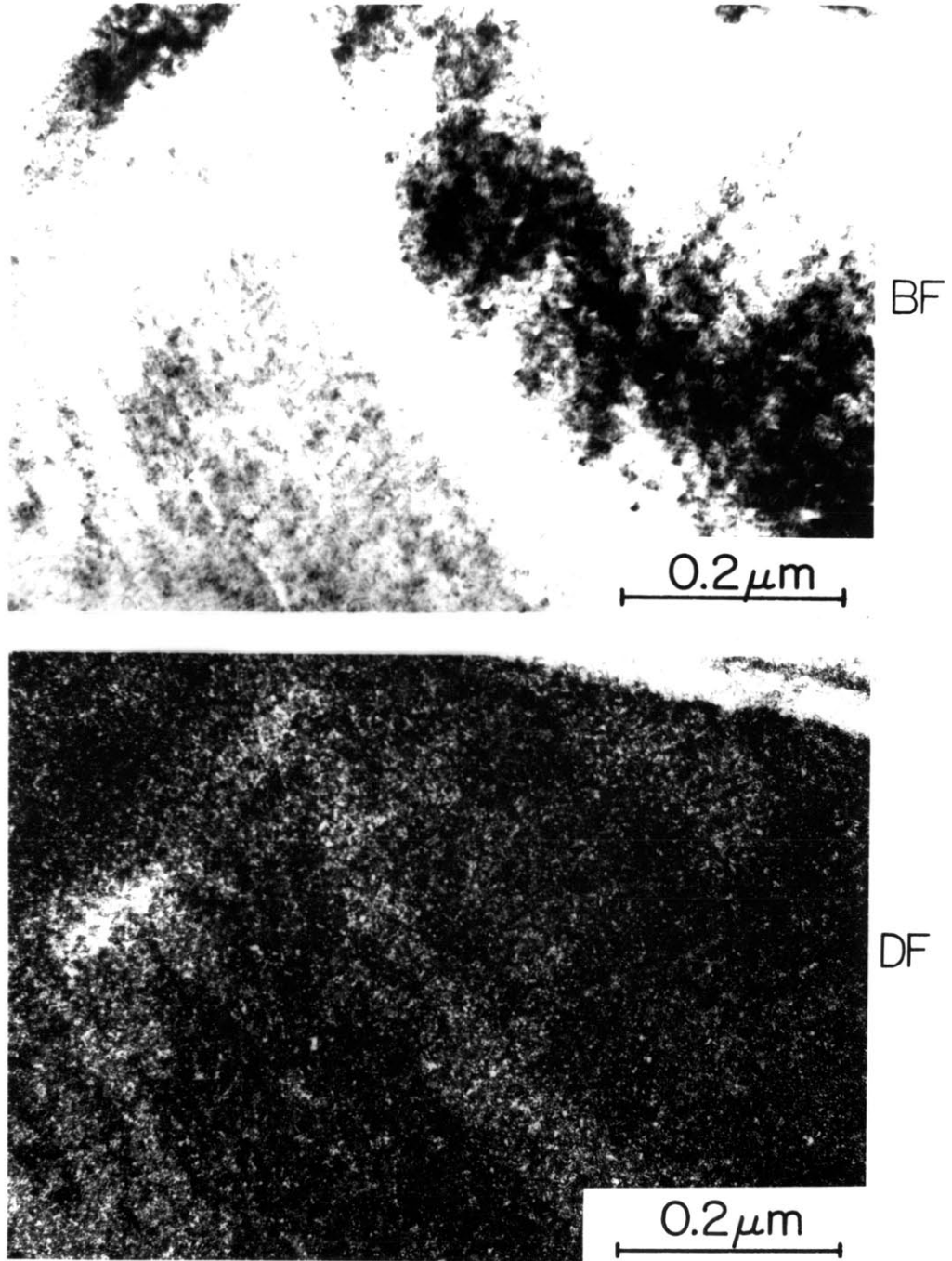
Figure D-5. Bright- and dark-field image pair of martensitic Fe-
15Ni-1C, aged 15 days at room temperature. The beam
direction is near $[001]_\alpha$ and near a <100> magnetite
zone. The dark-field image was formed with a
magnetite {022} reflection.

from similar dark-field images. However, this conclusion seems open to question since such small crystallites should, in theory, produce much more diffuse diffraction spots than those that are actually observed. It may rather be that a somewhat continuous layer of Fe_3O_4 covers the surface, and that the dark-field image contrast arises from local variations in strain and/or orientation.

Occasionally, relatively large crystals of what appears to be magnetite were also observed on the thin foils. An example is shown in the lattice fringe image of Figure D-4(C). The fringe spacing is 0.484 nm here, very close to the {111} interplanar spacing for magnetite.

The fine-grained magnetite or maghemite which gives rise to ring-type diffraction patterns is most commonly associated with the thinnest regions of a foil. This oxide was routinely found near the edges of holes, including those formed at the locations of inclusion particles. Sometimes large aggregates of the oxide formed, exhibiting a wrinkled texture (Figure D-4), probably due to the stresses generated by the impingment of different domains.

D.3 Discussion

The above observations of the oxidation of thin foils have some important implications. The microscopist must recognize that surface contamination can be a problem with metals and alloys susceptible to oxidation, and can lead to erroneous interpretation of images and diffraction patterns. For example, the {220} oxide reflections of Figure D-2 very nearly coincide with the forbidden {100} reflections of the BCC (A2) structure and could be taken as evidence of an ordered CsCl-type (B2) arrangement of iron and nickel atoms. More importantly (from the

264

standpoint of aging), the same oxide reflections can be mistaken for the $\{11\underline{0}\}$ reflections of coherent Fe_4C. Finally, some oxide reflections can also coincide with those of epsilon- or eta-carbide, and some care need be exercised when interpreting diffraction patterns from these phases. Difficulties of the above nature are discussed as they arise in the presentation of TEM results in Chapters 7 and 8.

In summary, at least two different oxide morphologies have been observed on the TEM foils of this investigation: magnetite (Fe_3O_4), which tends to form epitaxially, and a fine-grained oxide which may be maghemite ($\gamma-Fe_2O_3$) or magnetite and tends to be more randomly-oriented. The epitaxial oxide provides a more potent source of artifactual misinformation since its single-crystal diffraction pattern can be mistakenly associated with a bulk phase. On the other hand, the presence of the fine-grained, randomly-oriented oxide can often be easily deduced from its associated diffraction rings.

APPENDIX E
RESULTS OF THE BOWLES-MACKENZIE ANALYSIS

The following pages are reproductions of the output from the Ledbetter-Wayman [122] computer program. The parameters input by the user are listed under "INPUT." All parameters are defined in the legend.

Legend

E^* – eigenvalues of lattice deformation

$P2^*$ – internal accommodation shear plane

$D2^*$ – accommodation deformation direction

DETE – determinant of E (represents volume ratio of the product phase to the parent phase)

DEL – isotropic dilatation parameter (default: 1.0)

X1,X2 – invariant lines

N1,N2 – invariant normals

M1 – magnitude of shape deformation

M2 – magnitude of accommodation deformation

THETA – rigid body rotation angle

P1 – invariant (habit) plane

D1 – shape deformation

U – rotation axis

P1(3x3) – shape deformation matrix

P2(3x3) – accommodation deformation matrix

R – rotation matrix

B – lattice deformation matrix

S – invariant line strain matrix

SI – inverse of S

DETP1 – determinant of shape deformation matrix, P1(3x3)

CRN,DGN* – matrices whose column vectors are the normalized coordinates of the crystal space and the space in which B is diagonal, respectively.

*user-supplied input

Output for Fe-25Ni-0.4C

INPUT

E	P2	D2
1.127129	0.	0.
1.077801	1.000000	1.000000
0.952215	1.000000	-1.000000

1.156771=DETE
1.000000=DEL

INVARIANT LINES AND NORMALS

X1	X2	N1	N2
0.862271	0.862271	0.758244	0.758244
0.358112	-0.358112	0.461013	-0.461013
-0.358112	0.358112	0.461013	-0.461013

VARIANTS

(X1,N1) | (X2,N2) | (X1,N2) | (X2,N1)

M1	M2	THETA	M1	M2	THETA	M1	M2	THETA	M1	M2	THETA
0.262606	0.185498	7.774613	0.262606	0.185498	7.774613	0.262606	0.185498	7.774613	0.262606	0.185498	7.774613

P1 / D1 / U

P1	D1	U	P1	D1	U	P1	D1	U	P1	D1	U
-0.404878	0.491855	-0.696182	0.404878	-0.491855	-0.696182	0.404878	-0.491855	0.696182	-0.404878	0.491855	0.696182
0.062654	0.059660	-0.713054	0.062654	0.059660	0.713054	-0.912222	-0.868631	-0.082976	-0.912222	-0.868631	0.082976
-0.912222	-0.868631	-0.082976	-0.912222	-0.868631	0.082976	0.062654	0.059660	-0.713054	0.062654	0.059660	0.713054

P1

0.947704	0.008093	-0.117826	0.947704	-0.008093	0.117826	0.947704	0.117826	-0.008093	0.947704	-0.117826	0.008093
-0.006343	1.000982	-0.014292	0.006343	1.000982	-0.014292	-0.092356	1.208085	-0.014292	0.092356	1.208085	-0.014292
0.092356	-0.014292	1.208085	-0.092356	-0.014292	1.208085	0.006343	-0.014292	1.000982	-0.006343	-0.014292	1.000982

P2

1.000000	-0.000000	-0.000000	1.000000	0.000000	0.000000	1.000000	0.000000	0.000000	1.000000	-0.000000	-0.000000
0.	1.092749	0.092749	0.	1.092749	0.092749	0.	0.907251	-0.092749	0.	0.907251	-0.092749
0.	-0.092749	0.907251	0.	-0.092749	0.907251	0.	0.092749	1.092749	0.	0.092749	1.092749

R

0.995263	0.015788	-0.095928	0.995263	-0.015788	0.095928	0.995263	0.095928	-0.015788	0.995263	-0.095928	0.015788
-0.006662	0.995482	0.094721	0.006662	0.995482	0.094721	-0.096990	0.990871	-0.093633	0.096990	0.990871	-0.093633
0.096990	-0.093633	0.990871	-0.096990	-0.093633	0.990871	0.006662	0.094721	0.995482	-0.006662	0.094721	0.995482

B

0.952215	0.	0.	0.952215	0.	0.	0.952215	0.	0.	0.952215	0.	0.
0.	1.102465	-0.024664	0.	1.102465	-0.024664	0.	1.102465	-0.024664	0.	1.102465	-0.024664
0.	-0.024664	1.102465	0.	-0.024664	1.102465	0.	-0.024664	1.102465	0.	-0.024664	1.102465

S

0.947704	0.019771	-0.106147	0.947704	-0.019771	0.106147	0.947704	0.106147	-0.019771	0.947704	-0.106147	0.019771
-0.006343	1.095147	0.079874	0.006343	1.095147	0.079874	-0.092356	1.094710	-0.127666	0.092356	1.094710	-0.127666
0.092356	-0.127666	1.094710	-0.092356	-0.127666	1.094710	0.006343	0.079874	1.095147	-0.006343	0.079874	1.095147

SI

1.045208	-0.006996	0.101858	1.045208	0.006996	-0.101858	1.045208	-0.101858	0.006996	1.045208	0.101858	-0.006996
0.012380	0.905335	-0.064856	-0.012380	0.905335	-0.064856	0.086736	0.897327	0.106171	-0.086736	0.897327	0.106171
-0.086736	0.106171	0.897327	0.086736	0.106171	0.897327	-0.012380	-0.064856	0.905335	0.012380	-0.064856	0.905335

1.156771=DETP1	1.156771	1.156771	1.156771

CRN | DGN

CRN			DGN		
1.000000	0.	0.	0.	0.	1.000000
0.	1.000000	0.	0.707107	0.707107	0.
0.	0.	1.000000	-0.707107	0.707107	0.

Output for Fe-15Ni-1C

INPUT

E	P2	D2
1.140733	0.	0.
1.079139	1.000000	1.000000
0.961672	1.000000	-1.000000

1.183827=DETE
1.000000=DEL

INVARIANT LINES AND NORMALS

X1	X2	N1	N2
0.894583	0.894583	0.796718	0.796718
0.316008	-0.316008	0.427341	-0.427341
-0.316008	0.316008	0.427341	-0.427341

VARIANTS

(X1,N1)			(X2,N2)			(X1,N2)			(X2,N1)		
M1	M2	THETA	M1	M2	THETA	M1	M2	THETA	M1	M2	THETA
0.269337	0.195179	7.701402	0.269337	0.195179	7.701402	0.269337	0.195179	7.701402	0.269337	0.195179	7.701402
P1	D1	U	P1	D1	U	P1	D1	U	P1	D1	U
-0.356808	0.439235	-0.743188	0.356808	-0.439235	-0.743188	0.356808	-0.439235	0.743188	-0.356808	0.439235	0.743188
0.079278	0.076239	-0.663000	0.079278	0.076239	0.663000	-0.930808	-0.895132	-0.090017	-0.930808	-0.895132	0.090017
-0.930808	-0.895132	-0.090017	-0.930808	-0.895132	0.090017	0.079278	0.076239	-0.663000	0.079278	0.076239	0.663000
P1			P1			P1			P1		
0.957789	0.009379	-0.110117	0.957789	-0.009379	0.110117	0.957789	0.110117	-0.009379	0.957789	-0.110117	0.009379
-0.007327	1.001628	-0.019113	0.007327	1.001628	-0.019113	-0.086024	1.224411	-0.019113	0.086024	1.224411	-0.019113
0.086024	-0.019113	1.224411	-0.086024	-0.019113	1.224411	0.007327	-0.019113	1.001628	-0.007327	-0.019113	1.001628
P2			P2			P2			P2		
1.000000	-0.000000	-0.000000	1.000000	0.000000	0.000000	1.000000	0.000000	0.000000	1.000000	-0.000000	-0.000000
0.	1.097589	0.097589	0.	1.097589	0.097589	0.	0.902411	-0.097589	0.	0.902411	-0.097589
0.	-0.097589	0.902411	0.	-0.097589	0.902411	0.	0.097589	1.097589	0.	0.097589	1.097589
R			R			R			R		
0.995962	0.016508	-0.088245	0.995962	-0.016508	0.088245	0.995962	0.088245	-0.016508	0.995962	-0.088245	0.016508
-0.007619	0.994945	0.100133	0.007619	0.994945	0.100133	-0.089452	0.991053	-0.099057	0.089452	0.991053	-0.099057
0.089452	-0.099057	0.991053	-0.089452	-0.099057	0.991053	0.007619	0.100133	0.994945	-0.007619	0.100133	0.994945
B			B			B			B		
0.961672	0.	0.	0.961672	0.	0.	0.961672	0.	0.	0.961672	0.	0.
0.	1.109936	-0.030797	0.	1.109936	-0.030797	0.	1.109936	-0.030797	0.	1.109936	-0.030797
0.	-0.030797	1.109936	0.	-0.030797	1.109936	0.	-0.030797	1.109936	0.	-0.030797	1.109936
S			S			S			S		
0.957789	0.021040	-0.098455	0.957789	-0.021040,	0.098455	0.957789	0.098455	-0.021040	0.957789	-0.098455	0.021040
-0.007327	1.101241	0.080500	0.007327	1.101241	0.080500	-0.086024	1.103056	-0.140468	0.086024	1.103056	-0.140468
0.086024	-0.140468	1.103056	-0.086024	-0.140468	1.103056	0.007327	0.080500	1.101241	-0.007327	0.080500	1.101241
SI			SI			SI			SI		
1.035657	-0.007922	0.093018	1.035657	0.007922	-0.093018	1.035657	-0.093018	0.007922	1.035657	0.093018	-0.007922
0.012676	0.899594	-0.064520	-0.012676	0.899594	-0.064520	0.079153	0.891102	0.115176	-0.079153	0.891102	0.115176
-0.079153	0.115176	0.891102	0.079153	0.115176	0.891102	-0.012676	-0.064520	0.899594	0.012676	-0.064520	0.899594

1.183827=DETP1   1.183827   1.183827   1.183827

	CRN				DGN	
1.000000	0.	0.	0.	0.	1.000000
0.	1.000000	0.	0.707107	0.707107	0.
0.	0.	1.000000	-0.707107	0.707107	0.

REFERENCES

1. K. H. Jack, "Structural Transformations in the Tempering of High-Carbon Martensitic Steels," *JISI* 169 (1951) 26.

2. G. B. Olson and M. Cohen, "Early Stages of Aging and Tempering of Ferrous Martensites," *Metall. Trans.* 14A (1983) 1057.

3. J. Chipman, "Thermodynamics and Phase Diagram of the Fe-C System," *Metall. Trans.* 3 (1972) 55.

4. M. Cohen, G. B. Olson, and P. C. Clapp, "On the Classification of Displacive Transformations," *Proc. Int. Conf. on Martensitic Transformations* (ICOMAT-79), Cambridge, MA (1979) 1.

5. R. F. Bunshah and R. F. Mehl, "Rate of Propagation of Martensite," *Trans. AIME* 197 (1953) 1251.

6. L. Kaufman and M. Cohen, "Thermodynamics and Kinetics of Martensitic Transformations," *Progress in Metal Physics* 7 (1958) 165.

7. Z. Nishiyama, *Martensitic Transformation*, Academic Press, N.Y. (1978).

8. M. Cohen and C. M. Wayman, "Fundamentals of Martensitic Reactions," in *Metallurgical Treatises*, J. K. Tien and J. F. Elliott, eds., TMS-AIME, Warrendale, PA (1981) 445.

9. A. G. Khachaturyan, *Theory of Structural Transformations in Solids*, Wiley, New York (1983).

10. R. C. Ruhl, *Splat Quenching of Iron-Base Alloys*, Ph.D. Thesis, MIT (1967).

11. J. R. Genin and P. A. Flinn, "Mössbauer Effect Study of the Clustering of Carbon Atoms During the Room-Temperature Aging of Iron-Carbon Martensite," *Trans. AIME* 242 (1968) 1419.

12. W. K. Choo and Roy Kaplow, "Mössbauer Measurements on the Aging of Iron-Carbon Martensite," *Acta Metall.* 21 (1973) 725.

13. V. N. Gridnev, V. G. Gavrilyuk, V. V. Nemoshkalenko, Yu. A. Polushkin, and O. N. Razumov, "Mössbauer Study of the Structure of Iron-Carbon Martensite," *Phys. Met. Metallogr.* 43(#3) (1977) 109.

14. I. R. Entin, V. A. Somenkov, and S. Sh. Shil'shtein, "Atomic and Magnetic Structure of Martensite in Hardened Steel," *Sov. Phys. Dokl.* 17 (1973) 1021.

15. W. C. Leslie, *The Physical Metallurgy of Steels*, McGraw-Hill, New York (1981).

16. H. I. Aaronson, H. A. Domian, and G. M. Pound, "Thermodynamics of the Austenite → Proeutectoid Ferrite Transformation. I, Fe-C Alloys," *Trans. AIME* 236 (1966) 753.

17. R. E. Reed-Hill, <u>Physical Metallurgy Principles</u>, Van Nostrand, New York (1973).

18. E. C. Bain, "The Nature of Martensite," <u>Trans. AIME</u> <u>70</u> (1924) 25.

19. R. Kaplow, M. Ron, and N. DeCristofaro, "Mössbauer Effect Studies of Tempered Martensite," <u>Metall. Trans.</u> <u>14A</u> (1983) 1135.

20. F. E. Fujita, T. Moriya, and H. Ino, "Low-Temperature Phase and Tetrahedral Site of Carbon in Iron-Carbon Martensite," <u>Proc. Int. Conf. Sci. Technol. Iron Steel (1970)</u>, Iron and Steel Inst. Jpn. (1971) 1273.

21. H. Ino, T. Ito, S. Nasu, and U. Gonser, "A Study of Interstitial Atom Configuration in Fresh and Aged Iron-Carbon Martensite by Mössbauer Spectroscopy," <u>Acta Metall.</u> <u>30</u> (1982) 9.

22. N. DeCristofaro and R. Kaplow, "Interstitial Atom Configurations in Stable and Metastable Fe-N and Fe-C Solid Solutions," <u>Metall. Trans.</u> <u>8A</u> (1977) 35.

23. C. Zener, "Kinetics of the Decomposition of Austenite," <u>Trans. AIME</u> <u>167</u> (1946) 550.

24. C. Zener, "Theory of Strain Interaction of Solute Atoms," <u>Phys. Rev. (Ser.2)</u> <u>74</u> (1948) 639.

25. A. M. Sherman, <u>The Structure and Aging of Martensite</u>, Ph.D. Thesis, MIT (1972).

26. G. R. Speich and W. C. Leslie, "Tempering of Steel," <u>Metall. Trans. 3</u> (1972) 1043.

27. A. R. Marder and G. Krauss, "The Morphology of Martensite in Iron-Carbon Alloys," <u>Trans. ASM</u> <u>60</u> (1967) 651.

28. G. R. Speich, "Tempering of Low-Carbon Martensite," <u>Trans. AIME</u> <u>245</u> (1969) 2553.

29. M. Kehoe and P. M. Kelly, "The Role of Carbon in the Strength of Ferrous Martensite," <u>Scripta Metall.</u> <u>4</u> (1970) 473.

30. L. A. Norstrom, "On the Yield Strength of Quenched Low-Carbon Lath Martensite," <u>Scand. J. Metallurgy</u> <u>5</u> (1976) 159.

31. K. Wakasa and C. M. Wayman, "The Crystallography and Morphology of Lath Martensite in Fe-20Ni-5Mn," <u>Proc. Int. Conf. on Martensitic Transformations</u>(ICOMAT-79), Cambridge, MA (1979) 34.

32. G. Krauss and A. R. Marder, "The Morphology of Martensite in Iron Alloys," <u>Metall. Trans. 2A</u> (1971) 2343.

33. R. L. Patterson and C. M. Wayman, "The Crystallography and Growth of Partially-Twinned Martensite Plates in Fe-Ni Alloys," Acta Metall. 14 (1966) 347.

34. P. G. Winchell, The Structure and Mechanical Properties of Iron-Nickel-Carbon Martensites, Ph.D. Thesis, MIT (1958).

35. M. S. Wechsler, D. S. Lieberman, and T. A. Read, "On the Theory of the Formation of Martensite," Trans. AIME 197 (1953) 1503.

36. J. S. Bowles and J. K. Mackenzie, "The Crystallography of Martensite Transformations I-III," Acta Metall. 2 (1954) 129; 138; 224.

37. R. Bullough and B. A. Bilby, "The Continuous Distributions of Dislocations: Surface Dislocations and the Crystallography of Martensite Transformations," Proc. Phys. Soc. B69 (1956) 1276.

38. J. W. Christian, Theory of Transformations in Metals and Alloys, Pergamon, Oxford (1965).

39. A. L. Roytburd and A. G. Khachaturyan, "Interstitial Atoms and the Crystallographic Mechanism of Martensite Transformation in Steels," Phys. Met. Metallogr. 30(#6) (1970) 68.

40. G. V. Kurdjumov and A. G. Khachaturyan, "Nature of Axial Ratio Anomalies of the Martensite Lattice and Mechanism of Diffusionless $\gamma \rightarrow \alpha$ Transformation," Acta Metall. 23 (1975) 1077.

41. G. V. Kurdyumov, V. K. Kritskaya, and V. A. Il'ina, "Special Aspects of the Changes Taking Place in the Crystal Lattice Parameters of Iron-Aluminum-Carbon Martensite After Electron Irradiation," Sov. Phys. Dokl. 19 (1975) 850.

42. A. K. Sachdev, The Substructure and Aging of High-Carbon Ferrous Martensites, Sc.D. Thesis, MIT (1977).

43. M. Oka and C. M. Wayman, "{110} Twinning in Bct Martensite," Trans. AIME 242 (1968) 337.

44. M. Oka and C. M. Wayman, "Electron Metallography of the Substructure of Martensite in High-Carbon Steels," Trans. ASM 62 (1969) 370.

45. R. Oshima and C. M. Wayman, "Substructure of Thin Foil (225) Ferrous Martensites," Trans. JIM 16 (1975) 73.

46. D. H. Jack and K. H. Jack, "Carbides and Nitrides in Steel," Mater. Sci. Eng. 11 (1973) 1.

47. Y. Imai, "Phases in Quenched and Tempered Steels," Trans. JIM 16 (1975) 721.

48. C. S. Roberts, B. L. Averbach, and M. Cohen (with Appendix B by B. S. Lement), "The Mechanism and Kinetics of the First Stage of Tempering," Trans. ASM 45 (1953) 576.

49. M. G. H. Wells, "An Electron Transmission Study of the Tempering of Martensite in an Fe-Ni-C Alloy," Acta Metall. 12 (1964) 389.

50. H. W. Wagenblast and R. Glenn, "Dislocation Production in Alpha Fe-C Alloys by Rapid Heating," Metall. Trans. 1 (1970) 2299.

51. S. Murphy and J. A. Whiteman, "The Precipitation of Epsilon-Carbide in Twinned Martensite," Metall. Trans. 1 (1970) 843.

52. Y. Hirotsu and S. Nagakura, "Crystal Structure and Morphology of the Carbide Precipitated From Martensitic High Carbon Steel During the First Stage of Tempering," Acta Metall. 20 (1972) 645.

53. F. E. Werner, B. L. Averbach, and M. Cohen, "The Tempering of Iron-Carbon Martensite Crystals," Trans. ASM 49 (1956) 823.

54. M. Sarikaya, A. K. Jhingan, and G. Thomas, "Retained Austenite and Tempered Martensite Embrittlement in Medium Carbon Steels," Metall. Trans. 14A (1983) 1121.

55. Yu. A. Bagaryatskii, Dokl. Acad. Nauk SSSR 73 (1950) 1161.

56. I. V. Isaichev, Zhurnal Tekhnicheskoi Fiziki 17 (1947) 835.

57. D. Kalish, The Effect of Strain Tempering on Strength and Toughness of Steel, Sc.D. Thesis, MIT (1966).

58. D. Kalish and M. Cohen, "Structural Changes and Strengthening in the Strain Tempering of Martensite," Mater. Sci. Eng. 6 (1970) 156.

59. Y. Ohmori, "χ-carbide Formation and Its Transformation into Cementite during the Tempering of Martensite," Trans. JIM 13 (1972) 119.

60. S. Nagakura, T. Suzuki, and M. Kusunoki, "Structure of the Precipitated Particles at the Third Stage of Tempering of Martensitic Iron-Carbon Steel Studied by High-Resolution Electron Microscopy," Trans. JIM 22 (1981) 699.

61. K. W. Andrews, D. J. Dyson, and S. R. Keown, Interpretation of Electron Diffraction Patterns, Hilger and Watts Ltd., London, 1967.

62. S. Oketani, S. Hitomi, and S. Nagakura, "Study of Tempering of Quenched Carbon Steel by Specific Heat Measurement," J. Jpn. Inst. Metals 26 (1962) 494.

63. P. G. Winchell and M. Cohen, "The Strength of Martensite," Trans. ASM 55 (1962) 347.

64. V. I. Izotov and L. M. Utevskiy, "The Structure of the Martensite Crystals of High-Carbon Steel," Phys. Met. Metallogr. 25(#1) (1968) 86.

65.   S. Nagakura, Y. Hirotsu, M. Kusunoki, T. Suzuki, and Y. Nakamura, "Crystallographic Study of the Tempering of Martensitic Carbon Steel by Electron Microscopy and Diffraction," Metall. Trans. 14A (1983) 1025.

66.   P. J. Fillingham, H. J. Leamy, and L. E. Tanner, in Electron Microscopy and Structure of Materials, G. Thomas ed., Univ. Cal. Press, Berkeley, CA (1972) 163.

67.   Y. Nakamura and S. Nagakura, "UHV-HR-1 MV Electron Microscope Observation of Modulated Structure and Precipitated Carbide in Tempered Iron-Carbon Martensite," Proc. 7th Int. Conf. High Voltage Elec. Microsc. (1983) 221.

68.   P. C. Chen, B. O. Hall, and P. G. Winchell, "Atomic Displacements Due to C in Fe-Ni-C Martensite," Metall. Trans. 11A (1980) 1323.

69.   P. C. Chen and P. G. Winchell, "Martensite Lattice Changes During Tempering," Metall. Trans. 11A (1980) 1333.

70.   A. M. Sherman, G. T. Eldis, and M. Cohen, "The Aging and Tempering of Fe-Ni-C Martensites," Metall. Trans. 14A (1983) 995.

71.   M. Hillert, "The Kinetics of the First Stage of Tempering," Acta Metall. 7 (1959) 653.

72.   M. Kajatkari, K. Ullakko, and J. Pietikäinen, "On the Aging of Fe-Ni-C and Fe-Mn-C Martensites," Proc. Int. Conf. on Martensitic Transformations(ICOMAT-82), Leuven, Belgium (1982) 461.

73.   M. K. Miller, P. A. Beaven, G. D. W. Smith, and S. S. Brenner, Proc. Int. Conf. on Solid → Solid Phase Transformations, H. I. Aaronson, D. E. Laughlin, R. F. Sekerka and C. M. Wayman eds., TMS-AIME, Warrendale, PA (1982) 863.

74.   M. K. Miller, P. A. Beaven, S. S. Brenner, and G. D. W. Smith, "An Atom Probe Study of the Aging of Iron-Nickel-Carbon Martensite," Metall. Trans. 14A (1983) 1021.

75.   G. T. Eldis, Ausforming and Tempering of High-Alloy Steels, Ph.D. Thesis, MIT (1971).

76.   M. Umemoto and I. Tamura, "Butterfly Martensite in Fe-Ni-C Alloys," Proc. Int. Conf. on Martensitic Transformations(ICOMAT-79), Cambridge, MA (1979) 53.

77.   H. R. Clark, The Martensitic Transformation in Iron-Nickel Single Crystals and Bicrystals, Ph.D. Thesis, MIT (1982).

78.   M. Umemoto, T. Hyodo, T. Maeda, and I. Tamura, "Electron Microscopy Studies of Butterfly Martensite," Acta Metall. 32 (1984) 1191.

79. P. Hirsch, A. Howie, R. B. Nicholson, D. W. Pashley, and M. J. Whelan, Electron Microscopy of Thin Crystals, Krieger, Huntington, New York (1977).

80. M. Kehoe and P. M. Kelly, "The Role of Carbon in the Strength of Ferrous Martensite," Scripta Metall. 4 (1970) 473.

81. L. I. Lysak, S. P. Kondrat'yev, and Yu. M. Polishchuk, "Dependence of the Crystal Structure of κ'- and α-Martensites on Carbon Concentration," Phys. Met. Metallogr. 36(#3) (1973) 85.

82. X. Xie, research in progress at MIT.

83. D. W. Hoffman, Ausform-Strengthening of Iron-Nickel-Carbon Martensite, Ph.D. Thesis, MIT (1966).

84. D. W. Hoffman and M. Cohen, "Static Displacements and the Electrical Resistivity of Interstitial Alloys," Acta Metall. 21 (1973) 1215.

85. M. Cohen, "Self-Diffusion During Plastic Deformation," Trans. JIM 11 (1970) 145.

86. F. S. Buffington, K. Hirano, and M. Cohen, "Self-Diffusion of Iron," Acta Metall. 9 (1961) 434.

87. B. P. J. Sandvik and C. M. Wayman, "Direct Observations of Carbon Clusters in a High-Carbon Martensitic Steel," Metallography 16 (1983)429.

88. M. Kusunoki and S. Nagakura, "Modulated Structure of Iron-Carbon Martensite Studied by Electron Microscopy and Diffraction," J. Appl. Cryst. 14 (1981) 329.

89. D. E. Laughlin, A High Resolution Electron Microscopy Study of Spinodal Decomposition and Coarsening in Copper-Titanium Alloys, Ph.D. Thesis, MIT (1973).

90. J. J. Weins, The Effect of Environment on Coarsening, Ph.D. Thesis, MIT (1970).

91. A. J. Ardell and R. B. Nicholson, "On the Modulated Structure of Aged Ni-Al Alloys," Acta Metall. 14 (1966) 1295.

92. L. Chang, A. Cerezo, G. D. W. Smith, M. K. Miller, M. G. Burke, S. S. Brenner, K. A. Taylor, T. Abe, and G. B. Olson, "Aging of Fe-Ni-C Martensite," J. de Phys. 45 (1984) C9-409.

93. G. D. W. Smith, private communication.

94. P. Ferguson and K. H. Jack, "Quench-Aging and Strain-Aging of Nitrogen-Ferrite," in Heat Treatment '81, The Metals Society, London (1983) 158-63.

95. J. W. Cahn, "On Spinodal Decomposition in Cubic Crystals," Acta Metall. 10 (1962) 179.

96. C. Zener, "Equilibrium Relations in Medium-alloy Steels," Trans. AIME 167 (1946) 513.

97. J. C. Fisher, "The Free Energy Change Accompanying the Martensite Transformation in Steels," Trans. AIME 185 (1949) 688.

98. M. Cohen, E. S. Machlin, and V. J. Paranjpe, in Thermodynamics in Metallurgy, ASM, Cleveland (1949) 242.

99. L. Kaufman, S. V. Radcliffe, and M. Cohen, "Thermodynamics of the Bainite Reaction," in Decomposition of Austenite by Diffusion Controlled Processes, Interscience, New York (1962) 313.

100. G. J. Shiflet, J. R. Bradley, and H. I. Aaronson, "A Re-examination of the Thermodynamics of the Proeutectoid Ferrite Transformation in Fe-C Alloys," Metall. Trans. 9A (1978) 999.

101. Y. Imai, M. Izumiyama, and M. Tsuchiya, "Thermodynamic Study on the Transformation of Austenite into Martensite in Iron-High Nitrogen and Iron-Carbon Binary System," Sci. Rep. RITU 17 (1965) 173.

102. H. K. D. H. Bhadeshia and D. V. Edmonds, "The Mechanism of Bainite Formation in Steels," Acta Metall. 28 (1980) 1265.

103. J. Agren, "A Thermodynamic Analysis of the Fe-C and Fe-N Phase Diagrams," Metall. Trans 10A (1979) 1847.

104. R. B. McLellan and W. W. Dunn, "A Quasi-Chemical Treatment of Interstitial Solid Solutions: Its Application to Carbon Austenite," J. Phys. Chem. Solids 30 (1969) 2631.

105. L. Kaufman and H. Nesor, "Coupled Phase Diagrams and Thermochemical Data for Transition Metal Binary Systems--IV," CALPHAD 2 (1978) 295.

106. H. K. Hardy, "A 'Sub-Regular' Solution Model and its Application to Some Binary Alloy Systems," Acta Metall. 1 (1953) 202.

107. L. Kaufman, "Summary of the Proceedings of the Twelfth CALPHAD Meeting," CALPHAD 7 (1983) 273.

108. L. Kaufman and H. Nesor, "Calculation of the Binary Phase Diagrams of Iron, Chromium, Nickel and Cobalt," Z. Metallk. 64 (1973) 249.

109. H. K. D. H. Bhadeshia, "Driving Force for Martensitic Transformation in Steels," Met. Sci. (1981) 175.

110. W. S. Owen, F. J. Schoen, and G. R. Srinivasan, in Phase Transformations, ASM, Metals Park (1970) 157.

111. W. A. Soffa and D. E. Laughlin, "Recent Experimental Studies of Continuous Transformations in Alloys: An Overview," Proc. Intl. Conf. on Solid → Solid Transformations, H. I. Aaronson et al. eds., TMS-AIME, Warrendale, PA (1982) 159.

112. S. M. Allen and J. W. Cahn, "Mechanisms of Phase Transformations Within the Miscibility Gap of Fe-Rich Fe-Al Alloys," Acta Metall. 24 (1976) 425.

113. M. van Rooyen and E. J. Mittemeijer, "Differential Thermal Analysis of Iron-Carbon Martensites," Scripta Metall. 16 (1982) 1255.

114. E. J. Mittemeijer and F. C. van Doorn, "Heat Effects of Preprecipitation Stages on Tempering of Carbon Martensites," Metall. Trans. 14A (1983) 976.

115. J. W. Cahn, "Spinodal Decomposition," Trans. AIME 242 (1968) 166.

116. K. Shimizu and H. Okamoto, "High Voltage Electron Microscopy Study of the Metastable Iron Carbide in a Eutectoid Fe-C Alloy," Trans. JIM 15 (1974) 193.

117. Y. Tanaka and K. Shimizu, "Carbide Formation upon Tempering at Low Temperatures in Fe-Mn-C Alloys," Trans. JIM 22 (1981) 779.

118. D. L. Williamson, K. Nakazawa, and G. Krauss, "A Study of the Early Stages of Tempering in an Fe-1.2 Pct C Alloy," Metall. Trans. 10A (1979) 1351.

119. Y. Hirotsu, Y. Itakura, K. Su, and S. Nagakura, "Electron Microscopy and Diffraction Study of the Carbide Precipitated from Martensitic Low and High Nickel Steels at the First Stage of Tempering," Trans. JIM 17 (1976) 503.

120. E. Tekin and P. M. Kelly, "A Study of the Tempering of Steel Using Transmission Electron Microscopy," in Precipitation from Iron-Base Alloys, G. R. Speich and J. B. Clark eds., AIME (1965) 173.

121. C. M. Wayman, Introduction to the Crystallography of Martensitic Transformations, MacMillan, New York (1964).

122. H. M. Ledbetter and C. M. Wayman, "A Computer Program for Martensite Crystallography," Mater. Sci. Eng. 7 (1971) 151.

123. A. G. Crocker and B. A. Bilby, "On the Theory of Martensite Crystallography," Acta Metall. (1961) 992.

124. W. Rong and G. L. Dunlop, "The Crystallography of Secondary Carbide Precipitation in High Speed Steel," Acta Metall. 32 (1984) 1591.

125. G. Krauss, "Tempering and Structural Change in Ferrous Martensitic Structures," in Proc. Int. Conf. on Phase Transformations in Ferrous Alloys, A. R. Marder and J. I. Goldstein eds., TMS-AIME, Warrendale, PA (1984) 101.

126. R. L. Brown, H. J. Rack, and M. Cohen, "Stress Relaxation During the Tempering of Hardened Steel," Mater. Sci. Eng. 21 (1975) 25.

127. T. Vilo and J. Pietikäinen, "Microcracks in Fe-Ni-C Martensites," Proc. Intl. Conf. on Martensitic Transformations (ICOMAT-79), Cambridge, MA (1979) 721.

128. M. P. Cassidy and C. M. Wayman, "Crystallography of Shear Transformations in Zirconium Hydrides," Proc. Intl. Conf. on Martensitic Transformations (ICOMAT-79), Cambridge, MA (1979) 202.

129. C. Kittel, Introduction to Solid State Physics, Wiley, New York (1976).

130. B. D. Cullity, Introduction to Magnetic Materials, Addison-Wesley, Reading, MA (1972) 67.

131. R. P. Smith, "The Diffusivity and Solubility of Carbon in Alpha-Iron," Trans. AIME 224 (1962) 105.

132. S. I. Ali and G. C. Wood, "Oxidation of Iron at Room Temperature," Br. Corros. J. 4 (1969) 133.

133. J. B. Wagner, Jr., K. R. Lawless, and A. T. Gwathmey, "The Rates of Formation and Structure of Oxide Films Formed on a Single Crystal of Iron," Trans. AIME 221 (1961) 257.

134. L. E. Collins and O. S. Heavens, "The Epitaxial Growth and Oxidation of Nickel, Cobalt and Iron on Rocksalt," Proc. Phys. Soc. 70 (1957) 265.

135. S. Chen and J. W. Morris, Jr., "Electron Microscopy Study of the Passivating Layer on Iron-Nickel Martensite," Metall. Trans. 8A (1977) 19.

136. Z. Nishiyama, Sci. Rep. Tohoku Univ. 23 (1934) 638.

137. G. Wasserman, Arch. Eisenhuettenw. 16 (1933) 647.

BIOGRAPHICAL NOTE

Keith Allen Taylor was born in the midwestern town of Manitowoc, Wisconsin on February 21, 1958. His family moved to Sarasota, Florida in 1968, where he graduated from Pine View School in June, 1976. The following September he migrated back north to Cambridge, Massachusetts where he entered the Massachussetts Institute of Technology and was awarded the S.B. degree in Materials Science and Engineering in June, 1980. During the summers of 1979 and 1980 he also worked at ManLabs, Inc. in Cambridge.

In July of 1980, Keith and the former Deena Mae Grant took the vows of matrimony and promptly settled in MIT's Random Hall, where they became graduate residents. Keith re-entered MIT in September, 1980 as a graduate student in Metallurgy. He held a Rockwell International Fellowship for his first two years and was admitted to the doctoral program in November, 1981. He will assume a research position in industry upon completion of a postdoctoral appointment at MIT.